$Al_2O_3:Er^{3+}$ as a Gain Platform for Integrated Optics

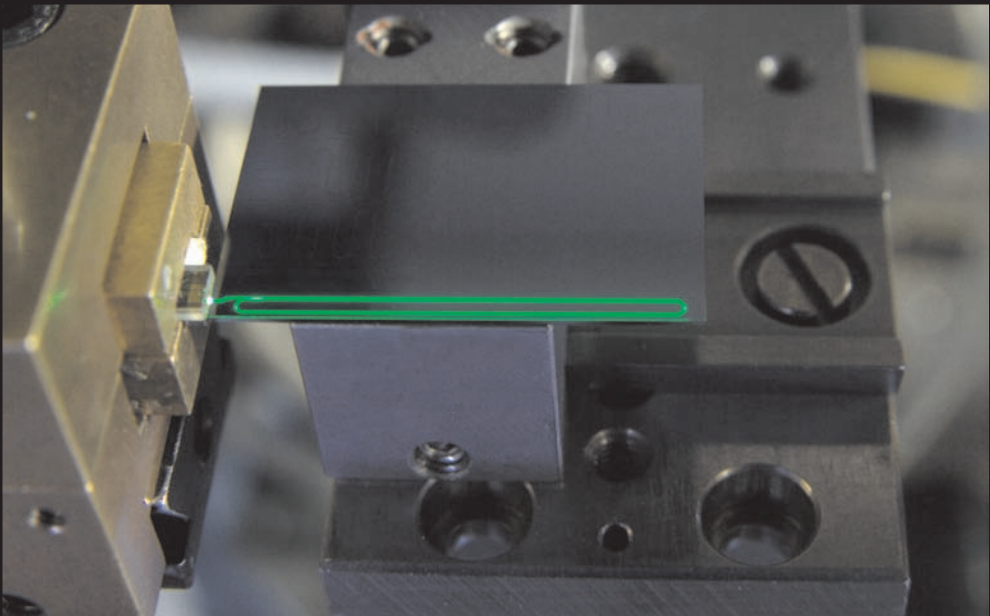

Jonathan Bradley

$Al_2O_3:Er^{3+}$ as a Gain Platform for Integrated Optics

Jonathan Bradley

Graduation committee:

Chairman and Secretary:

Prof. Dr. Ir. A. J. Mouthaan	University of Twente

Promoter:

Prof. Dr. M. Pollnau	University of Twente

Assistant Promoter:

Dr. K. Wörhoff	University of Twente

Members:

Prof. Dr. R. Baets	Ghent University
Prof. Dr. K. J. Boller	University of Twente
Prof. Dr. J. L. Herek	University of Twente
Dr. K. Petermann	University of Hamburg

The research described in this thesis was carried out at the Integrated Optical MicroSystems (IOMS) Group, Faculty of Electrical Engineering, Mathematics and Computer Science, MESA+ Institute for Nanotechnology, University of Twente, P.O. Box 217, 7500 AE Enschede, The Netherlands.

This work was financially supported by the European Union's Sixth Framework Programme (Specific Targeted Research Project "PI-OXIDE", contract no. 017501) and by the Smartmix Memphis programme of the Dutch Ministry of Economic Affairs.

Cover design:

Front: The first integrated $Al_2O_3:Er^{3+}$ laser with 976 nm pump light injected and emitting at 1532 nm. The characteristic green light emission due to energy transfer upconversion is visible.

Reverse: Scanning electron microscope image of an aluminum oxide channel waveguide (top), thermally oxidized silicon wafer with integrated $Al_2O_3:Er^{3+}$ photonic devices (middle) and top view of an $Al_2O_3:Er^{3+}$ channel waveguide injected with 976 nm pump light (bottom). *Cover photographs courtesy of Henk van Wolferen.*

ISBN: 978-90-365-2877-1

Printed by PrintPartners IPSKAMP, Enschede, The Netherlands

Copyright © 2009 by Jonathan Bradley, Enschede, The Netherlands

$Al_2O_3:ER^{3+}$ AS A GAIN PLATFORM FOR INTEGRATED OPTICS

DISSERTATION

to obtain
the degree of doctor at the University of Twente,
on the authority of the rector magnificus,
prof. dr. H. Brinksma,
on account of the decision of the graduation committee,
to be publicly defended
on Thursday the 17th of September 2009 at 15:00

by

Jonathan David Barnes Bradley
born on the 19th of January 1980
in Oakville, Ontario, Canada

This dissertation is approved by:

the promoter: Prof. Dr. M. Pollnau

the assistant promoter: Dr. K. Wörhoff

This thesis is dedicated to my family…

Contents

1. Introduction: Er-doped Thin Films for Integrated Optics 1

1.1 Integrated Optics 2
1.2 Rare-Earth-Doped Optical Waveguides 4
1.3 Active Planar Devices Based on Er-Doped Thin Films 4
1.3.1 Erbium-doping 5
1.3.2 Host Materials 5
1.3.3 Integrated Er-doped Optical Amplifiers and Lasers 6
1.3.4 $Al_2O_3:Er^{3+}$ for Active Devices 7
1.4 Outline of this Thesis 8

2. Reactive Co-Sputtering of $Al_2O_3:Er^{3+}$ Thin Films 11

2.1 Introduction 12
2.2 Experimental Details 13
2.2.1 Deposition Process 13
2.2.2 Sample Fabrication Procedure 13
2.2.3 Film Characterization 14
2.3 Deposition of Un-doped Al_2O_3 Films 15
2.4 Deposition of Er-doped Al_2O_3 Films 22
2.5 Summary 25

3. $Al_2O_3:Er^{3+}$ Channel Waveguides: Fabrication, Design and Optical Characterization 27

3.1 Introduction 28
3.2 Experimental Details 29
3.2.1 Etching Experiments 29
3.2.2 Optical Measurements 30
3.3 Channel Waveguide Etching Results 30
3.3.1 Al_2O_3 Etching 31
3.3.2 Etching of mask materials 32
3.3.3 Structuring of Al_2O_3 Channel Waveguides 33
3.3.4 Optical Performance of Channel Waveguides 37
3.3.5 Structuring of Waveguides in Other Rare-Earth-Host Materials 39
3.4 Channel Waveguide and Device Elements Design 41
3.4.1 Waveguide Design 41
3.4.1.1 Design Criteria 41
3.4.1.2 Simulations 42
3.4.1.3 Design Choice 46

3.4.2 Device Elements Design 47
3.4.2.1 Bent Waveguides 47
3.4.2.2 Y-Splitters 49
3.4.2.3 Directional Couplers 50
3.5 Optical Results 51
3.5.1 Fabrication of Waveguides and Device Elements 51
3.5.2 Propagation Losses: Straight Waveguides 52
3.5.3 Propagation Losses: Bent Waveguides 53
3.5.4 Y-Splitters 54
3.5.5 Directional Couplers 55
3.6 Summary 58

4. Investigation of Er Concentration and Optimization of Gain in $Al_2O_3:Er^{3+}$ Amplifiers 59

4.1 Introduction 60
4.2 Spectroscopy of Er^{3+} Ions 61
4.2.1 Energy Transitions in Erbium 61
4.2.2 Absorption and Emission Cross Sections 63
4.2.3 Lifetime 66
4.2.4 Energy Transfer Between Ions 67
4.2.5 Gain 69
4.3 Amplifier Fabrication, Propagation Loss Measurements and Spectroscopic Results 69
4.3.1 Sample Fabrication 69
4.3.2 Propagation Losses 70
4.3.3 Absorption and Emission Cross Sections 71
4.3.4 Luminescent Lifetimes 73
4.4 Optical Gain Measurements 73
4.5 Optical Gain Calculations 79
4.5.1 Amplifier Model 79
4.5.2 Gain Results 83
4.6 Summary 91

5. Applications 93

5.1 Introduction 94
5.2 Design and Characterization of a Zero-Loss Splitter 94
5.2.1 Motivation 94
5.2.2 Lossless Splitter Fabrication and Design 95
5.2.3 Experimental Results 95
5.2.4 Conclusions 100
5.3 High Bit Rate Transmission in an $Al_2O_3:Er^{3+}$ Amplifier 100
5.3.1 Motivation 100
5.3.2 $Al_2O_3:Er^{3+}$ Channel Waveguide Gain 100
5.3.3 170 Gbit/s Transmission Measurements 102
5.3.4 Conclusions 106
5.4 Integrated $Al_2O_3:Er^{3+}$ Ring Laser 106
5.4.1 Motivation 106

5.4.2 Laser Fabrication and Design 107
5.4.3 Laser Measurements 108
5.4.4 Conclusions 111
5.5 Summary 111

6. Conclusions 113

Appendix 117

References 125

Acknowledgements 137

List of Publications 141

Chapter 1

Introduction: Er-doped Thin Films for Integrated Optics

In this chapter an introduction to integrated optics and the aim of combining active and passive functions on a chip is presented. Rare-earth-doped thin films and, in particular, Er-doped thin films are introduced as a solution for integrated light sources and amplifiers. The advantages of $Al_2O_3:Er^{3+}$ *as a material for active integrated devices are discussed. Finally, the layout of this thesis is presented.*

1.1 Integrated Optics

Over the last few decades, integrated optics has been a continuously expanding field along-side the growth of fiber-optic communications and the internet. While fiber-optic components are large and bulky, the aim of integrated optics is to reduce the size and cost by realizing many such functions on a single chip. The applications of integrated optics are wide and varied. There is a drive to speed up computing through optical interconnects between integrated electrical circuits. Applications are emerging in bio-molecule analysis. Other established and potential applications include medical laser and imaging devices, sensors, and telecommunications components including those facilitating fiber-to-the home.

Many basic functions are required in an optical circuit. Besides miniature optical waveguides for directing light on the chip, these include optical sources for producing light, amplifiers for compensating for signal losses, detectors for converting the signal into the electrical domain, modulators, combiners/splitters, filters and switches. These functions can be divided into both passive devices (those that simply guide and direct light) and active devices (those that emit or amplify light or convert light energy to electrical energy). Unlike integrated electronics, which is well-established with its multi-billion dollar silicon electronics industry, a single medium has not come to dominate all others for integrated optical applications. While certain materials systems have been optimized for either passive or active components, no single material system effectively provides full passive and active functionality on the same chip. Silicon photonics has emerged in the last 10 years as an explosive field, with many prominent breakthroughs [1]. However, a monolithic amplifier or laser source has not yet been achieved directly in silicon. One could argue that III-V semiconductor materials demonstrate good active and passive functionality. However, these materials are costly for mass production.

An integrated optical waveguide consists of multiple layers, usually including a ~0.5-1-mm-thick substrate for support, a lower index cladding layer, a higher index waveguide core material and a second cladding layer on top. The various common material systems applied in integrated optics, which are described by the waveguide core material, can be grouped in terms of cost. III-V semiconductor and crystalline core materials typically require costly lattice-matched substrates and cladding layers. In contrast, inexpensive silicon wafers and silicon dioxide are normally applied as substrates and cladding layers, respectively, for silicon waveguides. Silicon or glass substrates and silicon dioxide, glass or polymer cladding materials are usually applied for polymer- and glass-core waveguides.

The different material systems can also be compared in terms of their refractive index contrast. The contrast between refractive index of the core and cladding of the integrated waveguide determines the minimum bend radius, thus the size of devices on the chip. Semiconductors such as indium phosphide and silicon have a relatively high index, allowing miniature devices. As a result, a very high integration density is possible, which, together with their excellent electrical properties, makes these materials highly useful for their application in optoelectronic integrated circuits. Dielectric materials such as silicon nitride and silicon oxynitride provide a moderate refractive index contrast, thus a reasonably high integration density, and are well-suited to passive photonic applications. Polymers and glasses such as silica have a low refractive index which is similar to that of optical fibers. The refractive index match between integrated

or planar silica devices and optical fibers means both have similar light-guiding properties, allowing for low fiber-chip coupling losses. Because of the low coupling losses and their high stability and low cost planar silica-based devices are often considered as good candidates for larger stand-alone fiber-pigtailed components.

Besides the type and size of device required, the signal wavelength is an important consideration when choosing the material. In silicon photonics, for example, only wavelengths higher than 1100 nm are of interest because the material is absorbing at shorter wavelengths. Wavelengths around 1300 nm and 1550 nm are of particular interest because they correspond to the second and third telecommunications window, respectively, allowing for compatibility with optical fiber-based telecommunications systems. For other, especially biomedical applications a wider range of wavelengths, including the visible and UV spectral regions, are of interest, thus requiring different materials.

While III-V materials provide a platform for both passive and active devices, such materials are costly and require complex fabrication methods. Due to the large infrastructure already available for silicon electronics and the lower material costs, silicon-based photonics is a much more attractive platform. In addition, the possibility for combination with electronic devices on the same chip is highly attractive. A large effort has been made to develop active functionality in the material, with some successes. However, due to its indirect bandgap, light emission in silicon is highly inefficient. Efficient stimulated light emission is essential in order to achieve optical gain and a fundamental requirement for active gain devices such as optical amplifiers and lasers. Thus, monolithically integrated optical amplifiers and lasers are the main missing components in silicon photonic circuits. One potential solution is hybrid integration, applying electrically pumped III-V laser sources and amplifiers, which has been investigated extensively in recent years [2]. However, hybrid integration significantly increases fabrication complexity and cost. Another option is combining optically pumped rare-earth-doped waveguides with silicon waveguides. These materials can be directly deposited and patterned on oxidized silicon, hence providing a monolithic solution. Nevertheless, this option has seen limited investigation until now [3], due to the fact that glasses have a lower index contrast, and thus are difficult to integrate with silicon. In addition, an external pump laser is required. However, the recent reduction in cost through mass-production of laser diode components begins to reduce the second problem to a pump source / chip coupling issue. One such source could potentially pump many active devices in one photonic circuit through a single fiber-chip connection. This perspective of integration with Si photonics has enhanced the market potential for integrated rare-earth-doped lasers and amplifiers. A particular focus exists on Er-doped devices because of the characteristic Er^{3+} ion emission around 1550 nm.

In this thesis amorphous aluminum oxide (a-Al_2O_3 or simply Al_2O_3, as opposed to its crystalline counterpart α-Al_2O_3 which is known as sapphire), doped with Er^{3+} ions is investigated as an active material. This material offers an improved match with silicon or other well-established passive materials such as silicon oxynitride in terms of refractive index contrast, since of the Er-doped glasses it has one of the higher refractive indices. In addition, its higher index contrast means smaller devices can be realized compared to other glass materials. It can also be deposited directly on oxidized silicon wafers, allowing for monolithic integration. The host Al_2O_3 is also a highly promising material platform on its own because it allows for integrated passive and active

functions in one material. Furthermore, an advantage of Al_2O_3 compared to silicon or other semiconductor optical materials is that it exhibits low absorption at visible and infrared wavelengths. This increases the range of potential applications to include, for example, a number of biomedical applications. In the next sections rare-earth-doped optical waveguides, Er-doping and Er host materials, the status of integrated Er-doped waveguide devices and the advantages of $Al_2O_3:Er^{3+}$ as a gain platform are discussed in more detail.

1.2 Rare-Earth-Doped Optical Waveguides

Original investigations of rare-earth ions began in the early 1900s with the work of Becquerel, who observed sharp emission lines in compounds containing these elements when they were cooled to low temperatures. Throughout the next 70 years rare-earth-doped crystal spectra were extensively investigated and theories were developed to accurately explain their optical properties. The most widely influential application of rare-earth ions was established in the 1980s, that of the erbium-doped fiber amplifier.

The rare-earth elements include elements 57-71 (the lanthanides) and 89-103 (the actinides) of the periodic table. The rare-earth ions are unique in that when they are introduced in a suitable host as ions, most commonly in the trivalent state, they maintain certain atomic-like properties. As a result of shielding of the 4f electron shells by the outer 5s and 5p shells various electronic transitions and energy spectra remain relatively independent of host medium. When optically pumped, exciting the electrons to a higher energy level, a large number of transitions are possible, producing optical emission at characteristic wavelengths. In addition, ms-long fluorescence lifetimes of certain excited levels quickly established rare-earth-doped hosts as excellent candidates for optical amplifiers and continuous-wave lasers. In addition, they also offer excellent properties for Q-switched and mode-locked lasers because the long lifetime allows the storage of large pulse energies.

Several of the rare-earth ions have been applied extensively in amplifiers and lasers. These include Yb^{3+}, with its broadband emission at around 1020 nm, Nd^{3+} which emits at around 880 nm, 1060 nm and 1330 nm, and Pr^{3+}, Ho^{3+} and Tm^{3+} with various emission wavelengths ranging from 0.48 up to 2.9 µm. Er is of particular interest because it provides emission around 1550 nm in the low-loss and low-dispersion window of optical fibers. This characteristic emission wavelength resulted in the application of Er-doped fiber amplifiers in optical telecommunications networks, allowing for signal regeneration and thus optical data transmission over long distances. The excellent performance of the Er-doped fiber amplifier in this application is one of the biggest reasons for the explosion of the internet throughout the 1990s [4, 5].

1.3 Active Planar Devices Based on Er-Doped Thin Films

Compared to erbium-doped optical fibers, erbium-doped waveguides on a chip introduce advantages in terms of size and cost. Over the last two decades they have been investigated extensively for their application in integrated amplifiers and laser sources. In this section active devices based on Er-doped waveguides are discussed.

1.3.1 Erbium-doping

Besides its absorption and emission around 1550 nm, the Er^{3+} ion has several additional spectral absorption and ground-state emission lines, including those centered at 530 nm, 650 nm, 800 nm and 980 nm. Furthermore, emission into excited states at 850 nm, 1200 nm and 2800 nm are of interest. In Er-doped glasses, the lines become broadened due to the amorphous nature of the host and the variety of sites in which the Er^{3+} ion is situated. This allows amplification or lasing at a wide range of wavelengths. Fig. 1.1 shows a typical absorption spectrum measured in Er-doped glass [6]. The level to which the Er^{3+} ion is excited from the ground state corresponding to each peak is indicated as well as the background non-Er-related scattering loss of the host material (dashed line). In comparison to the absorption spectrum, the Er^{3+} emission spectrum exhibits red-shifted emission peaks corresponding to the reverse transitions as well as, depending on the excitation wavelength, additional peaks corresponding to transitions between excited states.

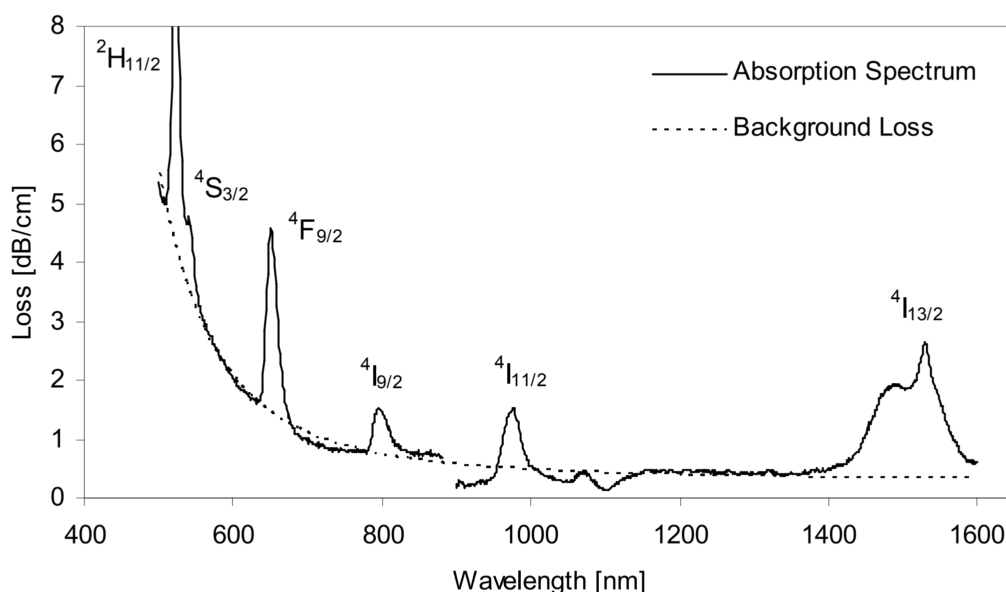

Fig. 1.1. Absorption spectrum of Er^{3+} in $Al_2O_3:Er^{3+}$ [6].

1.3.2 Host Materials

A key consideration in the design and realization of Er-doped devices is the choice of host material. There are several requirements which must be met for a good host material, including availability of suitable Er^{3+} ion bonding sites, high Er solubility without clustering, a sufficiently low phonon energy to prevent non-radiative decay and a high $^4I_{13/2}$ radiative lifetime. For integrated optical devices the host material must also allow for ease of waveguide fabrication and have low background optical propagation losses. Not all integrated optics materials meet these requirements. For example, Er incorporation in silicon has been studied extensively with the aim of developing a monolithic light source. However, only limited success has been realized due to ionic radii mismatch, resulting in low Er^{3+} ion solubility, and the presence of strong non-radiative recombination pathways [7]. Er incorporation in α-Al_2O_3 is also prevented due to ionic radii mismatch.

Suitable Er host materials can be separated into different categories, as shown in Table 1.1. These include crystalline, polymer and glass hosts. Each material type has advantages and disadvantages, depending on the required application. Crystalline and polycrystalline materials offer sharp emission cross sections and high stability for excellent laser performance [8-13]. The drawbacks of such materials are the narrow wavelength range, limiting their potential for amplifiers or on-chip tunable lasers, and the fact that they can only be grown on lattice-matched substrates, hence cannot be integrated with other materials platforms. Polymer waveguides are of interest due to their low cost and straight-forward integration with other materials and have shown promise as rare-earth hosts [14-17]. However, the thermal stability of such materials is poor and the host material itself often exhibits additional absorption lines (colour centers). Amorphous Er-doped glasses exhibit a broad emission spectrum, generally possess a high thermal stability and can be deposited on a wide range of substrates. Because of these advantages, and the success of Er-doped glass fiber amplifiers and lasers, many glass host materials have been investigated for active planar devices. These include silica [18-22], phosphate glass [23-32], fluoride glass [33], aluminum oxide [34-38] and numerous multi-component glasses [39-57]. Glass hosts have relatively low refractive indices, which are closely matched to those of standard optical fibers. This is an advantage if one is attempting to combine the Er-doped device with external fiber-based components. However, it can be a disadvantage in terms of achieving large integration density.

Table 1.1. Comparison of thin film host materials for Erbium

Host Type	Examples	Advantages	Disadvantages
Crystalline	$LiNbO_3$ Y_2O_3 $(Gd, Lu)_2O_3$ $Y_3Al_5O_{12}$ $YAlO_3$ $KY(WO_4)_2$	High emission and absorption cross sections; highly stable output (lasers); high thermal conductivity	Narrow wavelength range (for amplifiers or tunable lasers); epitaxial growth on specific substrates required
Polymer	PPMA PMMA 6-fluorinated-dianhydride/epoxy	Broad emission spectrum; low cost; deposition on a variety of substrates	Thermal instability; colour centers
Glass	Silica Phosphate glass Fluoride glass a-Al_2O_3 Multicomponent glass	Broad emission spectrum; high stability; deposition on a variety of substrates	Low refractive index contrast

1.3.3 Integrated Er-doped Optical Amplifiers and Lasers

Since the establishment of Er-doped fiber amplifiers in optical networks, significant efforts have been undertaken to bring this same functionality onto the chip (see Fig. 1.2a). The key difference between Er-doped fiber amplifiers (EDFAs) and Er-doped waveguide amplifiers (EDWAs) is that in the second case, much higher concentrations

are required to achieve the same gain due to the much shorter lengths. This has led to the investigation of many different materials which have high Er solubilities.

Various devices have been reported in the literature, including numerous examples of integrated amplifiers [18, 19, 22, 24-26, 30-34, 40, 41, 44, 49-51], lossless power splitters with loss compensation achieved in amplified Er-doped waveguides [43, 58-60] and integrated continuous-wave [21, 27, 29, 39, 60-71] and mode-locked [28, 72] Er-doped lasers. In terms of amplifiers commercial fiber-pigtailed devices have been produced which show gain of 27 dB over a wavelength range of 30 nm [73], making such a device competitive with well-established EDFAs and semiconductor optical amplifier components [74]. Commercial 1×4 and 1×8 power splitter modules have also been developed [73]. In order to achieve lasing in active Er-doped waveguides, a resonant cavity is required. To do this external mirrors [64], external fiber-Bragg gratings [29, 61, 62] or butt-coupled mirrors [21, 39, 63] are often applied. However, these are not fully integrated solutions because the resonant cavity is not located entirely on the chip and, hence, the light emitted from the laser inevitably leaves the chip. Integrated resonators and lasers have been realized by various means, including a ring [65, 66], distributed Bragg grating reflectors [66-68] (see Fig. 1.2b) and distributed feedback based on Bragg gratings [69, 70]. The ultimate aim of such a laser source is high stability, high efficiency and single-frequency operation. Er-doped glasses provide the added advantage of potential tunability of such a source.

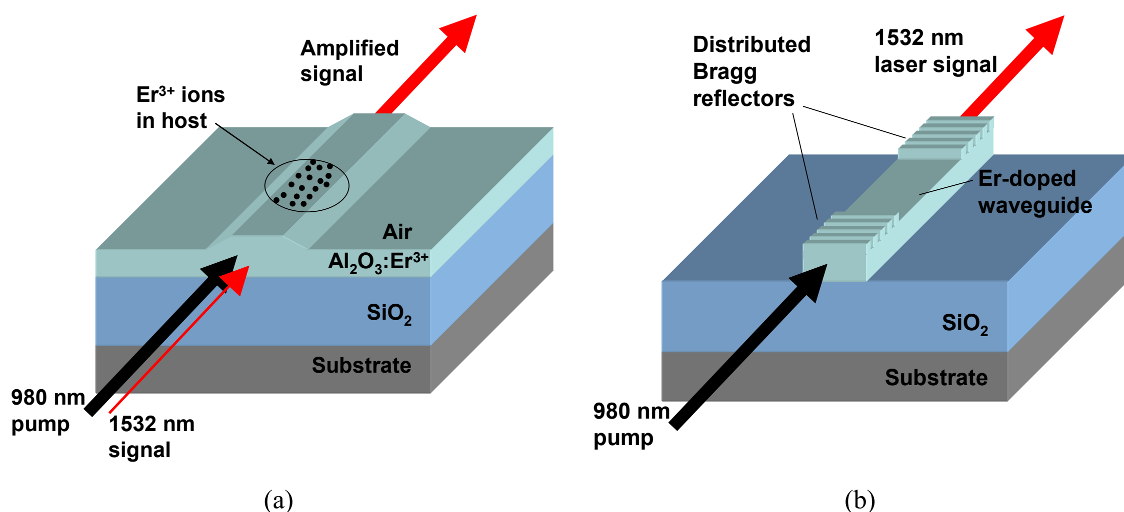

Fig. 1.2. Illustrations of (a) an Er-doped waveguide amplifier (EDWA) and (b) an integrated distributed Bragg reflector Er-doped waveguide laser.

1.3.4 $Al_2O_3:Er^{3+}$ for Active Devices

In the past, amorphous Al_2O_3 has been studied as a host material for Er^{3+} ions by several research groups [34-38]. In the 1980s Al_2O_3 was demonstrated to be a good material for passive integrated optics due to low losses and high transparency over a wide wavelength range. In addition, it has a higher refractive index contrast in comparison to other glass hosts, allowing smaller waveguide bend radii [75]. Furthermore, the material acts as an excellent host for Er, because the Er^{3+} ions are well-matched to the oxygen bonding sites [76], allowing high Er solubilities. In addition, $Al_2O_3:Er^{3+}$ exhibits a wide emission bandwidth around 1550 nm [36], allowing for gain across a wide range of

wavelengths. Whereas other glasses have been shown to be suitable primarily for stand-alone components, Al_2O_3 offers better integration potential for active devices due to its higher index contrast.

In order to establish $Al_2O_3:Er^{3+}$ as an active medium, however, several challenges existed prior to this work. Unreliable deposition methods or relatively complex and costly ion implantation steps were applied. In addition, due to the high chemical stability of Al_2O_3, channel waveguide etching proved difficult, and physical etching was required. In the particular case of [37] this led to channel waveguides with high scattering losses. Finally, while net gain was demonstrated in $Al_2O_3:Er^{3+}$ waveguides [34, 37], compared to other EDWA materials, the peak gain in the $Al_2O_3:Er^{3+}$ amplifiers was among the lowest. Therefore, in order to exploit the advantages of $Al_2O_3:Er^{3+}$ as an active medium and compete with other Er-doped planar waveguide technologies, it was established in the beginning of this work that reliable fabrication methods (film growth and channel waveguide etching) and demonstration of higher optical gain were required. Once these two goals were achieved, new and promising active integrated devices based in $Al_2O_3:Er^{3+}$ could be designed and realized.

1.4 Outline of this Thesis

This thesis revolves around the development of fabrication technologies for $Al_2O_3:Er^{3+}$ waveguides and their use towards demonstrating new active devices and applications. The first two chapters are devoted to the development of the necessary fabrication methods: $Al_2O_3:Er^{3+}$ film growth and channel waveguide etching. The following chapter reports on $Al_2O_3:Er^{3+}$ optical amplifiers with higher gain. In the final chapter, applications of $Al_2O_3:Er^{3+}$ waveguides, including loss compensation in power splitters, amplification at high bit rates and integrated lasers are presented.

In Chapter 2 the development of a new procedure for depositing $Al_2O_3:Er^{3+}$ films by reactive co-sputtering is presented. The investigation focuses on reliability and growing films of high quality with low background losses suitable for active devices. In addition, an emphasis is placed on achieving excellent film uniformity over a large area on standard silicon substrates in order to have a large available area for devices. This is largely the work of K. Wörhoff, which was presented in [77].

In Chapter 3 a new method for etching channel waveguides by applying reactive ion etching is presented. The structural properties of the resulting waveguides are investigated, with an emphasis on obtaining smooth sidewalls, good pattern resolution and sufficient etch depths for appropriate channel waveguide properties. Based on this new method, optical waveguides and basic integrated waveguide components for bending, coupling and splitting light on a chip are designed and tested. A significant portion this work presented in this chapter was published in [78].

In Chapter 4 the fabrication methods are applied to realize $Al_2O_3:Er^{3+}$ optical amplifiers with different Er^{3+}-doping concentrations. The aim of this work is to investigate the maximum possible gain in $Al_2O_3:Er^{3+}$ waveguides. An analytical model is also presented, which accurately describes the amplifier behaviour and can be used to predict the gain in longer amplifiers. The results presented in this chapter were submitted to the *Journal of the Optical Society of America B*.

In Chapter 5 various applications are presented which demonstrate $Al_2O_3:Er^{3+}$ to be an excellent medium for active integrated optics. The first device consists of a 2-way lossless power splitter and demonstrates on-chip loss compensation for an optical signal split into 2 separate channels. The second device is a high-speed optical amplifier for 170 Gbit/s signals for future-generation integrated photonic circuits. The third device is an $Al_2O_3:Er^{3+}$ ring laser, the first laser reported in this material. The lossless splitter, high-speed amplifier and laser results were submitted separately to *IEEE Photonics Technology Letters*, *Optics Express* and *Optics Letters*, respectively.

Chapter 2

Reactive Co-Sputtering of $Al_2O_3:Er^{3+}$ Thin Films

In this chapter a reliable and reproducible deposition process for the fabrication of amorphous Al_2O_3 and $Al_2O_3:Er^{3+}$ thin film waveguides is presented. First the process for the fabrication of undoped Al_2O_3 films was optimized. Both DC and RF reactively-sputtered films were investigated in terms of deposition rate, refractive index, density, stress, material birefringence and optical loss. Based on the results of this detailed study, RF sputtering and optimized deposition parameters were selected. The resulting undoped thin films are grown at ~5 nm/min deposition rate, exhibit thickness non-uniformity within 1% over a 50x50 mm^2 area and have no detectable OH^- incorporation. Planar propagation losses as low as 0.11 dB/cm were demonstrated at a wavelength of 1523 nm in the undoped films. To activate the layers, the implementation of rare-earth-ion doping was investigated by co-sputtering of erbium during the Al_2O_3 layer growth. Dopant levels between $0.2\text{-}5\times10^{20}$ cm^{-3}, uniform throughout the film and across the substrate, were attained. Propagation losses as low as 0.21 dB/cm and 0.16 dB/cm were demonstrated at wavelengths of 633 nm and 1320 nm, respectively in the Er-doped films. The repeatable and straightforward wafer-scale deposition procedure, uniform Er doping levels and low losses make these layers highly suited to the realization of active integrated optical devices.

2.1 Introduction

During the past decades a number of research groups have investigated and developed Al_2O_3 deposition processes based on different techniques: pulsed laser deposition (PLD) [79, 80], atomic layer deposition (ALD) [81, 82], chemical vapour deposition (CVD) [36, 83-85], the sol-gel method [80, 86, 87], sputtering from a dielectric target [75, 88], and reactive co-sputtering based on a metallic target [37, 89, 90].

Besides general requirements for thin film applications in integrated optics, like low propagation loss, uniform growth over a large substrate area, good process reproducibility, and sufficiently high deposition rates, specific demands arising from applications in optically active devices need to be taken into account. For devices based on rare-earth-ion transitions OH^--free deposition is required, because these bonds induce strong luminescence quenching and, hence, greatly diminish or prohibit optical gain. When comparing the properties of previously applied deposition techniques, it becomes obvious that CVD and sol-gel techniques inherently suffer from OH^- incorporation [36, 83, 84, 86] due to the presence of hydrogen in the process precursors. The application of ALD for optical waveguides, although resulting in thin films with excellent quality, is limited due to its very low deposition rate, which typically results in film thicknesses of only up to several tens of nanometers. The main draw-back of PLD consists in the limited substrate area, typically 1-2 cm^2, which can be covered by a thin film with acceptable uniformity. This size limitation restricts the integration scale of complex integrated optical devices. Based on the results of previous studies, the sputtering technique is very promising for the fabrication of amorphous Al_2O_3 thin films for integrated optics, since it combines an inherently low OH^- content with relatively fast, uniform, and controlled deposition over substrate areas of wafer scale.

Although the potential of rare-earth-ion-doped Al_2O_3 waveguides in integrated optical amplifiers has been demonstrated by the achievement of 0.58 dB/cm net optical gain [34], breakthrough has been hampered by two problems: further loss reduction in slab and channel-type waveguides and the availability of a low-cost, stable fabrication process. In planar Al_2O_3 waveguides, propagation losses of 0.23 dB/cm at 633 nm have been reported for annealed thin films [88]. For the incorporation of rare-earth ions an ion implantation process in combination with subsequent annealing has been applied [91], leading to increased fabrication complexity and cost. Exploiting reactive co-sputtering based on DC-driven sputtering guns has resulted in as-deposited $Al_2O_3:Er^{3+}$ waveguides with losses as low as 0.25 dB/cm for light propagating at 1.5-µm wavelength [37]. However, the main drawback of the applied method turned out to be the poor process stability and reproducibility, which was highly dependent on the condition of the sputtering target.

In this chapter the optimization of reliable and highly stable growth of undoped Al_2O_3 films is first described. The emphasis is placed on the realization of as-deposited, low-loss optical waveguides. Following this, incorporation of Er^{3+} into the optimized Al_2O_3 host material is studied. The physical and optical properties of the both the undoped and Er^{3+}-doped Al_2O_3 films are discussed. The final result is a stable, straightforward and relatively low-cost deposition process providing high quality $Al_2O_3:Er^{3+}$ layers suitable for active integrated optical devices.

2.2 Experimental Details

In this section the deposition process, sample fabrication procedure and methods applied for characterization of the Al_2O_3 and $Al_2O_3:Er^{3+}$ films are discussed.

2.2.1 Deposition Process

For the Al_2O_3 layer growth, an AJA ATC 1500 sputtering system equipped with a load-lock and three sputtering guns was applied. A schematic illustration of the sputtering system is displayed in Fig. 2.1. The sample was fixed in a bottom-up sputtering configuration on a substrate holder which can be rotated and heated up to a maximum temperature of 800ºC. The temperature was regulated within ±3ºC. The deposition chamber can be pumped to a background pressure of 10^{-7} mTorr, which is essential in order to reach a negligible OH^{-} level in the deposition process. The pressure of the deposition process was adjusted by a valve with an accuracy of ±0.1 mTorr. The three sputtering guns are designed for 2-inch sputtering targets and can be driven individually by RF or DC power supplies, having a maximum range of 500 W. The power is set within ±1 W. Flow-controlled Ar gas lines are connected to the sputtering guns. The Ar flow per gun is 100 sccm and can be controlled with an accuracy of 1%. The distance between the substrate holder and the sputtering target can be adjusted within a range of 10 to 18 cm. In order to allow for oxide deposition from metallic targets (Al, Er), an oxygen (O_2) flow was added to the deposition process through a flow-controlled gas line which is connected to a gas inlet in the chamber wall. For the deposition of Al_2O_3 and doping with erbium, a high-purity Al target (99.999% purity) and a metallic Er target (99% or 99.95% purity) were mounted to the sputtering guns.

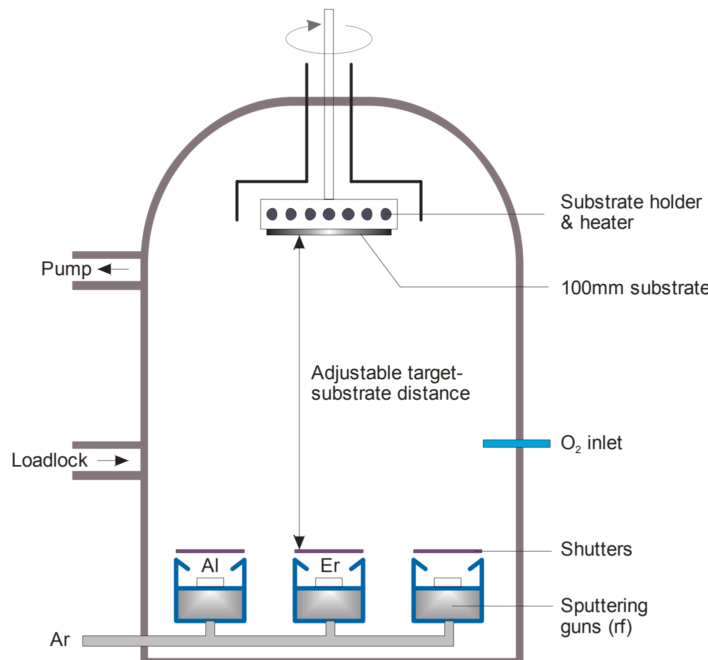

Fig. 2.1. Schematic illustration of the reactive co-sputtering system used for the Al_2O_3 and $Al_2O_3:Er^{3+}$ film growth.

2.2.2 Sample Fabrication Procedure

Slab-type waveguides were fabricated by deposition of Al_2O_3 thin films on thermally oxidized 100-mm Si wafers. In order to ensure sufficient separation of the light

propagating in the waveguide from the silicon substrate an 8-µm thick thermal oxide was applied to all samples. Prior to deposition all samples were cleaned by applying a standard cleaning process. After substrate loading the sample was fixed at a distance of 17 cm and the substrate rotation was switched on. Since preliminary tests showed that this rotation speed has no impact on any of the layer parameters, it was fixed to a constant value for all processes. Then, the substrate was heated up to the deposition temperature followed by temperature stabilization for 15 minutes. After that the Ar and O_2 gas flows and the chamber pressure were adjusted to their process set-points. Then, the Al target was pre-sputtered at processing power and with closed shutter for approximately 10 minutes. The deposition started by opening the shutter and after the deposition was finished the procedure was followed in reverse order. The sputtering time was adjusted for all depositions in order to grow waveguide layers within a typical thickness range of 0.5-1 µm.

2.2.3 Film Characterization

The thickness (d) and refractive index (n) of the layers were measured by a Woollam M44 spectroscopic ellipsometer and a Metricon 4-wavelength prism-coupling set-up. The prism-coupling setup provided measurements at wavelengths of 633, 830, 1300 and 1550 nm. The measurement accuracy of the presented thickness and refractive index values are below 0.5% and 5×10^{-4}, respectively. The non-uniformity of the layer thickness (δd) and the refractive index (Δn) over the wafer were measured by both ellipsometry (Plasmos SD 2000) and prism coupling. The non-uniformity has been determined over a 70 x 70-mm^2 area and will be defined as the half min-max value over the measured area. From refractive index measurements utilizing TE and TM polarized light (prism coupling), the material birefringence given by $\Delta n_{TM\text{-}TE} = n_{TM} - n_{TE}$ was calculated. The layer stress, which in amorphous thin films is known to be related to the material's birefringence, was measured by the wafer bow method. The stress values were calculated by combining data on the change in wafer bow over 80 mm before and after film deposition, the layer thickness, and substrate specific properties. For the determination of the layer density, the substrates were weighed before and after the deposition on a 5-digit balance. Based on the weight difference and average layer thickness of the deposited film a straight-forward density calculation has been carried out.

For optical loss measurements of slab-type waveguides the moving prism method was applied [92, 93]. Details of the home-made prism coupling apparatus are presented in [6]. The measurement accuracy was ±0.05 dB/cm. Absolute values of the optical loss were determined at fixed wavelengths based on laser sources at 633, 980, 1320, and 1522 nm. The infrared loss spectrum was measured with 1-nm step size over a wide wavelength range of 1200-1600 nm provided by a white-light source (Fianium supercontinuum SC450), in combination with a spectrometer, and the spectral response was fitted to the absolute loss values obtained by the single-wavelength measurements.

Composition and dopant concentration of the Al_2O_3:Er^{3+} films were measured by Rutherford back scattering (RBS) at the University of Utrecht. Samples of ~10×10 mm^2 size from the central part of the 100-mm wafers were prepared for measurements. The samples were exposed to a beam of 2.0 MeV He^+ ions with a current of 30 nA. The backscattered ions were detected under an angle of 170º. The sampled surface area was approximately 1 mm^2. The RBS spectra were evaluated by applying the RUMP software tool [94].

2.3 Deposition of Un-doped Al_2O_3 Films

In order to optimize the Al_2O_3 deposition process towards reliable fabrication with high optical layer quality, the impact of processing parameters on relevant layer properties (deposition rate R, refractive index n, film density ρ, stress σ, material birefringence Δn_{TM-TE}, and optical loss α) was studied. Initially, both DC and RF-based sputtering were considered. The different processing parameters and the range studied for the DC and RF sputtering processes are shown in Table 2.1.

Table 2.1. Process parameter range for the optimization study of Al_2O_3 layer deposition applying DC- and RF-based reactive co-sputtering.

Parameter	DC process	RF process
Temperature T [°C]	400 - 500	350 - 550
Pressure p [mTorr]	3-5	3.5-6
Power P [W]	150 – 275	75 - 250
Total flow [sccm]	11 – 24.5	21 - 42
O_2 flow percentage [%]	10 - 25	5 – 10

Details on the change of deposition rate, refractive index, density and thickness non-uniformity upon variation of sputtering power applied to the Al target, substrate temperature, chamber pressure and total (Ar and O_2) flow are shown in Figures 2.2, 2.3, 2.4 and 2.5, respectively. When comparing the DC and RF process, it becomes evident that the deposition rates of layers deposited by RF sputtering (3 to 5 nm/min) are typically a factor 2-4 lower than for DC-grown layers (4 to 13 nm/min). In both cases, the deposition rate is mainly influenced by the sputtering power on the Al target, showing a nearly linear increase with power. Moreover, the difference in deposition rates of RF and DC grown layers becomes more pronounced at higher sputtering powers. The substrate temperature has hardly any impact on the deposition rate. Furthermore, the deposition rate decreases slightly at higher processing pressures and larger flow rates, which is connected to the impact of the decreased mean free path length of the species in the deposition chamber.

Compared to the DC-grown films the refractive index of the RF-grown layers is significantly higher. The difference is typically on the order of 3×10^{-2}. This rather large difference, which is nearly independent of the process parameter variations, can be explained by a particularity of the DC process: arcing on the sputtering target. This phenomenon is attributed to the oxidation of the target surface, resulting in the formation of an insulating layer and regular break-through (arcing) upon DC current application. With each arcing event a large amount of clustered material is sputtered. Incorporation of such clusters in the thin film results in an increased amount of voids around those irregularities. This interpretation is supported by the film density measurements; the DC-grown layers have a significantly lower density.

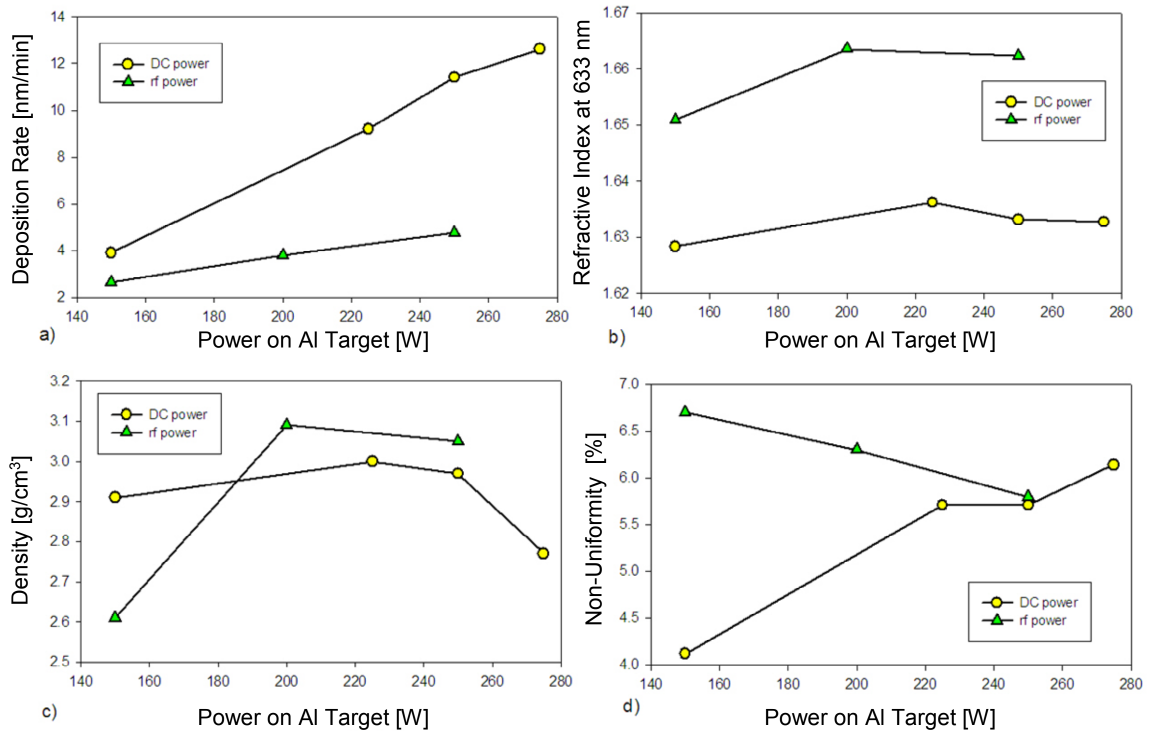

Fig. 2.2. Impact of varied Al target power on (a) deposition rate, (b) refractive index, (c) density and (d) thickness non-uniformity over 70×70 mm^2 of Al_2O_3 films grown with DC and RF sputtering.

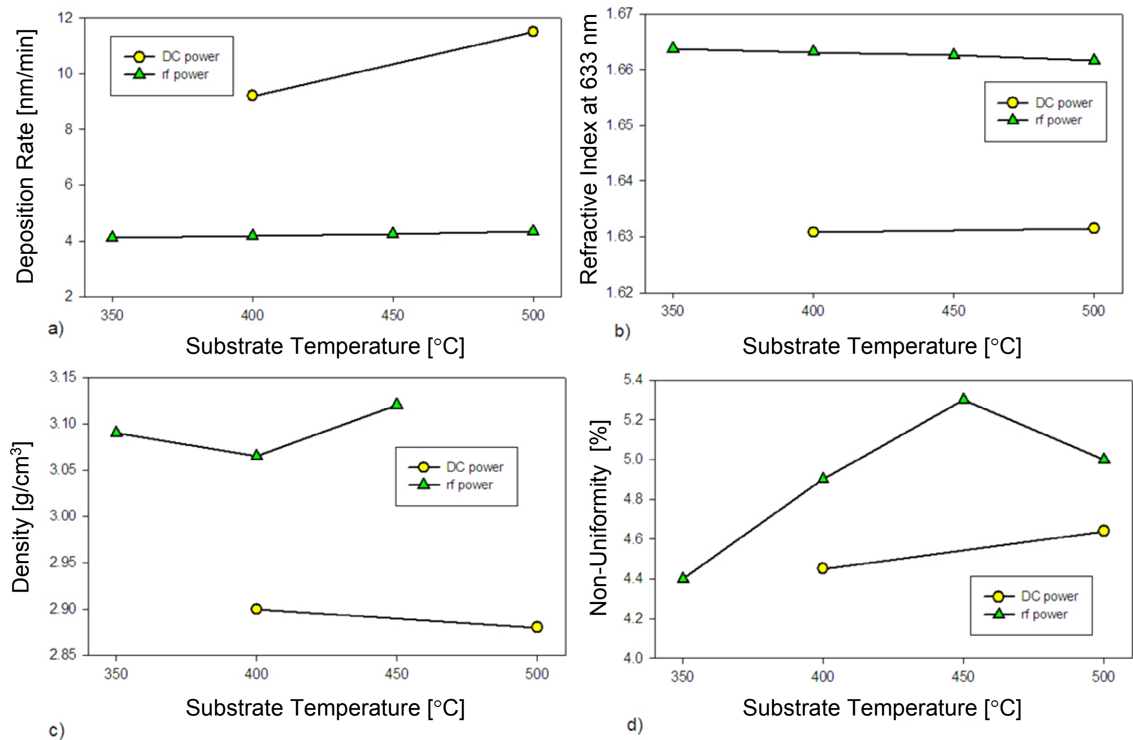

Fig. 2.3. Impact of varied substrate temperature on (a) deposition rate, (b) refractive index, (c) density and (d) thickness non-uniformity over 70×70 mm^2 of Al_2O_3 films grown with DC and RF sputtering.

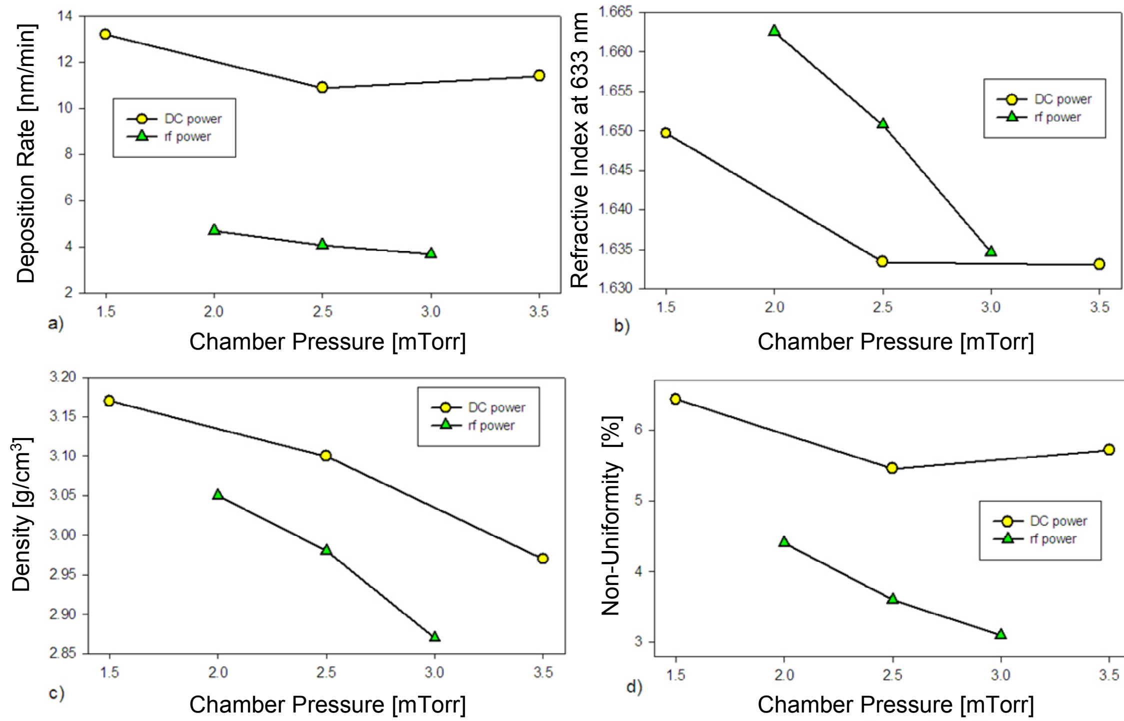

Fig. 2.4. Impact of varied chamber pressure on (a) deposition rate, (b) refractive index, (c) density and (d) thickness non-uniformity over 70×70 mm^2 of Al_2O_3 films grown with DC and RF sputtering.

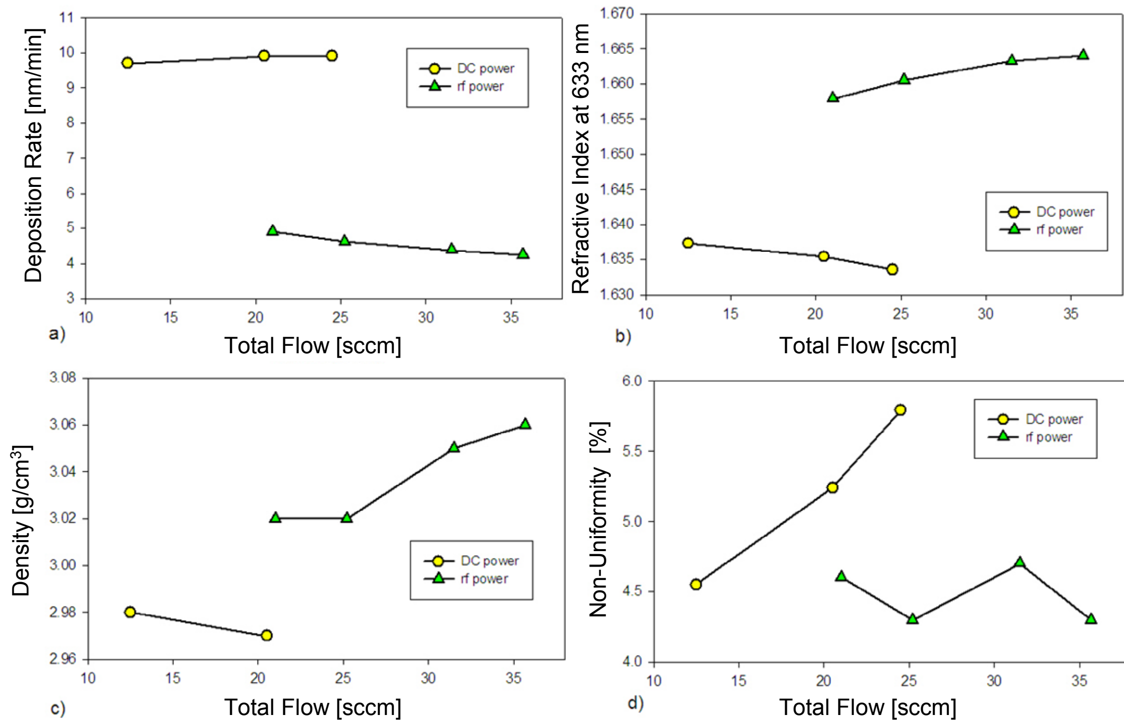

Fig. 2.5. Impact of varied total (Ar and O_2) flow on (a) deposition rate, (b) refractive index, (c) density and (d) thickness non-uniformity over 70×70 mm^2 of Al_2O_3 films grown with DC and RF sputtering. The DC and RF grown layers are deposited at constant oxygen flow and constant O_2 / Ar flow ratio, respectively.

When studying the change of refractive index upon process parameter variation we observe the most significant impact when changing the chamber pressure; higher pressure results in a lower refractive index. This observation can be understood when considering an increased amount of collisions between species before reaching the sample surface, due to a decreased mean free path length in the case of deposition at higher pressures. These collisions increase the amount of gas phase reactions and formation of clusters, which are incorporated into the growing layer and result in a more porous, less dense structure. This finding is confirmed by the decrease of film density when grown at higher pressures.

The refractive index change upon variation of the other process parameters is less pronounced. Nevertheless, it yields information on the growth behaviour, which becomes relevant when optimizing the deposition process towards highest film quality. Sputtering at powers below 200 W results in an increase of refractive index with increasing power, whereas at higher power the refractive index remains nearly constant. The same trend is observed in the density measurements. This behaviour can be understood when considering that, once the sputtered particles arrive at the sample surface, their kinetic energy is transformed to energy involved in the surface diffusion process. At low sputtering power the energy is too low to ensure sufficient surface mobility. At high sputtering powers further contribution of the kinetic energy to the surface diffusion process is most likely inhibited by the increased deposition rate.

An interesting observation was made for the refractive index and density change as a function of substrate temperature in the case of RF-grown layers. Based on the assumption of increased surface mobility at elevated substrate temperatures, one would expect thin films with increased refractive index and density when increasing the substrate temperature. From the measurements, however, a slight decrease of the refractive index was found at higher temperatures, while the density slightly increased. While the higher density is in line with the expectation of fewer voids at higher growth temperature, the refractive index response seems to be contradictory. However, when considering that the refractive index is not only determined by the film density but also by the material composition, this behaviour can be understood. The slightly lower refractive index indicates a more complete oxidation of the aluminum in the layer (less Al-Al bonds) at elevated temperatures. Since both, voids in the film and incompletely oxidized Al, result in higher losses in the shorter wavelength range, this interpretation is supported by the reduced optical losses of waveguides deposited by RF sputtering at higher temperatures (see Fig. 2.8a, page 20).

The thickness non-uniformity is significantly influenced by all processing parameters. For low sputtering powers and high substrate temperatures the non-uniformity of the RF sputtered material is higher compared to the DC grown layers. In all other cases the non-uniformity of the RF-deposited films is either comparable or significantly better. Furthermore it should be noted that the non-uniformity over the 70x70 mm^2 area, which is typically in the range of 3-7 %, can be considered to be rather high, mainly when it is compared to values obtained in well-established Si-based integrated optics technology where non-uniformities are typically in the 1-2 % range [95]. However, when taking into account the typical thickness distribution of the Al_2O_3 film over the wafer, which is depicted in the 9-point scan in Fig. 2.6, it can be clearly seen that the non-uniformity rapidly increases towards the edge of the wafer. If measured over a slightly smaller area of 50x50 mm^2, the non-uniformity is decreased to

± 0.8%, which can compete well with the achievements in Si-based waveguide technology.

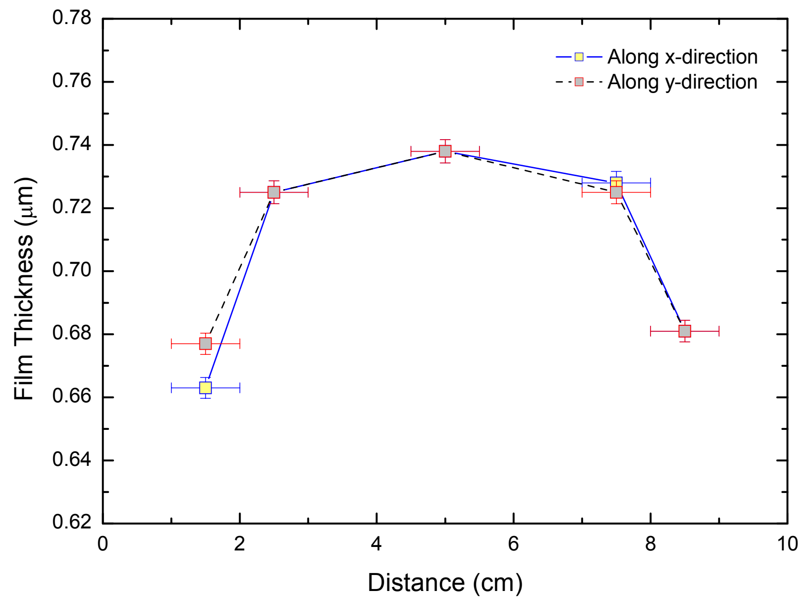

Fig. 2.6. 9-point scan of layer thickness along two perpendicular directions on the 100-mm wafer.

Besides the quality of the individual grown samples, knowing the stability of the deposition process from run to run is important for controlled layer growth. For this purpose, the change of the deposition rate and the refractive index has been extracted from measurement of layers deposited under exactly the same processing conditions at various total thickness stages. The deposition rate, which is shown in Fig. 2.7a, increases linearly as the target consumption progresses. This thickness change can be directly related to the decrease of the bias voltage on the sputtering target. Based on this direct relationship, the actual deposition rate can be calculated and a good control of the deposited thickness can be achieved by adjusting the deposition time accordingly. As it can be seen in Fig. 2.7b, the refractive index is reproduced within $\pm 10^{-3}$.

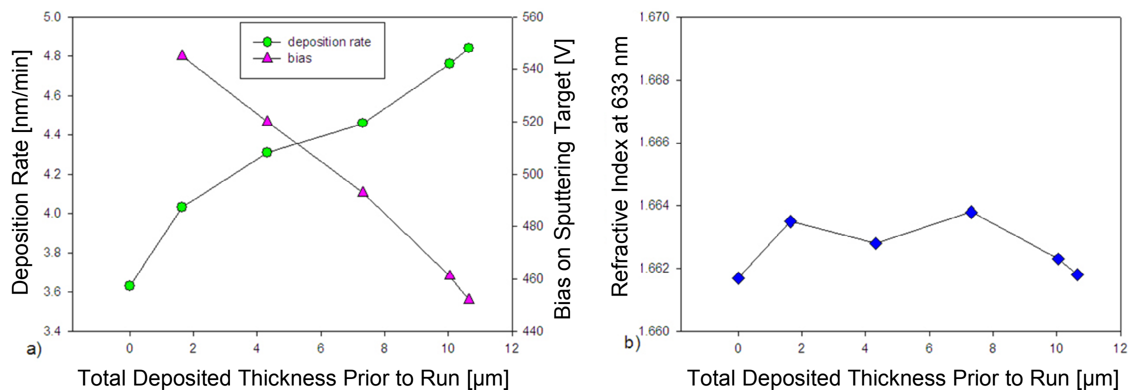

Fig. 2.7. Reproducibility of (a) deposition rate and (b) refractive index as a function of the total layer thickness sputtered.

With respect to optical loss we observed a significant difference between the DC and RF sputtering processes. While in the case of DC-grown layers light propagation failed, for the RF-grown layers a clear dependence of the optical losses on the various process parameters was found. Therefore, at this point RF-sputtering was selected over DC-sputtering for the deposition process. The main impact on optical losses in the RF-sputtered films could be attributed to the substrate temperature (see Fig. 2.8a). The losses decrease strongly as a function of temperature. Upon growth at 550 ºC the losses of as-deposited waveguides reached values as low as 0.29 ± 0.04 dB/cm and 0.11 ± 0.02 dB/cm at wavelengths of 633 nm and 1522 nm, respectively (see Fig. 2.8b). When increasing the deposition temperature further (≥ 600 ºC), however, light propagation in undoped Al_2O_3 waveguides failed. One explanation for this is a change in the material properties at the higher temperature, possibly resulting in the onset of crystallization. The losses also decreased at lower flow rates, lower pressures and higher Al-target sputtering powers (up to 200 W). In each case we expect this to be due to decreased clusters and voids in the material, as supported by the higher refractive index and density.

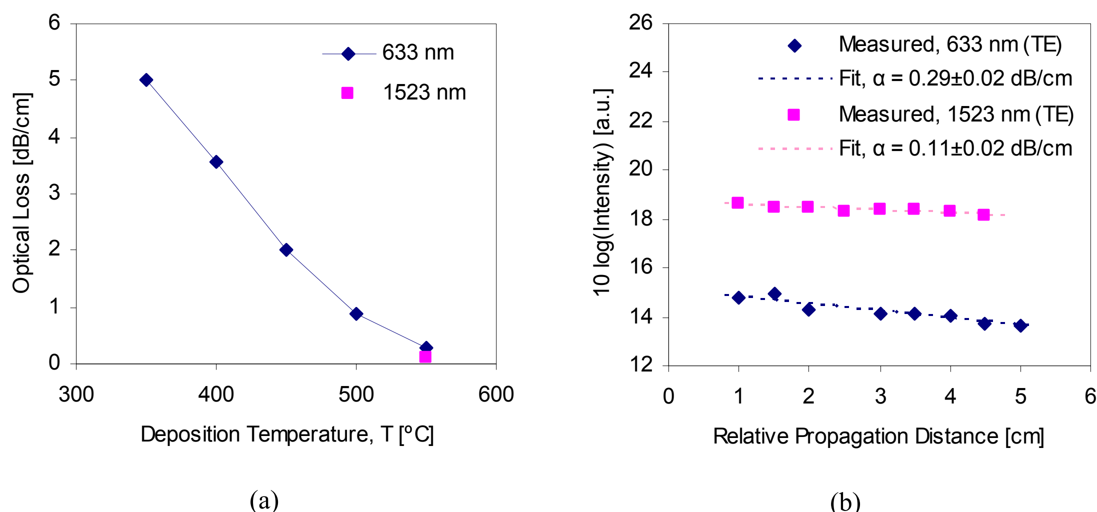

Fig. 2.8. (a) Optical losses of RF-sputtered Al_2O_3 waveguides at wavelengths of 633 nm and 1523 nm and for TE polarization as a function of deposition temperature and (b) loss measurement of an as-deposited sample grown at optimized deposition parameters.

In order to investigate the level of OH^- incorporation in the films, the optical loss spectrum of an unoptimized 660-nm thick Al_2O_3 waveguide deposited at 500 °C was measured by the moving prism method. The optical loss throughout the near infrared (NIR) wavelength range of 1200-1600 nm was about 0.3 ± 0.15 dB/cm, as shown in Fig. 2.9. No loss increase around 1400 nm, which would be indicative of the presence of OH^- groups in the film, is observed.

Based on the impact of processing parameters on the layer properties discussed above, the following optimized parameters for undoped Al_2O_3 films were chosen. RF sputtering as opposed to DC sputtering was selected. The substrate temperature is kept at 550 ºC; the sputtering power is 200 W; the total flow rate is 31.5 sccm with 5% oxygen addition; the chamber pressure is set at the lowest possible value at maximum pump capacity. These deposition parameters are summarized in Table 2.2. The layer parameters of an Al_2O_3 waveguide, grown under optimized deposition conditions, were

measured and are summarized in Table 2.3. From the non-uniformity and reproducibility values as shown in the table the high process stability becomes evident. Thickness and refractive index uniformity values of the Al_2O_3 sputtering process compare well with the uniformities obtained in Si-based CVD technologies [96]. As expected, the small birefringence is in line with the low values of tensile stress in the thin films. The optical propagation losses are low at both visible and NIR wavelengths demonstrating that such films can be useful for integrated optics applications with a wide range of wavelengths.

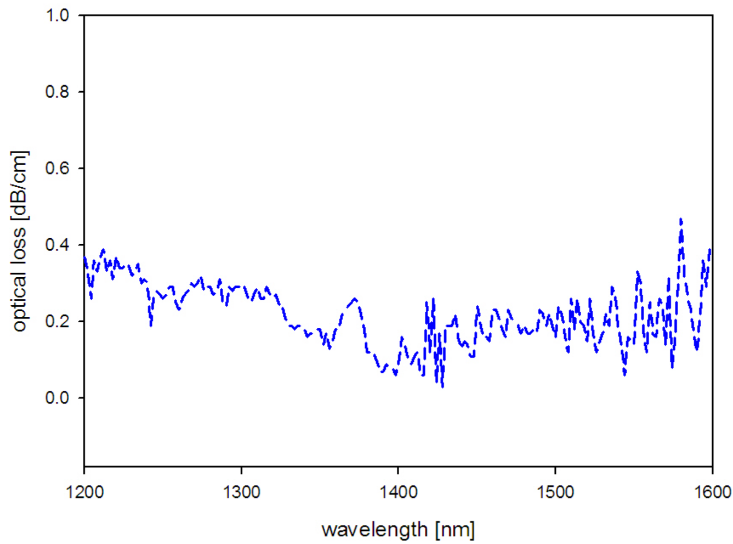

Fig. 2.9. Optical loss spectrum at NIR wavelengths of optimized Al_2O_3 layer deposited at 500 °C by RF-sputtering.

Table 2.2. Optimized processing parameters for Al_2O_3 layers deposited by reactive co-sputtering.

Parameter	Value
Temperature T [°C]	550
Pressure p [mTorr]	~3.5
Power P [W]	200
Total flow [sccm]	31.5
O_2 flow percentage [%]	5

Table 2.3. Layer properties at optimized processing parameters for Al_2O_3 layers by reactive co-sputtering.

Layer property	Value
Deposition rate *R* [nm/min]	5
Thickness non-uniformity [%] (5x5 cm^2 area)	± 0.8
Thickness reproducibility [%] (run-to-run)	± 4.5
Refractive index *n* at λ = 633 nm (TE)	1.659 ± 0.0005
Refractive index *n* at λ = 1550 nm (TE)	1.642 ± 0.0005
Material birefringence Δn_{TE-TM}	2×10^{-4}
Refractive index non-uniformity (5x5 cm^2 area)	$\pm 2 \times 10^{-4}$
Refractive index reproducibility (run-to-run)	$\pm 2 \times 10^{-4}$
Stress σ [MPa]	- 50 ± 5
Optical loss α [dB/cm]	0.3 (λ = 633 nm) 0.1 (λ = 1523 nm)

2.4 Deposition of Er-doped Al_2O_3 Films

In order to investigate the growth behaviour of Er^{3+}-doped Al_2O_3 layers, the RF power connected to the gun with the Er target (99% purity) was initially varied between 10 and 150 W. The remaining deposition parameters were kept at the values optimized for the Al_2O_3 deposition. The Er^{3+} concentration as obtained from RBS measurements is shown in Fig. 2.10. At Er co-sputtering powers above 25 W (not shown in Fig. 2.10) the concentration increases drastically. From the literature it is known that concentrations near 1×10^{20} cm^{-3} are useful for amplification at 1.5 μm [97]. Er^{3+} concentrations between 2×10^{19} cm^{-3} and 4×10^{20} cm^{-3} can be achieved at sputtering powers between 10-25 W.

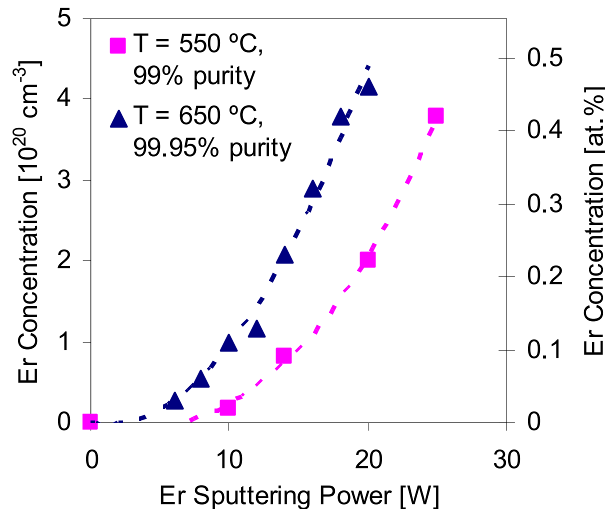

Fig. 2.10. Er^{3+} concentration of reactively co-sputtered $Al_2O_3:Er^{3+}$ as a function of sputtering power on the Er target for growth at 550ºC using a 99% purity Er target and growth at 650ºC using a 99.95% purity Er target.

To reduce the number of undesired impurities in the layers, which could act as optical quenching centers, the Er target used in the initial experiments was later replaced by a higher purity (99.95%) Er target. Using a deposition temperature of 650 ºC and the higher purity Er target, a second set of $Al_2O_3:Er^{3+}$ layers with thicknesses of 0.9 to 1.3 µm were deposited. The Er-target power was set at values ranging from 6 to 20 W. The resulting Er concentration of each sample versus sputtering power applied to the Er target is also shown in Fig. 2.10. In comparison to the previous values, higher Er concentrations were obtained for the same sputtering power with the new target, demonstrating that each new Er target should be properly calibrated. This is in line with the observed change in sputtering properties as the condition of the Al target changes. The refractive index at 633 nm, 830 nm, 1300 nm and 1550 nm versus Er concentration are shown in Fig. 2.11. The refractive index at each wavelength is higher than in undoped samples and increases with Er concentration.

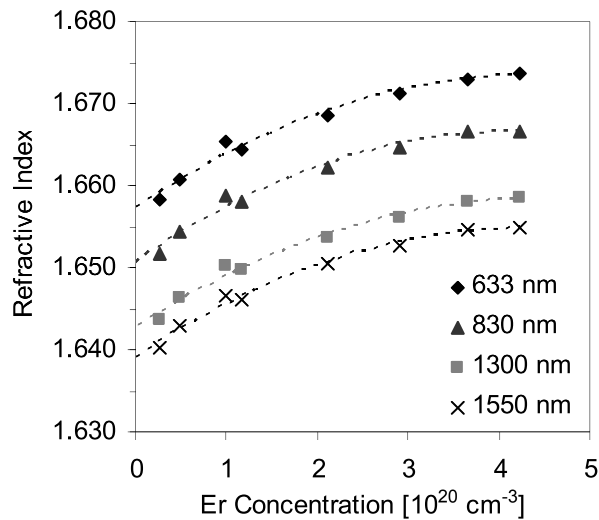

Fig. 2.11. Refractive index of $Al_2O_3:Er^{3+}$ layers at wavelengths of 633 nm, 830 nm, 1300 nm and 1550 nm as a function of Er concentration.

In order to investigate the doping uniformity and thickness uniformity across the wafer in such relatively thick layers, the Er concentration and layer thickness were also measured as a function of distance from the center of the wafer. The results are shown for a 1.1-µm-thick sample sputtered at 12 W Er target power in Fig. 2.12. The layer thickness was found to decrease by 7% at a radius of 3 cm from the center of the wafer and the Er concentration was found to be highly uniform across the entire sample ($\pm 0.02 \times 10^{20}$ cm^{-3}).

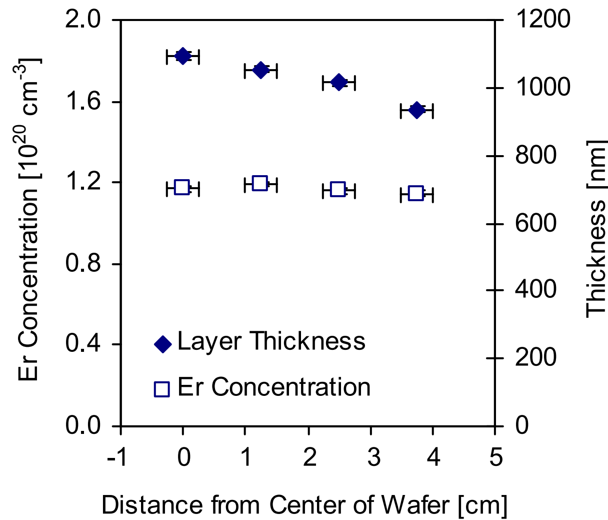

Fig. 2.12. $Al_2O_3:Er^{3+}$ layer thickness and Er concentration as a function of distance from the center of the wafer for a sputtering power of 12 W applied to the Er target.

Unlike the undoped Al_2O_3 layers, it was found that deposition of high-quality $Al_2O_3:Er^{3+}$ films at higher temperatures was possible. The presence of large Er ions in the Al_2O_3 host material prevented crystallization and maintained the amorphous character of the films at these higher temperatures. Fig. 2.13 shows the optical propagation losses at 633 nm and 1320 nm (outside the Er absorption bands) in $Al_2O_3:Er^{3+}$ films versus deposition temperature, up to a maximum temperature of 650 ºC. The samples were deposited 20 W Er-target sputtering power using the 99% purity Er target, corresponding to an Er concentration of ~2×10^{20} cm^{-3}, and the losses shown are the average values for TE and TM polarization. The optical losses at 1320 nm were relatively constant, while those at 633 nm decreased significantly with increasing temperature. At 650 ºC deposition temperature, optical propagation losses of 0.3 ± 0.1 dB/cm and 0.2 ± 0.1 dB/cm were measured at 633 nm and 1320 nm, respectively. Similar optical propagation loss values were measured in samples grown using the higher purity Er target. For films deposited with Er concentrations in the range shown in Fig. 2.10, the loss values at 633 nm and 1320 nm did not show any dependency on doping concentration or layer thickness. The losses were also comparable to those measured in the undoped layers, demonstrating that the incorporation of Er at dopant levels relevant for active devices does increase the background losses of the films.

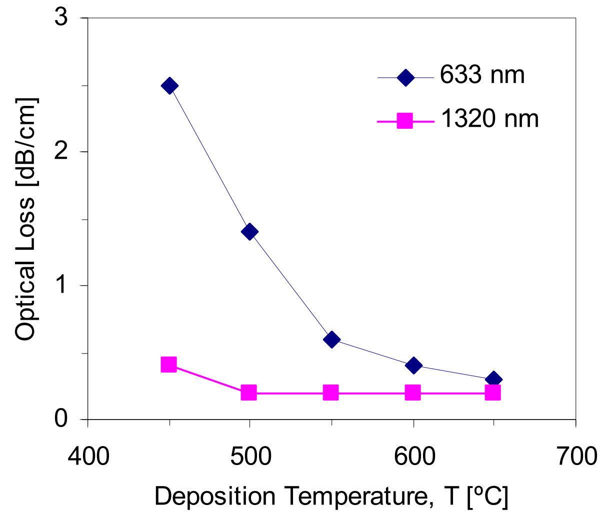

Fig. 2.13. Optical losses of $Al_2O_3:Er^{3+}$ slab waveguides at wavelengths of 633 nm and 1320 nm as a function of deposition temperature.

2.5 Summary

Al_2O_3 and $Al_2O_3:Er^{3+}$ waveguides have been fabricated by a simple, reliable, and reproducible reactive co-sputtering process and their fundamental optical properties have been investigated. The amorphous films are highly uniform over 50×50 mm^2 (<1% thickness non-uniformity), and have no detectable OH^- incorporation. Losses as low as 0.3 dB/cm and 0.1 dB/cm at 633 nm and 1523 nm, respectively, have been shown in undoped Al_2O_3 waveguides. Highly uniform incorporation of Er in the films in concentrations ranging from 0.2 to 5×10^{20} cm^{-3} was demonstrated. Background losses of 0.3 dB/cm at 633 nm and 0.2 dB/cm at 1320 nm were demonstrated in the Er-doped layers. Based on these results, very compact integrated optical devices such as low-loss splitters and ring-resonators, high-speed amplifiers, integrated lasers, and the like become feasible. The fact that these devices will operate near 1550 nm and can be integrated directly on a silicon chip makes the approach especially attractive.

Chapter 3

$Al_2O_3:Er^{3+}$ Channel Waveguides: Fabrication, Design and Optical Characterization

In this chapter a new process for fabricating channel waveguides in Al_2O_3 films using reactive ion etching is presented. Etching of amorphous Al_2O_3 films was investigated using an inductively coupled reactive ion etch system. The etch behaviour was studied by applying various common process gases and combinations of these gases, including CF_4/O_2, BCl_3, BCl_3/HBr, Cl_2, Cl_2/Ar and Ar. Based on analysis of the film etch rates and an investigation of the selectivity and patterning feasibility of possible mask materials, optimized optical Al_2O_3 channel-waveguide structures with optimized optical properties were fabricated. The channel waveguides were fabricated with BCl_3/HBr plasma and using a standard resist mask. The etched structures exhibit straight sidewalls with minimal roughness and sufficient etch depths (up to 530 nm) for defining waveguides with strong optical confinement. Using the developed etch process, low optical propagation losses (on the order of 0.2 dB/cm around 1550 nm) were demonstrated in single-mode Al_2O_3 ridge waveguides. Bent waveguides, y-splitters, and directional couplers were also designed and fabricated. Their optical properties were measured at 1550 nm and typical pump wavelengths of 1480 nm and 980 nm using different design parameters in order to select the best designs for implementing these functions in integrated active $Al_2O_3:Er^{3+}$ devices.

3.1 Introduction

In the preceding chapter an optimized deposition method, resulting in $Al_2O_3:Er^{3+}$ films with excellent optical quality was presented. However, in order to realize integrated active waveguide devices in such layers, a method for patterning channel waveguides is required. Amorphous Al_2O_3 is known to be a difficult material to pattern due to its relatively high physical and chemical stability. In fact, it is often used in the walls of etch chambers or as a mask material for reactive ion etch processes because of its high resistance to etching.

Previously, the definition of Al_2O_3 ridge waveguides by Ar^+-ion beam milling (or sputtering) [97] and wet chemical etching in heated 50% phosphoric acid [38] has been reported. Similar etching procedures, including wet etching in ODP 2420 resist developer, standard aluminum etch and phosphoric acid, Ar^+-ion beam milling, and Ar+ ion implantation followed by wet etching in hot phosphoric acid, have also been investigated within the IOMS research group [98, 99]. However, both general techniques (physical etching via Ar^+-ion beam milling and wet chemical etching by various means) result in sloped waveguide sidewalls and limit the overall resolution of the process. In particular, this inhibits the ability to open the small gaps ($\leq$ 2.0 µm) required for the directional couplers commonly used in integrated devices. Furthermore, the etch depths were limited to 300 nm in the Ar^+ milling case and less than 400 nm for wet etching of Al_2O_3. The channel waveguide fabrication process applied in [37], which relied on Ar^+-ion beam milling, was found to significantly increase the propagation losses compared to the $Al_2O_3:Er^{3+}$ slab waveguides.

With the aim of achieving excellent design flexibility and high optical gain in active waveguide devices, a fabrication technique is required with high resolution, sufficient etch depth and low additional losses introduced by the etch process itself. For high resolution, good selectivity to the mask material and steep (anisotropically etched) sidewalls are required. Deeply-etched channels (as opposed to shallow-etched ridge-type structures) are also necessary for strong lateral confinement of the optical mode and to minimize the bend radius (without significantly adding to the losses). A large range of possible etch depths allows for better flexibility in channel waveguide design, which depends on the desired wavelength, bend radius and percentage confinement of the propagating light within the waveguide core. Finally, for low additional losses due to channel etching, smooth sidewalls are required. Reactive ion etching (RIE) is the preferred etching method to achieve all of these goals, because it combines both physical and chemical etching mechanisms. When the etch process is optimized for a given material, the result is structures with steep, smooth sidewalls. The plasma etching characteristics of Al_2O_3 films in various chemistries have been widely studied [100-105]. RIE of optical waveguides in Al_2O_3 films has also been reported [106]. However, the process involved a complicated 3-level masking procedure and utilized a metal Cr-mask, which is less desirable than other materials because metals can introduce additional losses in the waveguide.

In this chapter, the etching behaviour of amorphous Al_2O_3 films and possible masking materials are investigated using an inductively coupled plasma (ICP) RIE system. Based on the etching data, an optimized process has been developed for fabricating high-quality, low-loss channel waveguides. The optical propagation losses of the obtained channel waveguide structures are reported and test structures for performing basic on-chip optical functions are designed, fabricated and characterized.

The test structures include 90º bends, y-splitters and directional couplers, and based on the measurements optimized designs are selected for applying these functions in $Al_2O_3:Er^{3+}$ integrated devices.

3.2 Experimental Details

In this section the details of the etch experiments, including the etch system which was used and the materials which were investigated, are presented. The setup for optical characterization of the Al_2O_3 channel waveguides and test structures is also described.

3.2.1 Etching Experiments

Amorphous Al_2O_3 films were reactively co-sputtered on thermally oxidized <100> Si substrates. The thickness of the deposited films ranged from approximately 500 to 900 nm. To develop the Al_2O_3 channel waveguide fabrication process, various potential common mask materials were investigated in terms of patterning methods, etch selectivity and possible removal after etching. Accordingly, 3-µm-thick plasma-enhanced chemical vapour deposited (PECVD) SiO_2 and Si_3N_4 films, standard 1.6-µm photoresist films, and 200-nm-thick electron-beam evaporated Ni and Cr layers were also prepared on Si substrates. These materials were primarily selected because they were readily available in the MESA+ cleanroom.

The etch experiments were carried out using an Oxford Plasmalab 100 inductively-coupled plasma (ICP) RIE system (illustrated in Fig. 3.1). The system is designed for 100-mm wafers, which are introduced to the chamber through a load-lock and fixed on a substrate holder with water-cooled electrode. He gas flow between the electrode and substrate is applied to control the substrate temperature. After the chamber is pumped down, the process gases are injected into the chamber within the inductive coils. There the electrons flowing due to the applied RF field bombard the gas molecules, ionizing them and generating a plasma. The ionized species are then directed onto the wafer by the RF bias applied to the table electrode. The ICP source is controlled by a 3-kW, 13.56-MHz RF generator, while substrate bias is controlled separately by a 600-W, 13.56-MHz RF generator. Various standard process gases and combinations of these gases were used in the experiments, including BCl_3, BCl_3/HBr (50:50), CF_4/O_2 (90:10), Cl_2, Cl_2/Ar and Ar.

In preliminary etching experiments, the etch rate was found to be relatively independent of gas flow, and to increase with decreasing chamber pressure, increasing ICP power, and increasing RF substrate electrode power and self-bias. Therefore, in order to compare the etch rate in various gas chemistries, the total gas flow was held constant at 50 sccm (measured by mass flow control units), while process pressure (measured by a capacitance manometer gauge) was maintained as low as possible, varying between 7-12 mTorr. Unless otherwise stated, the ICP power was held constant at 1500 W and the applied RF electrode power was varied from 100 to 400 W. For the etch experiments involving photoresist, the table temperature was set to 1 ºC and the He-backing pressure to 15 mTorr. This was because burning of the resist films was observed when the temperature was not regulated. Otherwise the substrate temperature was not regulated. The etch rates of the films were determined by measuring the film thickness before and after the etch process using a spectroscopic ellipsometer, while the etch rates of the Ni and Cr layers, patterned prior to etching by photolithography and

wet chemical etching, were measured using a Dektak surface profilometer. The process developed for the fabrication of channel waveguides in Al_2O_3 layers is discussed following the results of the etching experiments.

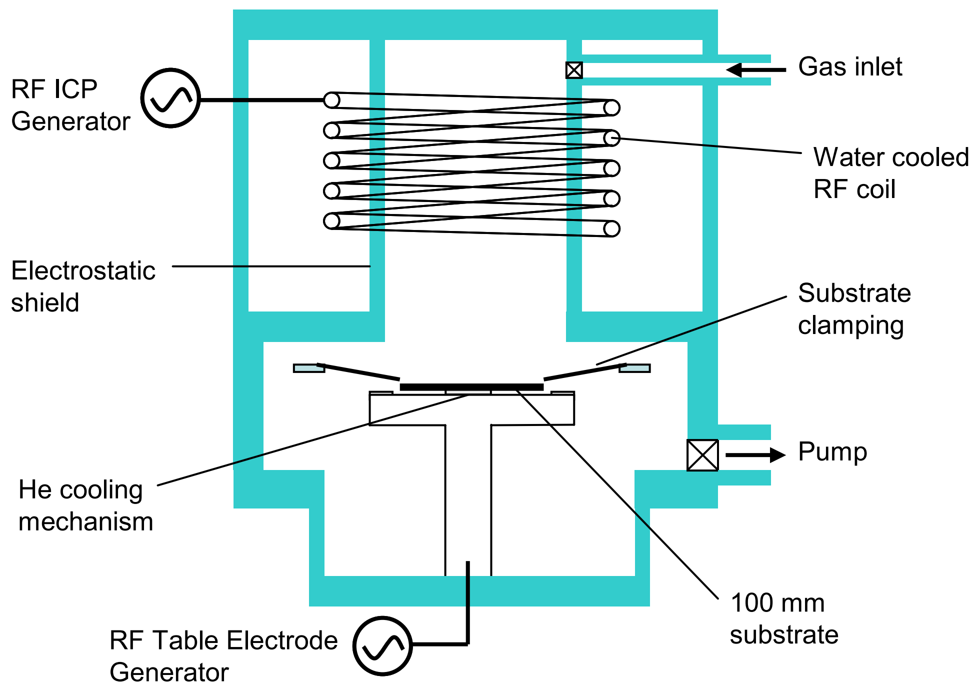

Fig. 3.1. Illustration of inductively coupled plasma reactive ion etch system.

3.2.2 Optical Measurements

All channel waveguide optical measurements were carried out using a fiber-coupling setup with computer-controlled piezoelectric alignment stages. Software developed in-house allowed automated alignment and adjustment of the stages with a step size down to 25 nm. A broadband erbium-doped fiber light source (1520-1580 nm), Hewlett-Packard 8168 C tunable laser source (1480 – 1600 nm), 1480 nm JDS Uniphase 3400 series diode laser source, 1320 nm Amoco ALC 1320-25P diode-pumped solid state source or 980 nm JDS Uniphase 2900 series diode laser was used as the light source. The light was coupled to the chip using 9-µm core single mode fiber (designed for 1320 nm and 1550 nm), single-mode polarization maintaining (PM) fiber (with a polarizer after the source used to select TE or TM polarization) or 6 µm-core single mode fiber (single-mode at 980 nm). The transmitted light was collected using a 9-µm-core single mode fiber or 50-µm-core multimode fiber and the optical power was measured using a Hewlett-Packard 8153A lightwave multimeter.

3.3 Channel Waveguide Etching Results

In this section the etching behaviour of the Al_2O_3 films in the various ICP RIE chemistries and their selectivity to potential mask materials will be discussed and compared. Based on these results, a process for etching Al_2O_3 channel waveguides was

developed and is described. In the last section, the use of Al_2O_3 as a mask material for etching waveguides in other rare-earth-ion host materials, namely Y_2O_3, is discussed.

3.3.1 Al_2O_3 Etching

The etch rate of the Al_2O_3 films was investigated as a function of applied RF power for various plasma compositions. Figure 3.2 shows the measured etch rate of Al_2O_3 films as a function of RF power for CF_4/O_2 (90%:10%), BCl_3 (100%), BCl_3/HBr (50%:50%), Cl_2 (100%) and Ar (100%) gases. The process pressure (which was the lowest attainable under each of the plasma conditions) was measured to be 10-12 mTorr (CF_4/O_2), 9 mTorr (BCl_3), 9 mTorr (BCl_3/HBr), 7-8 mTorr (Cl_2) and 8 mTorr (Ar).

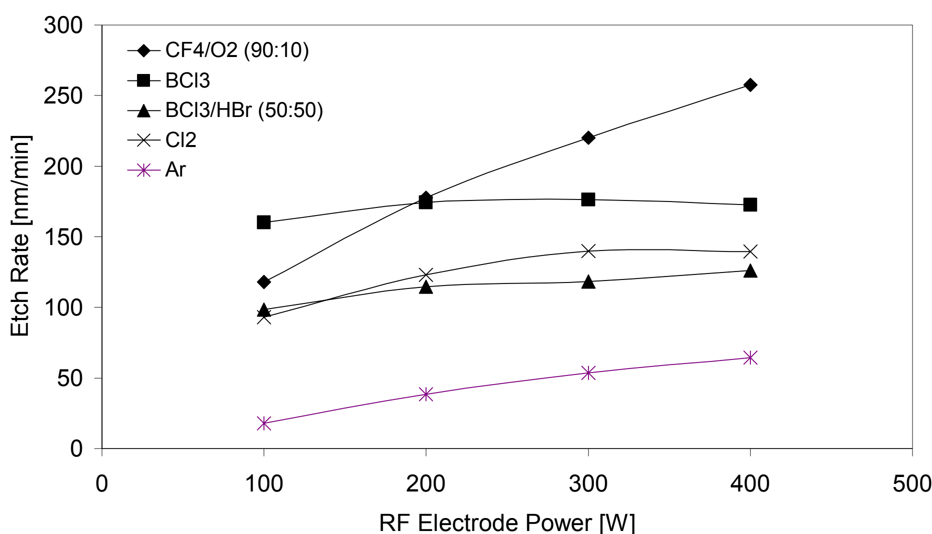

Fig. 3.2. Etch rate as a function of RF power for Al_2O_3 films in $CF_4:O_2$ (90%:10%), BCl_3 (100%), $BCl_3:HBr$ (50%:50%), Cl_2 (100%) and Ar (100%) at a total flow rate of 50 sccm.

The highest etch rate, 257 nm/min was measured for CF_4/O_2 at 400 W. The etch rate in CF_4/O_2 also shows the greatest dependence on RF power, indicating that etching under these conditions depends strongly on the energy of ions directed onto the substrate (it is strongly ion-assisted). We can gain further insight into the etching behaviour by looking at the melting and boiling points of potential etch products at atmospheric pressure, which can be used to predict their volatility under the non-equilibrium, low-pressure conditions during plasma etching. The melting and boiling points for potential etch products for Al_2O_3 are summarized in Table 3.1. The potential F-based etch products of Al_2O_3 are expected to have lower volatilities (based on higher melting and boiling points) than Cl-based products, which is consistent with the observed stronger effect of ion energy on removing material from the surface and assisting the reaction. These data generally agree with the previous etching results for similar Al_2O_3 layers in CF_x gases [100]. The etching in Cl-containing gases is shown to be less dependent on RF-power, indicating that chemical etching, rather than ion-assisted etching, more strongly affects the etch rate and behaviour. Of the Cl-containing gases, the etch rate is shown to be significantly higher in BCl_3 than Cl_2 or BCl_3/HBr (50%:50%). In the case of all the halogen-based (Cl, F) processes, the etch rate is almost an order of magnitude higher than etching in Ar, which strongly indicates that an additional chemical component aids the etching process for Al_2O_3 in those cases.

Table 3.1. Melting and boiling points of possible etch products of Al_2O_3 and Y_2O_3 [107].

Al_2O_3			Y_2O_3		
Etch Product	Melting Point (°C)	Boiling Point (°C)	Etch Product	Melting Point (°C)	Boiling Point (°C)
AlB_2	> 920	-	YB_6	2600	-
Al_4C_3	2100	> 2200	YC_2	~2400	-
$AlBr_3$	97.5	255	YBr_3	904	-
$AlCl_3$	192.6	180 (s)	YCl_3	721	-
AlF_3	~2250 (t)	1276 (s)	YF_3	~1150	-
Al_2O_3	2053	~3000	Y_2O_3	2438	-
Al	660.32	2519	Y	1522	3345
$Al(BH_4)_3$	-64.5	44.5	-		
AlH_3	> 150	-	-		
H_2O	0	100			
O_2	-218.4	-182.9			

s = sublimation point, t = triple point

3.3.2 Etching of Mask Materials

The etch rates of several common mask materials, chosen for structuring Al_2O_3 because these mask materials can be easily deposited and patterned in our laboratory, were also investigated. The main requirements for a good mask material are that it can be easily patterned, it has a high selectivity compared to the material to be etched (for good pattern transfer and high resolution), and it must be possible to selectively and completely remove the mask material from the substrate after etching. Generally, selectivities much greater than 1 are preferred. However for Al_2O_3, which is known to be highly stable, we expect lower selectivities. Table 3.2 shows the maximum selectivity measured for Al_2O_3 to the various prospective mask materials. The selectivity compared to a standard silicon wafer was also measured for reference. The process window used to determine the mask material etch rates was essentially the same as that used for the Al_2O_3 etching experiments (ICP power = 1500 W, RF Electrode Power = 100 to 400 W, pressure = 6 to 14 mTorr, total gas flow = 50 sccm). The selectivity in general was found to be 2 times lower for patterned as opposed to un-patterned mask layers.

Table 3.2. Maximum selectivities of Al_2O_3 to possible mask materials, for various process chemistries, at a total gas flow rate of 50 sccm, ICP power of 1500 W, varying RF electrode power (100 to 400 W) and process pressure in the range of 6 to 14 mTorr.

	Process Gas				
Material	CF_4/O_2 (90:10)	BCl_3	BCl_3/HBr (50:50)	Cl_2	Ar
Photoresist	< 0.20	0.67	0.54	0.16	0.57
PECVD SiO_2	0.60	0.95	0.80	0.70	0.35
PECVD Si_3N_4	0.35	1.35	1.80	0.65	0.45
Silicon	0.39	0.98	2.15	0.30	0.25
Nickel	5.82	-	3.51	1.38	0.27
Chromium	-	-	-	< 0.94	-

For all mask materials except Ni, the selectivity versus Al_2O_3 was generally higher in BCl_3 and BCl_3/HBr. The selectivities for Si_3N_4 were > 1 for these gases,

however selective removal of Si_3N_4 from the Al_2O_3 layer after etching was found to be a problem. The selectivities to Ni are also quite high in comparison to other materials, as we would expect for a harder metal mask, however, if possible it is better to avoid metal masks for optical applications, as any residual metal remaining after etching and the mask removal can introduce additional optical losses. For Cr, significant data is missing because it was realized early in the experiments that patterning mask layers with smooth sidewalls was difficult – perhaps due to the layer deposition process or quality of the Cr films. Furthermore, the etch rates were generally higher for Cr than for Ni, so Cr was ruled out as a possible mask material. In comparison to the other materials, photoresist could be easily removed by using a combination of O_2 plasma etching and wet HNO_3 cleaning. Patterning of photoresist also requires the least fabrication steps. Therefore, it was decided to use photoresist as a mask, varying the parameters to improve the selectivity and using the BCl_3/HBr system because this gave the highest overall selectivities. These process gases have previously been demonstrated as a suitable gas mixture for etching straight, vertical ridge structures with smooth sidewalls in sapphire (crystalline Al_2O_3) [108, 109], with channel waveguides being demonstrated in Ti:sapphire layers using a BCl_3/Cl_2 mixture [110].

3.3.3 Structuring of Al_2O_3 Channel Waveguides

Al_2O_3 channel waveguides ranging from 1.2 to 8.0 µm in width were fabricated using a BCl_3/HBr gas mixture and 1.6-µm photoresist mask layer patterned by standard lithography. As a starting point for etching our amorphous Al_2O_3 films a gas ratio of 5:2 (BCl_3:HBr), ICP power of 1750 W, RF substrate electrode power of 100 W, pressure of 12 mTorr and a total gas flow of 35 sccm were selected. The ICP power and flow rates were slightly adjusted based on proprietary knowledge shared by Oxford Instruments [111], but these parameters did not greatly affect the etch rates. An RF substrate power of 100 W was applied because this power resulted in the highest selectivity in the 100-400 W range. Good etching results were obtained for etch depths ≤ 300 nm. However, when etching deeper (~ 500 nm), which was required for the channel waveguide designs eventually applied in devices, rounding at the top of the waveguide occurred. This was due to ions bombarding the upper corners of the resist mask which resulted in eventual thinning of the entire mask strip after a certain etch depth (see Fig. 3.3a). When the mask width began to decrease during etching, rounding at the top corners of the Al_2O_3 waveguide began to occur (see Fig. 3.3b).

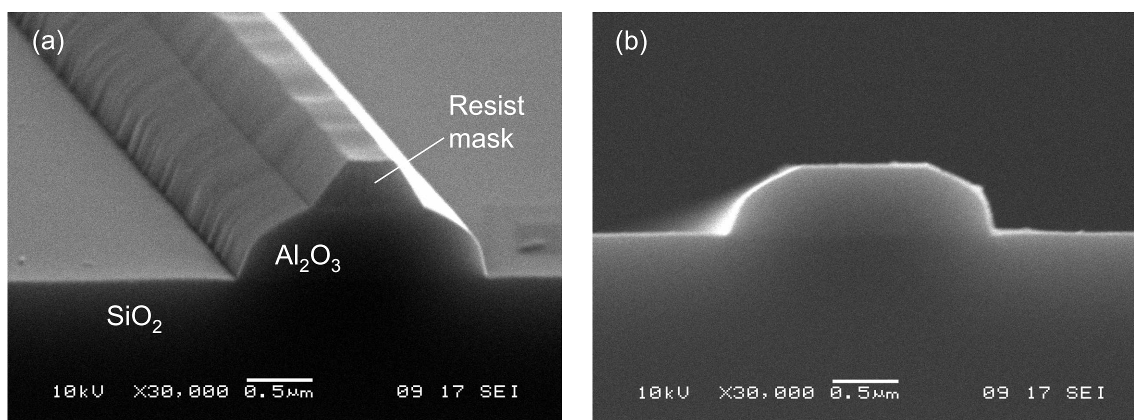

Fig. 3.3. SEM micrographs of (a) Al_2O_3 waveguide profile with resist mask on top and (b) Al_2O_3 waveguide cross-section with resist mask removed. The 1.4-µm-wide and 550-nm-deep channel waveguide was etched using 100 W RF table electrode power.

While such rounding at the corners of the Al_2O_3 waveguides may not negatively impact their optical performance, it significantly complicates the waveguide design by adding another parameter. In order to avoid this effect, either a thicker resist mask or better etch selectivity was required. Since the 1.6-µm thickness of the resist mask was already at the upper limit for defining small gaps by standard lithography, it was decided to vary the process parameters in order to improve the selectivity to the resist mask. For this purpose, the RF electrode power was varied because it was found to have the most significant impact on etch rates of resist and Al_2O_3. Figure 3.4 shows the etch rate of Al_2O_3 and selectivity to photoresist as a function of RF electrode power in the range 25 to 300 W. As the RF power is decreased, the etch rate of the Al_2O_3 layer decreases, and the selectivity to the resist mask increases. Both effects can be beneficial to waveguide fabrication – the higher selectivity means greater etch depths are possible, while the lower etch rate allows better control of the final etch depth.

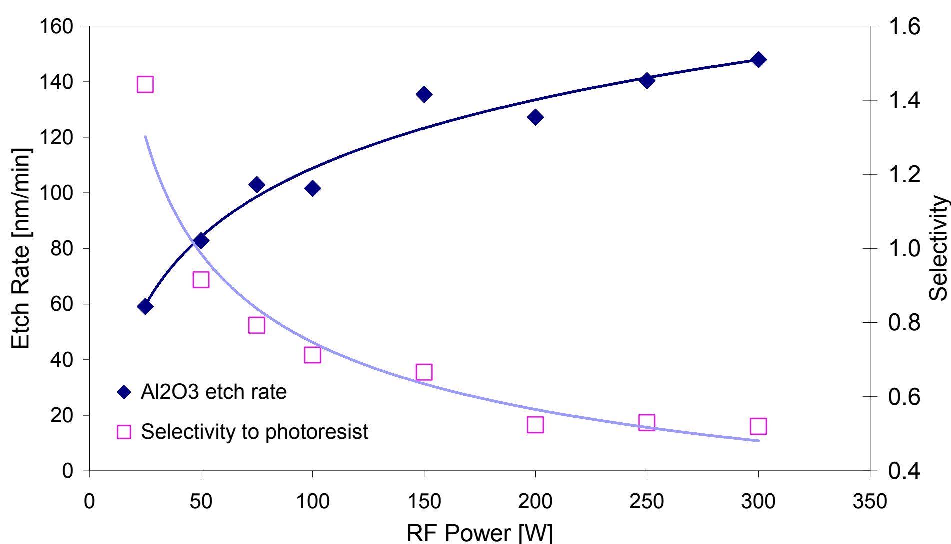

Fig. 3.4. Al_2O_3 etch rate and selectivity to resist for full layers as a function of applied RF substrate electrode power for an ICP power of 1750 W and total flow rate of 35 sccm. The fitted lines serve as a guide to the eye.

Figures 3.5a and 3.5b show a side profile and cross-section, respectively, of a 1.2-µm-wide Al_2O_3 channel waveguide etched with the same parameters as before but with an applied substrate electrode power of 25 W. The etch depth was determined to be 530 nm and the selectivity to the resist mask was 0.76 (about half the selectivity shown in Fig. 3.4 because those selectivities were based on film etch rates). The channel sidewall angle ranged from 56º to 68º depending on the waveguide width and a slight trench was observed beside the waveguide, typical of RIE processes. The small sidewall roughness in the picture can be attributed to pattern transfer from the mask layer itself. Such roughness could be decreased with the use of an E-beam (as opposed to laser-lithography written) mask for the lithographic mask-patterning step. Based on these considerations, this etch process was deemed to be well-suited to the fabrication of Al_2O_3 channel waveguides.

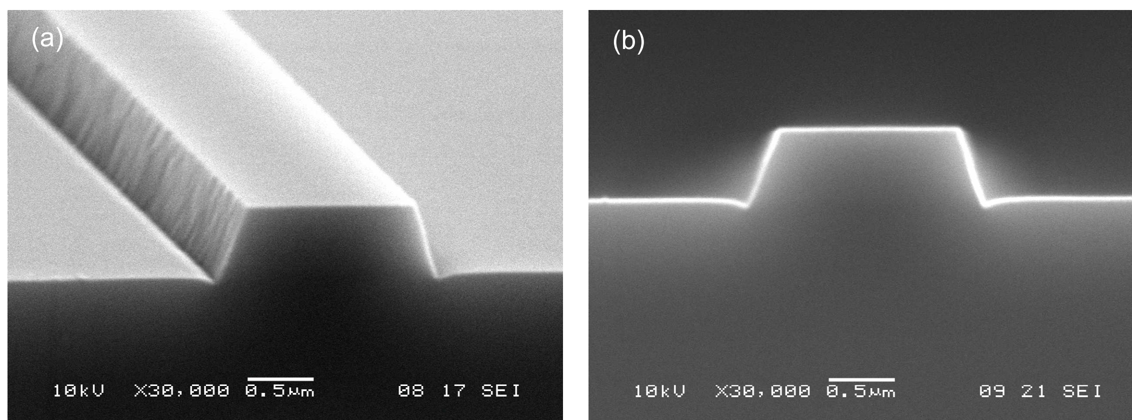

Fig. 3.5. SEM (a) profile and (b) cross-section images of a 1.2-μm-wide and 530-nm-deep channel waveguide in Al_2O_3 etched using 25 W RF electrode power.

Typically in integrated optical devices, such as ring resonators, coupling of light between adjacent waveguides is necessary. This requires waveguides to be separated by gaps on the order of the waveguide width (1.0 to 2.0 μm). In order to investigate the opening of gaps, a laser-written waveguide mask with varying gap width and waveguide widths of 2.0 μm was used to pattern a 500-nm-thick Al_2O_3 layer. The gap was not fully etched for separations less than 1.8 μm. Good results were obtained for a gap width of 2.0 μm, as shown in the SEM images in Figs. 3.6a and 3.6b.

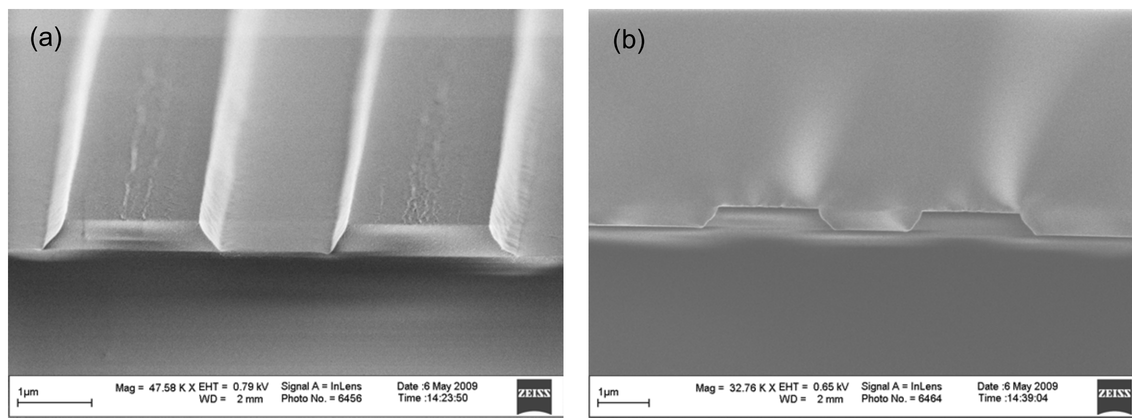

Fig. 3.6. SEM (a) profile and (b) cross-section images of 2.0-μm-wide Al_2O_3 channel waveguides separated by gaps of 2.0μm.

Finally, in channel waveguide design it is usually desirable to apply a top cladding. A top cladding reduces the refractive index contrast compared to a core-air interface, which can reduce optical losses due to scattering. It also helps to protect the optical waveguides from physical damage. Therefore, cladding layer deposition was also investigated for our Al_2O_3 channel waveguides. A 5-μm-thick plasma enhanced chemical vapour deposition (PECVD) SiO_2 cladding was deposited using an Oxford PECVD 80 system. The processing parameters were as follows: gas flow rates of 200 sccm and 710 sccm for 2% SiH_4/N_2 and N_2O, respectively, an applied power of 60 W, a chamber pressure of 650 mTorr, a substrate temperature of 300 ºC and total deposition time of 3 hours. After fabrication of the first cladded channel waveguides, it was found that due to its slightly higher refractive index than the thermal SiO_2 layer, an optical slab

waveguide was formed by the thermal SiO_2-PECVD SiO_2-Air layer stack beside the Al_2O_3 channel waveguides. However, by annealing the films at 500 ºC for 3 hours in an N_2 atmosphere, the refractive index of the PECVD layer could be reduced to below that of the thermal oxide layer. At the same time, the refractive index of the thermal oxide layer remained unchanged because it was grown at a significantly higher temperature. This annealing temperature is also below the deposition temperature of the Al_2O_3 and $Al_2O_3:Er^{3+}$ films. Therefore the cladding deposition and subsequent annealing was not expected to affect the optical properties of the channel waveguide core material (this was later confirmed by optical propagation loss measurements). A SEM image of the cross-section of an Al_2O_3 waveguide with top-cladding deposited is displayed in Fig. 3.7.

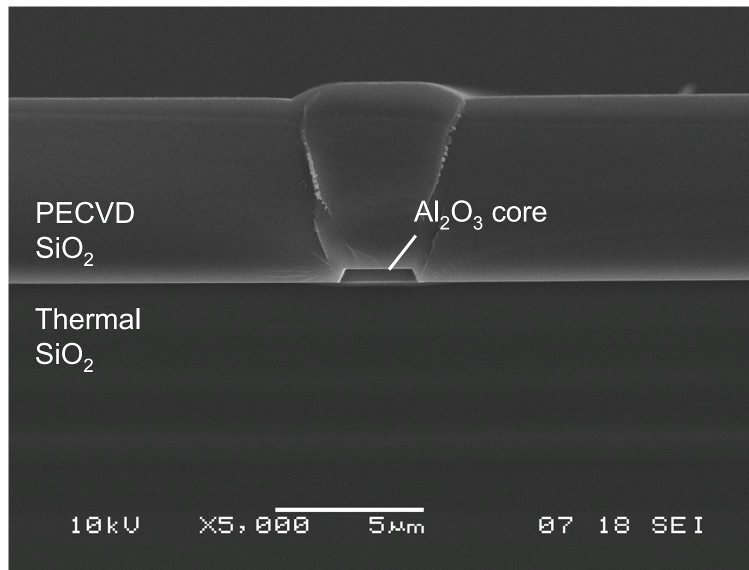

Fig. 3.7. SEM cross-section image of an Al_2O_3 waveguide with PECVD SiO_2 top-cladding.

The full channel waveguide fabrication procedure, including optional top-cladding deposition, is summarized in Table 3.3. The samples, Al_2O_3 or $Al_2O_3:Er^{3+}$ films on thermally oxidized silicon wafers, are cleaned in 100% HNO_3 followed by lithography using OiR 097-17 resist and an EVG 620 mask aligner. After lithography, the resist mask is hard baked for 30 minutes at 110 °C using a hot plate. The samples are then etched applying ICP RIE. After etching the mask is removed using an O_2 plasma followed by wet cleaning in 100% HNO_3. The cladding layer is then deposited and annealed and the samples are cleaved or diced using a Loadpoint Microace dicing saw to prepare end facets.

Table 3.3. Al_2O_3 channel waveguide fabrication procedure.

Step	Equipment	Description
1. Sample cleaning	-	~10 min. in wet HNO_3 (100%)
2. Lithography	EVG 620 mask aligner	OiR 907-17 resist (thickness ≅ 1.6 μm)
3. Hard resist bake	Standard hot plate	~30 min. at 110 °C
4. Etching	Oxford Plasmalab 100 ICP RIE	Al_2O_3 etch rate ≅ 70 nm/min.
5. Mask removal	Tepla 300E plasma etcher	1) ~30 min. in O_2 plasma 2) ~10 min. in wet HNO_3 (100%)
6. Cladding deposition and annealing	Oxford PECVD 80 Annealing oven	1) SiO2 deposition, 3 hours (thickness ≅ 5 to 6 μm) 2) Annealing in N_2 atmosphere for 3 hours at 500 °C
7. End-facet preparation	Loadpoint Microace 3 dicing saw	Dicing or cleaving

3.3.4 Optical Performance of Channel Waveguides

Before proceeding with waveguide and $Al_2O_3:Er^{3+}$ device design, it was important to demonstrate low propagation losses in the channel waveguides. Therefore, the propagation losses were measured in single mode Al_2O_3 waveguides prepared using the etch procedure outlined in this section. Here, the theory related to propagation losses in channel waveguides is also presented.

The Lambert-Beer law for the change of light intensity I at wavelength λ propagating through a medium of short length Δz reads:

$$\frac{dI}{dz} = -a(\lambda) I \,,$$

$$I(z + \Delta z) = I(z) \exp[-a(\lambda)\Delta z], \tag{3.1}$$

where $a(\lambda)$ is the wavelength-dependant absorption coefficient (in cm^{-1}). Solving for $a(\lambda)$,

$$a(\lambda) = -\frac{1}{\Delta z} \ln\left[\frac{I(z + \Delta z)}{I(z)}\right]. \tag{3.2}$$

The refractive index N of an absorbing material has both a real and an imaginary part and can be written as $N = n - ik$. The imaginary part of the refractive index k represents the absorption of light in the material. In a channel waveguide, the optical field propagates according to an effective index $N_{eff} = n_{eff} - ik_{eff}$. The absorption coefficient is related to the imaginary refractive index by:

$$a(\lambda) = \frac{4\pi k_{eff}}{\lambda}. \tag{3.3}$$

Often in electrical engineering or when describing the propagation losses in optical waveguides, the absorption coefficient is given in units of dB/cm. In this case the absorption coefficient is written as $\alpha(\lambda)$ and related to $a(\lambda)$ by:

$$\begin{aligned} \alpha(\lambda) &= 10\log e \cdot a(\lambda) \\ &= -\frac{10}{\Delta z}\log\left[\frac{I(z+\Delta z)}{I(z)}\right]. \end{aligned} \tag{3.4}$$

The total absorption coefficient or background loss in channel waveguides can be written as a sum of the different loss mechanisms:

$$\alpha_{Total}(\lambda) = \alpha_{mat}(\lambda) + \alpha_{scat}(\lambda) + \alpha_{abs}(\lambda), \tag{3.5}$$

where $\alpha_{mat}(\lambda)$ is the material-dependant background loss, $\alpha_{scat}(\lambda)$ is the loss due to scattering at the core-cladding interface or roughness of the waveguide sidewalls, and $\alpha_{abs}(\lambda)$ is the absorption due to active processes (in our case it may be written as $\alpha_{Er}(\lambda)$ to describe the absorption due to the Er^{3+} ions in doped waveguides). Optical measurements are required to determine each of these contributions to the total propagation loss. In Chapter 2 the losses due to the material, including perhaps some scattering losses at the Al_2O_3-air and Al_2O_3-SiO_2 interfaces, were determined in the slab waveguide measurements. Here we are interested in determining any extra scattering losses introduced in the case of channel waveguides by the etching process.

In order to test the additional losses introduced by channel etching, single-mode uncladded ridge waveguide structures were patterned in a low-loss Al_2O_3. 2.5-µm-wide waveguides were defined using the optimized recipe, to an etch depth of 220 nm in a 740-nm-thick film. The etch-depth uniformity over the substrate was found to be ± 10%. Prior to etching, the optical losses of the film were measured to be 0.12 ± 0.10 dB/cm at a wavelength of 1523 nm using the prism coupling method. The optical losses of the uncladded 2.5-µm-wide ridge waveguides, designed to be single mode at wavelengths around 1550 nm, were investigated using a fiber butt-coupling setup and broadband erbium-doped fiber amplifier (1520-1580 nm) source. Using the cut-back method, with waveguide lengths of 5.65, 4.0, and 1.65 cm, a propagation loss of 0.21 ± 0.05 dB/cm was measured. This indicates that only small additional losses up to 0.1 dB/cm, such as scattering losses caused by sidewall roughness, are introduced by the dry-etching process.

3.3.5 Structuring of Waveguides in Other Rare-Earth-Host Materials

In the course of this research, the etching behaviour of other sesquioxide host materials (so-called because of the ratio of anions to cations is 1.5), such as Y_2O_3, Sc_2O_3, Lu_2O_3 and $(Gd, Lu)_2O_3$ were also studied. These other materials also act as excellent hosts for rare earth ions, but differ from Al_2O_3 in that they are polycrystalline or crystalline, as opposed to amorphous. Due to their sharp emission peaks, high peak cross sections, low phonon energies, high thermal conductivities and high damage thresholds these materials are promising for such applications as highly frequency-stable and high peak power lasers [10]. Since they are not within the focus of this thesis, however, their etching behaviour is only discussed briefly here for two purposes: firstly, to serve as a comparison to the etching behaviour of Al_2O_3; secondly, because the Al_2O_3 waveguide etching procedure described is an important step in the etching procedure which was developed for these materials. In particular, the etching behaviour of polycrystalline Y_2O_3 films is discussed, since the same procedure for etching Y_2O_3 was applied to the other sesquioxides.

Deposition of the Y_2O_3 films used in this study is described in detail in [112]. Due to its high chemical stability, Y_2O_3 is known to be an even more difficult material to etch by chemical means than Al_2O_3. The melting and boiling points for potential etch products of Y_2O_3 using the halide gases are shown in Table 3.1 and are generally much higher than those for Al_2O_3. An etch study was carried out for Y_2O_3 using the same process gases as applied here for Al_2O_3 [78], and it was found that etching in Ar resulted in higher etch rates compared to the other process gases. In the Cl-containing gas chemistries a chemical reaction was observed which was in agreement with a previous study [113]. However, this resulted in a non-volatile layer on the surface, probably YCl_3, which actually inhibited further etching of the film and reduced the etch rate. Since Ar ions are non-reactive and provide only physical etching, it was concluded that none of the etch chemistries available could be used to enhance Y_2O_3 etching by chemical means.

A comparison of Y_2O_3 etch rates to potential mask materials was also carried out and the selectivities (see Table 3.4) were much poorer than Al_2O_3 because of the lower etch rates. Besides a value of 1.31 for Ni in CF_4/O_2, the only selectivities close to or greater than 1 were in Ar, where values of 0.81, 0.90 and 2.05 were measured for photoresist, Si_3N_4 and Al_2O_3, respectively. The etch rates of Al_2O_3 and Y_2O_3 are compared in Fig. 3.8 for applied substrate electrode powers of 100-400 W. The etch rates of the Al_2O_3 films are significantly lower within this range (which also highlights the difficulty of etching Al_2O_3 by physical means such as Ar^+-ion beam etching). Although some chemical component to the etching would be preferred, due to the poor selectivities, the blocking layer in Cl_2, BCl_3 and BCl_3/HBr, and primarily overall physical etching of Y_2O_3, it was decided to use Ar as a process gas. Because Al_2O_3 provided the best selectivity, and an etching procedure for this material was available, it was chosen as the mask material.

Table 3.4. Maximum selectivities of Y_2O_3 to possible mask materials, for various process chemistries, at a total gas flow rate of 50 sccm, ICP power of 1500 W, varying RF electrode power (100 to 400 W) and process pressure in the range of 6 to 14 mTorr.

	Process Gas				
Material	CF_4/O_2 (90:10)	BCl_3	BCl_3/HBr (50:50)	Cl_2	Ar
Photoresist	< 0.03	0.05	0.03	0.03	0.81
PECVD SiO_2	0.15	0.20	0.25	0.25	0.65
PECVD Si_3N_4	0.10	0.20	0.25	0.15	0.90
Silicon	0.09	0.06	0.44	0.11	0.43
Al_2O_3	0.30	0.25	0.35	0.45	2.05
Nickel	1.31	-	0.59	0.50	0.46
Chromium	-	-	-	< 0.30	-

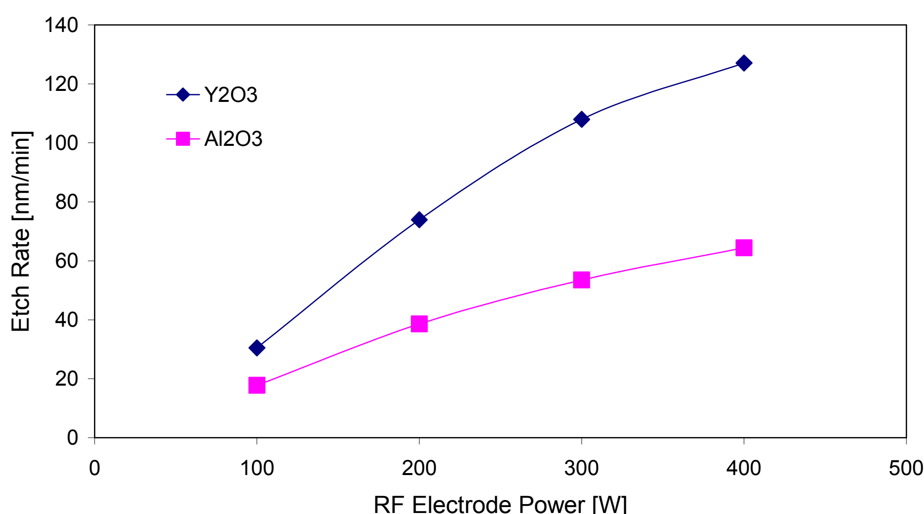

Fig. 3.8. Etch rate as a function of RF substrate electrode power for Al_2O_3 and Y_2O_3 films in Ar.

A ~460-nm-thick Al_2O_3 layer was sputtered at 200ºC on a Si wafer containing a sputter-deposited Y_2O_3 film. The Al_2O_3 layer was then patterned using the same lithography and BCl_3/HBr etch process for etching Al_2O_3 channel waveguides. The results are shown in the cross-section in Fig. 3.9a. The resist mask was then removed and the sample was etched in Ar at an applied RF power of 100 W to a depth of 250 nm at a Y_2O_3 etch rate of 29 nm/min and selectivity to Al_2O_3 of 1.55, as shown in Fig. 3.9b. The sidewall profile and angle matched that of the Al_2O_3 mask layer, and the sidewall quality was not strongly influenced by the columnar polycrystalline structure of the Y_2O_3 layer, which is visible in the SEM micrograph cross-sections shown in Fig. 3.9. Waveguides ranging from 1.4-µm to 8.0-µm wide were successfully patterned in the layer. The resulting waveguides, after Al_2O_3 mask layer removal in 50% HF solution, are shown in Figs. 3.9c and 3.9d. Since Al_2O_3 has a lower refractive index than the sesquioxide materials mentioned at the beginning of this section, it can also be deposited as the top cladding layer. As proof of the excellent optical quality of the resulting channel waveguides, the same etch procedure has been applied to other monocrystalline rare-earth-doped sesquioxides, resulting in net gain and lasing in (Gd, Lu)$_2O_3$:Er^{3+} [114] and (Gd, Lu)$_2O_3$:Nd^{3+} [115] channel waveguides, respectively.

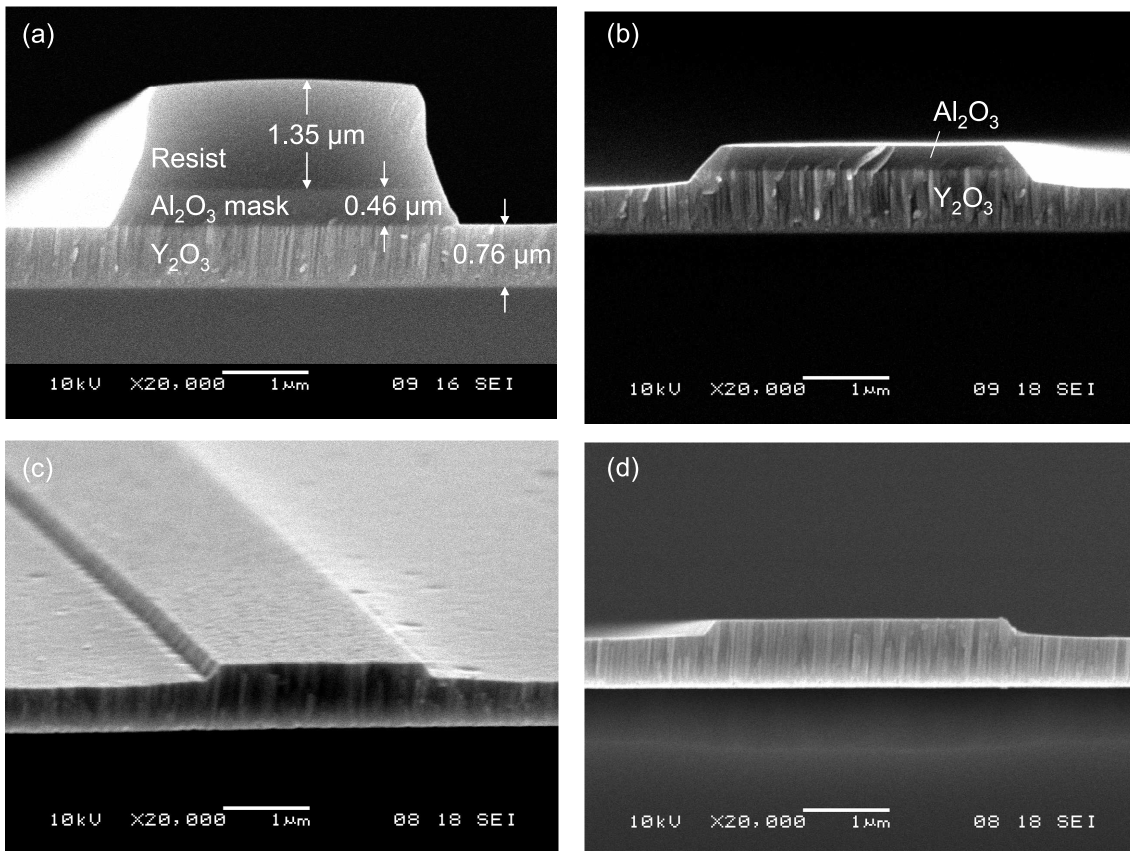

Fig. 3.9. SEM micrographs of (a) a photoresist-patterned Al_2O_3 mask on Y_2O_3, (b) an Ar-etched Y_2O_3 waveguide with Al_2O_3 mask layer remaining on top, (c) a 2.4-µm-wide, 250-nm-deep Y_2O_3 channel waveguide after Al_2O_3 mask layer removal and (d) cross-section of a 3.4-µm-wide, 250-nm-deep Y_2O_3 waveguide on the same sample.

3.4 Channel Waveguide and Device Elements Design

It is the goal of this section to provide a basis for the design of $Al_2O_3:Er^{3+}$ waveguides with suitable properties for the demonstration of active devices. The considerations for the waveguide design include single-mode behaviour, fabrication tolerances, high confinement within the active $Al_2O_3:Er^{3+}$ core material and minimized propagation losses in straight and bent waveguides. Based on these considerations, the waveguide geometry is selected and basic elements required in integrated devices, including bent waveguides, y-splitters and directional couplers, are designed. The section is divided into two sub-sections: waveguide design and device elements design.

3.4.1 Waveguide Design

In this sub-section the design criteria, waveguide simulations and Al_2O_3 and $Al_2O_3:Er^{3+}$ waveguide design choices based on the simulation results are presented.

3.4.1.1 Design Criteria

Four key criteria were considered in the channel waveguide design: the single mode condition, fabrication tolerances, the confinement factor, and the minimum bend radius.

Single mode condition: For photonic devices, it is generally desirable to design single mode channel waveguides for both TE and TM polarization. In the case of Er-doped amplifiers and lasers, this condition should be fulfilled for the signal wavelength around 1550 nm, and if possible, the pump wavelength of either 1480 nm or 980 nm. Multimode behaviour can result in higher losses and in general can complicate the device design and characterization.

Fabrication tolerances: Besides the single-mode condition, there are limits placed on the waveguide dimensions by the fabrication process. In order to entirely etch through the films the upper limit for the film thickness is around 600 nm. At the same time, the minimum channel width that can be defined using standard lithography in the MESA+ cleanroom is about 0.8 µm. However, to ensure that devices are defined properly, especially over large areas of the substrate where the lithography quality can vary, it is safer to use a 1-µm width limit instead.

Confinement: For strong interaction of the optical signal and pump with the Er ions and for high peak gain in $Al_2O_3:Er^{3+}$ amplifiers, it is desirable to have high confinement of the propagating optical modes within the $Al_2O_3:Er^{3+}$ core of the waveguide. The confinement factor, which describes the percentage of the optical power which propagates in the $Al_2O_3:Er^{3+}$ core, strongly depends on the waveguide dimensions.

Bend radius: Another important parameter is the minimum bend radius of a certain waveguide design. The minimum bend radius is defined here as the smallest radius for which the bend losses are below 10^{-3} dB/360°. A lower bend radius allows for more compact devices, which means that the on-chip integration density can be increased.

3.4.1.2 Simulations

Two main waveguide designs were considered for the $Al_2O_3:Er^{3+}$ active devices in this thesis. Design I, shown in Fig. 3.10a, consists of an uncladded, shallow-etched ridge-type waveguide using a ~1.0-µm-thick $Al_2O_3:Er^{3+}$ layer. This design was selected because it minimizes the scattering losses due to etching in channel waveguides. As will be shown, it also allowed for single-mode channels at a pump wavelength of 980 nm and signal wavelengths around 1550 nm and high confinement of both signal and pump within the active $Al_2O_3:Er^{3+}$ waveguide core. Design II, shown in Fig. 3.10b, is a deeply-etched channel waveguide in a thinner (~0.3 to 0.7 µm) $Al_2O_3:Er^{3+}$ layer with a top cladding layer deposited. In general, deeper-etching increases the lateral confinement of the optical mode, which allows smaller bend radii. For device design, it also eliminates one parameter, the etch depth, in which only slight variations can heavily affect the designed performance.

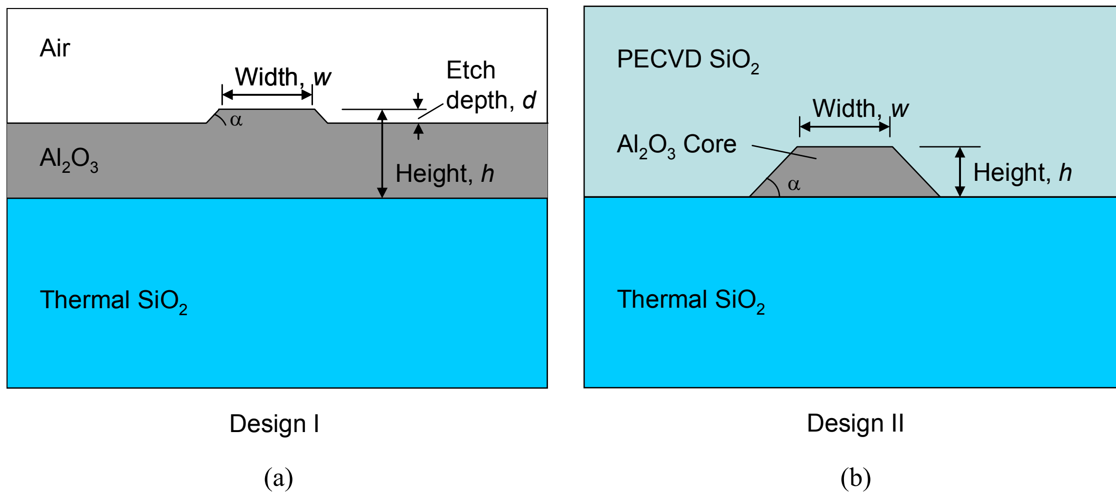

(a) (b)

Fig. 3.10. Channel waveguide cross sections with relevant parameters used in simulations for (a) design I and (b) design II.

PhoeniX's FieldDesigner modesolver software package was used for all of the optical waveguide simulations. The refractive indices used in the waveguide design are shown in Table 3.5. This data was obtained using the 4 wavelength Metricon prism coupling system. The refractive index values at 980 nm and 1480 nm, typical pump wavelengths for Er-doped amplifiers and lasers, are extrapolated. Since all the layers are amorphous and yield low stress values, the birefringence is low and the difference between TE and TM refractive indices is typically 1×10^{-3}. The waveguide simulations were carried out using the refractive indices of undoped Al_2O_3 layers, which are slightly lower than those measured in Er-doped films. For comparison, the refractive indices measured in an $Al_2O_3:Er^{3+}$ film with an Er concentration of 2.1×10^{20} cm^{-3} are also shown in Table 3.5. Waveguide widths up 10 µm and film thicknesses up to 1.2 µm were investigated. The etch angle (in the range 56 to 68°) was not found to have a significant influence on the simulation results. Therefore an etch angle α of 56° used in all the waveguide simulations.

Table 3.5. Refractive indices (for TE polarization) measured by prism coupling of PECVD SiO_2, Al_2O_3, $Al_2O_3:Er^{3+}$ (Er concentration = 2.1×10^{20} cm^{-3}) and thermal SiO_2 layers used in waveguide design.

Layer	$n_{633\ nm}$	$n_{980\ nm}$ [1]	$n_{1300\ nm}$	$n_{1480\ nm}$ [1]	$n_{1550\ nm}$
Annealed PECVD SiO_2	1.452	1.447	1.442	1.440	1.439
Al_2O_3	1.659	1.649	1.643	1.642	1.641
$Al_2O_3:Er^{3+}$	1.669	1.659	1.654	1.652	1.651
Thermal SiO_2	1.458	1.453	1.448	1.446	1.445

[1] Extrapolated.

In order to investigate the number of propagating modes, the field-mode-matching method was employed in PhoeniX FieldDesigner modesolver software. Fig. 3.11a shows the maximum width w_{max} for single mode behaviour at wavelengths of 980 nm, 1480 nm and 1550 nm in design I for different film thicknesses h and an etch depth d of 50 nm. Fig. 3.11b shows the maximum waveguide width for single mode behaviour at 980 nm, 1480 nm and 1550 nm in design II for different waveguide heights.

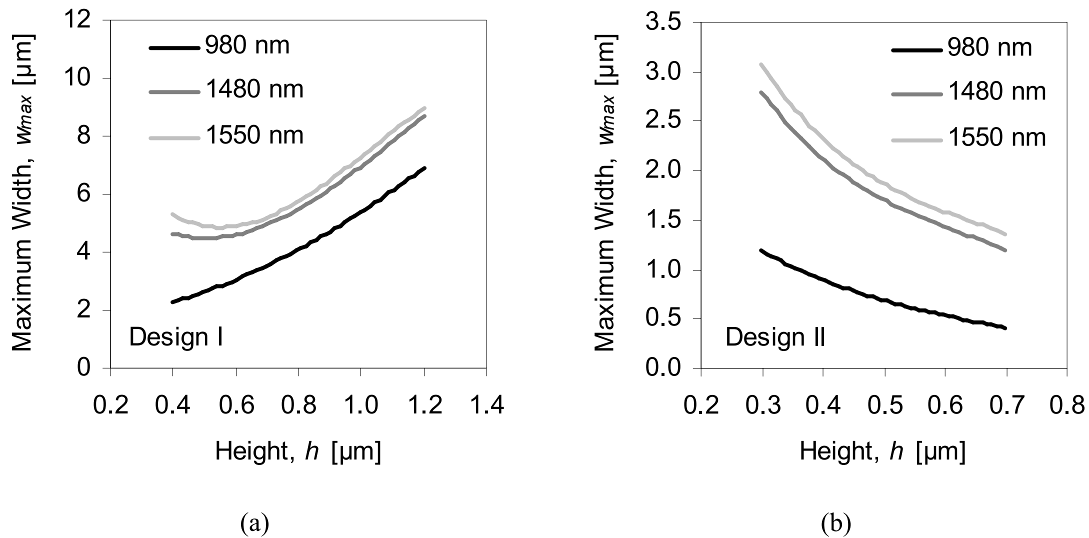

(a) (b)

Fig. 3.11. Maximum channel waveguide width for single mode behaviour at 980 nm, 1480 nm and 1550 nm vs. waveguide height for (a) waveguide design I (uncladded, shallow-etched channel waveguide) and an etch depth d = 50 nm and (b) waveguide design II (cladded, deeply-etched channel waveguide).

The optical confinement Γ within the Al_2O_3 core for the fundamental TE mode is shown as a function of film thickness and wavelength in Fig. 3.12a for design I (d = 50 nm) and in Fig. 3.12b for design II. The confinement was calculated for the maximum possible waveguide width for single mode behaviour at each film thickness. In waveguide design I the confinement of the fundamental TM mode was typically 10-20% lower than that of the fundamental TE mode, while for design II it was typically 1-10% lower.

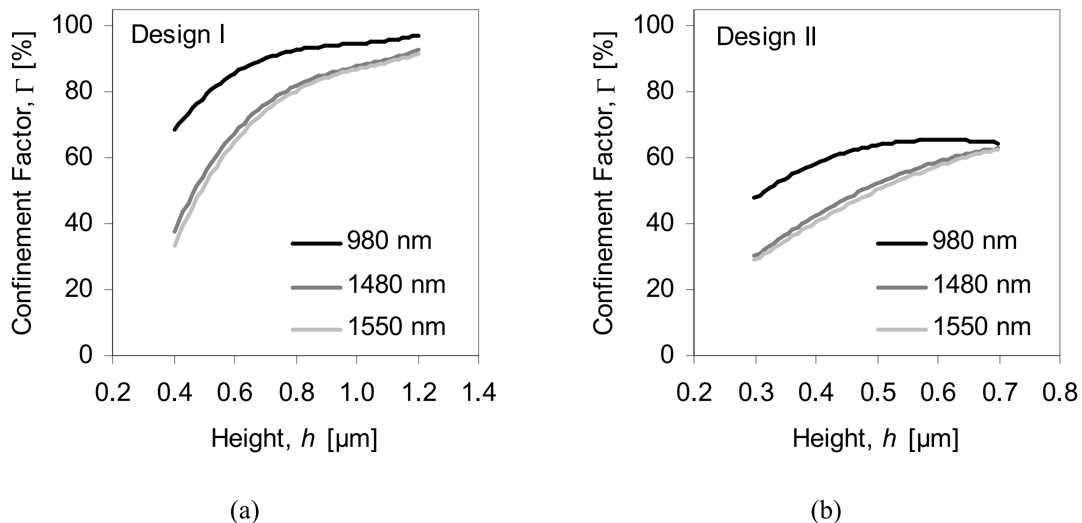

(a) (b)

Fig. 3.12. Optical power confinement of the fundamental TE mode within the Al_2O_3 core at 980 nm, 1480 nm and 1550 nm vs. waveguide height for (a) waveguide design I (uncladded, shallow-etched channel waveguide) and an etch depth d = 50 nm and (b) waveguide design II (cladded, deeply-etched channel waveguide). The confinement is calculated for $w = w_{max}$ at each wavelength.

In bend waveguides, the field is always shifted to the outside, and the smaller the bend radius for a given index contrast, the more light leaks to the cladding. Using a finite difference mode solver, such as the one applied in PhoeniX FieldDesigner, the expected bend loss can be calculated. The bend loss α_{Bend} (in dB/cm) can be calculated from the imaginary part of the effective refractive index of the bend mode, k_{Bend}, where $N_{Bend} = n_{Bend} - ik_{Bend}$:

$$\alpha_{Bend} = 10 \cdot \log e \cdot \frac{4\pi k_{Bend}}{\lambda}. \tag{3.6}$$

The losses can also be stated as the loss per 360° bend (in dB/360°):

$$\alpha_{Bend,360^\circ} = 10 \cdot \log e \cdot \frac{4\pi k_{Bend}}{\lambda} \cdot 2\pi r, \tag{3.7}$$

where r is the bend radius. This form is more useful for describing the roundtrip losses in a microring resonator, for example.

For design I, the calculated minimum bend radius is a strong function of the etch depth. For example, when w = 4.0 µm and h = 1.0 µm, for an etch depth d =100 nm, the minimum bend radius is on the order of several mm, while for an etch depth d = 50 nm, the minimum bend radius is several cm. However, since this design was primarily meant to be applied to the investigation of straight waveguide amplifiers, the minimum bend radius was not an important consideration. For design II, the bend loss was investigated in detail. In Fig. 3.13, the bend loss is shown as a function of bend radius for varying waveguide height and TE polarization. At each height the corresponding maximum single-mode waveguide width was used, since lower bend losses were calculated for larger w. As the waveguide height is increased, a smaller minimum bend radius is calculated. Waveguide bend radii < 200 µm with low bend losses are expected when applying design II. For TM polarization, higher bend losses were calculated.

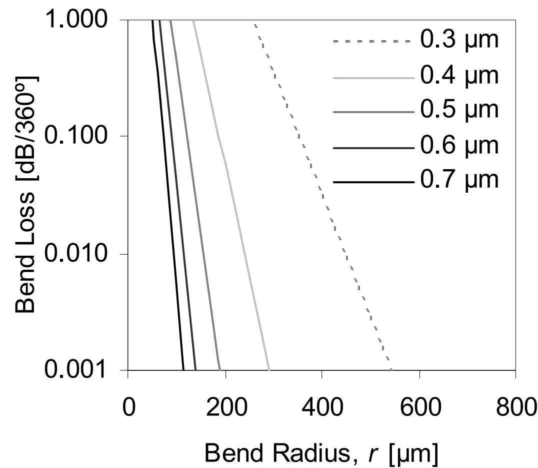

Fig. 3.13. Bend loss (λ = 1550 nm, TE polarization) as a function of bend radius for design II and varying waveguide height (with $w = w_{max}$).

3.4.1.3 Design Choice

For design I it was possible to satisfy the single-mode criterion for wavelengths of 980 nm, 1480 nm and 1550 nm. For example, satisfying the single-mode criterion for all wavelengths in such a design is possible a film thickness of 1 µm and waveguide widths up to 4 µm. Besides the minimized channel waveguide scattering losses expected due to a shallow etch depth of 50 nm, this design also allows for high confinement of the optical signal around 1550 nm and pump at either 1480 nm or 977 nm within the active layer (~80-95%). As mentioned, this is important for $Al_2O_3:Er^{3+}$ amplifiers, because it increases both the interaction with Er^{3+} ions and the maximum achievable gain. For these reasons, such a design was used for the $Al_2O_3:Er^{3+}$ gain study in Chapter 4 and the high-bit-rate amplification measurements in Chapter 5.

Based on the fabrication limits ($w \geq 1.0$ µm and d, $h \leq 0.6$ µm) there is only a very narrow window at which design II is single mode at all three wavelengths. Only for films thinner than 370 nm is it possible to define single mode waveguides at 980 nm which are greater wider than 1.0 µm. For the devices demonstrated in this work, however, it was much more important that the waveguide is single mode at the signal wavelength of ~1550 nm. As the best trade-off between single-mode behaviour at 1550 nm, reasonable confinement, low bend losses, and waveguide dimensions safely within the fabrication tolerance, a film thickness and waveguide width of 0.5 µm and 1.5 µm were selected for design II, respectively. The minimum bend radius for this waveguide design was calculated to be 225 µm. The drawback of such a design is less overlap of the propagating optical field cross-section with the Al_2O_3 (or $Al_2O_3:Er^{3+}$) waveguide core (i.e. 47% for TE polarization). This lowers the maximum achievable gain compared to design I because a larger portion of the field is propagating outside the core region without interaction with the Er ions. However, because the optical mode is smaller than in design I, the optical intensity within the core is typically higher for a given pump power, which means that the threshold power required for achieving net gain can be significantly smaller. Based on its design simplicity and smaller minimum bend radius design II was used for the ring laser and zero-loss splitter devices reported in Chapter 5. Both designs used here are compared in Table 3.6. This work is restricted to the two design types. However, in future active devices a combination of the two

designs could be advantageous, allowing for better overlap of the optical field with the active layer while maintaining low bend losses, depending on the specific requirements of the device.

Table 3.6. Comparison of channel waveguide designs applied in this thesis.

Parameter	Design I	Design II
Waveguide height, h [μm]	1.0	0.5
Waveguide width, w [μm]	4.0	1.5
Etch depth, d [μm]	0.05	0.5
Cladded?	No	Yes
Single-mode at λ = 980 nm?	Yes	No
Confinement factor[1], Γ [%]	87	47
Minimum bend radius[1], r_{min} [mm]	~ 50	0.225

[1]At a wavelength of 1550 nm and for TE polarization.

3.4.2 Device Elements Design

In this sub-section the design of bent waveguides, y-splitters and directional couplers based on waveguide cross-section II are discussed. The objective was the selection of suitable test structures to be fabricated in Al_2O_3 layers. This was followed by the fabrication of test structures and characterization of their optical performance in order to select the optimum parameters for application in $Al_2O_3:Er^{3+}$ devices (see section 3.5).

3.4.2.1 Bent Waveguides

In the case of abrupt straight waveguide to bend waveguide transitions, additional losses are incurred because of the optical mode mismatch. In order to reduce these losses, typically two approaches are used. In the first approach, an offset is used in order to more closely match the bend and straight waveguide modes (see Fig. 3.14a). In the second approach, a gradually increasing bend radius such as a sine bend [116] is applied to adiabatically change from the infinite curvature of a straight waveguide to the bend waveguide curvature (see Fig. 3.14b). While the abrupt transition with offset results in smaller structures and requires less space, the sine approach was used in the device design in this thesis to ensure smooth transitions and minimize the total bending losses. The shape of an s-shaped sine bend is described by the following equation:

$$x(y) = \frac{H_S}{L_S} y - \frac{H_S}{2\pi} \sin\left(\frac{2\pi}{L_S} y\right) \tag{3.8}$$

where x and y are the co-ordinate locations, H_S is the height and L_S is the length of the s-shaped bend. If $H_S << L_S$, the radius $r(y)$ of the sine bend is given by the following relation:

$$r(y) = \left[\frac{2\pi H_S}{{L_S}^2} \sin\left(\frac{2\pi y}{L_S}\right)\right]^{-1} \tag{3.9}$$

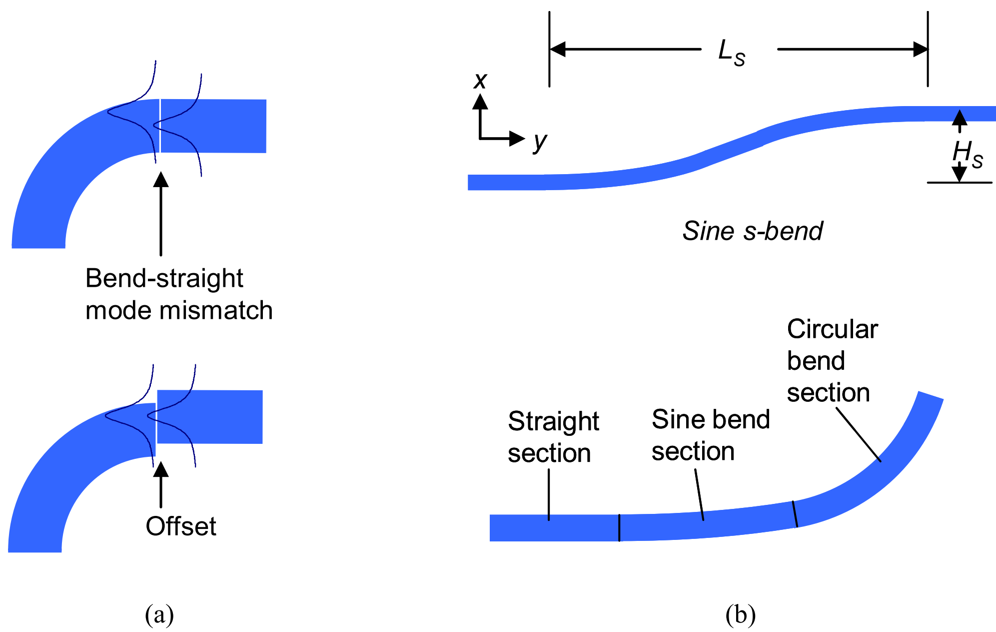

(a) (b)

Fig. 3.14. Design of low-loss bends: (a) offset applied between bend and straight sections of waveguide to reduce mode-mismatch; (b) s-shaped sine bend showing height and length parameters and sine bend section used for gradual transition from straight waveguide to circular bend section.

Bend losses are also influenced by scattering due to roughness at the sidewalls, or a poor interface quality between waveguide and cladding material. Since the field is shifted a higher intensity overlaps with the interface compared to straight waveguides, so it is particularly important to compare measured and simulated bend loss values. Therefore, appropriate test structures were designed to determine the actual bend losses. For this purpose straight waveguides, each with three bend sections, were designed as shown in Fig. 3.15a. A closer view of the bend sections (each consisting of four 90° bends) is shown in Fig. 3.15b. The transition into and out of each 90° bend was completed using a sine bend with length and height parameters of 150 and 20 μm, respectively. The transition was designed such that the sine bend was ended before reaching the halfway point of the full length, L_S, of the s-bend and the normal circular bend with constant radius started at the point where its radius matched that of the sine bend. By comparing the transmitted light in the waveguides including bends with the light transmitted in straight waveguides, it will be possible to measure the extra losses in the bend sections. The bend radii were varied from 50 to 500 μm based on the simulated bend losses (see Fig. 3.13).

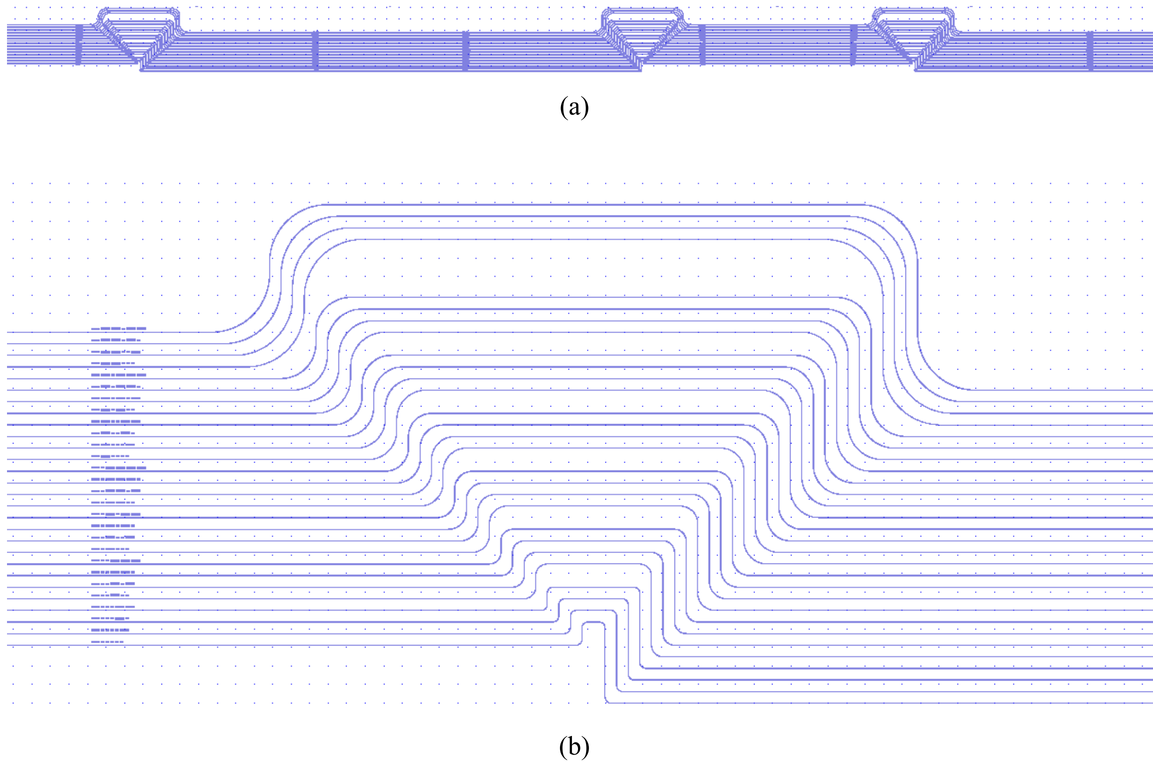

(a)

(b)

Fig. 3.15. (a) Design of straight waveguides each with three 360° bends; (b) close-up view of 360° bends.

3.4.2.2 Y-Splitters

Y-splitters are commonly used in integrated optical circuits to split the propagating light into two separate waveguides. In the ideal case a symmetrical y-junction design results in a 3 dB reduction of optical power in each output branch of the splitter. One of the goals of our active waveguides is to compensate for such 3 dB losses.

For this purpose, symmetrical y-splitters were designed as shown in Fig. 3.16a. The y-junctions consist of an input waveguide followed by two sine bends which separate the waveguides by 30 μm over a certain length, $L_{splitter}$. At the junction, the input waveguide was tapered and the output waveguides were separated with a semicircular indentation between them (see Fig. 3.16b). The width of this separation, w_{sep} and the length $L_{splitter}$ were varied in order to determine the y-junction with lowest additional losses. w_{sep} was varied from 0.5 to 1.5 µm while $L_{splitter}$ was varied from 500 to 2000 µm.

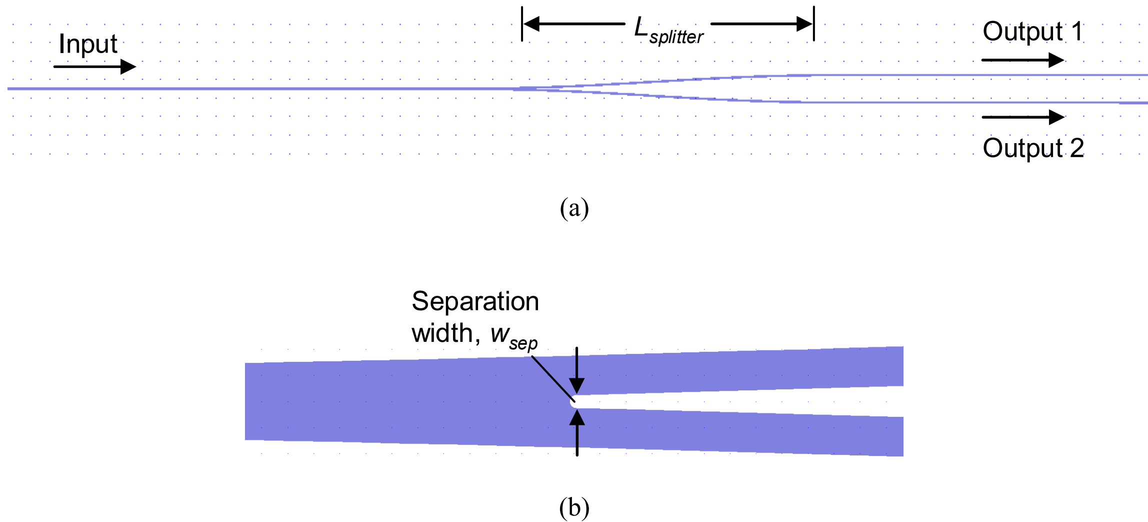

Fig. 3.16. (a) Design of y-splitter test structures; (b) close-up of y-junction.

3.4.2.3 Directional Couplers

In order to couple light from one waveguide to another, a directional coupler is typically used. Because the two waveguides are closely spaced, the evanescent tail of the optical mode propagating in one waveguide interacts with the other waveguide, and in the case of a symmetrical coupler the coupled mode theory predicts that the light will transfer entirely from waveguide to another over some distance [117]. In the design used here (see Fig. 3.17) the two waveguides approach each other via sine bends until they are separated by a gap of width w_g. The amount of coupled power depends on the interaction length, which includes both the length of the straight section ℓ, and the effective interaction length introduced in the input and output sine bend sections. The coupling length L_c for 100% coupling of the optical power from one waveguide to another is given by:

$$L_c = \frac{\lambda}{2\left(n_{eff,0} - n_{eff,1}\right)}, \tag{3.10}$$

where $n_{eff,0}$ and $n_{eff,1}$ are the effective refractive indices of the symmetric and anti-symmetric modes of the directional coupler solved for a given polarization and wavelength, respectively. The effective indices can be calculated using modesolver software. Once the coupling length is known, the amount of coupled power P_c can be calculated by:

$$P_c = P_\circ \sin^2\left[\frac{\pi\left(\ell + 2\ell_{bends}\right)}{2L_c}\right], \tag{3.11}$$

where P_o is the input power and ℓ_{bends} is the effective contribution of the sine bends to the total coupler length. In order to solve for ℓ_{bends}, an iterative simulation routine was used to calculate the coupled power in small propagation steps and for decreasing gap width $w_g(y)$ along the bend portion of the coupler. At each step Δy the amount of coupled power was calculated, and this value was used to calculate the effective $\ell'_{bends}(y)$ for the next propagation step until the gap width of the straight section was reached. Since the coupler is symmetrical, the two bend sections contribute equally to the total effective coupler length. In the initial test structures sine bends with L_S = 150 µm and H_S = 20 µm were used, while the coupler length was varied from 0 to 1200 µm and the gap width was varied from 2.0 to 2.5 µm.

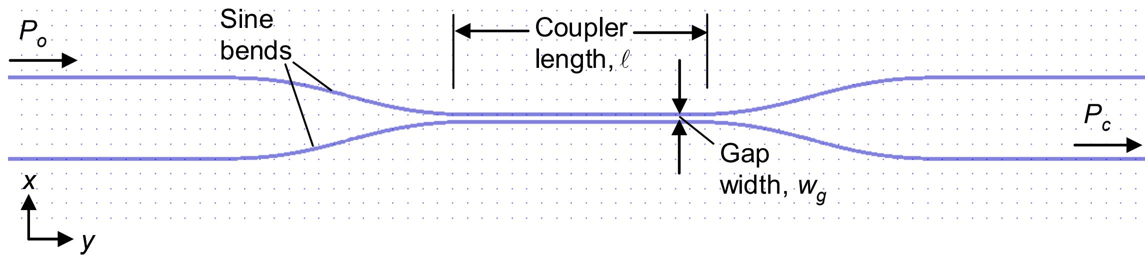

Fig. 3.17. Design of directional coupler test structures. The coupler length and gap width were varied.

3.5 Optical Results

In this section the fabrication and optical properties of Al_2O_3 and $Al_2O_3:Er^{3+}$ channel waveguides and basic device elements are reported.

3.5.1 Fabrication of Waveguides and Device Elements

An e-beam photomask was fabricated with straight channel waveguides with widths varying from 0.75 to 4.0 µm and the various elements described in the previous section. Based on the low propagation losses demonstrated in Al_2O_3 waveguides etched to a depth of 220 nm in section 3.3.4, it was concluded that the waveguides geometry of design I, with an etch depth of 50 nm, would also result in low propagation losses. Since it was only applied for straight waveguides, and low optical propagation losses were already confirmed, no further testing of the optical performance of this design was required. Therefore, two samples based on design II were fabricated using the e-beam mask and the procedure described in Table 3.3. In the first case 0.75 to 4.0-µm-wide channel waveguides were etched to a depth of 484 nm (including a ~ 20 nm overetch into the thermal oxide lower cladding layer) in an unoptimized 463-nm-thick Er-doped Al_2O_3 film with an estimated Er concentration of 1 × 10^{20} cm^{-3} (sample Er-1163). A 5-µm-thick PECVD SiO_2 cladding was deposited. The optical losses of the slab waveguides were also measured prior to etching and are reported with the channel waveguide propagation loss measurements (see Table 3.8). A second sample (sample 4322) was fabricated with the bent waveguide, y-splitter and directional coupler test structures based on waveguide design II. The film thickness, waveguide width and etch depth were 0.498 µm, 1.5 µm and 0.552 µm, respectively, and an annealed PECVD

SiO_2 top-cladding was applied. Examples of an integrated Al_2O_3 channel waveguide y-splitter and directional coupler in sample 4322 prior to cladding deposition are shown in the optical microscope pictures in Fig. 3.18a and Fig. 3.18b, respectively. Each of these samples is summarized in Table 3.7.

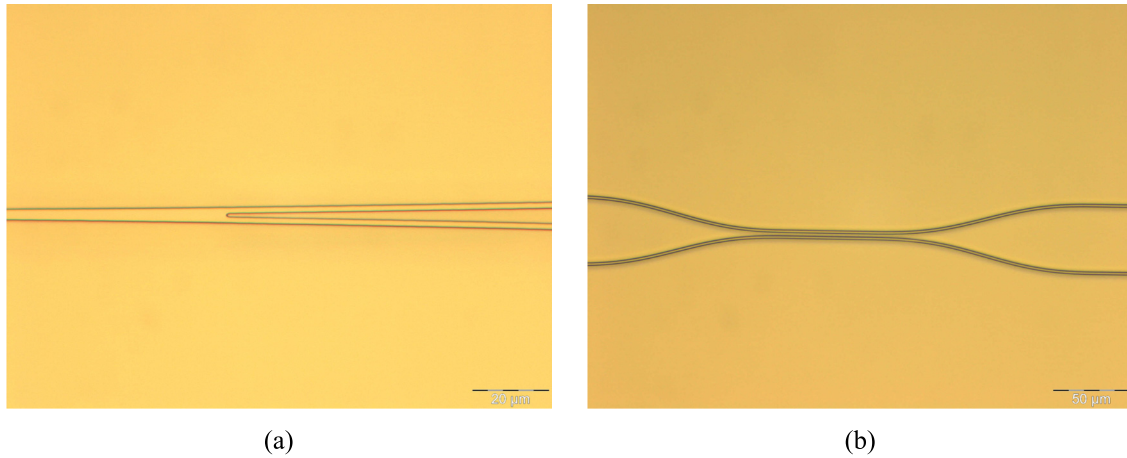

(a) (b)

Fig. 3.18. Optical microscope pictures showing an Al_2O_3 waveguide (a) y-splitter and (b) directional coupler prior to cladding layer deposition.

Table 3.7. Properties of samples containing $Al_2O_3:Er^{3+}$ and Al_2O_3 channel waveguides used for straight waveguide propagation loss, bend loss, y-splitter and directional coupler measurements.

	Sample Code	
Parameter	Er-1163	4322
PECVD SiO_2 Cladding Thickness [µm]	~5.0	~5.0
Er Concentration [cm^{-3}]	1×10^{20}	-
$Al_2O_3/Al_2O_3:Er^{3+}$ Layer Thickness [µm]	0.463	0.498
Thermal Oxide Thickness [µm]	~8.0	~8.0
Channel Waveguide Etch Depth (Centre) [µm]	0.484	0.552
Waveguide Width [µm]	1.2	1.5
Chip Length(s) [cm]	1.8, 4.0, 5.8	3.2
Measurements	Propagation losses (straight waveguides)	Bent waveguides, y-splitters, couplers

3.5.2 Propagation Losses: Straight Waveguides

To investigate the potentially higher losses in deeply-etched, cladded channel waveguides, the optical propagation losses were measured in sample Er-1163. Prior to channel waveguide fabrication, the slab losses were measured using the moving prism method and 1320 nm and 1480 nm diode-pumped solid state laser and diode laser sources, respectively. The losses at 1320 nm do not include any absorption due to Er^{3+} ions (therefore, they represent the background material losses, while the losses at 1480 nm include some additional absorption due to Er^{3+} ions. After channel waveguide fabrication, the cut-back method was applied using waveguide lengths of 5.8, 4.0 and 1.8 and the same laser sources to measure the channel losses. Six waveguides of 1.25-µm width, single mode at 1320 nm and above, were included in the measurement, selecting the best four values at each length. The calculated confinements in both the slab and channel waveguide cases were similar. The loss values and calculated

confinement of the optical mode within the $Al_2O_3:Er^{3+}$ layer are summarized in Table 3.8. The differences in propagation loss between the slab and channel waveguides at all wavelengths and polarizations are within the experimental error of the measurement methods. This confirms that only negligible additional propagation losses are also introduced in top-cladded, deeply-etched $Al_2O_3:Er^{3+}$ channel waveguides.

Table 3.8. Propagation losses at 1320 nm and 1480 nm measured in slab and top-cladded 1.25-µm-wide $Al_2O_3:Er^{3+}$ channel waveguides.

	Slab Waveguide			Cladded Channel Waveguide		
Wavelength [nm]	Polarization	Confinement Factor	Loss [dB/cm]	Polarization	Confinement Factor	Loss [dB/cm]
1320	TE	0.60	0.69 ± 0.11	TE	0.52	0.59 ± 0.21
	TM	0.43	0.76 ± 0.16	TM	0.44	0.78 ± 0.15
1480	TE/TM	0.40	1.17 ± 0.20	TE	0.45	1.12 ± 0.35
				TM	0.36	1.35 ± 0.21

3.5.3 Propagation Losses: Bent Waveguides

The bend loss measurement results for sample 4322 and TE and TM polarized light are shown in Fig. 3.19. Using a fiber coupling setup and tunable laser source at 1550 nm, the transmitted light was measured in waveguides with one 4 × 90º bend section and bend radii varying from 50 to 500 µm. The calculated bend losses are shown in the same plot. For TM polarization the simulated and measured values are in close agreement. However, for TE-polarized light the measured bend losses are significantly higher than the simulated values for bend radii below 300 µm. This demonstrates the limits of such a modesolver in predicting the real bend losses and the importance of measuring the actual bend losses. The transmission was also measured at the pump wavelengths of 1480 nm and 980 nm, using the same setup and a tunable laser and diode laser source, respectively. At 1480 nm, similar results to 1550 nm were observed, with slightly lower losses. This behaviour is expected because the fundamental optical mode is more strongly confined at lower wavelengths. At 980 nm, the transmitted optical power was constant (within ± 1 dB) down to a bend radius of 50 µm, indicating that any additional losses were below ~ 1 dB/360º.

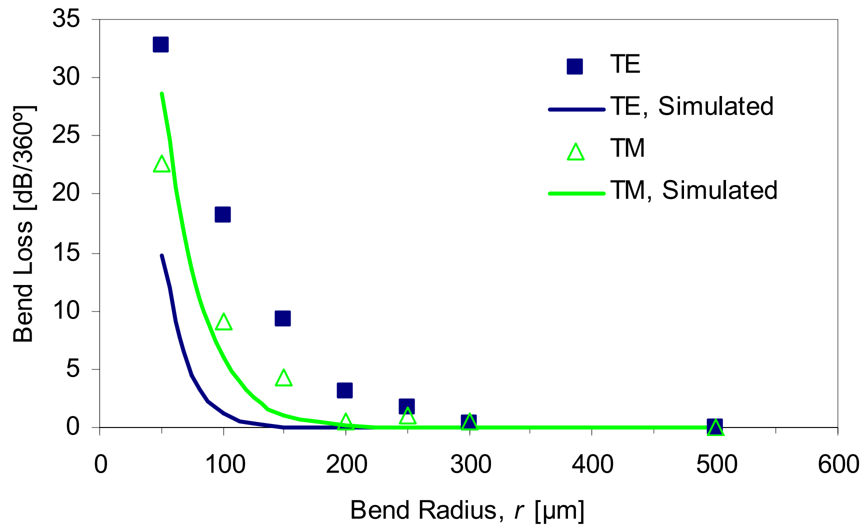

Fig. 3.19. Measured and simulated bend loss in Al_2O_3 channel waveguides for λ = 1550 nm and TE and TM polarization.

3.5.4 Y-Splitters

Using a fiber coupling setup and tunable laser source the transmitted power in each output branch of each y-splitter was measured. This value was subtracted from the transmitted power measured in a straight channel waveguide of equal length to determine the approximate power drop in each branch of the splitter within an error of ± 0.5 dB. The results for λ = 1550 nm and TE polarization are shown in Fig. 3.20.

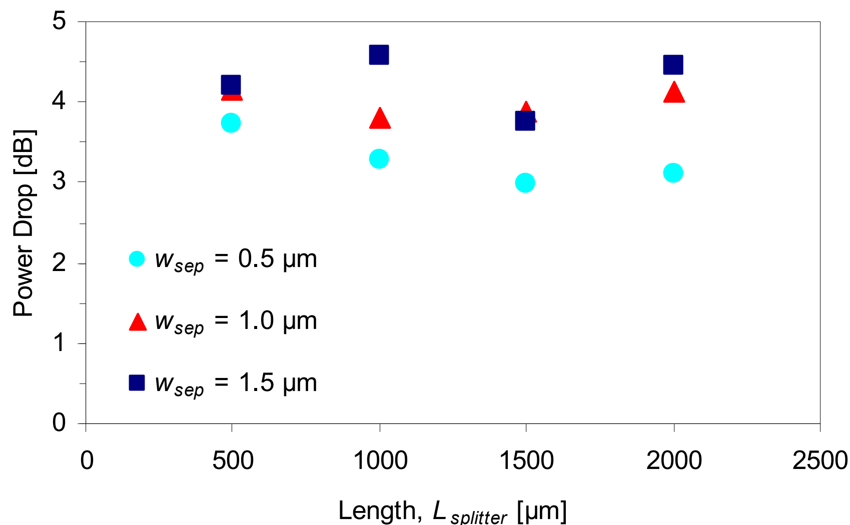

Fig. 3.20. Average power drop vs. $L_{splitter}$ in the two output branches of each y-splitter for varying separation width w_{sep}, λ = 1550 nm and TE polarization.

The power drop in each output branch of the y-splitter decreases towards the ideal 3-dB per output branch with decreasing separation width w_{sep}. For w_{sep} = 1.0 and 1.5 no clear trend is visible for the branching length $L_{splitter}$, while for w_{sep} = 0.5, the power drop tends to decrease with increasing branching length $L_{splitter}$. Similar trends were observed for 1480 nm light and for TM polarization at both wavelengths. For 980 nm, no clear trend was apparent. However, an average power drop of 7 ± 2 dB was measured in each branch of the y-splitters, which is significantly higher than at the other wavelengths. The higher losses can be attributed to the fact that the waveguides are multimode at 980 nm. Based on these results, y-splitter parameters of w_{sep} = 0.5 µm and $L_{splitter}$ = 2000 µm were selected and splitting of 980 nm pump light on the chip was avoided in the final device designs.

3.5.5 Directional Couplers

The fiber-coupling setup was used to characterize the directional couplers. Light from a tunable laser source (for 1550 and 1480 nm) or a diode laser source (for 980 nm) was launched into one branch of the directional coupler (see Fig. 3.17). The 1550 and 1480 nm light was polarized and coupled to the chip using a single mode polarization maintaining fiber while the 980 nm light was randomly polarized. The percentage of coupled power in each case was calculated by taking the ratio of transmitted powers measured in each output branch of the coupler. The measured data was compared to the calculated coupled power using the modesolver software to determine the effective indices and equations (3.10) and (3.11).

The measured and simulated coupled power is shown for 1550 nm, a gap w_g of 2.0 µm, coupler lengths ℓ of 0 to 1200 nm and TE and TM polarization in Fig. 3.21a and Fig. 3.21b, respectively. For TE polarization the simulated coupling closely matches the experimental data, where a 100% coupling at length L_c = 521 µm and sine bend contribution to the coupler length ℓ_{bends} = 35 µm were calculated. For TM polarization a shorter coupling length was calculated because the propagating TM fields in each waveguide are less confined than the TE fields. Thus there is stronger interaction between the fields in each branch of the coupler. However, for TM polarization, the experimental data does not agree with the calculated data. This result could not be explained, but was found consistently in directional couplers fabricated in different samples. Figures 3.21c and 3.21d show the same type of measurements, except for w_g = 2.5 µm. For both TE and TM polarization the measured data does not match with the calculated coupled power. Furthermore, the maximum coupled power in each case is below 40%, indicating that the gap is too wide for efficient coupling. Therefore, for all directional couplers based on channel waveguide design II it was decided to use TE polarized signal light and w_g = 2.0 µm.

The total transmitted power coupled from each directional coupler was also compared to the transmitted power in a straight waveguide of equal length for TE polarization. In comparison to the straight waveguide, average additional losses of 1.1 ± 0.2 dB were measured in the directional couplers. The measured losses were consistent in each coupler and independent of coupler length. A potential source of the additional losses was determined to be the input and output sine bends. According to equation (3.9) and L_S = 150 µm and H_S = 20 the minimum bend radius was 197 µm. This falls inside a range where the bend losses are high according to Fig. 3.19. Therefore, for the design of the final devices, it was decided to use more gradual sine bends with L_S = 250 µm and H_S = 20 µm, resulting in a minimum bend radius of 497 µm.

In Fig. 3.22, the coupling at potential pump wavelengths of 1480 nm and 980 nm are compared. In Fig. 3.22a, the measured and simulated coupled power is shown for 1480 nm and TE polarization. Again the experimental and calculated results are in good agreement. Due to the more strongly confined mode compared to 1550 nm, L_c was calculated to be 691 μm for λ = 1480 nm. Comparing to Fig. 3.21a, 100% coupling is predicted at ℓ = 486 μm for 1550 nm light, while 86% coupling occurs for the same coupler length for 1480 nm light. Because of the similar coupling characteristics at these wavelengths it is difficult to design a directional coupler which separates 1550 nm signal light from 1480 nm pump light when they are propagating in the same waveguide or strongly couples one wavelength but not the other. In Fig. 3.22b, the measured and simulated coupled power is shown for 980 nm and randomly polarized light. In this case ≤ 10% of the power is coupled. The simulated coupled power (≤ 1%) was calculated based on the average coupling length calculated for the TE and TM polarized fundamental modes ($L_c = 2.4 \times 10^4$ μm). The higher measured coupled power can be explained by the fact that higher order modes, which are less confined and have significantly shorter coupling lengths, can also propagate at 980 nm. However, the amount of coupled power is still significantly lower for 980 nm compared with 1480 nm. Therefore, for active devices which require strong signal coupling and weak pump coupling, 980 nm can be considered as the better choice of pump wavelength.

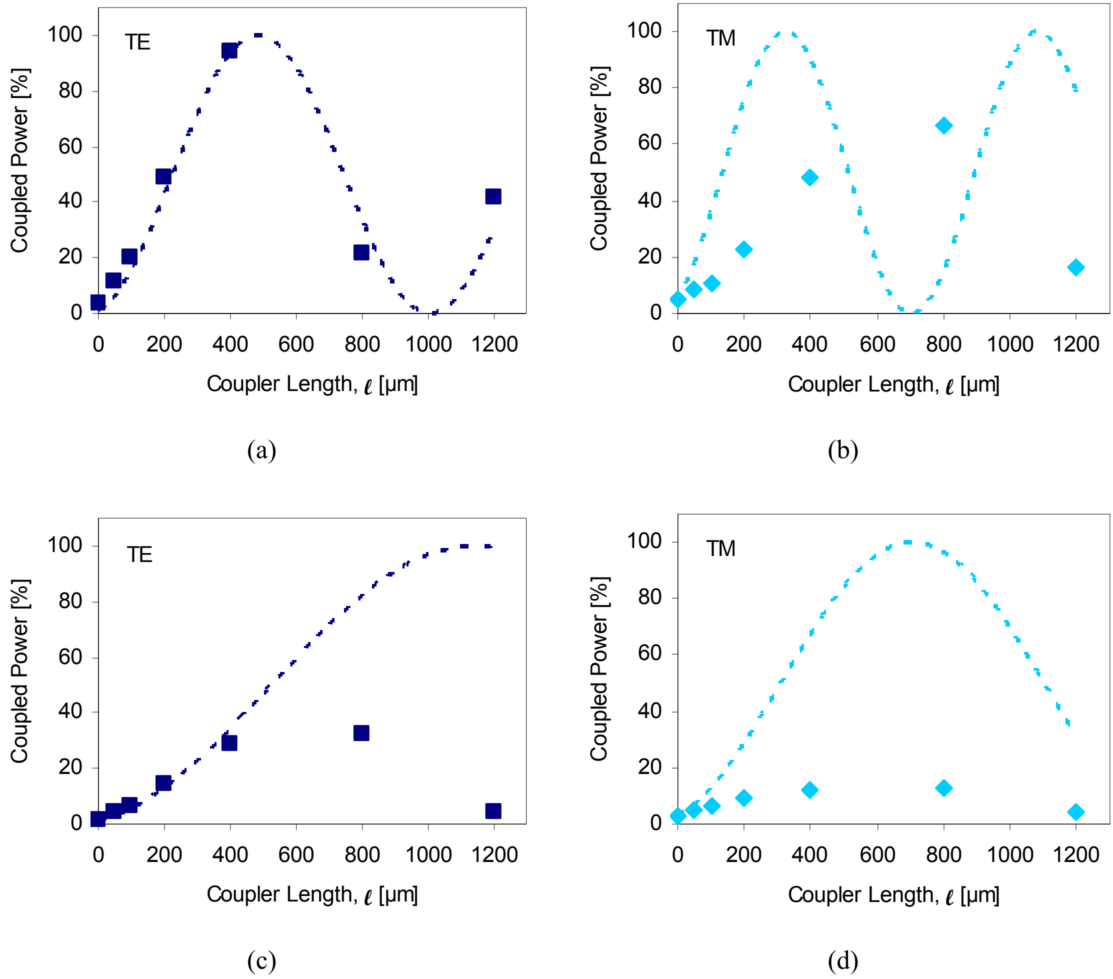

Fig. 3.21. Measured coupled power at 1550 nm as a function of coupler length ℓ for (a) a gap of 2.0 µm and TE polarization, (b) a gap of 2.0 µm and TM polarization, (c) a gap of 2.5 µm and TE polarization, and (d) a gap of 2.5 µm and TM polarization. The dashed lines indicate the simulated data.

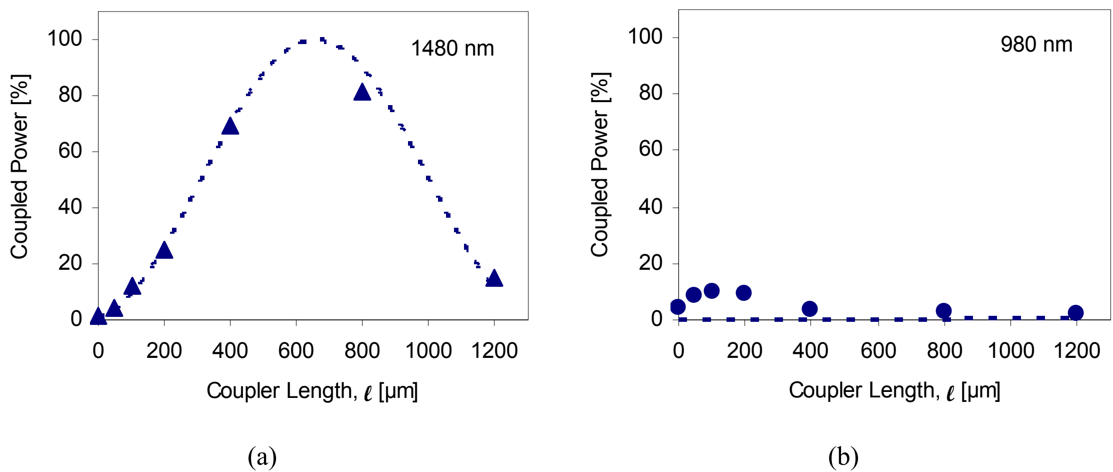

Fig. 3.22. Measured coupled power at (a) 1480 nm and TE polarization and (b) 980 nm and random polarization as a function of coupler length for a gap of 2.0 µm. The dashed lines indicate the simulated data.

3.6 Summary

The etch behaviour of amorphous Al_2O_3 films using ICP RIE has been investigated. The Al_2O_3 films have much higher etch rates in all reactive gas mixtures compared to Ar, indicating a strong chemical component to the etching process. The selectivity to several potential mask materials was also studied. Based on these results, channel waveguides were fabricated in Al_2O_3 films using a BCl_3-HBr plasma. The resulting waveguides had sufficiently steep and smooth sidewalls. The optical propagation loss was measured in uncladded single-mode ridge waveguides at 1550 nm and only small additional losses up to 0.1 dB/cm were found. SiO_2-cladded $Al_2O_3:Er^{3+}$ channel waveguides were also fabricated and similar propagation losses at 1320 nm and 1480 nm were observed compared to those in the unetched film. Bend waveguide, y-splitter and directional coupler test structures were designed and characterized with the aim of optimizing their design for integrated active devices. The minimum bend radius was determined to be 500 µm for sufficiently low losses at 1550 nm in $Al_2O_3:Er^{3+}$ devices. The y-splitter design was optimized for a decrease in power close to the ideal 3 dB in each output branch. For directional couplers, good agreement between the simulated and experimental results were found for TE polarization and a gap of 2.0 µm. Weak coupling at 980 nm and strong coupling at 1550 nm were also observed, demonstrating that such a directional coupler design could be useful for separating or combining pump and signal light in an integrated active device.

Chapter 4

Investigation of Er Concentration and Optimization of Gain in $Al_2O_3:Er^{3+}$ Amplifiers

$Al_2O_3:Er^{3+}$ amplifiers with different Er concentrations, ranging from 0.27 to 4.2 × 10^{20} cm^{-3}, were fabricated and characterized. The results, which provide insight into the optimum Er concentration for amplification in our material, are presented in this chapter. Background losses as low as 0.12 ± 0.10 dB/cm at 1320 nm were measured and the Er emission and absorption cross sections between 1400-1700 nm were determined. For optimum Er concentrations in the range of 1 to 2 × 10^{20} cm^{-3}, internal net gain was obtained over a wavelength range of 80 nm (1500-1580 nm) and a peak gain of 2.0 dB/cm was measured at 1533 nm. The broadband and high peak gain is attributed to an optimized fabrication process, improved waveguide design, and pumping at 977 nm as opposed to 1480 nm. In a 5.4-cm-long amplifier, total internal net gain of up to 9.3 dB was measured. By use of a rate-equation model, internal net gain of 33 dB at the 1533-nm gain peak and more than 20 dB for all wavelengths within the telecom C-band (1525-1565 nm) is predicted for a launched signal power of 1 µW, when launching 100 mW of pump power into a 24-cm-long amplifier. The high optical gain demonstrates that $Al_2O_3:Er^{3+}$ is a competitive technology for active integrated optics.

4.1 Introduction

$Al_2O_3:Er^{3+}$ has been studied as a gain medium for optically-pumped active devices operating at wavelengths around 1.53 µm by various research groups [34-38]. In [34, 37, 38], $Al_2O_3:Er^{3+}$ channel waveguide amplifiers were fabricated by various methods. Of these results, the highest gain figure reported was 0.58 dB/cm [34]. In Chapter 2 and 3 of this thesis new $Al_2O_3:Er^{3+}$ fabrication methods were demonstrated which resulted in low background propagation losses and the potential for higher gain in this material.

A number of parameters are involved in the amplifier design, each of which must be optimized to achieve the highest possible gain. Selection of the waveguide dimensions is critical to ensure a large overlap of the optical signal with the active waveguide core. The choice of pump wavelength, typically either 980 nm or 1480 nm, also affects the amplifier performance. In addition, in short (~ cm) on-chip Er-doped waveguide amplifiers (EDWAs) the Er concentration is a critical design parameter. Compared to longer (~ m) Er-doped fiber amplifiers, higher Er concentrations are required in order to achieve higher gain per unit length and comparable total gain. This means that material- and concentration-influenced gain quenching effects due to interactions between neighbouring Er^{3+} ions play an important role. It also means that absorption of pump light is stronger. Therefore, a balance must be found in which absorption of the available pump power is optimized and gain quenching effects are minimized while a sufficient amount of Er ions are still available to interact with and enhance the signal.

A survey of EDWAs fabricated from different materials is listed Table 4.1. They are compared in terms of substrate type, Er concentration, sample length, background loss, pump power and maximum net gain figure. Here, as is often the case, the maximum net gain is described in dB/cm to provide a general comparison. However caution should be taken in the interpretation of such a gain figure, because the gain is not linear and decreases gradually with increasing amplifier length. Therefore, the table only shows amplifiers with lengths of 1 cm and longer. Among these various EDWA materials, Er-doped phosphate glass or Er-doped silicates have become the materials of choice due to ease of fabrication, high Er solubility without introducing significant quenching effects and, as a result, comparatively high net gain per unit length. Peak gain figures of 3-4 dB/cm around 1535 nm are typically measured in Er-doped and Er-Yb co-doped phosphate glass [20, 24, 30, 32, 61, 118] and soda lime silicate glass [41, 119] amplifiers with up to 4.1 dB demonstrated in a short, highly Er-doped phosphate glass amplifier of 3-mm-length [31]. As is evident in the table, the highest peak gain reported in $Al_2O_3:Er^{3+}$ was the lowest among all these materials. In addition, this rather low value only represents the peak gain, whereas we are interested in high gain across the entire applicable wavelength range for Er (1525-1565 nm). Recently a gain figure of 5.2 dB/cm was reported in Er-Yb co-doped Al_2O_3 waveguides [120], but this value is questionable because the various losses were not documented. Therefore this result was disregarded.

In this chapter, $Al_2O_3:Er^{3+}$ channel waveguide amplifiers with different Er concentrations have been fabricated and optically investigated in order to determine the key spectroscopic parameters and maximize the optical gain. In section 4.2 the spectroscopic principles relevant to the operation of Er-doped amplifiers are discussed. In section 4.3, the fabrication of the $Al_2O_3:Er^{3+}$ amplifiers studied in this chapter, as well as their propagation losses and spectroscopic properties are presented. Following

this, optical gain measurements which establish significantly higher gain in this material are reported in section 4.4. Finally, a model for calculating the amplifier behaviour is presented in section 4.5. The model is applied to calculate the optimum $Al_2O_3:Er^{3+}$ amplifier length for a given pump power and Er concentration and to predict the maximum total gain which can be achieved over the wavelength range 1525-1565 nm. The model is also used to investigate the influence of Er concentration and waveguide design on gain and pump power requirements.

Table 4.1. Comparison of peak net gain in different integrated Er-doped waveguide amplifiers.

Host	Substrate	Er conc. [10^{20} cm^{-3}]	Yb Co-doped?	Sample length [cm]	Back-ground loss [dB/cm]	Pump power[1] [mW]	Net gain[2] [dB/cm]	Ref.
Phosphate glass	Oxidized silicon	5.3	No	1	0.9	21	4.1	[24]
Soda-lime silicate glass	Oxidized silicon	4.3	No	2.4	1	120	4.2	[119]
Boro-silicate glass	Boro-silicate glass	2.4	Yes	3.9	0.15	130	2.3	[43]
$LiNbO_3$	$LiNbO_3$	Unknown	No	5.7	0.1	170 (1484 nm)	2.0	[8]
Alumino-silicate	Oxidized silicon	Unknown	No	5	0.2	130	1.9	[121]
Y_2O_3	Oxidized silicon	1.3	No	4.3	0.9	10 (1480 nm)	1.3	[122]
Fluoride glass	Fluoride glass	Unknown	No	1.9	0.6	340 (1480 nm)	1.3	[33]
Alumino-phospho-silicate	Oxidized silicon	0.25 mol%	Yes	5	< 0.2	175	1.1	[51]
Polymer	Oxidized silicon	1 wt%	No	1.6	< 1	70	0.84	[15]
$P_2O_5:SiO_2$	Oxidized silicon	0.48 wt%	No	7.5	0.17	420	0.67	[123]
Al_2O_3	Oxidized silicon	2.7	No	4	0.35	9 (1480 nm)	0.58	[34]

[1]Pump wavelength indicated in brackets if a wavelength other than 975 to 980 nm was used.
[2]For a signal wavelength ranging from 1531 to 1540 nm.

4.2 Spectroscopy of Er^{3+} Ions

This section provides background spectroscopic theory related to the Er^{3+} ion. The various processes and parameters relevant to the amplifier operation, including absorption and emission cross sections, lifetimes, energy transfer upconversion and gain are discussed.

4.2.1 Energy Transitions in Erbium

We first look at the relevant energy transitions in the Er^{3+} ion. Due to shielding of the 4f electron shell by the larger 5s and 5p orbitals, the ion maintains an atomic-like energy

structure and various distinct energy transitions within the 4f shell are possible. The lower-lying energy levels of Er^{3+}, starting from the ground state and continuing up to the $^4F_{7/2}$ level are shown in Fig. 4.1. The levels are represented by Russell-Saunders notation $^{2S+1}L_J$, where 2S+1 represents the spin angular momentum, L represents the orbital angular momentum and J represents the total angular momentum. In rare earth ions the eigenstates of the electronic system are usually a linear combination of $^{2S+1}L_J$ states. However, to simplify the notation each level is represented by the leading term of the Russell-Saunders coupled states. Only those levels relevant to Er-doped amplifier operation for a signal around 1.53 μm are shown in the figure, however additional higher energy levels of the 4f shell exist. Also displayed in the figure are the approximate lifetime (for Er^{3+} ions in oxide glasses), the wavelength corresponding to the ground-state transition and the approximate energy in cm^{-1} relative to the ground state for each level (taken from [124]).

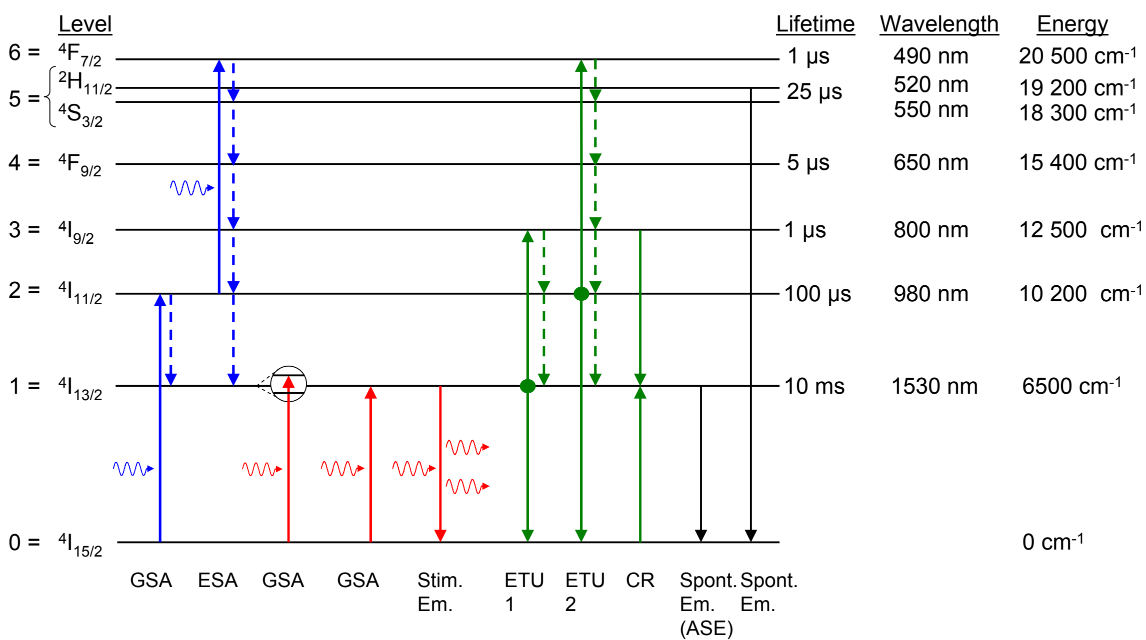

Fig. 4.1. Schematic of energy levels, selected transitions, and lifetimes relevant for Er^{3+} amplifier operation. The energy in cm^{-1} relative to the ground state and the wavelength corresponding to a photon of this energy are also indicated (taken from [124]).

Several transitions relevant to Er-doped amplifiers designed for wavelengths around 1.55 μm are also shown in Fig. 4.1. Such amplifiers operate based on stimulated emission on the $^4I_{13/2} \rightarrow {}^4I_{15/2}$ transition. In order to populate the $^4I_{13/2}$ level pump light at a wavelength of either 980 nm or 1480 nm is typically used. The first transition shown in the figure is that of ground state absorption (GSA) of pump light on the $^4I_{15/2} \rightarrow {}^4I_{11/2}$ transition. This is followed by either spontaneous emission of a photon and relaxation to the ground state (which is unlikely) or rapid non-radiative decay to the $^4I_{13/2}$ level. The second transition represents excited state absorption (ESA) of 980 nm pump light from the $^4I_{11/2}$ level to the $^4F_{7/2}$ level. The third transition illustrates GSA of 1480 pump light directly into the broadened $^4I_{13/2}$ level. The fourth and fifth transitions show GSA and stimulated emission of ~1530 nm signal light on the $^4I_{15/2} \leftrightarrow {}^4I_{13/2}$ transition (stimulated emission of 980 nm and 1480 nm pump light is also possible from

the $^4I_{11/2}$ and $^4I_{13/2}$ levels, respectively, but is not shown in the figure). The sixth and seventh transitions show two energy transfer upconversion (ETU) processes, which can have an important effect on amplifier performance. The first one involves energy transfer between two ions in the $^4I_{13/2}$ level resulting in promotion of one ion to the $^4I_{9/2}$ state and de-excitation of the other to the ground state. This process decreases the number of ions in the $^4I_{13/2}$ state available for stimulated emission. The second ETU process involves energy transfer between two ions in the $^4I_{11/2}$ state and excitation of one to higher-lying levels and de-excitation of the other to the ground state. After these processes a cross-relaxation (CR) process is shown, whereby an ion in the $^4I_{9/2}$ excited state interacts with another ion in the ground state with the result that both ions end up in the $^4I_{13/2}$ state. However, due to the extremely short $^4I_{9/2}$ lifetime in oxide glasses the population density of this level is very low, which means the CR process is very rare. Finally two important spontaneous emission processes are shown (although spontaneous emission can occur from each level). The first one is on the $^4I_{13/2} \rightarrow {}^4I_{15/2}$ transition. This process releases non-coherent photons in a broad spectrum around the signal wavelength. When such light is amplified by pumping processes in an optical amplifier, it is referred to as amplified spontaneous emission (ASE) and it adds noise to the amplifier signal. The second spontaneous emission process involves transition from the overlapping $^2H_{11/2}$ and $^4S_{3/2}$ levels to the ground state. It is shown because it results in the characteristic green light visible in highly-Er-doped amplifiers.

4.2.2 Absorption and Emission Cross Sections

In the previous section various transitions were introduced. Here an overview is given of the emission and absorption cross sections of the different transitions. The cross sections describe the probability of an excited ion emitting a photon of equal phase and frequency to a photon incident upon it (stimulated emission) or an ion being excited to a higher energy state by absorbing an incident photon (stimulated absorption). The amount of emitted or absorbed optical power is proportional to the cross section of the ion and the incident optical intensity:

$$P_{abs/em}(\lambda) = \sigma_{abs/em}(\lambda) I(\lambda) \tag{4.1}$$

where $P_{abs/em}(\lambda)$ is the absorbed or emitted optical power, $\sigma_{abs}(\lambda)$ and $\sigma_{em}(\lambda)$ are the absorption and emission cross sections at a given wavelength λ, respectively and $I(\lambda)$ is the optical intensity.

The fundamental concept of the cross sections derives from the Einstein relations. These relations describe absorption and emission of light in a degenerate two-level system based on quantum mechanical principles. Degeneracy describes the splitting of a level into strongly-coupled sub-levels (i.e. if level 1 has a degeneracy g_1 = 7, it is split into 7 sub-levels). When the sub-levels are equally occupied or the transition strengths between the sub-levels are all equal, the Einstein equations apply. Based on these assumptions, the emission and absorption cross sections are equal. However, with rare earth ions this is not the case, due to the Stark splitting of each level into many sub-levels and thermal distribution of electrons in each sub-level, as will be shown later. The following equations describe the change in population of level 1 due to emission and absorption, respectively when broadband light is incident on a simple two-level system:

$$\left(\frac{dN_1}{dt}\right)_{em} = -\left(A_{10} + B_{10}\rho(\nu)N_1\right), \tag{4.2}$$

$$\left(\frac{dN_1}{dt}\right)_{abs} = B_{01}\rho(\nu)N_0, \tag{4.3}$$

where N_0 and N_1 are the populations of the lower and upper states, respectively, $\rho(\nu)$ is the photon flux density (number of photons per unit frequency bandwidth per unit volume) and A_{10}, B_{10} and B_{01} are the Einstein coefficients describing the strength of the various transitions [125]. These processes and the associated rates are depicted in Fig. 4.2. The population of a given level in the case of a material containing Er^{3+} ions refers to the number of ions in that state (i.e. in the two level system shown in Fig. 4.2 the number of ions with outermost electron in the ground level or excited to the higher level).

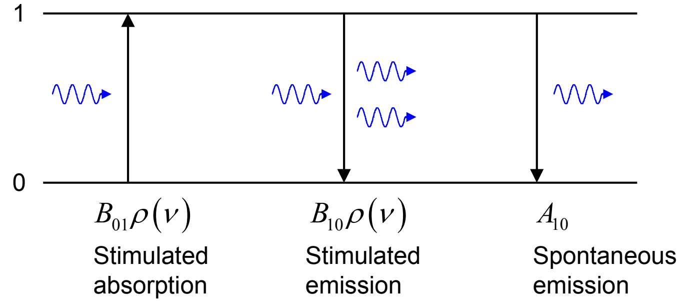

Fig. 4.2. Absorption and emission of photons in a two-level system. Stimulated absorption, stimulated emission and spontaneous emission are shown, as well as their associated rates.

In the situation where sub-levels exist (the states are degenerate) the change in population can be described by the sum of the rates of the various transitions. In this case the stimulated emission and absorption rates between the levels can be written as a sum of the various transitions. This leads to the following equations describing the change in populations over time:

$$\left(\frac{dN_1}{dt}\right)_{abs} = \sum_{i,j} R\left(m_{0,i}, m_{1,j}\right) N_{m_{0,i}}, \tag{4.4}$$

$$\left(\frac{dN_1}{dt}\right)_{em} = \sum_{i,j} \left[A\left(m_{0,i}, m_{1,j}\right) + R\left(m_{0,i}, m_{1,j}\right) \right] N_{m_{1,j}}, \tag{4.5}$$

where $m_{0,i}$ represents the sub-levels in level 0 (i=0 to g_0), $m_{1,j}$ represents the sub-levels in level 1 (j=0 to g_1) and $R\left(m_{0,i}, m_{1,j}\right)$ is the stimulated transition rate between sub-levels. The degenerate two-level system is depicted in Fig. 4.3. For Er^{3+} this represents

two Stark-split multiplets or manifolds (i.e. the $^4I_{15/2}$ ground-state manifold and upper $^4I_{13/2}$ manifold are split into 8 and 7 Stark sub-levels, respectively).

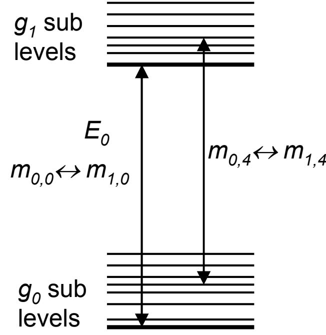

Fig. 4.3. Diagram showing two multiplets and degeneracy of levels. In the case of Er^{3+} the $^4I_{15/2}$ ground state has 8 sub-levels, while the $^4I_{13/2}$ state has 7 sub-levels.

From these relations and assuming each transition has a certain lineshape, the Füchtbauer-Ladenburg equation was derived [125]. The Füchtbauer-Ladenburg equation, which relates the radiative lifetime and the emission cross section, is given as follows:

$$\frac{1}{\tau_{rad,1}} = A_{10} = \frac{8\pi}{\lambda^2}\int \sigma_{em}(\nu)\,d\nu = \frac{8\pi}{\lambda^2}\frac{g_0}{g_1}\int \sigma_{abs}(\nu)\,d\nu \tag{4.6}$$

where $\tau_{rad,1}$ is the radiative lifetime of the upper level. Using this equation it is possible to calculate the emission cross sections from the absorption cross sections or vice-versa. However, the experimental results did not agree with the calculated ones because thermal Boltzmann statistics and the resulting unequal population of the various sub-levels were not taken into account [5].

A more accurate description was given by McCumber [126], who took into account the thermal distribution of the population. The following formula describes the relationship between the absorption and emission cross sections, assuming the time for the populations of the ground and excited state to reach thermal equilibrium is fast compared to the radiative lifetime of the excited level [127]:

$$\sigma_{em}(\lambda) = \sigma_{abs}(\lambda)\cdot\frac{Z_0}{Z_1}\cdot\exp\left(\frac{E_o - E(\lambda)}{kT}\right), \tag{4.7}$$

where Z_0/Z_1 is the energy partition function based on the Stark splitting and thermal distribution of the population of the ground and excited states, E_o is the zero-line energy (shown in Fig. 4.3), $E(\lambda)$ is the transition energy for the wavelength λ, k is Boltzmann's constant, and T is the temperature. From this analysis we also get a modified form of the Füchtbauer-Ladenburg equation:

$$\frac{1}{\tau_{rad}} = 8\pi n^2 c \int \frac{\sigma_{em}(\lambda)}{\lambda^4} d\lambda, \tag{4.8}$$

where τ_{rad} is the radiative lifetime, c is the speed of light in a vacuum, n is the refractive index of the medium, λ is the wavelength, and σ_{em} is the emission cross section. Using equations (4.7) and (4.8), it is possible to extract the absorption and emission cross sections from either the measured absorption or emission spectra.

The $^4I_{15/2} \leftrightarrow {}^4I_{13/2}$ absorption and emission cross sections are usually on the order of 10^{-21} in Er-doped glasses. Various peak cross section values are shown for comparison in Table 4.2.

Table 4.2. Peak $^4I_{15/2} \leftrightarrow {}^4I_{13/2}$ absorption and emission cross sections in Er-doped glasses.

Host	λ_{peak} [nm]	σ_{abs} [10^{-21} cm^2]	σ_{em} [10^{-21} cm^2]	Ref.
Al-P co-doped silica	1531	6.60	5.70	[128]
Silicate	1536	5.80	7.27	[128]
Fluorophosphate	1533	6.99	7.16	[128]
GeO_2-SiO_2	1530	7.9 ± 0.3	6.7 ± 0.3	[129]
Al_2O_3-SiO_2	1530	7.9 ± 0.3	7.9 ± 0.3	[129]
Phosphate	1535	5.4		[24]
Al_2O_3	1532	5.7± 0.7	5.7	[130]

4.2.3 Lifetime

The lifetime of a given energy level is the time constant describing the exponential decay of ions from that level. It is inversely proportional to the probability per unit time of the decay of an ion from that level. The number of ions excited to a given level can be represented by the intensity of spontaneous emission from that level. The emitted intensity can be plotted as a function of time to obtain a luminescence decay curve. In the absence of other energy-transfer processes, the luminescence decay is represented by a single exponential curve. The luminescent lifetime can be written as a sum of lifetimes which represent the different decay paths. These can be divided into radiative decay and non-radiative. Radiative decay results in the spontaneous emission of a photon, while in non-radiative decay the energy is transferred to phonons, or vibrations of the crystal or glass host material. The following equation relates the various contributions to the radiative lifetime of the *i*th level:

$$\frac{1}{\tau_i} = \frac{1}{\tau_{rad,i}} + \frac{1}{\tau_{nr,i}}, \tag{4.9}$$

where τ_i is the luminescence lifetime, $\tau_{rad,i}$ is the radiative lifetime and $\tau_{nr,i}$ is the non-radiative lifetime.

Non-radiative decay occurs by energy transfer to the host material through a number of photons with total energy equal to the energy gap between the levels, called multi-phonon relaxation. The probability of multiphonon relaxation decreases exponentially with the number of phonons required to bridge the energy gap. The average phonon energy is determined by the strengths of the bonds between the ions and the mass of the ligand ions (i.e. O, F, Cl etc.). A lighter ligand ion and larger restoring forces result in larger phonon energies. In Er-doped oxides the average phonon energies are relatively high (900-1400 cm^{-1}), which means that the number of phonon-transfer processes required to jump from one level to the next is lower. Therefore the probability of multiphonon relaxation is higher and the lifetimes are typically short (~1-100μs). The exception is the lifetime of the $^4I_{13/2}$ level, which remains high because several phonon excitations are required to bridge the gap to the $^4I_{15/2}$ level. Because of the longer lifetime of this level it is possible to build up the population and obtain inversion, which is necessary for gain in Er-doped amplifiers. The average phonon energy and typical lifetimes of the $^4I_{9/2}$ and $^4I_{13/2}$ levels measured in different Er-host materials are shown in Table 4.3.

Table 4.3. Average phonon energy and $^4I_{9/2}$ and $^4I_{13/2}$ luminescent lifetimes measured in different host materials [5, 131].

Host	Phonon Energy [cm^{-1}]	τ_4, $^4I_{9/2}$ [μs]	τ_1, $^4I_{13/2}$ [ms]
Borate glass	1400		
Phosphate glass	1200		10.7
Silicate glass	1100	0.5	14.7
Germanate glass	900		
YAG ($Y_3Al_5O_{12}$)	800		
Tellurate glass	700		4
YLF ($YLiF_4$)	550		
Fluoride glass	500	7	10.3
$Cs_3Er_2Cl_9$	280	4000	
$Cs_3Er_2Br_9$	190		
$Cs_3Er_2I_9$	160		

4.2.4 Energy Transfer Between Ions

Besides the transitions between energy levels due to absorption, stimulated emission and radiative and non-radiative decay, transitions caused by energy transfer between neighbouring ions play an important role. These processes, which exhibit a $1/r_{Er}^6$ dependence, are especially important in highly-doped Er amplifiers, where the average inter-ionic spacing r_{Er} becomes smaller. Two processes involving energy transfer between ions are illustrated in Fig. 4.4. Figure 4.4a shows the process of energy migration, whereby an excited ion (the donor) transfers its energy to a nearby ion in the ground state (the acceptor). The donor returns to the ground state while the acceptor is excited to a higher state. This process can eventually result in loss of excitation through diffusion and energy dissipation at an impurity such as an OH^- group. Figure 4.4b shows the case where two excited ions interact, with energy from the donor ion being

transferred to the acceptor, promoting it to a higher energy state. This second process is referred to energy transfer upconversion (ETU).

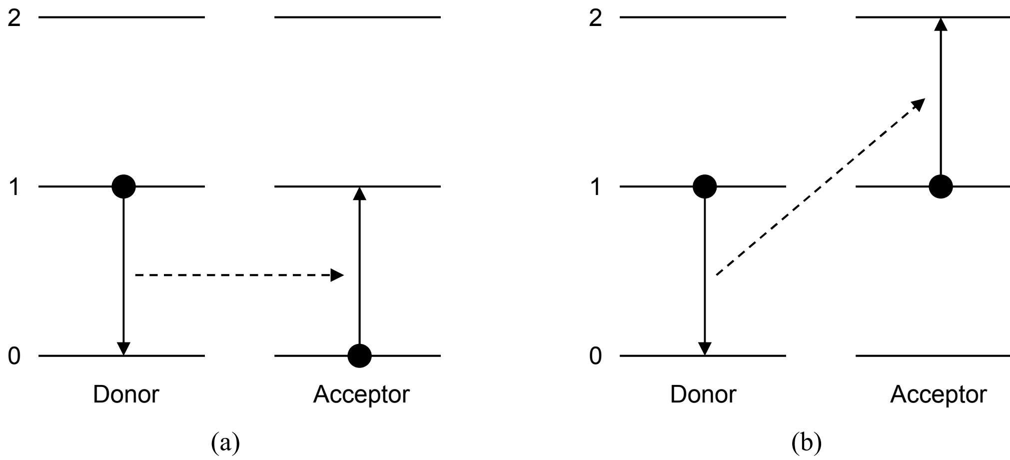

Fig. 4.4. Er^{3+}-Er^{3+} interionic energy transfer processes: (a) energy migration and (b) energy transfer upconversion.

In EDWAs, the upconversion process from the $^4I_{13/2}$ level has a significant impact on amplifier performance. This is because it results in de-population of the $^4I_{13/2}$ level, reducing the population inversion compared to the $^4I_{15/2}$ level and therefore the maximum gain that can be achieved. In the most straightforward model, the upconversion rate is determined by a macroscopic material-dependent parameter W_{ETU} and is proportional to the square of the population density of the Er level from which it occurs [132, 133]. The upconversion rate can be represented as follows:

$$R_{ETU} = W_{ETU} N^2 \tag{4.10}$$

where R_{ETU} is the volume upconversion rate in ($cm^{-3}s^{-1}$), and N is the population density. The value W_{ETU} is also concentration dependent. Typical values of the upconversion coefficient measured in Er-doped glasses originating from the $^4I_{13/2}$ level are summarized in Table 4.4. The upconversion strength also depends on the uniformity of Er in the host material, which can depend on the fabrication process. For example, in [45], thin films were found to exhibit an upconversion coefficient ~2.4 times higher than in bulk glasses. One of the primary reasons for the higher gain demonstrated in phosphate glass and soda lime glass is the low upconversion value demonstrated even at relatively high Er concentrations.

Table 4.4. ETU coefficient for the $^4I_{13/2}$ level measured in various Er-doped glasses.

Host material	Host type	Er concentration $[10^{20}\ cm^{-3}]$	ETU coefficient, W_{ETU} $[10^{18}\ cm^3s^{-1}]$	Ref.
Phosphate glass	Bulk	1	0.77 ± 0.07	[134]
	Waveguide	1	0.93 ± 0.07	[134]
	Bulk	2.0	1.2	[135]
	Bulk	0.2 to 4.0	~0.8 to ~1.1	[136]
	Waveguide	5.3	2.0 ± 0.5	[24]
Soda lime silicate	Waveguide	~1.4	3.2 ± 0.8	[42]
	Bulk	0.50 to 6.0	0.26 to 1.2	[45]
	Waveguide	0.70 to 4.1	0.61 to 2.3	[45]
Alumino-silicate	Bulk	0.4 to 4.8	0.3 to 1.4	[45]
Al_2O_3	Waveguide	~1.2	4 ± 1	[132]
Ge/Al/P-doped silica	Fiber	70 to 840 ppm by weight	~100	[137]

4.2.5 Gain

When the rate of stimulated emitted photons from a level is higher than the rate of absorbed photons at that wavelength, gain (amplification) is achieved. This is the basic principle of an optical amplifier. In order to achieve gain, a pump process is required to populate the higher level from which stimulated emission occurs. This pumping can be provided by electrical means (in semiconductor optical amplifiers) or by optical means (in the case of rare-earth-doped amplifiers. In the case of dielectric Er-doped materials optical pumping at a wavelength of either 980 nm or 1480 nm is used to excite ions from the ground state to the $^4I_{13/2}$ state, from which stimulated emission can occur to amplify a signal around 1530 nm. Therefore a population inversion is required between the $^4I_{13/2}$ and $^4I_{15/2}$ state (at least 50% of ions excited to the higher energy level). In addition, the number of stimulated emitted photons must exceed those lost by background losses, for example propagation losses due to scattering in a channel waveguide. This is why it is important to have such low background losses in an optical amplifier. A detailed model of the optical gain under 980-nm pumping, including all of the processes discussed in this section, is provided in section 4.5.1.

4.3 Amplifier Fabrication, Propagation Loss Measurements and Spectroscopic Results

In this section the amplifier fabrication details and the propagation losses, absorption and emission cross sections and lifetimes of the $Al_2O_3:Er^{3+}$ amplifiers are reported.

4.3.1 Sample Fabrication

$Al_2O_3:Er^{3+}$ channel waveguide amplifiers were fabricated based on design I presented in Chapter 3. $Al_2O_3:Er^{3+}$ layers with thicknesses of 0.9 to 1.3 µm were deposited on standard thermally oxidized 10-cm Si wafers by the optimized reactive co-sputtering process. The Er-target power was set at values ranging from 6 to 20 W in order to adjust the Er concentration in the different samples. The resulting Er concentrations, which were measured by RBS, varied from 0.27 to 4.22 × 10^{20} cm^{-3}. Subsequently, the optimized Al_2O_3 etch recipe was applied to fabricate shallow-etched 4.0-µm-wide waveguides in the $Al_2O_3:Er^{3+}$ layers while keeping one half of each sample unpatterned for planar waveguide experiments.. The etch depths of the channel waveguides, each

selected based on the realized film thickness, were measured to be 43 to 99 nm using a Dektak profilometer. End facets for the straight waveguides were prepared by cleaving the samples to lengths of approximately 6 cm. The fabricated amplifiers are summarized in Table 4.5.

Table 4.5. Fabricated $Al_2O_3:Er^{3+}$ amplifiers used in gain study. The waveguide width *w* was 4.0 μm.

Er Concentration[1] [10^{20} cm^{-3}]	Height, *h* [nm]	Etch Depth, *d* [nm]	Length, *L* [cm]
0.27	1204	82	6.4
0.49	1301	99	5.9
1.00	916	50	5.9
1.17	1093	69	5.4
2.12	928	53	5.7
2.91	1071	88	5.5
3.66	894	43	6.3
4.22	976	64	6.6

[1]Measured by RBS.

4.3.2 Propagation Losses

The background propagation losses and Er ground-state absorption at the pump and signal wavelengths were investigated by measuring the total optical propagation losses. The moving prism method with a HeNe laser, diode-laser module, diode-pumped solid-state laser, or tunable diode-laser source were used for measurements at 633 nm, 977 nm, 1320 nm, and 1533 nm, respectively. Background losses of 0.21 to 0.68 dB/cm at 633 nm and 0.12 to 0.34 dB/cm at 1320 nm were measured with ±0.10 dB/cm accuracy, confirming low scattering at visible and infrared wavelengths. The total propagation losses at the 977-nm pump wavelength and the 1533-nm signal wavelength increase with Er concentration due to absorption at the $^4I_{15/2} \rightarrow {^4I_{11/2}}$ and $^4I_{15/2} \rightarrow {^4I_{13/2}}$ transitions, respectively. The total propagation loss at each wavelength as a function of Er concentration is shown in Fig. 4.5.

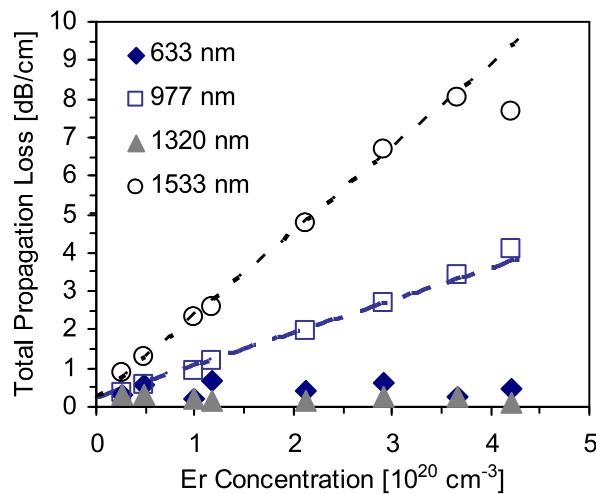

Fig. 4.5. Total planar waveguide propagation loss α_{Total} at 633 nm, 977 nm, 1320 nm, and 1533 nm as a function of Er concentration. The dashed lines represent the calculated propagation loss at 977 nm and 1533 nm using the absorption cross sections determined from this data set and the average background loss and average confinement factor at each wavelength in the eight samples.

4.3.3 Absorption and Emission Cross Sections

Using the measured total propagation losses, the wavelength-dependent Er absorption cross sections $\sigma_{abs}(\lambda)$ in cm^2 were calculated using the equation

$$\sigma_{abs}(\lambda) = \frac{\alpha_{Er}(\lambda)}{10 \cdot \log(e) \cdot \Gamma(\lambda) \cdot N_0}, \tag{4.11}$$

where $\alpha_{Er}(\lambda)$ is the Er absorption coefficient in dB/cm, $\Gamma(\lambda)$ is the calculated confinement factor of the slab mode within the active Al_2O_3:Er^{3+} layer, and N_0 is the ground-state population density in cm^{-3}. $\alpha_{Er}(\lambda)$ was found by subtracting the background propagation loss, $\alpha_{Loss}(\lambda)$, from the measured total propagation loss, $\alpha_{Total}(\lambda)$. The wavelength-dependent background propagation loss at 977 nm and 1533 nm was estimated using a Raleigh scattering fit to the background propagation losses measured at 633 nm and 1320 nm and N_0 was approximated as being equal to the total dopant concentration in the layer, N_d (valid at low excitation densities). Based on the cross sections calculated at each concentration, average absorption cross sections of $(2.01 \pm 0.16) \times 10^{-21}$ cm^2 and $(5.65 \pm 0.24) \times 10^{-21}$ cm^2 were determined at 977 and 1533 nm, respectively. For calculation of the 977-nm absorption cross sections the two lowest concentrations were neglected because the uncertainty in the background propagation loss became large compared to $\alpha_{Er}(\lambda)$, while for calculation of the 1533-nm absorption cross section the value at the highest concentration was not included due to the large relative uncertainty in the measurement at large propagation losses. These values have improved precision compared to results published previously in our material [77]. This is because the present measurement was carried out at a single wavelength using a tunable laser source as opposed to a broad spectrum using a white-light source and spectrometer with a resolution of 5 nm. Measuring at such low resolution, which was required in that particular spectrometer in order for sufficient signal intensity to reach the detector, tends to smooth out the spectrum, reducing the peak values.

Now that the cross sections are known, the Er-related absorption $\alpha_{Er}(\lambda)$ and the total small-signal propagation losses $\alpha_{Total}(\lambda)$ can be calculated for a given waveguide geometry (with a corresponding confinement factor), Er concentration and background propagation loss. The lines shown in Fig. 4.5 were obtained using the absorption cross sections determined above and the average confinement factor and background propagation losses of the Al_2O_3:Er^{3+} waveguides in this investigation.

The spectrum of luminescence from the $^4I_{13/2}$ level was also measured by launching 977-nm pump light into a channel waveguide and collecting the emission perpendicular to the waveguide using a liquid-core fiber. The spectrum, measured using a Horiba Jobin Yvon iHR550 spectrometer with a resolution of < 1 nm, was scaled using the Füchtbauer-Ladenburg relation given in equation (4.8) to determine the

emission cross section. Since the radiative lifetime was unknown, the emission spectrum was fitted to the measured absorption cross section value around the peak at 1533 nm. The average emission cross section calculated in this manner for Er concentrations ranging from 1.00 to 4.22 × 10^{20} cm^{-3} is displayed in Fig. 4.6. The fit gives a radiative lifetime of 8.6 ± 0.5 ms.

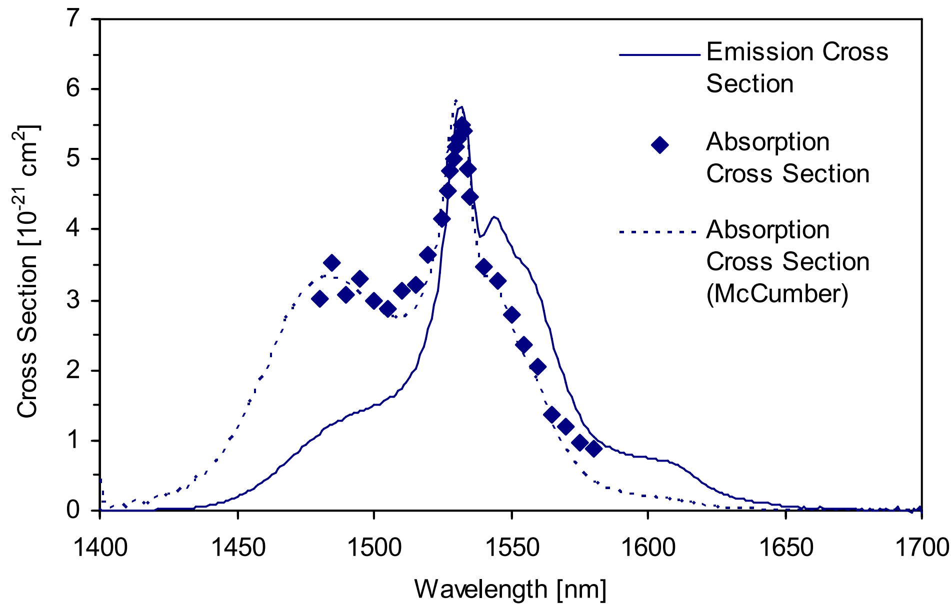

Fig. 4.6. Emission cross section determined from the luminescence spectra of samples with Er concentrations of 1.00 to 4.22 × 10^{20} cm^{-3}. The absorption spectrum calculated using McCumber theory and measured at single wavelengths in the range 1480-1580 nm are indicated by the dashed line and the plotted points, respectively.

The absorption cross section was also measured at wavelengths ranging from 1480 to 1580 nm in a single sample (N_d = 1.17 × 10^{20} cm^{-3}) using the tunable laser in the same manner as described for the measurement at 1533 nm. In order to calculate the entire absorption cross section spectrum at the relevant wavelengths for signal enhancement, McCumber theory was applied. In the case of $Al_2O_3:Er^{3+}$, the $^4I_{13/2}$ lifetime is several ms and the requirement of sufficient time for thermal relaxation is satisfied. The Stark level structure of $Al_2O_3:Er^{3+}$ is unknown. However, based on the partition functions calculated for Er_2O_3 and Er-doped aluminosilicate and phosphate glass, which are close to unity, we can reasonably make the assumption $Z_0 / Z_1 \approx 1$ [138]. Therefore, setting the energy partition function to unity (which has already been assumed by scaling the emission spectrum to the peak absorption value in Fig. 4.6), the absorption spectrum of the $Al_2O_3:Er^{3+}$ waveguides between 1400-1700 nm was calculated using 4.7. The measured values and the calculated absorption spectrum are shown in Fig. 4.6 and are in good agreement with each other. The absorption and emission spectra are similar to those reported previously for $Al_2O_3:Er^{3+}$ waveguides fabricated using a different technique [91], and the peak cross sections are typical of those measured in Er-doped glasses [127].

4.3.4 Luminescent Lifetimes

Luminescence decay measurements from the Er $^4I_{13/2}$ level were performed after exciting the channel waveguides with 976-nm pump light from a diode laser modulated by a square-pulse generator [139]. The pulse had a duration of 40 ms, allowing the Er population to reach steady state before the pump was switched off. The light near 1530 nm from the luminescent decay was collected using a high N.A. liquid fiber mounted normal to the sample surface and the resulting signal was acquired with a digital oscilloscope. Besides initial non-exponential parts owing to ETU, which are less pronounced than measured previously [132], exponential tails of the individual decay curves ranging from 7.5 ms at the lowest Er concentration to 6.1 ms at the highest concentration were measured. The lifetimes are plotted in Fig. 4.7. A fit to the data gives an intrinsic luminescent lifetime of 7.6 ± 0.2 ms, which is slightly lower than the estimated radiative lifetime of 8.6 ± 0.5 ms.

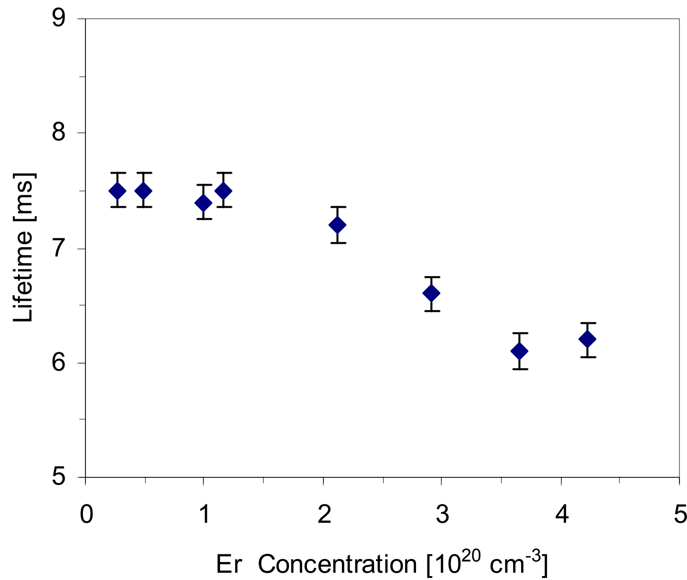

Fig. 4.7. $^4I_{13/2}$ luminescent lifetime in $Al_2O_3:Er^{3+}$ channel waveguides as a function of Er concentration.

4.4 Optical Gain Measurements

The experimental setup for measuring the optical gain in the $Al_2O_3:Er^{3+}$ channel waveguide amplifiers is depicted schematically in Fig. 4.8. Pump light from a tunable Ti:Sapphire laser at 977 nm and signal light at 1480-1580 nm from a tunable diode laser modulated at 283 Hz were coupled to and from the waveguide via objective lenses. The pump and signal light were randomly polarized since the optical modes supported by the $Al_2O_3:Er^{3+}$ waveguides had similar characteristics for both TE and TM polarization. Approximately 1 μW of signal power was launched into the waveguide to ensure the measured gain was in the small signal limit. Light coupled from the waveguide was passed through a silicon filter to remove transmitted pump light and onto a Ge detector, where standard lock-in detection was used to eliminate any residual transmitted pump light and spontaneous emission from the measured signal. The internal net gain, $\gamma(\lambda)$ (dB/cm), was calculated from the equation

$$\gamma(\lambda) = \frac{10 \cdot \log_{10}\left[I_{On}(\lambda) / I_{Off}(\lambda) \right]}{L} - \alpha_{Total}(\lambda), \qquad (4.12)$$

where I_{On} and I_{Off} are the optical signal intensity measured at the detector in the pumped and un-pumped case, respectively, and L is the amplifier length (cm). The background propagation loss in the shallow-etched channel waveguide was assumed to be the same as the measured slab loss, due to nearly identical confinement factors of the propagating light in the Al_2O_3:Er^{3+} core layer. This was later confirmed by measuring the channel waveguide losses by infrared camera measurements. In addition, the shallow etch depths selected for the channel waveguides ensured negligible additional scattering losses.

In order to estimate the percentage of incident Ti:Sapphire pump power launched into the waveguide, the gain curve was also measured on a separate fiber-coupling setup, which used 980/1550 WDM fiber couplers to combine pump and signal light in front of the waveguide and separate each at the output. In this second setup the coupling efficiency, and thus the launched pump power, could be experimentally determined by standard insertion loss measurements. However, only pump powers of up to ~ 5 mW could be coupled into the Al_2O_3;Er^{3+} amplifiers, making it unsuitable for measuring the full gain vs. launched pump power curve. Therefore it was only applied to determine the launch efficiency in the case of lens coupling, where much higher pump powers were available but it was difficult to measure the launched pump power. The procedure was as follows. The gain vs. launched pump power curve, up to a launched power of ~ 5 mW, was measured on the fiber-coupling setup (curve 1). Following this the gain vs. incident pump power was measured using the setup shown in Fig. 4.8 (curve 2), where the incident pump power (up to ~ 600 mW) was measured using a large-area free space optical power meter placed in front of the sample. For each sample, curve 2 was then fitted to curve 1 by multiplying the measured incident pump powers by a constant launch efficiency value (typically ranging from 14-16%) to determine the launched pump powers. By comparison, it was possible to inject pump powers of up to ~100 mW using the lens-coupling setup.

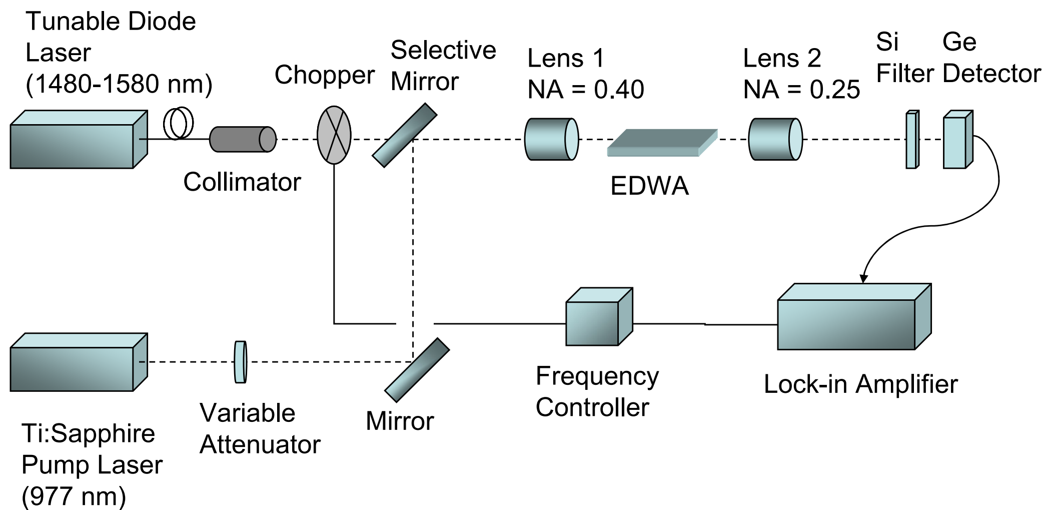

Fig. 4.8. Experimental setup for measuring gain in $Al_2O_3:Er^{3+}$ channel waveguides.

In order to compare the peak gain at different Er concentrations the total internal net small-signal gain was measured at 1533 nm, close to the peak emission and absorption cross sections of the $^4I_{15/2} \leftrightarrow {}^4I_{13/2}$ transition. In these initial experiments maximum pump powers ranging from 50-70 mW were launched into the different samples. Thus, for comparison, the total internal net gain measured for a launched pump power of ~50 mW in each ~6-cm-long amplifier is shown in Fig. 4.9a. Of the samples measured, the best Er concentration for this specific waveguide length and pump power was determined to be 1.17×10^{20} cm^{-3}, where approximately 8 dB of total internal net gain was measured. At higher concentrations, significant pump absorption, resulting in less inversion towards the end of the waveguide, and stronger ETU were suspected to contribute to the reduced total gain. The gain measured at 1533 nm for the 5.4-cm-long amplifier with an Er concentration of 1.17×10^{20} cm^{-3} is shown in Fig. 4.9b as a function of launched pump power. The threshold pump power for internal net gain is 7 mW, while the gain begins to saturate above 20 mW, before reaching a value of approximately 9 dB for a launched pump power of almost 100 mW. In the same figure, the gain is also shown when pumping at 1480 nm. The signal enhancement was measured on a separate setup by combining pump light from a 1480-nm Raman laser source and signal light via a fiber wavelength division multiplexer and coupling to and from the chip via tapered lensed fibers. The threshold pump power is slightly lower (4 mW), which is expected due to the higher photon density per unit pump intensity at this wavelength, in combination with similar confinement within the active layer at both wavelengths. However, the total internal net gain saturates at a lower value of approximately 6 dB. Under 1480-nm pumping lower population inversion is expected theoretically [140] due to stimulated emission at the pump wavelength from the highly populated $^4I_{13/2}$ level, thus reducing the maximum net gain which can be achieved. This effect is much less pronounced when pumping at 977 nm due to the fast non-radiative quenching and, hence, lower population density of the $^4I_{11/2}$ pump level. This comparison supports our selection of 977 nm as the pump wavelength in order to maximize the gain in our devices.

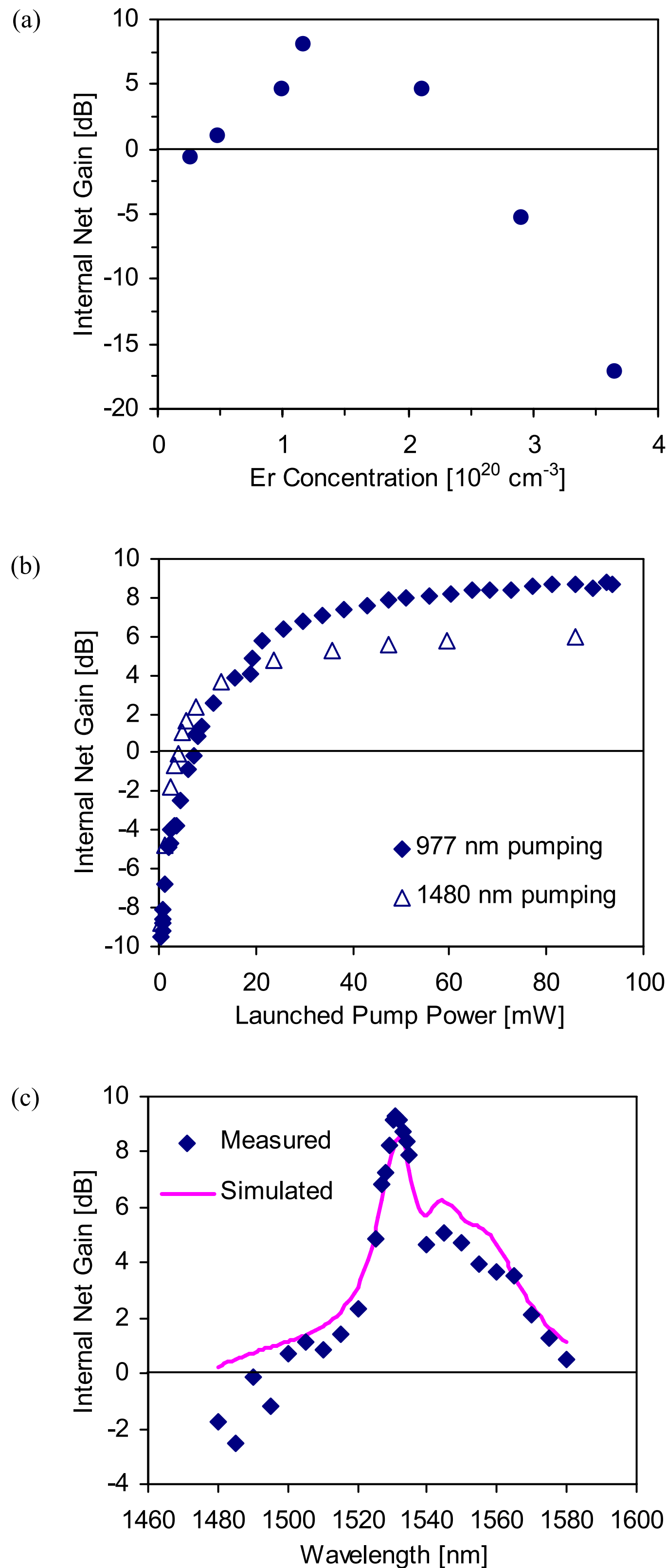

Fig. 4.9. (a) Internal net gain versus Er concentration for as signal wavelength of 1533 nm, an amplifier length of ~6 cm and a launched 977-nm pump power of ~50 mW; (b) gain versus launched pump power for an Er concentration of 1.17×10^{20} cm^{-3}, signal wavelength of 1533 nm and pump wavelengths of 977 nm and 1480 nm; (c) internal net gain as a function of wavelength for an amplifier length of 5.4 cm, Er concentration of $N_d = 1.17 \times 10^{20}$ cm^{-3}, and a launched pump power of 80 mW.

The net gain was also measured as a function of wavelength in the same amplifier, displayed in Fig. 4.9c. For a launched 977-nm pump power of 80 mW, net gain was demonstrated over a bandwidth of 80 nm. At the peak around 1533 nm gain of 9.3 dB was measured, while net gain of > 3.5 dB (> 0.65 dB/cm) was measured between the wavelengths of 1525-1565 nm, within the telecom C-band.

In Fig. 4.10a the maximum gain per unit length measured for each concentration is shown. This comparison is particularly important for laser applications, where often shorter sample lengths, but high gain per unit length are required [69]. The sample length was varied from 1.0 to 6.4 cm depending on Er concentration in order to optimize absorption of the available 977-nm pump light (~80-100 mW depending on the launch efficiency of the specific sample), but simultaneously avoid potential reabsorption of the signal light in the less excited end section of the waveguide. Accordingly, the sample length was reduced from those shown in Table 4.5 to 2.1 cm, 1.3 cm and 1.0 cm for concentrations of 2.12, 2.91 and 3.66 × 10^{20} cm^{-3}, respectively. At a concentration of 2.12 × 10^{20} cm^{-3}, a total internal net gain of 4.2 dB was measured in a 2.1-cm-long amplifier. This is equivalent to an internal net gain of 2.0 dB/cm, which is more than twice the highest gain figure previously reported in this material. Fig. 4.10b displays the total internal net gain versus launched pump power for this sample. At sufficiently high launched pump powers we also expect higher gain in the 5.7-cm-long amplifier at this concentration than that shown for a concentration of 1.17 × 10^{20} cm^{-3} in Fig. 4.10b and c.

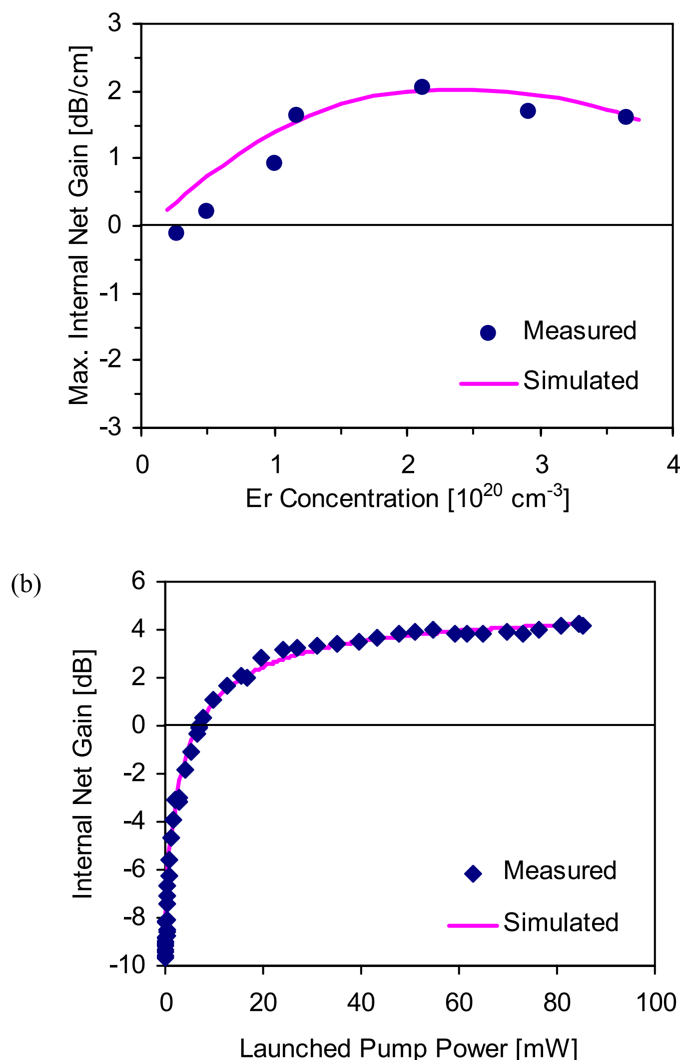

Fig. 4.10. (a) Internal net gain per unit length at a signal wavelength of 1533 nm for varying Er concentration and sample lengths optimized for a launched pump power of 80 mW; (b) measured and simulated gain at a signal wavelength of 1533 nm versus launched pump power for an amplifier length of 2.1 cm and Er concentration of 2.12×10^{20} cm^{-3}.

In Table 4.6 our results are compared to previous $Al_2O_3:Er^{3+}$ channel waveguide amplifiers in terms of fabrication method, concentration, and gain. The higher gain achieved can be attributed to larger waveguide cross sections which increases confinement of the signal within the $Al_2O_3:Er^{3+}$ core, pumping at 977 nm as opposed to 1480 nm and the low background losses obtained in our samples. Significantly lower pump powers were used in [34] and [37] compared to the maximum of 80 mW launched into our amplifier. However, by extrapolating the data in those cases, higher pump powers would only result in a small increase in gain. By comparison, total peak net gain similar to [34] was measured for a pump power of only 18 mW in our amplifier and the threshold pump power for net internal gain was a reasonable 7 mW. The threshold pump power could be reduced by selecting a design similar to design II in Chapter 3. In that case the smaller waveguide geometry results in higher pump intensities in the $Al_2O_3:Er^{3+}$ core of the waveguide. However, as was mentioned in that chapter, the lower

confinement in such a design would result in lower peak gain. This tradeoff will be explored in more detail based on the gain results in this chapter in section 4.5.2.

Table 4.6. Comparison of fabrication methods, waveguide characteristics and gain achieved in previous $Al_2O_3:Er^{3+}$ channel waveguide amplifiers and in this work.

Deposition method	Channel waveguide fabrication method	Er Conc. [10^{20} cm^{-3}]	Waveguide cross-section [µm × µm]	Wave-guide length [cm]	Back-ground loss [dB/cm]	Pump power[1] [mW]	Peak gain [dB/cm]	Ref.
Reactive co-sputtering	Reactive ion etching	2.1	0.9 ×4	2.1	0.13	80 (977)	2.0	This work
Sputter-deposition/ ion-implantation	Ar-atom beam etching	2.7	0.6 × 2	4.0	0.35	9 (1480)	0.58	[34]
Reactive co-sputtering	Ar-ion beam etching	2.2	0.8 × 2	5.5	1.1	8.7 (1480)	0.2	[37]
Atomic layer deposition	Wet-etching	3.2	2 × 6	3.9	~ 1.7	~25 (980)	-6	[38]

[1] Pump wavelength indicated in brackets in nm.

4.5 Optical Gain Calculations

Besides the gain per unit length versus Er concentration shown in Fig. 4.10a and the gain achieved for straight waveguides over the lengths patterned on our typical wafers shown in Fig. 4.9a, we are interested in the maximum gain achievable for each Er concentration, i.e. for optimized waveguide length. This value is naturally a function of launched pump power, as higher launched pump powers will excite the waveguide and produce net gain over longer lengths. In this section we use a simplified 3-level rate equation model, which includes the $^4I_{15/2}$ ground state, the $^4I_{13/2}$ first excited level, and the $^4I_{11/2}$ pump excitation level, to calculate the amplifier response. The model is applied to determine the optimum amplifier length for a given Er concentration and pump power. Calculations are also carried out to predict the gain over a wide wavelength range. Finally the gain at different pump powers and Er concentrations and the influence of waveguide design on amplifier performance are investigated.

4.5.1 Amplifier Model

Fig. 4.11 illustrates the simplified 3-level system and relevant absorption, emission and energy transfer processes. Pump ground state absorption, stimulated emission and excited state absorption, signal ground state absorption and stimulated emission, and ETU from the $^4I_{13/2}$ level are included in the model. We assume that all excited states except for the $^4I_{13/2}$ and $^4I_{11/2}$ levels have very short lifetimes and are virtually unpopulated. The $^4I_{11/2}$ population density is small due to a relatively short lifetime and rapid non-radiative relaxation to the $^4I_{13/2}$ level. Therefore, the influence of ETU from this second excited level into the higher-lying $^4F_{7/2}$ level on the population densities is negligible and it was excluded from the model.

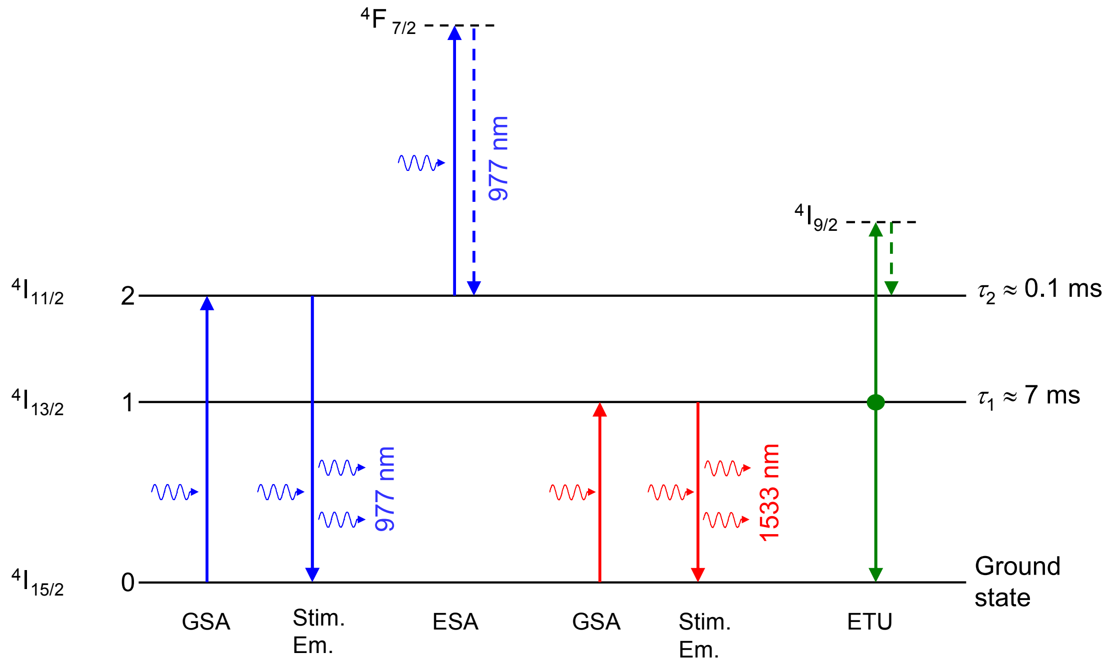

Fig. 4.11. Simplified Er3+ energy level diagram and relevant transitions for the 980-nm-pumped $Al_2O_3:Er^{3+}$ amplifier.

The Lambert-Beer law for the absorption and emission of pump and signal light intensities I_P and I_S at the wavelengths λ_P and λ_S, respectively, propagating through a medium over a short length interval Δz yields the following equation for transmitted pump or signal power in our 3-level system:

$$\begin{aligned} I_P(z+\Delta z) &= I_P(z)\exp\{[\sigma_{em}(\lambda_P)N_2(z)-\sigma_{abs}(\lambda_P)N_0(z) \\ &\quad -\sigma_{ESA}(\lambda_P)N_2(z)-\alpha_{Loss}(\lambda_P)]\Delta z\} \\ &\approx I_P(z)\{1+[\sigma_{em}(\lambda_P)N_2(z)-\sigma_{abs}(\lambda_P)N_0(z) \\ &\quad -\sigma_{ESA}(\lambda_P)N_2(z)-\alpha_{Loss}(\lambda_P)]\Delta z\} \end{aligned}, \tag{4.13}$$

where $\sigma_{em}(\lambda_P)$, $\sigma_{abs}(\lambda_P)$, $\sigma_{ESA}(\lambda_P)$, and $\alpha_{Loss}(\lambda_P)$ are the emission cross section, absorption cross section, excited-state absorption (ESA) cross section, and background propagation loss at the pump wavelength, respectively, and N_2, N_1, and N_0 are the population densities of the $^4I_{11/2}$, $^4I_{13/2}$, and $^4I_{15/2}$ levels, respectively. Likewise, the transmitted signal power is given by:

$$\begin{aligned} I_S(z+\Delta z) &= I_S(z)\exp\{[\sigma_{em}(\lambda_S)N_2(z)-\sigma_{abs}(\lambda_S)N_0(z) \\ &\quad -\alpha_{Loss}(\lambda_S)]\Delta z\} \end{aligned}$$

$$\approx I_S(z)\left\{1+\left[\sigma_{em}(\lambda_S)N_1(z)-\sigma_{abs}(\lambda_S)N_0(z)\right.\right.$$
$$\left.\left.-\alpha_{Loss}(\lambda_S)\right]\Delta z\right\}, \quad (4.14)$$

where $\sigma_{em}(\lambda_S)$, $\sigma_{abs}(\lambda_S)$, and $\alpha_{Loss}(\lambda_P)$ are the emission cross section, absorption cross section, and background propagation loss at the signal wavelength, respectively. For a propagation length interval Δz which is small compared to the absorption length and length variation of the population densities, the exponential functions have been expanded into a Taylor series. Unlike the assumption made in [132], in our model we assume $\sigma_{ESA}(\lambda_S)\approx 0$, because signal ESA on the $^4I_{13/2} \rightarrow {}^4I_{9/2}$ transition is typically strongly red-shifted from the $^4I_{13/2} \rightarrow {}^4I_{15/2}$ transition peak and, although it may affect long-wavelength lasers on the latter transition, is unlikely for wavelengths in the range 1480-1580 nm. We also assume ESA from the $^4I_{11/2}$ level only contributes to the reduction of pump power but not to the population dynamics in other ways, because any excitation to higher-lying levels results in fast relaxation back to the $^4I_{11/2}$ level. Therefore, extracting ESA and background losses, which do not contribute directly to the population densities, the net stimulated absorbed pump intensity $\Delta I_{Stim,P}$ and net stimulated emitted signal intensity $\Delta I_{Stim,S}$ are as follows:

$$\Delta I_{Stim,P}(z+\Delta z) = -I_P(z)\left[\sigma_{em}(\lambda_P)N_2(z)-\sigma_{abs}(\lambda_P)N_0(z)\right]\Delta z, \quad (4.15)$$

$$\Delta I_{Stim,S}(z+\Delta z) = I_S(z)\left[\sigma_{em}(\lambda_S)N_1(z)-\sigma_{abs}(\lambda_S)N_0(z)\right]\Delta z. \quad (4.16)$$

The corresponding net transition rates R_P and R_S for pump and signal, respectively, per unit volume and time in each segment of the waveguide are then given by

$$R_P(z) = \frac{\lambda_P}{hc}\frac{1}{\Delta z}\Delta I_{Stim,P}(z+\Delta z)$$
$$= \frac{\lambda_P}{hc}\frac{1}{\Delta z}I_P(z)\left[\sigma_{em}(\lambda_P)N_2(z)-\sigma_{abs}(\lambda_P)N_0(z)\right]\Delta z$$
$$= \varphi_P(z)\left[\sigma_{em}(\lambda_P)N_2(z)-\sigma_{abs}(\lambda_P)N_0(z)\right], \quad (4.17)$$

$$R_S(z) = \frac{\lambda_S}{hc}\frac{1}{\Delta z}\Delta I_{Stim,S}(z+\Delta z)$$
$$= \frac{\lambda_S}{hc}\frac{1}{\Delta z}I_S(z)\left[\sigma_{em}(\lambda_S)N_1(z)-\sigma_{abs}(\lambda_S)N_0(z)\right]\Delta z$$
$$= \varphi_S(z)\left[\sigma_{em}(\lambda_S)N_1(z)-\sigma_{abs}(\lambda_S)N_0(z)\right], \quad (4.18)$$

where h is Planck's constant and φ_P and φ_S are the pump and signal photon fluxes per unit area, respectively.

With the intrinsic lifetimes τ_i of the excited states and the assumption that the probability of ETU from the $^4I_{13/2}$ level is given by the macroscopic material-dependent parameter W_{ETU} and its rate depends quadratically on population density of this level, our 3-level system yields the following rate equations for the two excited states:

$$\frac{dN_2(z)}{dt} = R_P(z) + W_{ETU} N_1^2(z) - \frac{1}{\tau_2} N_2(z), \tag{4.19}$$

$$\frac{dN_1(z)}{dt} = -R_S(z) + \frac{1}{\tau_2} N_2(z) - \frac{1}{\tau_1} N_1(z) - 2W_{ETU} N_1^2(z), \tag{4.20}$$

In steady state dN_1/dt and dN_2/dt = 0, and together with the boundary condition $N_0(z) + N_1(z) + N_2(z) = N_d$ eqs. (4.19) and (4.20) can be solved analytically. This gives the following expressions for the population densities in each level at propagation length z:

$$N_1(z) = \frac{-B + \sqrt{B^2 - 4AC}}{2A}, \tag{4.21}$$

$$N_2(z) = \frac{\sigma_{abs}(\lambda_P)\varphi_P\left[N_d - N_1(z)\right] + W_{ETU} N_1^2(z)}{1/\tau_2 + \left[\sigma_{em}(\lambda_P) + \sigma_{abs}(\lambda_P)\right]\varphi_P}, \tag{4.22}$$

$$N_0(z) = N_d - \left[N_1(z) + N_2(z)\right]. \tag{4.23}$$

where A, B, and C are given by:

$$A = \frac{W_{ETU} - \tau_2 W_{ETU}\sigma_{abs}(\lambda_S)\varphi_S(z)}{\tau_2\left\{1/\tau_2 + \left[\sigma_{em}(\lambda_P) + \sigma_{abs}(\lambda_P)\right]\varphi_P(z)\right\}} - 2W_{ETU},$$

$$B = \frac{\sigma_{abs}(\lambda_P)\varphi_P(z)}{\tau_2\left\{1/\tau_2 + \left[\sigma_{em}(\lambda_P) + \sigma_{abs}(\lambda_P)\right]\varphi_P(z)\right\}} - \frac{1}{\tau_1} - \left[\sigma_{em}(\lambda_S) + \sigma_{abs}(\lambda_S)\right]\varphi_S(z),$$

$$C = N_d\sigma_{abs}(\lambda_S)\varphi_S(z) - \frac{N_d\sigma_{abs}(\lambda_P)\varphi_P(z)\left[\tau_2\sigma_{abs}(\lambda_S)\varphi_S(z) - 1\right]}{\tau_2\left\{1/\tau_2 + \left[\sigma_{em}(\lambda_P) + \sigma_{abs}(\lambda_P)\right]\varphi_P(z)\right\}}.$$

In addition to discretization in the z direction, a radial discretization which is not shown in the above equations for simplicity was included to approximate the pump and signal modes using a Gaussian profile. The mode intensity profile in our asymmetric waveguides closely matches that of an elliptical Gaussian profile. However, in preliminary calculations using another computer simulation program [141] it was found that nearly identical results were obtained when using a more simple circular Gaussian approximation of the mode shape (selecting the Gaussian profile to have the same $1/e^2$ intensity area as that of the ellipse). In this approximation, the amount of pump or signal power $P_{P/S}(r,z)$ passing through a circle of radius r at propagation distance z is described by the following equation:

$$P_{P/S}(r,z) = P_{P/S,Total}(z)\left[1-\exp\left(\frac{-2r^2}{w_{P/S}{}^2}\right)\right], \tag{4.24}$$

where $P_{P/S,Total}(z)$ is the total power propagating at distance z and $w_{P/S}$ is the Gaussian beam waist, which is defined as the radial distance at which the optical intensity drops to $1/e^2$ of the peak value. The average intensity in each radial element was calculated by dividing the power passing through that element by its area:

$$\begin{aligned} I_{P/S}(r,z) &= \frac{P_{P/S}(r+\Delta r,z)-P_{P/S}(r,z)}{\pi(r+\Delta r,z)^2-\pi r^2} \\ &= P_{P/S,Total}(z)\frac{\left[\exp\left(-2r^2/w_{P/S}^2\right)-\exp\left(-2(r+\Delta r)^2/w_{P/S}^2\right)\right]}{\pi(r+\Delta r,z)^2-\pi r^2}. \end{aligned} \tag{4.25}$$

The optical mode profiles and percentage confinement of optical power within the active $Al_2O_3:Er^{3+}$ layer for the pump and signal were determined using the measured amplifier dimensions and refractive indices with the PhoeniX FieldDesigner software package [142]. $1/e^2$ radii in the x and y directions were extracted using the resulting quasi-elliptical simulated mode profiles. These were then used to calculate w_P and w_S for a circular Gaussian profile with equivalent $1/e^2$ area for each amplifier. In the amplifier simulations, the radius of the active medium r_a was chosen such that the confinement of the pump and signal matched the values calculated in FieldDesigner within ± 0.5%. The percentage of pump and signal power which was outside the active region did not contribute to the population dynamics and simply decreased according to the wavelength-dependent background losses. After each propagation step the total remaining power in the pump and signal beams were each re-distributed in a Gaussian profile before entering the next propagation step. An example of the Matlab code used for the amplifier calculations is given in the Appendix.

4.5.2 Gain Results

The experimentally determined spectroscopic parameters were used to simulate the amplifier behaviour. The population and propagation equations were solved using 20

radial discretizations and a longitudinal step size of 100 μm. The only unknown parameters were the lifetime τ_2 of the $^4I_{11/2}$ level, the pump emission cross section $\sigma_{em}(\lambda_P)$, the pump ESA cross section $\sigma_{ESA}(\lambda_P)$, and the ETU parameter W_{ETU}. Within the normal range of values reported for Er-doped oxides, the first three parameters were found to have little impact on the simulation results. Therefore, the lifetime τ_2 was chosen to be 100 μs, based on typical lifetimes of the $^4I_{11/2}$ level measured in Er-doped oxide glasses [124]. The pump emission cross section was set equal to the ground-state absorption cross section, since 977 nm is at the zero-line energy of the $^4I_{15/2} \leftrightarrow {}^4I_{11/2}$ transition, and the ESA cross section at 977 nm was chosen to be 0.8×10^{-21} cm^2 based on experimental results obtained for fluoride glass [143].

Since of the unknown parameters, W_{ETU} has the most significant influence on the amplifier performance and its value is highly host-material-dependent, it was used as the only fitting parameter in the simulations. In Fig. 4.12 the fitted W_{ETU} values are shown based on the measured data points in Fig. 4.10a (the three lowest concentrations were excluded because the error in the fitted W_{ETU} was $> 5 \times 10^{-18}$ cm^{3}s^{-1}). The error bars in the fitted W_{ETU} values correspond to the uncertainty in the measured gain (~0.1 dB/cm due to uncertainty in the propagation loss). At concentrations of 0.5, 1.0, 2.0, and 3.0×10^{20} cm^{-3}, W_{ETU} parameters of 4.2, 6.0, 8.7 and 8.8 (± 1.0) × 10^{-18} cm^{3}s^{-1} were determined, respectively. These values are comparable to the singular value of (4 ± 1) × 10^{-18} cm^{3}s^{-1} reported in [132], but give more insight into the influence of ETU at different Er concentrations.

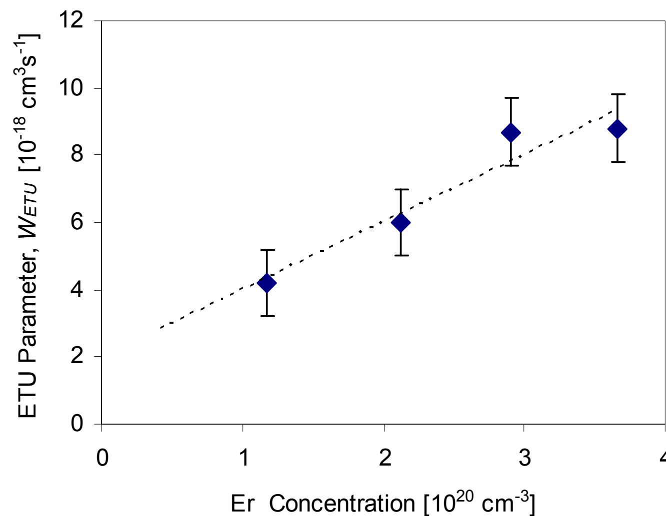

Fig. 4.12. W_{ETU} fitted for different Er concentrations based on the measured gain results.

Using the average amplifier dimensions and background losses, and concentration-dependent W_{ETU} and τ_1 the simulated values of peak gain were calculated for 80 mW pump power, amplifier lengths of 1.0 cm and varying concentration, and are shown with the measured data in Fig. 4.10a. Good agreement with the experimental data is demonstrated, which includes variations due to differences in background loss and waveguide dimensions between the different amplifiers. In Fig. 4.9c and Fig. 4.10b, the

simulated amplifier response is shown in direct comparison with the measured response versus wavelength and launched pump power for the two different amplifiers, respectively. In both specific cases good agreement with the experimental results is also demonstrated.

Table 4.7. Parameters used in $Al_2O_3:Er^{3+}$ amplifier simulations.

Parameter	Symbol	Value	Unit	Source
Pump wavelength	λ_P	0.977	[μm]	This work
Signal wavelength	λ_S	1.533	[μm]	This work
Amplifier length	L	Variable	[cm]	This work
Radius, pump focus	w_P	1.15	[μm]	This work
Radius, signal focus	w_S	1.39	[μm]	This work
Confinement factor, pump wavelength	$\Gamma(\lambda_P)$	96	[%]	This work
Confinement factor, signal wavelength	$\Gamma(\lambda_S)$	89	[%]	This work
Radius, active medium	r_a	~1.05 w_S	[μm]	This work
Er concentration	N_d	0.5, 1.0, 2.0, 3.0	[10^{20} cm^{-3}]	This work
Pump absorption cross section	$\sigma_{abs}(\lambda_P)$	2.0	[10^{-21} cm^2]	This work
Signal absorption cross section	$\sigma_{abs}(\lambda_S)$	5.7	[10^{-21} cm^2]	This work
Pump emission cross section	$\sigma_{em}(\lambda_P)$	2.0	[10^{-21} cm^2]	Estimated
Signal emission cross section	$\sigma_{em}(\lambda_S)$	5.7	[10^{-21} cm^2]	This work
Excited State Absorption cross section	σ_{ESA}	0.8	[10^{-21} cm^2]	[143]
Fluorescent lifetimes	τ_1	7.5, 7.4, 7.1, 6.7	[ms]	[139]
	τ_2	0.1	[ms]	[124]
ETU parameter	W_{ETU}	3, 4, 6, 8	[10^{-18} cm^3/s]	This work
Background loss pump	$\alpha_{Loss}(\lambda_P)$	0.17	[dB/cm]	This work
Background loss signal	$\alpha_{Loss}(\lambda_S)$	0.11	[dB/cm]	This work

In order to compare the gain which can be achieved in longer waveguides, amplifier calculations were carried out for Er concentrations of 0.5, 1.0, 2.0, and 3.0 × 10^{20} cm^{-3}. The optimized parameters used in the amplifier simulations are listed in Table 4.7. Fig. 4.13a and b show the calculated population inversion fraction $\beta(z) = N_1(z)/\left[N_0(z)+N_1(z)\right]$ averaged over the waveguide cross section and total net gain, respectively, versus waveguide length for a launched signal power of 1 μW and varying Er concentrations. The launched pump power was selected to be 100 mW, which is comparable to or less than what is typically required for high total net gain in other EDWAs [20, 43]. In Fig. 4.13a, as the Er concentration increases, the population inversion fraction in the beginning of the waveguide decreases due to the increasing influence of ETU. The population inversion fraction also decreases more strongly with propagation length. This is because the larger number of ions in the ground state due to

lower population inversion fraction and higher Er concentration results in stronger pump absorption. The optimum amplifier length for the pump power of 100 mW and each Er concentration can be determined from Fig. 4.13b. At the lowest concentration, high total net gain can be achieved due to a high excitation fraction throughout the amplifier, but only for comparably long amplifiers. At the highest concentration the maximum gain is lower, because the combination of a greater number of total Er ions and a larger percentage of these ions in the ground state results in stronger pump absorption and also ETU claims its share of the induced excitation. Similar total net gain is predicted for Er concentrations of 1.0 and 2.0 × 10^{20} cm^{-3}; however maximum gain is achieved for a shorter amplifier length at the higher concentration. For a concentration of 2.0 × 10^{20} cm^{-3}, a maximum total gain of 33 dB is predicted for a waveguide length of 24 cm, while for a concentration of 1.0 × 10^{20} cm^{-3} up to 36 dB is predicted at a length of 38 cm.

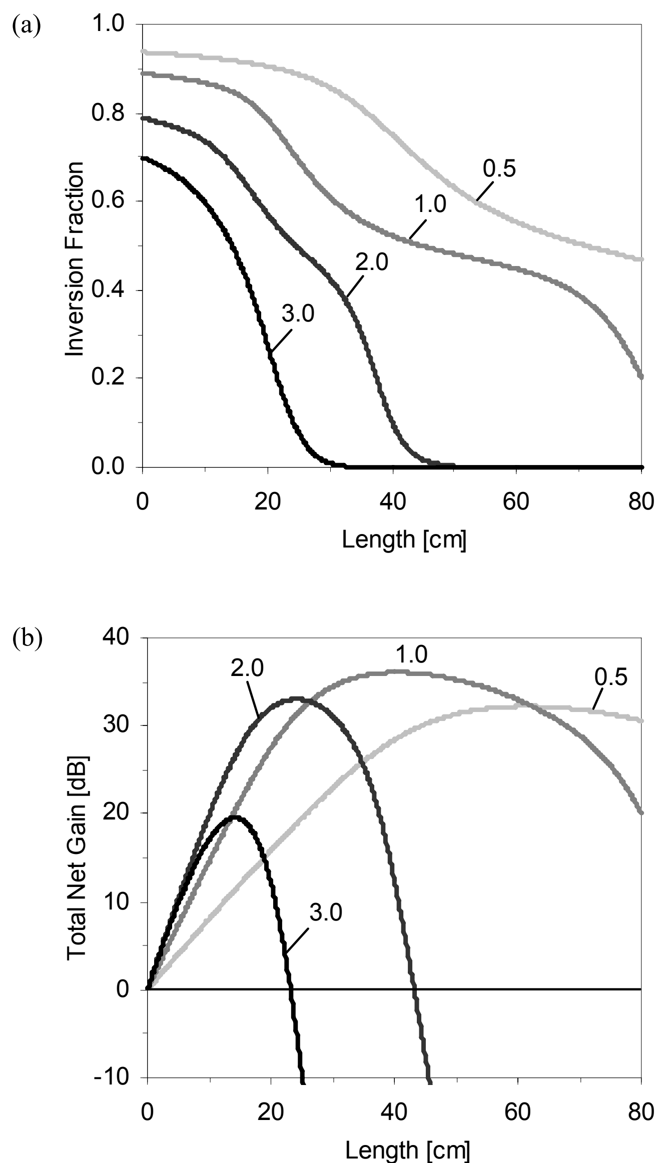

Fig. 4.13. (a) Population inversion fraction and (b) total internal net gain at 1533 nm vs. waveguide length for launched signal and pump powers of 1 μW and 100 mW, respectively, and varying Er concentration (indicated in units of 10^{20} cm^{-3}).

In such long amplifiers, the signal power typically becomes saturated at a certain length and the gain is no longer in the small signal limit. This gain saturation, which is responsible for the change in curvature that can be observed in the curves presented in Fig. 4.13a, is especially pronounced for the amplifier with an Er concentration of 1.0×10^{20} cm^{-3}. For this concentration, Fig. 4.14a shows the pump power and signal power as a function of length for launched signal powers of 1 μW and 1 nW. For 1 μW launched signal power, the amplified signal power eventually increases to a value higher than the remaining pump power and is then strongly absorbed with further increasing length. For a launched signal power of 1 nW, the maximum amplified signal power remains lower, but larger signal enhancement is achieved, because signal saturation effects are reduced. In potential applications ranging from amplification of external fiber-coupled signals to compensation of losses in a photonic circuit, it may be necessary to amplify a wide range of signal powers. Fig. 4.14b shows the resulting gain vs. length for launched signal powers of 1 nW, 10 nW, 100 nW, 1 μW, and 10 μW for the same Er concentration. Up to 55 dB gain is predicted for a launched signal power of 1 nW. Net gain over such long lengths is a direct result of low absorption of pump light due to selecting an optimized Er concentration, which avoids strong ground-state absorption. More important, it shows that the background losses in our waveguides obtained at both, the pump and signal wavelength, due to improved layer deposition, structuring method, and waveguide geometry are sufficiently low to exploit optical gain over such long lengths. Since in practical applications integrated amplifier lengths will probably be shorter than the 40-50 cm calculated in Fig. 4.14b, the obtained background losses can be considered as sufficiently low for the envisaged applications.

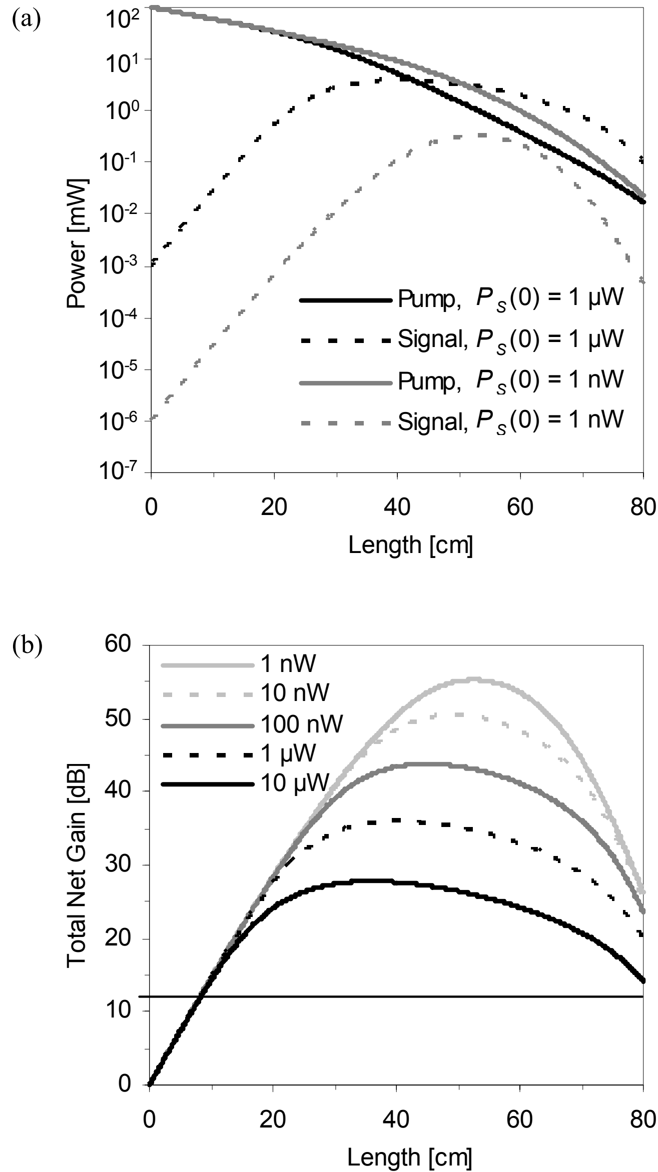

Fig. 4.14. (a) 977-nm pump and 1533-nm signal power and (b) total internal net gain vs. waveguide length for a launched pump power of 100 mW, Er concentration of 1.0× 10^{20} cm^{-3}, and varying launched signal power $P_S(0)$.

In addition to amplification at 1533 nm, where peak gain is observed, we are interested in gain over a wide wavelength range in order to exploit the broad gain spectrum observed in $Al_2O_3:Er^{3+}$. Accordingly, Fig. 4.15 shows the total gain predicted at the gain peak and at 1525 nm and 1565 nm, where the gain is smallest within the C-band, for an amplifier with Er concentration of 2.0 × 10^{20} cm^{-3} and launched pump power of 100 mW. The absorption and emission cross sections measured at 1525 nm and 1565 nm were substituted in each calculation. From these results, more than 20 dB gain is predicted across the entire C-band for an amplifier length of 24 cm. Assuming a bend radius of 300 µm, which is feasible due to the relatively high refractive index contrast between core and cladding (compared to other EDWA materials) in $Al_2O_3:Er^{3+}$ waveguides, such an amplifier could have a footprint as small as 6 × 6 mm^2 by applying a spiral design on the chip.

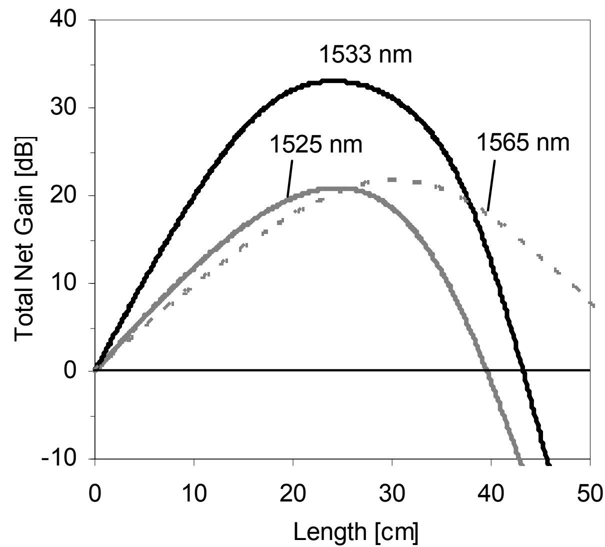

Fig. 4.15. Simulated total internal net gain vs. waveguide length for an Er concentration of 2.0×10^{20} cm^{-3}, launched signal power of 1 μW, launched pump power of 100 mW, and varying signal wavelength within the telecom C-band.

We are also interested in the gain at different pump powers, especially when several amplifiers may be required on the same chip and the available pump power has to be distributed efficiently between them. In Fig. 4.16a and b the total gain vs. length is shown for varying pump powers and Er concentrations of 1×10^{20} cm^{-3} and 2×10^{20} cm^{-3}, respectively. At a pump power of 20 mW, much higher gain can be achieved at a concentration of 1×10^{20} cm^{-3}. However, when the pump power is increased to 100 mW, similar total gain and a higher gain per unit length can be achieved for an Er concentration of 2×10^{20} cm^{-3}. Therefore the optimum Er concentration will depend on the available pump power and the application, which determines the gain required and the amplifier length.

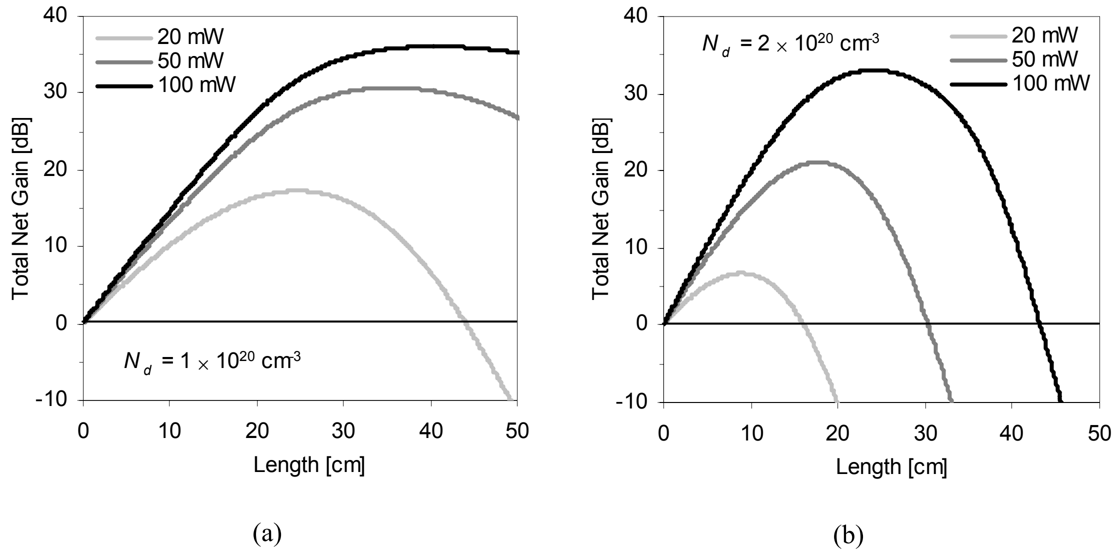

Fig. 4.16. Total gain vs. length for varying launched pump powers and an Er concentration of (a) 1×10^{20} cm^{-3} and (b) 2×10^{20} cm^{-3}.

Finally, the waveguide geometry has been mentioned as an important factor in achieving high gain. The emission and absorption probabilities, thus their rates, are proportional to the incident optical intensity (as opposed to the total optical power). Therefore, more compact pump and signal beams will result in higher optical intensities, higher rates, and sufficient population inversion and net gain at lower pump powers. In Fig. 4.17a, the gain vs. pump power is compared in 1-cm-long amplifiers with varying pump beam radii (0.2 to 5.0 μm) and signal beam radii (0.25 to 6.2 μm). The relative radius of the pump beam, signal beam and active medium are kept constant, in the same ratio as in Table 4.7 ($w_p / w_s / r_a = 1.15/1.39/1.46$). At lowest pump beam radius, the threshold pump power is less than 1 mW and net gain up to 2.4 dB/cm is predicted. As the radius is increased more pump power is required to achieve threshold, until finally pump powers higher than 100 mW are required for net gain with a pump radius of 5.0 μm in such a short 1-cm-long amplifier. In Fig. 4.17b, the gain is compared in 1-cm-long amplifiers with a constant pump and signal beam radius of 1.0 and 1.24, respectively, and varying active region radius, resulting in varying signal beam confinement factors (39% to 99%). The maximum net gain which can be achieved is dependent on the confinement factor, varying from 1.0 dB/cm at $\Gamma = 39\%$ to 2.1 dB/cm at $\Gamma > 87\%$. Of particular interest, the maximum possible gain remains constant when the confinement is increased beyond 87% for pump powers up to 100 mW. The threshold pump power increases only a small amount, from 2.5 to 6.5 mW, with higher confinement. It becomes clear based on these two figures that the waveguide design is critical in order to achieve high gain while minimizing the required pump power. In reality, when decreasing the pump and signal beam radius by decreasing the waveguide cross-sectional area, the confinement factor will also decrease (as demonstrated in the case of design I vs. design II). Based on Fig. 4.17a, with a pump radius of ~ 1.15 μm, design I is suitable for obtaining high gain with a reasonable threshold pump power, which supports our selection of such a design. However, we can also conclude based on the simulations presented here that an improvement in terms of threshold pump power is possible. For example, waveguide design II results in a pump beam radius of 0.60 μm, which means we can expect the threshold pump power to be ~5-10 times lower.

Therefore, by selecting a compromise between the two designs, for example more deeply etched ridge-type waveguides which reduce the lateral size of the optical mode compared to design I, the threshold pump powers can be improved, while maintaining a relatively high confinement factor and high gain.

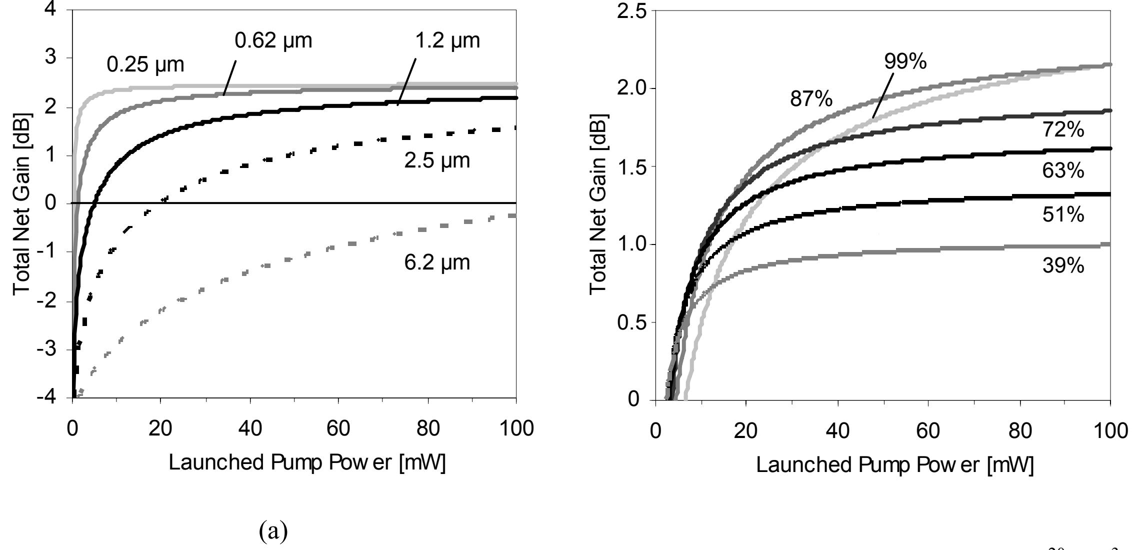

(a)

Fig. 4.17. Total gain vs. pump power for 1-cm-long amplifiers with an Er concentration of 2×10^{20} cm^{-3}. In (a) the pump beam radius w_P is varied from 0.2 to 5.0 µm and the signal beam radius w_S is varied from 0.25 µm to 6.2 µm (indicated). In (b) w_P and w_S are held constant at 1.0 µm and 1.24 µm, respectively, while the active region radius r_a is varied from $0.4w_S$ to $1.2w_S$ such that the pump confinement factor $\Gamma(\lambda_P)$ varies from 54% to 100% and the signal confinement factor $\Gamma(\lambda_S)$ varies from 39% to 99% (indicated).

4.6 Summary

$Al_2O_3:Er^{3+}$ optical amplifiers with different Er concentrations have been fabricated on oxidized silicon substrates. Due to an optimized deposition procedure, resulting in high $^4I_{13/2}$ lifetimes and low background losses, an improved waveguide design, and pumping at 977 nm, internal net gain of up to 2.0 dB/cm was measured at 1533 nm, thereby more than doubling the gain compared to previously published results. In addition, internal net gain was achieved over a bandwidth of 80 nm between 1500-1580 nm, with a maximum of 9.3 dB at the gain peak at 1533 nm in a 5.4-cm-long amplifier. For an optimized amplifier length and Er concentration, launched pump and signal powers of 100 mW and 1 µW, respectively, total gain of up to 33 dB is predicted at 1533 nm, while more than 20 dB gain is predicted across the entire telecom C-band. When avoiding gain saturation by reducing the launched signal power to 1 nW, even higher gain of 55 dB is predicted in a longer amplifier. The high net gain per unit length, large gain bandwidth, and high predicted total gain for low launched pump power demonstrate that $Al_2O_3:Er^{3+}$ qualifies as a competitive material for active integrated optical devices.

Chapter 5

Applications

In this chapter various novel applications of active $Al_2O_3:Er^{3+}$ waveguides are investigated and reported on. These include a zero-loss optical power splitter, high bit-rate amplification in an $Al_2O_3:Er^{3+}$ amplifier and an integrated ring laser.

5.1 Introduction

Previously, work on $Al_2O_3:Er^{3+}$ focused primarily on development of the material, particularly on the deposition methods. In two specific cases amplification was demonstrated in $Al_2O_3:Er^{3+}$ waveguides [34, 37], and simulations were applied which predicted higher gain in longer waveguides [140, 144]. In the case of [34], a novel spiral waveguide with wavelength division multiplexers (WDMs) were applied on the same chip, demonstrating a step towards high integration capability. However, fabrication reliability issues persisted and higher gain was not demonstrated. Hence no significant progress in terms of integrated optical devices or applications based on $Al_2O_3:Er^{3+}$ was made since that result.

In Chapters 2-3 of this thesis new $Al_2O_3:Er^{3+}$ fabrication methods were demonstrated that result in channel waveguides with low losses and provide high flexibility for integrated device design. In Chapter 4, significantly higher gain was achieved than previously shown in $Al_2O_3:Er^{3+}$, finally demonstrating the material to be a competitive gain medium. A model was also applied, which accurately described the gain results, and which can be applied to predict the behaviour in active devices. All of these results, when combined, put $Al_2O_3:Er^{3+}$ in a significantly improved position for its application in active on-chip devices.

In this chapter various applications are demonstrated. Each device or application is the first of its kind in $Al_2O_3:Er^{3+}$. The first application, presented in section 5.2, is a zero-loss splitter, whereby a signal on the chip is divided into two separate waveguides. The power reduction due to splitting is compensated for by amplification in $Al_2O_3:Er^{3+}$ waveguides with pump coupling achieved on the chip. The second application, described in section 5.3, is the demonstration of amplification of a 170 Gbit/s encoded 1550 nm signal. This result confirms the potential application of $Al_2O_3:Er^{3+}$ amplifiers in future high speed photonic integrated circuits. In addition to being the first transmission measurement in $Al_2O_3:Er^{3+}$ waveguides, it is the first time to our knowledge that 170 Gbit/s data transmission has been demonstrated in an EDWA. The third application, presented in section 5.4, is a fully-integrated $Al_2O_3:Er^{3+}$ ring laser. The laser produces several wavelengths over a 27-nm-range and could in future be applied as a tunable on-chip light source.

5.2 Design and Characterization of a Zero-Loss Splitter

5.2.1 Motivation

Integrated optical amplifiers allow for loss compensation within photonic circuits. Typically in such an integrated photonic circuit the optical signal power must be split into two or more separate branches, resulting in a 50% power decrease in each branch. In addition, any added losses such as scattering losses in the optical waveguides and losses in other integrated devices in front of the splitter should be compensated for.

In the past integrated Er-doped planar lossless splitters have been demonstrated in Er-doped silicate glass [20, 43, 59] and phosphate glass hosts [58, 60]. Net gain was measured over wavelength ranges of up to 16 nm for launched pump powers in excess of 100 mW. Compared to these other materials $Al_2O_3:Er^{3+}$ offers advantages due to its higher refractive index contrast, which allows for smaller bend radii and higher integration density. Its higher index contrast also reduces the waveguide cross-section,

resulting in higher pump intensities in the Er-doped waveguide core, thus lower pump power required for net gain. Furthermore, its broad emission spectrum allows for amplification and potentially lossless splitting over a wide wavelength range. In this section a fully integrated $Al_2O_3:Er^{3+}$ lossless power splitter, including WDM coupling of signal and pump light on-chip, is described.

5.2.2 Lossless Splitter Fabrication and Design

A 508-nm-thick $Al_2O_3:Er^{3+}$ film was deposited using the optimized growth recipe described in chapter 2 and a sputtering power of 12 W applied to the Er target. $Al_2O_3:Er^{3+}$ channel waveguides based on design II were prepared as described in chapter 3. The $Al_2O_3:Er^{3+}$ core height was 508 nm and the waveguide width was 1.5 µm. The waveguide width was inverse-tapered to 0.8 µm at the signal input and outputs to expand the guided mode and reduce fiber-chip coupling losses. A 5-µm-thick SiO_2 top-cladding layer was deposited by plasma-enhanced chemical vapour deposition, and end facets were prepared by dicing.

An illustration of the $Al_2O_3:Er^{3+}$ lossless splitter layout is shown in Fig. 5.1. The splitter design consists of two pump inputs in order to ensure sufficient pump power to excite the 8.6-cm-long $Al_2O_3:Er^{3+}$ waveguides. To facilitate this two couplers were applied which were designed to selectively couple signal light, while coupling minimal pump light (≤ 10%). The couplers and waveguides were designed for TE-polarized signal light and randomly polarized pump light. The lengths of the pump input sections in front of the couplers (2.3 mm) and the length of the bend section between the couplers (bend radius = 500 µm, length = 1.5 mm) were minimized to avoid pump absorption and reabsorption of signal light, respectively. The two pumped $Al_2O_3:Er^{3+}$ waveguide sections were folded so that the entire device fits in an area of 4.2 × 30 mm.

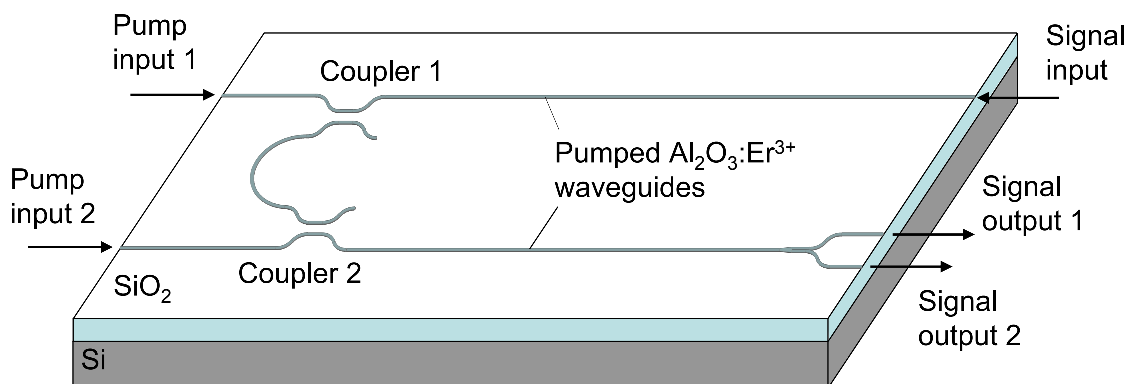

Fig. 5.1. Illustration of $Al_2O_3:Er^{3+}$ on-chip lossless splitter.

5.2.3 Experimental Results

In order to characterize the $Al_2O_3:Er^{3+}$ splitter separate optical loss measurements and signal enhancement measurements were carried out. The optical propagation losses were measured by launching signal light from a tunable laser source into straight waveguides on the same chip and analyzing the change in light intensity captured by an infrared camera [145]. The setup used to characterize the signal enhancement of the splitter is shown in Fig. 5.2. Fiber-array units (FAUs) were aligned simultaneously to

the input and output ports of the chip using piezoelectric computer-controlled stages. The FAUs consisted of Nufern UHNA3 fibers and standard 1550-nm single-mode fibers for the pump and signal inputs, respectively. 976-nm pump light from diode laser and Ti:Sapphire laser sources and modulated TE-polarized signal light from a tunable laser source (1500-1580 nm) were launched into the device. The output signal was coupled to an InGaAs detector followed by a lock-in amplifier to eliminate residual pump light and amplified spontaneous emission. The percentage of pump and signal power coupled from the fiber to the chip were determined separately using insertion loss measurements in straight channel waveguides.

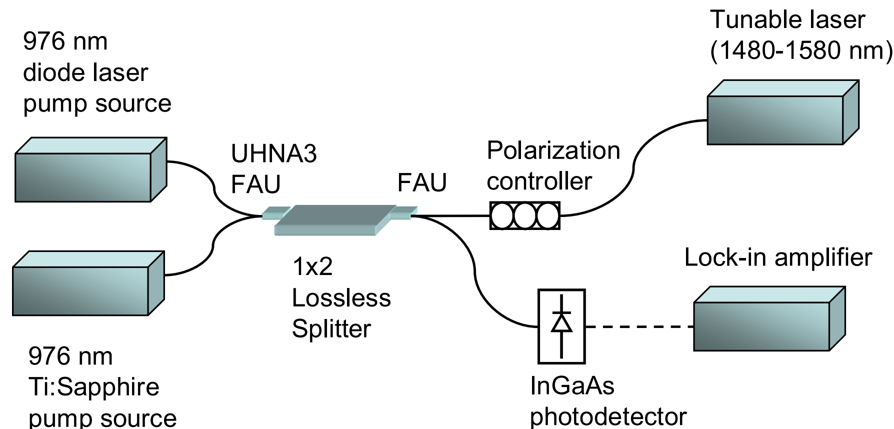

Fig. 5.2.Optical setup for characterizing Al_2O_3:Er^{3+} 1x2 power splitter.

The small-signal optical propagation loss for TE polarization was measured at different wavelengths in the range 1522 nm to 1568 nm. By plotting the data as a function of the known $^4I_{15/2} \rightarrow {}^4I_{13/2}$ absorption cross section at each wavelength and applying a linear fit, as shown in Fig. 5.3a, a signal-wavelength background propagation loss of 0.15 ± 0.06 dB/cm was determined (the y-intercept of the graph). Solving equation (4.11), where $\alpha_{Er}(\lambda)/\sigma_{abs}(\lambda)$ is the slope of the fit to the data, and $\Gamma(\lambda)$ was calculated to be 49% (assumed to be constant over the measured wavelength range), the Er concentration N_d was determined to be 1.3 ± 0.1 × 10^{20} cm^{-3}. The small-signal optical propagation loss was extrapolated over the wavelength range of interest using the absorption cross sections and is shown with the measured loss data in Fig. 5.3b.

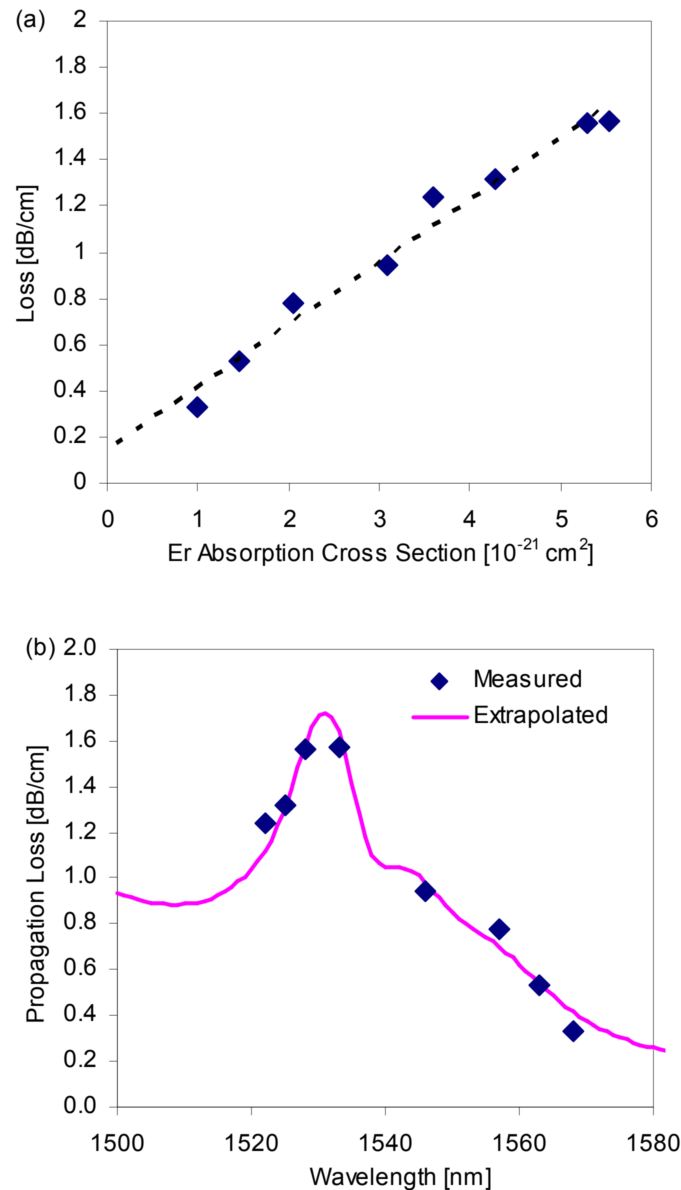

Fig. 5.3. (a) Measured small-signal propagation loss for TE polarization at different wavelengths plotted as a function of the $^4I_{15/2} \rightarrow {}^4I_{13/2}$ Er absorption cross section. (b) Measured and extrapolated propagation loss as a function of wavelength.

The total propagation loss determined for the unpumped splitter is shown as a function of wavelength in Fig. 5.4a. The losses include the total propagation loss calculated for the full splitter length, the losses at each coupler and the loss at the y-splitter. While the coupled power in the splitter device could not be measured directly, when measuring in separate devices the coupled power was found to be in agreement with the calculated power within ± 3 % (see chapter 3 of this thesis). Using the waveguide dimensions and wavelength-dependant refractive index corresponding to the Er concentration of the splitter, the percentage of coupled power was calculated to be >90% between 1500-1600 nm. The loss in each output branch of an identically designed

y-splitter was also measured in a separate device and found to be close to the ideal 3 dB (3.1 ± 0.5 dB, see also chapter 3).

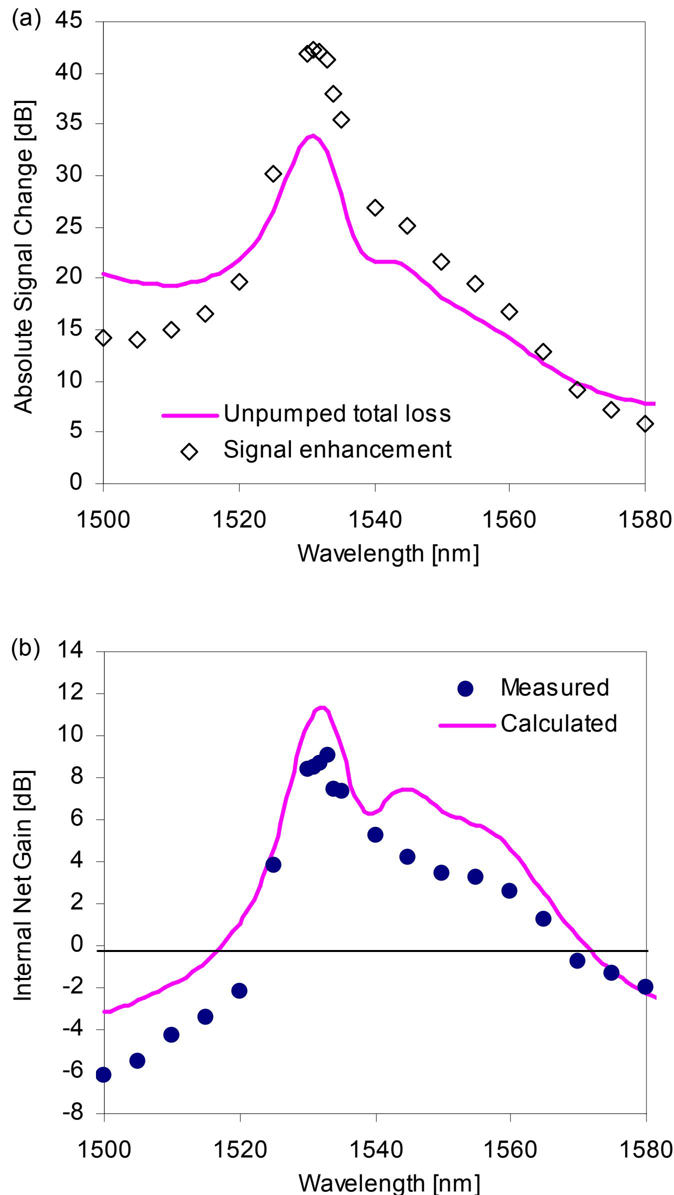

Fig. 5.4. (a) Total unpumped losses including propagation loss, coupler losses and splitter loss and measured signal enhancement when pumped; (b) realized net gain in each splitter output waveguide vs. wavelength and calculated net gain vs. wavelength for a pump power of 15 mW launched into each pumped waveguide.

In the same figure, the measured signal enhancement is shown for incident pump powers of 130 mW and 89 mW at pump inputs 1 and 2, respectively. Based on the insertion loss measurements it was determined that approximately 27 mW and 19 mW were launched into each waveguide. However, because the waveguides are multimode at the pump wavelength, resulting in higher losses compared to the signal wavelength, and because approximately 10% of pump power was lost due to coupling at each

directional coupler, less pump power was actually launched into each of the amplifying sections than was coupled into the chip. Approximately 1 μW of signal power was launched into the chip to ensure the signal enhancement measurement was within the small signal limit. By subtracting the total loss from the measured signal enhancement, the net gain was calculated per output branch of the splitter and is shown in Fig. 5.4b. Net gain of up to 9.0 dB and over a wavelength range of 1525 to 1565 nm, covering the entire C-band, was achieved.

Using the rate-equation model applied in chapter 4 and the experimental parameters determined here the total gain was calculated for a pump power of 15 mW launched into each amplifying branch of the device. The parameters used in the simulation are summarized in Table 5.1 (where different from those shown in Table 4.7). A pump background loss of 0.24 dB/cm was assumed based on previous measurements in single-mode waveguides. The net calculated gain is also shown in Fig. 5.4b. In this ideal case lossless splitting is predicted over a wavelength range of 53 nm. Applying a similar design with two additional y-splitters at each signal output it would be possible to fabricate a 1×4 splitter. Based on the calculated gain displayed in Fig. 5.4b, and assuming an additional loss of 3 dB introduced by the extra splitter, net gain is predicted over a wavelength range of 40 nm in such a device. Similarly, lossless splitting is predicted over 25 nm (1527-1552 nm) in the ideal case for a 1×8 configuration.

Table 5.1. Parameters used in $Al_2O_3:Er^{3+}$ 1×2 splitter calculation.

Parameter	Symbol	Value	Unit
Amplifier length	L	8.6	[cm]
Radius, pump focus	w_P	0.59	[μm]
Radius, signal focus	w_S	0.82	[μm]
Confinement factor, pump wavelength	$\Gamma(\lambda_P)$	73	[%]
Confinement factor, signal wavelength	$\Gamma(\lambda_S)$	49	[%]
Radius, active medium	r_a	0.58 w_S	[μm]
Er concentration	N_d	1.3	[10^{20} cm^{-3}]
Fluorescent lifetime	τ_1	7.3	[ms]
ETU parameter	W_{ETU}	4.6	[10^{-18} cm^3/s]
Background loss pump	$\alpha_{Loss}(\lambda_P)$	0.24	[dB/cm]
Background loss signal	$\alpha_{Loss}(\lambda_S)$	0.15	[dB/cm]

Improvements in the current splitter design are possible. A single pump input followed by a splitter on-chip would minimize the number of fiber-chip connections. In addition, it is possible to design highly polarization insensitive waveguides [146], which could lead to polarization insensitive lossless splitting. Finally, while the gain achieved here is rather flat, in the ideal case there is a large variation in gain vs. wavelength. The length of the un-pumped device section between the two couplers could be tailored to flatten the amplifier response.

5.2.4 Conclusions

A broadband on-chip 1×2 lossless power splitter applying integrated $Al_2O_3:Er^{3+}$ waveguide amplifiers has been demonstrated. Loss compensation was demonstrated over a wavelength range of 40 nm (1525-1565 nm). Using a similar design, calculations predict a 1×4 lossless splitter over the same wavelength range when launching a total of 30 mW into the amplifying sections of the splitter.

5.3 High Bit Rate Transmission in an $Al_2O_3:Er^{3+}$ Amplifier

5.3.1 Motivation

One of the key driving forces behind integrated optics, and particularly silicon photonics, is the potential for higher data transmission rates compared to integrated electronic circuits [147]. Data rates as high as 160 Gbit/s have been demonstrated in long-haul optical fiber networks and in the future transmission at this speed can also be expected at the chip level [148]. In such integrated photonic circuits, several enabling elements would be required, including an amplifier to boost the optical signal at various stages. Semiconductor optical amplifiers (SOAs) are well established as packaged components. However fabrication of such devices is complex, requiring many processing steps, and for incorporation of a SOA between silicon-based passive components hybrid integration methods are required. In addition, due to their short carrier lifetimes of ~50 ps, when they are operated in the saturated or quasi-saturated gain regime SOAs exhibit transient gain suppression and recovery which is dependent on both the bit rate and the bit sequence [149]. This can result in cross-talk between different wavelength channels when amplifying wavelength division multiplexed (WDM) signals. Alternatively, planar erbium-doped waveguide amplifiers (EDWA) offer a potential solution for amplification at high speed on a chip [18]. Er-doped amplifiers with their long excited-state lifetime of ~10 ms and accordingly longer gain recovery time do not exhibit such transient channel cross-talk. EDWAs can be deposited directly on thermally oxidized silicon or other materials allowing all-optical signal enhancement with a straightforward process flow [150]. In the past, transmission experiments at up to 10 Gbit/s using an EDWA have been carried out [25, 41, 121] and a packaged photoreceiver using an EDWA for 40 Gbit/s applications has also been reported [151]. In this section amplification at 170 Gbit/s is demonstrated in an $Al_2O_3:Er^{3+}$ EDWA.

5.3.2 $Al_2O_3:Er^{3+}$ Channel Waveguide Gain

A 5.7-cm-long $Al_2O_3:Er^{3+}$ straight channel waveguide amplifier was fabricated based on device design I (see Chapter 3). The waveguide dimensions were 0.9 μm × 4.0 μm with an etch depth of approximately 50 nm. The uncladded waveguide was single mode at wavelengths of 1480 nm and above. The doping concentration, uniform throughout the $Al_2O_3:Er^{3+}$ core layer, was 2.1×10^{20} cm^{-3}.

Prior to transmission experiments, the continuous-wave small-signal gain of the amplifier was measured at 1532 nm (the $^4I_{13/2} \rightarrow {}^4I_{15/2}$ Er transition gain peak) and 1550 nm (the wavelength at which transmission experiments were performed). Pump light from a 1480 nm Raman laser source and signal light at 1532 nm or 1550 nm from a tunable laser were combined using a WDM fiber multiplexer (MUX) and coupled to and from the chip via lensed fibers [152]. Both microlensed fibers have a mode field

diameter 2.9 µm at $1/e^2$ of the intensity profile. This mode field diameter was selected as the best match to the asymmetric waveguide. At the output, the residual pump light and amplified spontaneous emission (ASE) were filtered using a 0.25 nm tunable bandpass filter and the signal power was measured with an optical power meter. Both co- and counter-propagating pump cases were investigated. The internal net small signal gain was calculated by subtracting the total propagation loss from the measured signal enhancement with pump on and pump off. The total small signal propagation loss was calculated at each wavelength using the known background loss of 0.13 dB/cm, calculated confinement of the signal light within the $Al_2O_3:Er^{3+}$ waveguide core (85%) and measured $^4I_{15/2} \rightarrow {}^4I_{13/2}$ absorption cross sections. The residual pump light and ASE were measured by shifting the bandpass filter 2 nm from the signal wavelength and determined to be negligible (> 20 dB lower than the amplified signal).

The resulting gain vs. pump power curves are shown in Fig. 5.5. The average gain for both TE- and TM-polarized signal light is shown, since similar signal enhancement was measured for each polarization (± 0.2 dB). In the co-propagating case, up to 11 dB total internal net gain at 1532 nm was measured for a launched pump power of 63 mW, while 6.6 dB gain was measured at 1550 nm. The threshold launched pump power for internal net gain was 4 mW and 3 mW at 1532 nm and 1550 nm, respectively. For a launched pump power of 65 mW constant internal net gain was measured when varying the launched signal power from 1 µW to 1 mW, demonstrating unsaturated gain for launched signal powers in this range. While high internal net gain was demonstrated, external fiber-chip-fiber net gain was not obtained, because the amplifier was designed for on-chip amplification, hence achieving low fiber-chip coupling loss was not considered in the design. However, with improved lensed fibers and appropriate waveguide design fiber-chip coupling losses on the order of 1 dB/facet are predicted, thus principally also allowing for fiber-chip-fiber net gain. The net internal gain measured at 1550 nm using a counter-propagating pump setup and the 170 Gbit/s modulated signal is also shown in Fig. 5.5. A higher threshold pump power is observed for counter-propagating pumping as compared to the co-propagating pump measurement. The difference in the two curves is probably due to a difference in pump coupling efficiency between the two lensed fibers. Net gain of up to 6.3 dB at 1550 nm was achieved in the counter-propagating setup when the launched pump power was increased to 110 mW.

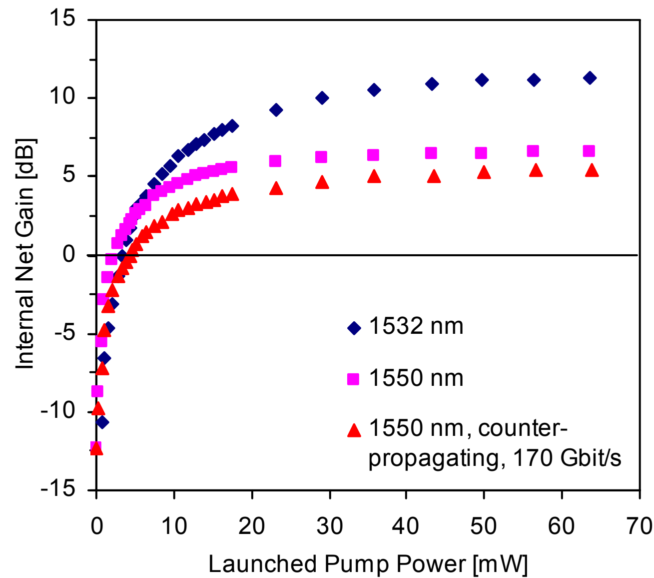

Fig. 5.5. Internal net small signal gain at 1532 nm and 1550 nm (for co-propagating pumping and counter-propagating pumping with 170 Gbit/s signal) as a function of launched 1480 nm pump power.

5.3.3 170 Gbit/s Transmission Measurements

Transmission experiments were performed at a bit rate of 170 Gbit/s on the PERSYST platform. The experimental setup is depicted schematically in Fig. 5.6. The transmitter was composed of a 42.5 GHz optical clock generated from a filtered and chirp-compensated quantum dash Fabry-Perot mode-locked laser source at 1550 nm [153, 154]. Following this, a $LiNbO_3$ Mach-Zehnder Interferometer (MZI) was modulated electronically by a pattern generator to obtain a 42.5 Gbit/s 2^7-1 return-to-zero pseudo-random bit sequence (PRBS). The transmitter ended with an optical time division multiplexing (OTDM) bit rate multiplier that multiplexed four delayed versions of the signal, resulting in a 170 Gbit/s data stream consisting of pulses with a full width at half maximum (FWHM) of 1.5 ps. An erbium-doped fiber amplifier (EDFA) was then used to boost the signal followed by an optical attenuator and polarization controller to adjust the amount of power and the polarization of the signal light coupled to the device, respectively. An optical isolator was used to eliminate any back-scattered pump or signal light. The 1550 nm 170 Gbit/s signal was coupled to and from the chip via the microlensed fibers. 1480 nm pump light from a Raman pump laser source was coupled to the chip in a counter-propagating approach using a fiber multiplexer (MUX). A reverse-pumping scheme was selected, because it simplified the transmission setup by eliminating the need for filtering of residual pump light in front of the receiver. The transmitted signal was amplified by an EDFA before entering the receiver part of the setup. The first part of the receiver was composed of a 170 to 42.5 Gbit/s optical demultiplexer and an optical clock recovery based on an electro-optic absorption modulator (EAM) and phase-locked loop. Following this, the signal light was detected by a 42.5 Gbit/s electrical time division demultiplexing receiver (ETDM). An optical sampling oscilloscope (with 1 ps resolution) was used for visualization.

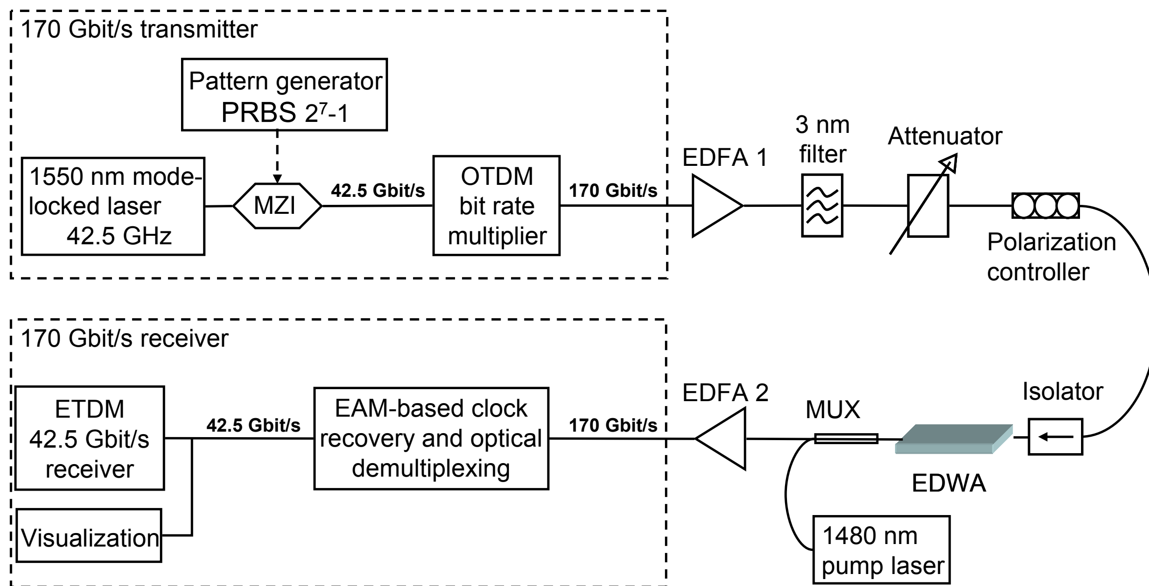

Fig. 5.6. Experimental setup for 170 Gbit/s transmission measurements.

In initial transmission experiments with a randomly polarized signal it was observed that two polarization modes were present. In order to investigate the polarization dependence of the amplifier, the differential group delay (DGD) between the fundamental TE and TM modes in the pumped and unpumped EDWA was measured using a continuous tunable laser source and a DGD analyzer. In both cases the DGD was found to be approximately 2 ps corresponding to a waveguide birefringence of ~7 x 10^{-3}. The impact of DGD on the 170 Gbit/s signal was also clearly observed on the eye diagram as shown in Fig. 5.7 (a-c), by varying the polarization controller state. This polarization dependence should not affect the system when used in a transmitter in a photonic integrated circuit, for instance, even though it would affect signal quality in an in-line use of the device. However, by careful design of the waveguides the birefringence can be largely reduced [146] so that polarization-independent amplification even at these bit rates can be obtained. For all bit error rate (BER) measurements a single polarization state was selected by adjusting the polarization controller on one fundamental mode. Typical eye diagrams without the EDWA and with the EDWA and a single polarization are shown in Fig. 5.8a and Fig. 5.8b, respectively. The eye pattern is open and the pulse FWHM is 2 ps in both cases.

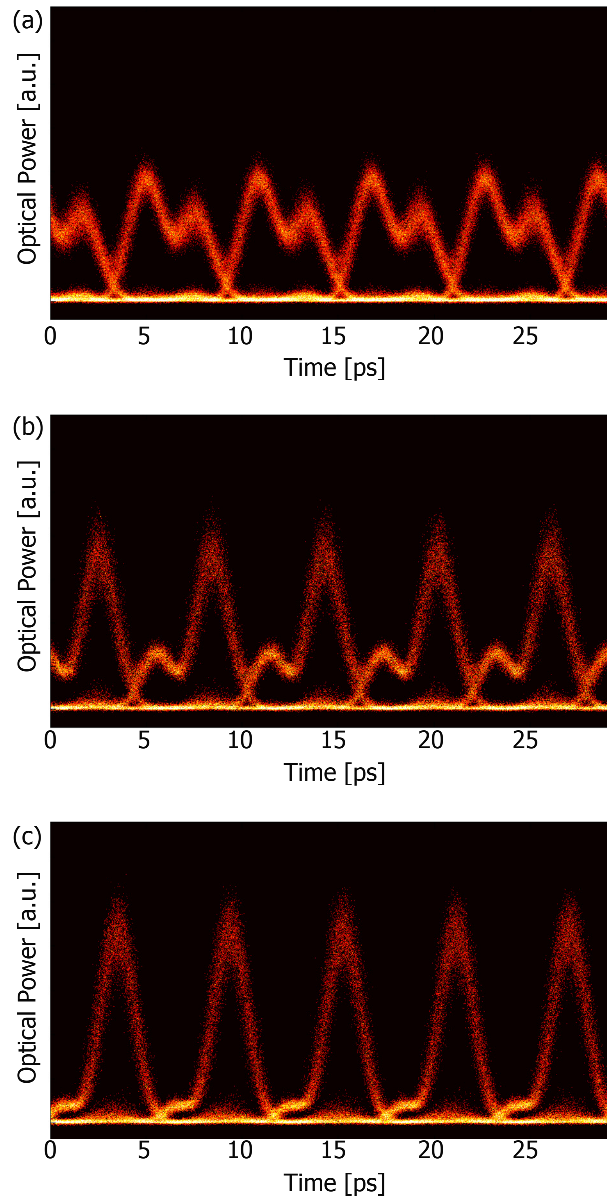

Fig. 5.7. Transmission eye diagrams for different polarization states of the 170 Gbit/s signal coupled to the EDWA. In each image two overlaid pulse trains are visible as a result of differential group delay between the fundamental TE and TM polarized modes supported by the EDWA. The input signal polarization state was adjusted such that in (a) both modes propagated with almost equal intensity, (b) one mode was more strongly excited, and (c) almost a single polarization mode was excited.

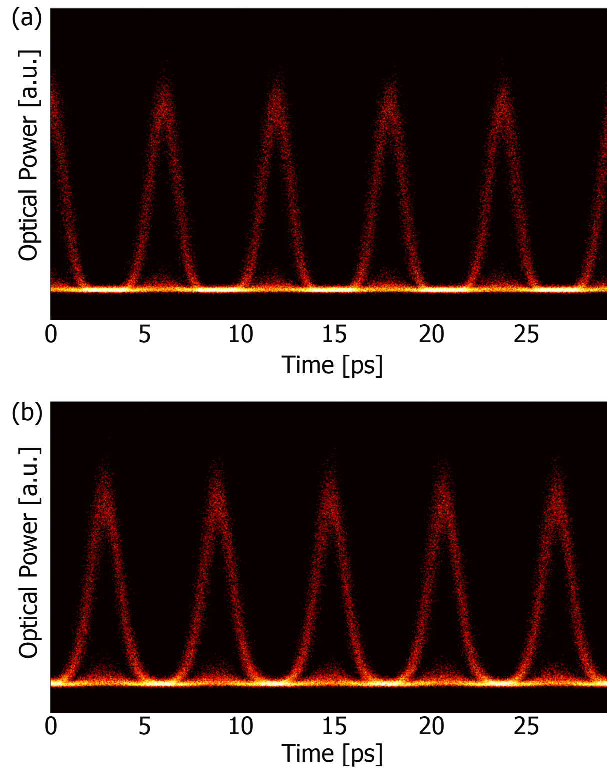

Fig. 5.8. Transmission eye diagrams at 170 Gbit/s (a) without EDWA and (b) with EDWA and a launched signal power of 0.5 mW and counter-propagating pump power of 65 mW.

In order to determine the compatibility of the device in a telecommunication application, BER assessments were performed on the device. The BER was measured as a function of the input power on the ETDM 42.5 Gbit/s receiver for 0.5 mW and 0.1 mW of signal power and a pump power of 65 mW launched into the EDWA. A reference was measured with the same input power in EDFA 2 as with the EDWA included in order to take into account the fiber-to-fiber losses (~10 dB when pumped) of the EDWA. The results are shown in Fig. 5.9. For each input signal power, the curve with the EDWA is superposed with the reference, showing that when the polarization state is properly adjusted, the EDWA does not add any penalty to the system. A minimum launched signal power of 0.1 mW was investigated in this setup in order to ensure sufficient power reached the receiver. However, based on the negligible ASE in the small signal gain measurements and with improved coupling losses, no penalties can also be expected in the EDWA for launched signal powers in the 1-10 µW range.

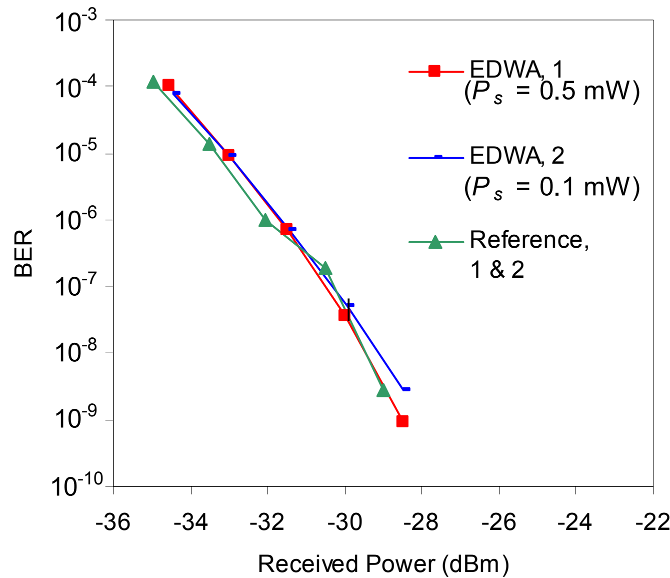

Fig. 5.9. 170 Gbit/s BER measurements for different launched signal powers P_s and a launched pump power of 65 mW as a function of the input power at the 42.5 Gbit/s receiver. A reference measurement with EDWA removed and identical optical power launched into the receiver is also shown.

5.3.4 Conclusions

Net internal gain of up to 11 dB at 1532 nm and data transmission at 170 Gbit/s at 1550 nm have been demonstrated in an integrated $Al_2O_3:Er^{3+}$ amplifier when pumping at 1480 nm. Despite a DGD of 2 ps between the two guided polarization modes of the amplifier, no BER power penalty was observed at 170 Gbit/s by injecting the signal in a single fundamental polarization state. The ability to amplify signals at high data rates, when combined with straightforward fabrication techniques and the possibility to integrate with various materials, confirm such amplifiers as potential components in future high-speed photonic integrated circuits.

5.4 Integrated $Al_2O_3:Er^{3+}$ Ring Laser

5.4.1 Motivation

Rare-earth-ion-doped dielectric lasers offer several potential advantages over semiconductor lasers, including higher stability, lower noise, narrower linewidth emission, broader wavelength tunability, and shorter laser pulses [27]. An integrated solution is desired, for combination with other photonic components on the same chip, offering high functionality at low cost. Such on-chip integrated lasers have potential applications in biophotonics, sensing, communications and space, and as femtosecond pulsed sources [72]. In particular, Er-doped waveguide lasers are of interest for their emission at wavelengths around 1.55 μm in the third telecommunication window. Several methods have been applied to achieve resonant structures and lasing in Er-doped planar waveguides, including distributed-Bragg-reflector (DBR) [67, 68], distributed-feedback (DFB) [69], and microdisk lasers [155]. Compared to DBR and DFB lasers a ring resonator laser offers a simple and straightforward solution, reducing the number and complexity of processing steps, while compared to a microdisk laser it

allows much more straightforward coupling of pump and signal in an integrated manner.

Previously rare-earth-ion-doped ring lasers have been demonstrated in SiO_2 [65, 156] and $LiNbO_3$ hosts [66]. $Al_2O_3:Er^{3+}$ offers several advantages compared with these materials. Compared to silica, it has a larger emission bandwidth, increasing the potential for tunability and generation of ultrashort pulses. In addition, its larger refractive index contrast allows for more compact devices and potentially reduces the laser threshold pump power due to a more tightly confined optical mode. As opposed to lithium niobate, it can be deposited on a number of substrates, including thermally oxidized silicon. This flexibility of deposition combined with its moderately high refractive index contrast could potentially allow monolithic integration of $Al_2O_3:Er^{3+}$ lasers with other optical waveguide platforms which are optimized for passive functions, such as silicon. The higher optical gain presented in chapter 4 opened the possibility for an integrated laser in this material.

In this section, the first integrated laser in $Al_2O_3:Er^{3+}$ is presented. The laser is based on a unique ring resonator design and by varying the degree of output coupling several laser wavelengths in the range 1530-1557 nm were demonstrated, exploiting the broad emission spectrum of this material.

5.4.2 Laser Fabrication and Design

The $Al_2O_3:Er^{3+}$ laser design was based on waveguide design II, presented in chapter 3. A 500-nm-thick $Al_2O_3:Er^{3+}$ layer was deposited on an 8-µm-thick thermally oxidized 10-cm-wide standard Si using the optimized recipe. A sputtering power of 11 W was applied to the Er target such that the resulting Er concentration was approximately 1×10^{20} cm^{-3}. Subsequently, 1.5-µm-wide channel waveguides were defined in the $Al_2O_3:Er^{3+}$ layer and an annealed 5-µm-thick SiO_2 top-cladding layer was deposited by plasma-enhanced chemical vapour deposition and end facets were prepared by dicing. The resulting channel waveguides were single-mode around 1550 nm for both TE and TM polarization and multimode at the 980-nm pump wavelength. The waveguide width was inverse-tapered to 0.8 µm at the signal output to increase the mode size and improve chip-fiber output coupling of the laser signal. In the same manner as described in section 5.2.3, the small-signal background propagation loss for TE polarization was determined to be 0.27 ± 0.04 dB/cm. The confinement factor for TE polarization was calculated to be 46%, and the Er concentration was determined to be $0.7 \pm 0.1 \times 10^{20}$ cm^{-3}.

A schematic of the $Al_2O_3:Er^{3+}$ ring laser is shown in Fig. 5.10. The ring cavity was designed such that a high Q-factor of the ring resonator is obtained when the ring coupler (Coupler 1 in Fig. 5.10) permits strong coupling. Such a directional coupler exhibits stronger coupling for longer wavelengths, i.e. for the laser wavelength in a Stokes-shifted emitting laser, while coupling at the shorter pump wavelength can be minimized in order to launch a significant part of the pump power into the ring. For our specific ring lasers strong coupling at the signal wavelength around 1550 nm of > 95 % for TE-polarization and weak coupling of < 10% at the pump wavelength of 980 nm was achieved. The coupler lengths were varied from 350 to 600 µm in increments of 50 µm. This was to ensure a range in which the out-coupled power and the total cavity roundtrip losses were sufficiently low for laser action. The resonator length was varied from 2.0 to 5.5 cm.

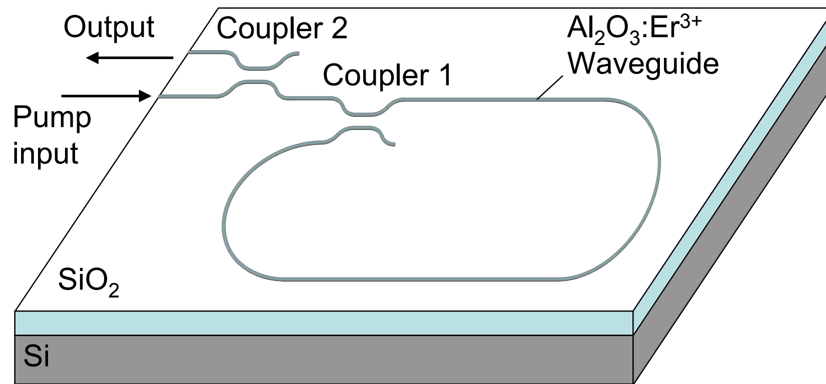

Fig. 5.10. Schematic of $Al_2O_3:Er^{3+}$ ring laser

5.4.3 Laser Measurements

In order to characterize the $Al_2O_3:Er^{3+}$ ring laser devices, a FAU which consisted of Nufern UHNA3 fibers to match the small optical mode size of the waveguides was aligned simultaneously to the input and output ports of the chip using piezoelectric computer-controlled stages. Pump light from a 980-nm diode laser was coupled to the chip through one fiber of the FAU. The output signal was collected in a second fiber of the FAU and the optical power was measured using a lightwave multimeter (Hewlett-Packard 8153A). The fiber-chip coupling losses were determined separately using insertion loss measurements in straight channel waveguides on the same chip. A small amount of back-reflected pump light was measured below the lasing threshold and subtracted from the total power measured at the multimeter to determine the output power of the laser. The laser spectra were measured using a spectrometer (Horiba Jobin Yvon iHR550).

The laser output power is shown as a function of launched pump power for devices with coupler lengths ranging from 400 to 550 µm and resonator lengths of 2.0, 3.0, and 5.5 cm in Fig. 5.11. The resonator length, coupler length, and main lasing wavelength are indicated. The highest slope efficiency of 0.11% was observed in a 5.5-cm-long resonator, with an output power of up to 9.5 µW measured at 19 mW launched pump power. The threshold pump power varied from 6.4 to 15.5 mW. This threshold power is significantly lower than those reported in previous Er-doped ring lasers [65, 66].

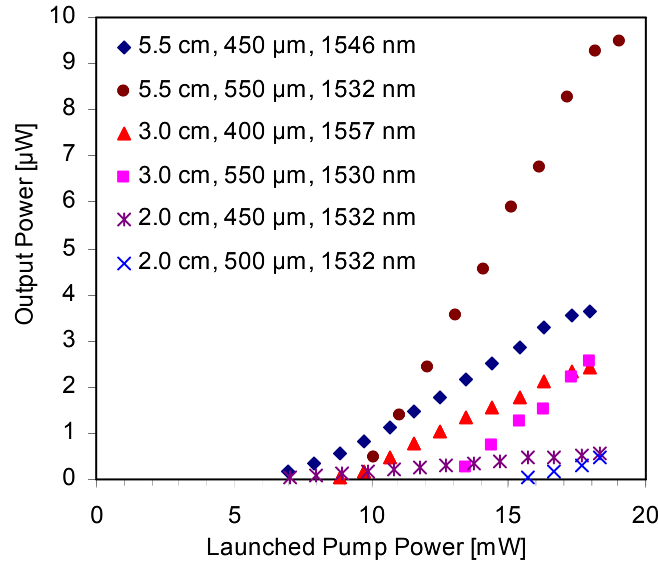

Fig. 5.11. On-chip integrated laser output power vs. pump power launched into the chip for varying resonator and output coupler length. The resonator length, coupler length, and main lasing wavelength are indicated.

Laser output spectra for three devices with different wavelengths are shown in Fig. 5.12. Because of the long resonator length, which results in a free spectral range of between 0.3 and 0.8 pm, the spectra include several longitudinal modes. Due to the limited resolution of the spectrometer (~0.1 nm), it is expected that many more longitudinal modes are present than are visible in the figure. In general, we expect the laser to select the wavelength and polarization with lowest threshold power, which is directly affected by the resonator roundtrip losses and the percentage of coupled power at Coupler 1. A greater amount of coupled power (designed to be more than 10 % higher for TE- as opposed to TM polarization in all the lasing devices) results in a lower total roundtrip loss and a lower lasing threshold. Accordingly, in Fig. 5.13 the predicted percentage of coupled power, calculated using commercial simulation software [142], is shown versus Coupler 1 length for the four observed main laser wavelengths and TE polarized light. Indeed, at a coupler length of 400 μm, a significantly higher percentage of coupled power is predicted at 1557 nm where lasing was observed. When the coupler length is increased to 550 μm, greater coupling is predicted at 1530 nm and 1532 nm, and the laser output shifts to these wavelengths. No lasing was observed in devices with coupler lengths of 350 μm and 600 μm, where the calculated coupled power was below 91 % and 94 %, respectively, for all the laser wavelengths. Besides the outcoupling degree, the emission cross section also determines the roundtrip gain. The most common lasing wavelength was close to 1532 nm, at the peak emission cross section of the $^4I_{13/2} \rightarrow {}^4I_{15/2}$ Er^{3+} transition [157]. The high gain per unit length at this wavelength makes it more likely that round-trip net gain is achieved in the cavity, and lasing is possible even for a lower degree of coupling at Coupler 1. The wavelength variation of the laser output is supported by the broadband gain observed [157]. By adjusting the coupling length of Coupler 1 in a single device, it would be possible to change the lasing wavelength, opening the possibility for a tunable laser source based on an adjustable output coupler.

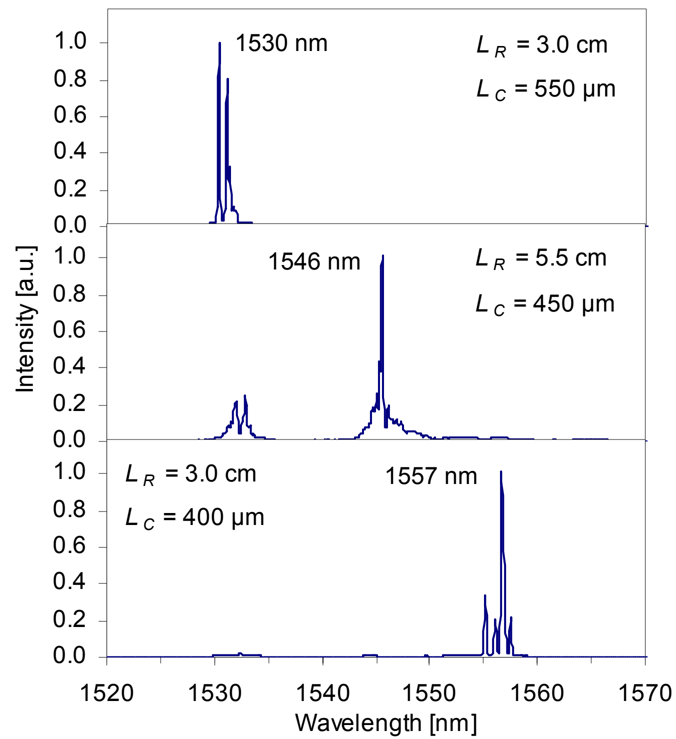

Fig. 5.12. Laser output spectra for coupler lengths L_C of 550, 450, and 400 µm and resonator lengths L_R of 3.0 and 5.5 cm. The peak lasing wavelength is indicated.

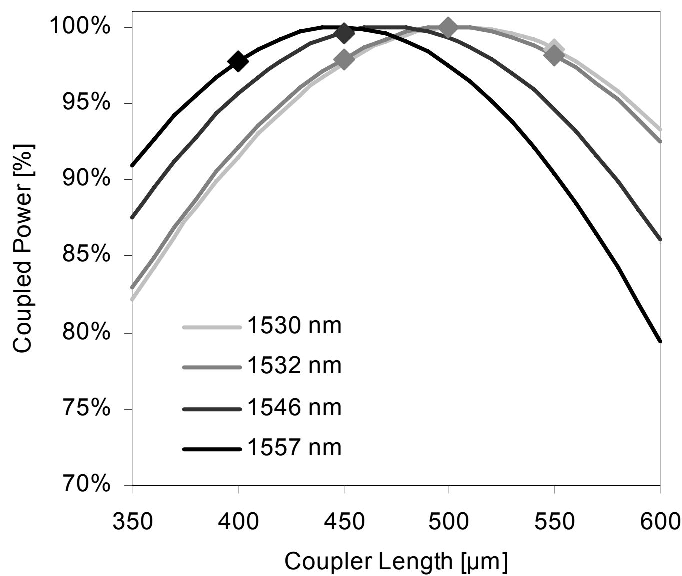

Fig. 5.13. Simulated coupled power in Coupler 1 vs. coupler length for the observed laser wavelengths and TE polarization. The coupler lengths for which lasing was observed are indicated by the diamonds on the curves.

Improvements of the current design are possible. The addition of Yb^{3+} as a co-dopant could optimize pump absorption, allowing smaller ring structures and reducing the number of longitudinal modes. Furthermore, in the design reported here, lasing is possible in both directions in the ring. To ensure that the entire lasing power is emitted in one direction, a loop mirror can be included in the lower arm of Coupler 1. Alternatively, a Bragg reflector element incorporated within the ring has been proposed [158]. Finally, in order to promote single-frequency operation, which is desirable for higher stability and is required for many applications, the addition of DFB elements within the ring are being investigated.

5.4.4 Conclusions

In conclusion, we have demonstrated the first $Al_2O_3:Er^{3+}$ laser to our knowledge. The laser is based on a novel ring-resonator design which allows strong coupling of pump light into the ring while simultaneously allowing only a small percentage of output coupling at the signal wavelength. Output powers of up to 9.5 µW were observed with threshold pump powers as low as 6.4 mW. Due to the broad gain spectrum in $Al_2O_3:Er^{3+}$, the output wavelength varied between 1530 to 1557 nm in devices with different output coupler lengths. With small design changes, coverage of the wavelength range of the entire telecom C-band from 1525 nm to 1565 nm seems feasible with this ring-laser design. The comparatively high refractive index contrast of the material allows the design of more compact ring lasers than shown here, results in low threshold pump power, and opens the potential for a tunable or ultrashort-pulse laser source integrated on a silicon substrate combined with passive silicon photonic devices for high functionality on a single chip.

5.5 Summary

Various novel active devices applying $Al_2O_3:Er^{3+}$ have been demonstrated. On-chip loss compensation was measured in a 2-way splitter over the wavelength range 1525-1565 nm. Signal transmission at a data rate of 170 Gbit/s and with no additional penalties was demonstrated in an $Al_2O_3:Er^{3+}$ amplifier at a wavelength of 1550 nm. Finally an $Al_2O_3:Er^{3+}$ integrated ring laser was realized with a slope efficiency and output power of up to 0.11% and 9.5 µW, respectively. By changing the output coupling, lasing at multiple wavelengths in the range 1530 nm to 1557 nm was demonstrated.

Chapter 6

Conclusions

In the course of this work $Al_2O_3:Er^{3+}$ *has been proven to be a material well-suited for integrated active device applications. In this chapter the main results of this thesis are summarized, conclusions are drawn and an outlook for future work is provided.*

In this thesis $Al_2O_3:Er^{3+}$ has been established as a viable platform for active integrated optical devices. Several specific aims, including developing reliable and high-quality fabrication methods and demonstrating higher gain in $Al_2O_3:Er^{3+}$ have been achieved. In addition, new devices and applications have been investigated and realized.

A new fabrication method for depositing $Al_2O_3:Er^{3+}$ thin films by reactive co-sputtering was developed, which was largely the work of K. Wörhoff. Investigations showed that the resulting thin films have high thickness uniformity, are uniformly doped and can be deposited over a large substrate area. Deposition can be carried out on thermally oxidized silicon wafers or other substrates. By adjusting the sputtering power to the metallic Er-target the Er concentration in the Al_2O_3 host material can be adjusted to within the useful range suitable for active devices. The films are highly transparent, having low background propagation losses from visible to infrared wavelengths.

In order to realize active devices in the $Al_2O_3:Er^{3+}$ films, a new method for etching $Al_2O_3:Er^{3+}$ waveguides by reactive ion etching was also developed. This method improves on prior techniques and results in channel waveguides with low additional optical propagation losses. The channel waveguide design was investigated based on issues such as pump and signal confinement within the active $Al_2O_3:Er^{3+}$ core and single-mode behaviour of pump and signal wavelengths. Using the new etching method various integrated test structures were defined and characterized. These included bent waveguides, y-splitters and directional couplers. Based on optical measurements, suitable designs were selected for active devices. Integrated waveguide devices were also fabricated in other active materials by applying undoped Al_2O_3 as an etch-mask material, and amplification and lasing was achieved in those materials by collaborators from the University of Hamburg, Germany.

The fabrication methods were applied to realize integrated $Al_2O_3:Er^{3+}$ channel waveguide amplifiers with varying Er concentrations. The amplifiers were investigated to determine various basic optical and spectroscopic properties, including the propagation losses, Er^{3+} absorption and emission cross sections and lifetimes. The optical gain around 1530 nm was measured when injecting 980 nm and 1480 nm pump light into the amplifiers. 980 nm pumping was found to facilitate higher Er^{3+} excitation, thus higher gain. The optimum Er^{3+} concentrations were determined and significantly higher optical gain of 2 dB/cm was measured compared to previous values reported in $Al_2O_3:Er^{3+}$. Using the optical and spectroscopic parameters a simplified rate-equation model was used to accurately describe the amplifier behaviour. The model was applied to predict the optimum amplifier length and investigate the influence of different parameters, such as the pump power and the waveguide cross-section. In future, this model can be applied in the design of active $Al_2O_3:Er^{3+}$ devices.

As the final portion of this work, various applications were demonstrated. An integrated optical power splitter was realized whereby $Al_2O_3:Er^{3+}$ waveguides were used to compensate for the optical losses. The device operates over a wide wavelength range of 40 nm. Lossless optical power splitting was also predicted over a wavelength range of 40 nm in a 1×4 splitter using a similar design. With a view towards future high-speed photonic circuits on a chip, transmission and amplification of a 170 Gbit/s encoded signal was measured in an $Al_2O_3:Er^{3+}$ amplifier. The amplifier was found to add little additional noise to the signal. Besides amplifiers, the first integrated

$Al_2O_3:Er^{3+}$ laser was demonstrated. The laser is based on a ring design and lasing was exhibited at several wavelengths over a wide range within the gain spectrum of $Al_2O_3:Er^{3+}$.

Based on the results reported in this thesis, $Al_2O_3:Er^{3+}$ can be considered as a competitive active medium for integrated optics. The reliable deposition and structuring methods and high gain allow for the design and realization of many new active devices and applications. The first steps in terms of devices and applications have been demonstrated in this work. Further improvements in terms of the device designs, for example reducing pump power requirements, increasing the lasing efficiency and realizing single-frequency, directly on-chip tunable, and short-pulse laser output, are possible and will enable a wide range of new devices.

Co-doping the material with Yb^{3+} ions for increased resonant pump absorption near 980 nm and subsequent energy transfer of the excitation energy to Er^{3+} ions will be necessary for achieving significantly shorter device lengths and, hence, higher integration density. Space-selective doping methods and integration of passive and active devices within $Al_2O_3/Al_2O_3:Er^{3+}$ waveguides or using $Al_2O_3:Er^{3+}$ in combination with other integrated optical materials are on the horizon, albeit more difficult to realize owing to involved material fabrication issues. Integration of $Al_2O_3:Er^{3+}$ amplifiers and laser sources with silicon photonic waveguides, which provide a high level of passive functionality, is currently investigated. This integration, which will add active functionality to the world of silicon photonics in a monolithically integrated manner, is highly promising. In future, $Al_2O_3:Er^{3+}$ amplifiers and lasers can be applied to provide much-needed active functionality in integrated photonic circuits for a wide variety of applications.

Appendix

```
% Erbium-doped aluminum oxide amplifier calculation
% Uses 3-level rate-equation model to simulate population densities
% and output of Erbium-doped Al2O3 amplifier pumped at 977 nm
% Jon Bradley
% 25/06/2009
%======================================================================
% Constants etc.
format short;
close all;
clear all;
clc;
h = 6.626068e-34;             % Planck's constant, m^2kg/s
c = 299792458.;               % Speed of light, m/s
e = 2.718281828;              % e
pi = 3.141592654;             % Pi
%======================================================================
% Amplifier Variables
N_d = 2.0e20;                 % Erbium ion concentration, cm^-3
sigma_e_s = 5.7e-21;          % Emission cross section, signal, cm^2
sigma_a_s = 5.7e-21;          % Absorption cross section, signal,
cm^2
sigma_e_p = 2.0e-21;          % Emission cross section, pump, cm^2
sigma_a_p = 2.0e-21;          % Absorption cross section, pump, cm^2
sigma_esa_p = 0.8e-21;        % Excited state absorption cross
section, pump, cm^2
W_ETU = 6.0e-18;              % Energy transfer upconversion
parameter from level 1, cm^3s^-1
tau_1 = 7.1e-3;               % First excited state lifetime, s
tau_2 = 100.0e-6;             % Second excited state lifetime, s
L = 1.0;                      % Amplifier length, cm
alpha_s = 0.11;               % Background absorption, signal, dB/cm
alpha_p = 0.17;               % Background absorption, pump, dB/cm
PL_s = 0.001;                 % Launched signal power, mW
PL_p_max = 100.0;             % Maximum launched pump power, mW
w_s = 1.39;                   % 1/e^2 radius of Gaussian signal
beam, µm
w_p = 1.15;                   % 1/e^2 radius of Gaussian pump beam,
µm
lambda_s = 1533.;             % Signal wavelength, nm
lambda_p = 977.;              % Pump wavelength, nm
%======================================================================
a_s = alpha_s/4.34294482;     % Absorption coefficient, signal, cm^-
1
a_p = alpha_p/4.34294482;     % Absorption coefficient, pump, cm^-1
%======================================================================
r_active = 1.05*w_s;          % Calculate radius of active medium
based on confinement
%======================================================================
NumPumpPowers = 400;          % Number of pump powers in gain vs.
pump power simulation
%======================================================================
length_simulation = 0;        % 1 = gain vs. amplifier length
calculation, 0 = gain vs. pump power calculation
```

```
Upconversion_yes = 1;            % Set to 1 if include upconversion in
3-level model
ESA_yes = 1;                     % Set to 1 if include excited state
absorption in 3-level model
%======================================================================
% Simulation, assuming a three level system, Gaussian profiles of pump
and signal:
%======================================================================
% Initialize longitudinal discretizations of optical power, photon
flux and population densities:
Xnum = 20;                       % Number of discretizations in the
radial direction
dZ = 0.01;                       % Longitudinal step size, cm
Znum = L/dZ;                     % Number of discretizations in the
longitudinal direction
dX = r_active/(Xnum-1);          % Radial step size, µm
P_s = zeros(Xnum,Znum+1);        % Initialize array for signal power in
the waveguide, mW
P_p = zeros(Xnum,Znum+1);        % Initialize array for pump power in
the waveguide, mW
phi_s = zeros(Xnum,Znum);        % Initialize array for photon flux,
signal, cm^-2*s^-1
phi_p = zeros(Xnum,Znum);        % Initialize array for photon flux,
pump, cm^-2*s^-1
N_0 = N_d.*ones(Xnum,Znum);      % Fill array in X and Z direction of
ground state population density, cm^-3
N_1 = zeros(Xnum,Znum);          % Fill array in X and Z direction of
population density of first excited level, cm^-3
N_2 = zeros(Xnum,Znum);          % Fill array in X and Z direction of
population density of second excited level, cm^-3
dA = zeros(Xnum,1);              % Fill array in X direction of areas
of cylindrical rings, µm^2
P_s_confined = 0;                % Variable for tallying amount of
signal power confined in active layer, mW
P_p_confined = 0;                % Variable for tallying amount of pump
power confined in active layer, mW
%======================================================================

% Initialize area elements and input pump and signal power arrays
for k =1:(Xnum-1)
 dA(k,1) = pi*(dX*k)^2-pi*(dX*(k-1))^2;
 P_s(k,1) = PL_s*(1-e^(-2*(k*dX)^2/w_s^2))-PL_s*(1-e^(-2*((k-
1)*dX)^2/w_s^2));
 P_p(k,1) = PL_p_max*(1-e^(-2*(k*dX)^2/w_p^2))-PL_p_max*(1-e^(-2*((k-
1)*dX)^2/w_p^2));
 P_s_confined = P_s_confined + P_s(k,1);
 P_p_confined = P_p_confined + P_p(k,1);
end

% Initialize outer element of each power array, accounting for
r_active to infinity, to include rest of power which is outside the
active region and does not contribute to population dynamics
P_s(Xnum,1) = PL_s-P_s_confined;
P_p(Xnum,1) = PL_p_max-P_p_confined;

% Display percentage of pump and signal power confined in the active
region
disp(['Percentage signal power confined in active region =
',num2str(P_s_confined/PL_s)]);
```

```
disp(['Percentage pump power confined in active region =
',num2str(P_p_confined/PL_p_max)]);

% If gain vs. length simulation, initialize variables to store the
length, inversion fraction at the center of the waveguide, average
inversion fraction in the active region, average population densities,
pump and signal absorption and emission rates, ETU, spontaneous
emission, ESA and background absorption rates and gain at each length
if length_simulation == 1
 NumPumpPowers=1;
 LengthArray = zeros(Znum,1);
 InversionCenter = zeros(Znum,1);
 InversionAverage = zeros(Znum,1);
 N2Average = zeros(Znum,1);
 N1Average = zeros(Znum,1);
 N0Average = zeros(Znum,1);
 RabsPAverage = zeros(Znum,1);
 RemPAverage = zeros(Znum,1);
 RabsSAverage = zeros(Znum,1);
 RemSAverage = zeros(Znum,1);
 RETUAverage = zeros(Znum,1);
 Rspont2Average = zeros(Znum,1);
 Rspont1Average = zeros(Znum,1);
 RESAAverage = zeros(Znum,1);
 RBackgroundPAverage = zeros(Znum,1);
 RBackgroundSAverage = zeros(Znum,1);
 GainLength = zeros(Znum,1);
 counter = 1;
 % If gain vs. length simulation, display headings of output
parameters
 disp(['Length [cm]  Pump Power [mW] Signal Power [mW]   N2 [cm^-3]
N1 [cm^-3]  N0 [cm^-3]  Average Inversion [%]   Inversion at Center
[%]    Gain [dB]   Pump Abs Rate [cm-3s-1] Pump Em Rate [cm-3s-1]
Sig. Abs Rate [cm-3s-1] Sig. Em Rate [cm-3s-1]  ETU Rate [cm-3s-1]
Level 2 Spont Em Rate [cm-3s-1] Level 1 Spont Em Rate [cm-3s-1] Pump
ESA Rate [cm-3s-1] Pump Background Abs. Rate [cm-3s-1] Signal
Background Abs. Rate [cm-3s-1]']);
else
 % If gain vs. launched pump power simulation, display headings of
output parameters
 disp(['Launched Pump Power [mW]     Output Pump Power [mW]  Output
Signal Power [mW]    Gain [dB]']);
end

% Initialize variables to store total pump and signal power at each Z
step and for each launched pump power and variables to store total
gain, gain/cm, launched pump power, and output pump and signal power
for each launched pump power
P_p_Total = zeros(Znum+1,NumPumpPowers+1);
P_s_Total = zeros(Znum+1,NumPumpPowers+1);
Gain = zeros(1, NumPumpPowers+1);
Gain_percm = zeros(1, NumPumpPowers+1);
P_pStart = zeros(1, NumPumpPowers+1);
P_pEnd = zeros(1, NumPumpPowers+1);
P_sEnd = zeros(1, NumPumpPowers+1);

% Main loop for incrementing launched pump power and solving for
output signal power, gain etc.
if length_simulation == 1
 loops = NumPumpPowers;
```

```
else
 loops = NumPumpPowers+1;
end
for j=1:loops

 % Establish total signal and pump power at the input and fill
launched pump power array (the launched signal array is constant).
 P_s_Total(1,j) = PL_s;
 if length_simulation == 1
  P_p_Total(1,j) = PL_p_max;
 else
  P_p_Total(1,j) = PL_p_max/NumPumpPowers*(j-1);
 end
 P_p_confined = 0;
 for k =1:(Xnum-1)
  P_p(k,1) = P_p_Total(1,j).*(1-e^(-2*(k*dX)^2/w_p^2))-
P_p_Total(1,j).*(1-e^(-2*((k-1)*dX)^2/w_p^2));
  P_p_confined = P_p_confined + P_p(k,1);
 end
 P_p(Xnum,1) = P_p_Total(1,j)-P_p_confined;

  % Second loop for solving rate equations along amplifier length
  % by propagating in Z direction and solving population density
  % equations at each Z step:
  % Fill signal and pump power arrays at each Z step, redistributing
  % the total power remaining from the previous step in a Gaussian
  for m=1:Znum

   % Third loop for solving rate equations in radial direction:
   for i=1:Xnum-1

    % Photon fluxes (in cm^-2*s^-1):
    phi_s(i,m) = P_s(i,m).*1e-3.*lambda_s.*1e-9./(dA(i,1)*1e-
12*h*c)*1e-4;
    phi_p(i,m) = P_p(i,m).*1e-3.*lambda_p.*1e-9./(dA(i,1)*1e-
12*h*c)*1e-4;

    % Solve for population densities in section:
    if(Upconversion_yes==1)
    % 1) Using analytical solutions to population densities, including
upconversion
    CONST = 1./(1/tau_2+sigma_e_p.*phi_p(i,m)+sigma_a_p.*phi_p(i,m));
    QuadC = sigma_a_s.*phi_s(i,m).*N_d+(1/tau_2-
sigma_a_s.*phi_s(i,m)).*CONST.*sigma_a_p.*phi_p(i,m).*N_d;
    QuadB = -
(1/tau_1+sigma_e_s.*phi_s(i,m)+sigma_a_s.*phi_s(i,m)+(1/tau_2-
sigma_a_s.*phi_s(i,m))*CONST.*sigma_a_p.*phi_p(i,m));
    QuadA = (1/tau_2-sigma_a_s.*phi_s(i,m))*CONST.*W_ETU-2*W_ETU;
    N_1(i,m) = (-QuadB-sqrt(QuadB^2-4*QuadA*QuadC))/(2*QuadA);
    N_2(i,m) = CONST.*(sigma_a_p.*phi_p(i,m).*(N_d-
N_1(i,m))+W_ETU.*N_1(i,m)^2);
    N_0(i,m) = N_d-N_1(i,m)-N_2(i,m);
    else
    % 2) Using analytical solutions to population densities, without
upconversion
    CONST =
sigma_a_p.*phi_p(i,m)./(1/tau_2+sigma_e_p.*phi_p(i,m)+sigma_a_p.*phi_p
(i,m));
```

```
    N_1(i,m) =
(sigma_a_s.*phi_s(i,m).*N_0(i,m)+1/tau_2*CONST*N_d)/(1/tau_1+sigma_e_s
.*phi_s(i,m)+1/tau_2*CONST);
    N_2(i,m) = CONST.*(N_d-N_1(i,m));
    N_0(i,m) = N_d-N_1(i,m)-N_2(i,m);
    end;

    % Power remaining after propagation through section in each radial
element:
    P_s(i,(m+1)) = P_s(i,m).*e^((sigma_e_s.*N_1(i,m)-
sigma_a_s.*N_0(i,m)-a_s).*dZ);
    if(ESA_yes==1)
    P_p(i,(m+1)) = P_p(i,m).*e^((sigma_e_p.*N_2(i,m)-
sigma_esa_p.*N_2(i,m)-sigma_a_p.*N_0(i,m)-a_p).*dZ);
    else
    P_p(i,(m+1)) = P_p(i,m).*e^((sigma_e_p.*N_2(i,m)-
sigma_a_p.*N_0(i,m)-a_p).*dZ);
    end;
    % Total power remaining in active region after propagation through
section:
    P_s_Total(m+1,j) = P_s_Total(m+1,j) + P_s(i,m+1);
    P_p_Total(m+1,j) = P_p_Total(m+1,j) + P_p(i,m+1);
    % If gain vs. length simulation, add inversion fractions,
population densities and rates in each radial element for calculating
average values after loop:
    if length_simulation == 1
     InversionAverage(m,1) = InversionAverage(m,1) +
N_1(i,m)./(N_0(i,m)+N_1(i,m));
     N2Average(m,1) = N2Average(m,1) + N_2(i,m);
     N1Average(m,1) = N1Average(m,1) + N_1(i,m);
     N0Average(m,1) = N0Average(m,1) + N_0(i,m);
     RabsPAverage(m,1) = phi_p(i,m).*sigma_a_p.*N_0(i,m);
     RemPAverage(m,1) = phi_p(i,m).*sigma_e_p.*N_2(i,m);
     RabsSAverage(m,1) = phi_s(i,m).*sigma_a_s.*N_0(i,m);
     RemSAverage(m,1) = phi_s(i,m).*sigma_e_s.*N_1(i,m);
     RETUAverage(m,1) = W_ETU.*N_1(i,m).*N_1(i,m);
     Rspont2Average(m,1) = N_2(i,m)./tau_2;
     Rspont1Average(m,1) = N_1(i,m)./tau_1;
     RESAAverage(m,1) = phi_p(i,m).*sigma_esa_p.*N_2(i,m);
     RBackgroundPAverage(m,1) = phi_p(i,m).*a_p;
     RBackgroundSAverage(m,1) = phi_s(i,m).*a_s;
    end

   end  % End of third loop (radial direction)

   % Power outside the active region sees only the background loss:
   P_s(Xnum, (m+1)) = P_s(Xnum,m).*e^(-a_s.*dZ);
   P_p(Xnum, (m+1)) = P_p(Xnum,m).*e^(-a_p.*dZ);
   % Add the power outside the active region to total power at Z = m+1
propagation distance:
   P_s_Total((m+1),j) = P_s_Total((m+1),j) + P_s(Xnum,(m+1));
   P_p_Total((m+1),j) = P_p_Total((m+1),j) + P_p(Xnum,(m+1));

    % If gain vs. length simulation calculate average inversion
fraction, population densities and rates at each longitudinal step:
   if length_simulation == 1
    LengthArray(m,1) = m*dZ;
    InversionCenter(m,1) = N_1(1,m)./(N_0(1,m)+N_1(1,m));
    InversionAverage(m,1) = InversionAverage(m,1)./(Xnum-1);
    N2Average(m,1) = N2Average(m,1)./(Xnum-1);
```

```
    N1Average(m,1) = N1Average(m,1)./(Xnum-1);
    N0Average(m,1) = N0Average(m,1)./(Xnum-1);
    RabsPAverage(m,1) = RabsPAverage(m,1)./(Xnum-1);
    RemPAverage(m,1) = RemPAverage(m,1)./(Xnum-1);
    RabsSAverage(m,1) = RabsSAverage(m,1)./(Xnum-1);
    RemSAverage(m,1) = RemSAverage(m,1)./(Xnum-1);
    RETUAverage(m,1) = RETUAverage(m,1)./(Xnum-1);
    Rspont2Average(m,1) = Rspont2Average(m,1)./(Xnum-1);
    Rspont1Average(m,1) = Rspont1Average(m,1)./(Xnum-1);
    RESAAverage(m,1) = RESAAverage(m,1)./(Xnum-1);
    RBackgroundPAverage(m,1) = RBackgroundPAverage(m,1)./(Xnum-1);
    RBackgroundSAverage(m,1) = RBackgroundSAverage(m,1)./(Xnum-1);
    GainLength(m,1) = 10*log10(P_s_Total((m+1),j)./PL_s);
    % If gain vs. length simulation, display propagation distance,
total pump and signal power, population densities, average inversion
fraction and rates:
    if counter == 10
        disp([num2str(LengthArray(m,1),'%4.4g'),'
',num2str(P_p_Total(m+1,1),'%4.4g'),'
',num2str(P_s_Total(m+1,1),'%4.4g'),'    ',num2str(N2Average(m,1)),'
',num2str(N1Average(m,1)),' ',num2str(N0Average(m,1)),'
',num2str(InversionAverage(m,1)),'  ',num2str(InversionCenter(m,1)),'
',num2str(GainLength(m,1)),'    ',num2str(RabsPAverage(m,1)),'
',num2str(RemPAverage(m,1)),'   ',num2str(RabsSAverage(m,1)),'
',num2str(RemSAverage(m,1)),'   ',num2str(RETUAverage(m,1)),'
',num2str(Rspont2Average(m,1)),'    ',num2str(Rspont1Average(m,1)),'
',num2str(RESAAverage(m,1)),'   ',num2str(RBackgroundPAverage(m,1)),'
',num2str(RBackgroundSAverage(m,1))]);
        counter = 0;
    end
    counter = counter +1;
   end

   % Establish pump and signal power arrays for input into the next
section by redistributing the power in a Gaussian:
   P_s_confined = 0;
   P_p_confined = 0;
   for n=1:Xnum-1
    P_s(n,(m+1)) = P_s_Total((m+1),j).*(1-e^(-2*(n*dX)^2/w_s^2))-
P_s_Total((m+1),j).*(1-e^(-2*((n-1)*dX)^2/w_s^2));
    P_p(n,(m+1)) = P_p_Total((m+1),j).*(1-e^(-2*(n*dX)^2/w_p^2))-
P_p_Total((m+1),j).*(1-e^(-2*((n-1)*dX)^2/w_p^2));
    P_s_confined = P_s_confined + P_s(n,(m+1));
    P_p_confined = P_p_confined + P_p(n,(m+1));
   end
   % Initialize outer element of each power array, accounting for
r_active to infinity, to include rest of power which is outside the
active region and does not contribute to population dynamics
   P_s(Xnum,(m+1)) = P_s_Total((m+1),j)-P_s_confined;
   P_p(Xnum,(m+1)) = P_p_Total((m+1),j)-P_p_confined;

  end  % End of second loop(Z-propagation)

 % Solve for gain and fill gain, gain/cm, launched pump power and
output pump and signal power arrays for output:
 Gain(1,j)=10.*log10(P_s_Total(Znum+1,j)./P_s_Total(1,j));
 Gain_percm(1,j)=Gain(1,j)./L;
 P_pStart(1,j) = P_p_Total(1,j);
 P_pEnd(1,j) = P_p_Total(Znum+1,j);
```

```
 P_sEnd(1,j) = P_s_Total(Znum+1,j);
 % If gain vs. launched pump power simulation, display launched pump
power, output pump and signal powers and gain:
 if length_simulation == 0
  disp([num2str(P_pStart(1,j),'%4.4g'),'
',num2str(P_pEnd(1,j),'%4.4g'),'
',num2str(P_sEnd(1,j)),'
',num2str(Gain(1,j))]);
 end

end  % End of main loop (increasing launched pump power)

% If gain vs. length simulation, display plots of inversion fraction
vs. length and total gain vs. length:
if length_simulation == 1
 % Plot inversion fraction vs. length
 figure;
 plot(LengthArray,InversionAverage,'g','Linewidth',2);
 hold on
 plot(LengthArray,InversionCenter,'y','Linewidth',2);
 grid off;
 xlabel('Length [cm]');
 ylabel('Inversion [%]');
 axis([0 L 0 1]);
 drawnow;
 hold off;
 % Plot total gain vs. length
 figure;
 plot(LengthArray,GainLength,'b','Linewidth',2);
 hold on
 grid off;
 xlabel('Length [cm]');
 ylabel('Gain [dB]');
 drawnow;
 hold off;
% If gain vs. launched pump power simulation, display plots of output
signal power vs. launched pump power and total gain vs. launched pump
power:
else
 % Plot output signal power vs. launched pump power
 figure;
 plot(P_pStart,P_sEnd,'r','Linewidth',2);
 hold on
 grid on;
 xlabel('Pump Power [mW]');
 ylabel('Signal [mW]');
 drawnow;
 hold off;
 % Plot total gain vs. launched pump power
 figure;
 plot(P_pStart,Gain,'b','Linewidth',2);
 hold on
 %plot(measured_PpL_adjusted,measured_gain,'r.','Markersize',16);
 grid off;
 xlabel('Pump Power [mW]');
 ylabel('Gain [dB]');
 drawnow;
 hold off;
end
```

References

[1] *Silicon Photonics: The State of the Art*. Chichester: John Wiley & Sons Ltd, 2008.

[2] G. Roelkens, J. Van Campenhout, J. Brouckaert, D. Van Thourhout, R. Baets, P. R. Romeo, P. Regreny, A. Kazmierczak, C. Seassal, X. Letartre, G. Hollinger, J. M. Fedeli, L. Di Cioccio, and C. Lagahe-Blanchard, "III-V/Si photonics by die to wafer bonding," *Materials Today*, vol. 10, pp. 36-43, 2007.

[3] C. A. Barrios and M. Lipson, "Electrically driven silicon resonant light emitting device based on slot- waveguide," *Optics Express*, vol. 13, pp. 10092-10101, 2005.

[4] R. J. Mears, L. Reekie, I. M. Jauncey, and D. N. Payne, "Low-noise erbium-doped fiber amplifier operating at 1.54 µm," *Electronics Letters*, vol. 23, pp. 1026-1028, 1987.

[5] P. C. Becker, N. A. Olsson, and J. R. Simpson, *Erbium-Doped Fiber Amplifiers: Fundamentals and Technology*. London: Academic Press, 1999.

[6] T. P. Blauwendraat, "Characterization of sputtered Er:Al_2O_3 for active integrated optics," vol. M.Sc. Enschede, The Netherlands: University of Twente, 2007.

[7] A. J. Kenyon, "Erbium in silicon," *Semiconductor Science and Technology*, vol. 20, pp. R65-R84, 2005.

[8] R. Brinkmann, I. Baumann, M. Dinand, W. Sohler, and H. Suche, "Erbium-doped single- and double-pass Ti:$LiNbO_3$ waveguide amplifiers," *IEEE Journal of Quantum Electronics*, vol. 30, pp. 2356-2360, 1994.

[9] T. H. Hoekstra, P. V. Lambeck, H. Albers, and T. J. A. Popma, "Sputter-deposited erbium-doped Y_2O_3 active optical waveguides," *Electronics Letters*, vol. 29, pp. 581-583, 1993.

[10] S. Bär, H. Scheife, K. Petermann, and G. Hüber, *"Sesquioxides as host materials for rare-earth-doped bulk lasers and active waveguides," in Rare Earth Oxide Thin Films: Growth, Characterization, and Applications*. Berlin: Springer-Verlag, 2007.

[11] G. Facchini, A. Zappettini, A. Canali, M. Martinelli, G. Gabetta, and G. Tallarida, "Erbium-doped crystalline YAG planar and ridge waveguides on quartz and sapphire substrates: deposition and material characterisation," *Optical Materials*, vol. 17, pp. 251-254, 2001.

[12] M. Szachowicz, S. Tascu, M.-F. Joubert, P. Moretti, and M. Nikl, "Realization and infrared to green upconversion luminescence in Er^{3+}:$YAlO_3$ ion-implanted optical waveguides," *Optical Materials*, vol. 28, pp. 162-166, 2006.

[13] S. García-Revilla, R. Valiente, Y. E. Romanyuk, and M. Pollnau, "Temporal dynamics of upconversion luminescence in Er^{3+}, Yb^{3+} co-doped crystalline $KY(WO_4)_2$ thin films," *Journal of Luminescence*, vol. 128, pp. 934-936, 2008.

[14] L. H. Slooff, A. Polman, M. P. O. Wolbers, F. van Veggel, D. N. Reinhoudt, and J. W. Hofstraat, "Optical properties of erbium-doped organic polydentate cage complexes," *Journal of Applied Physics*, vol. 83, pp. 497-503, 1998.

[15] A. Q. Le Quang, R. Hierle, J. Zyss, I. Ledoux, G. Cusmai, R. Costa, A. Barberis, and S. M. Pietralunga, "Demonstration of net gain at 1550 nm in an erbium-

doped polymer single mode rib waveguide," *Applied Physics Letters*, vol. 89, pp. 141124/1-3, 2006.

[16] D. Zhang, C. Chen, C. M. Chen, C. S. Ma, D. M. Zhang, S. Bo, and Z. Zhen, "Optical gain at 1535 nm in LaF_3:Er, Yb nanoparticle-doped organic-inorganic hybrid material waveguide," *Applied Physics Letters*, vol. 91, pp. 161109/1-3, 2007.

[17] J. Yang, M. B. J. Diemeer, D. Geskus, G. Sengo, M. Pollnau, and A. Driessen, "Neodymium-complex-doped photodefined polymer channel waveguide amplifiers," *Optics Letters*, vol. 34, pp. 473-475, 2009.

[18] T. Kitagawa, K. Hattori, K. Shuto, M. Yasu, M. Kobayashi, and M. Horiguchi, "Amplification in erbium-doped silica-based planar lightwave circuits," *Electronics Letters*, vol. 28, pp. 1818-1819, 1992.

[19] K. Hattori, T. Kitagawa, M. Oguma, Y. Ohmori, and M. Horiguchi, "Erbium-doped silica-based waveguide amplifier integrated with a 980/1530nm WDM Coupler," *Electronics Letters*, vol. 30, pp. 856-857, 1994.

[20] D. Barbier, M. Rattay, F. SaintAndre, G. Clauss, M. Trouillon, A. Kevorkian, J. M. P. Delavaux, and E. Murphy, "Amplifying four-wavelength combiner, based on erbium/ytterbium-doped waveguide amplifiers and integrated splitters," *IEEE Photonics Technology Letters*, vol. 9, pp. 315-317, 1997.

[21] P. M. Peters, D. S. Funk, A. P. Peskin, D. L. Veasey, N. A. Sanford, S. N. Houde-Walter, and J. S. Hayden, "Ion-exchanged waveguide lasers in Er^{3+}/Yb^{3+} codoped silicate glass," *Applied Optics*, vol. 38, pp. 6879-6886, 1999.

[22] K. Ennser, S. Taccheo, T. Rogowski, and J. Shmulovich, "Efficient Erbium-doped waveguide amplifier insensitive to power fluctuations," *Optics Express*, vol. 14, pp. 10307-10312, 2006.

[23] T. Ohtsuki, N. Peyghambarian, S. Honkanen, and S. I. Najafi, "Gain characteristics of a high-concentration Er^{3+}-doped phosphate glass waveguide," *Journal of Applied Physics*, vol. 78, pp. 3617-3621, 1995.

[24] Y. C. Yan, A. J. Faber, H. deWaal, P. G. Kik, and A. Polman, "Erbium-doped phosphate glass waveguide on silicon with 4.1 dB/cm gain at 1.535 µm," *Applied Physics Letters*, vol. 71, pp. 2922-2924, 1997.

[25] J. M. P. Delavaux, S. Granlund, O. Mizuhara, L. D. Tzeng, D. Barbier, M. Rattay, F. SaintAndre, and A. Kevorkian, "Integrated optics erbium-ytterbium amplifier system in 10-Gb/s fiber transmission experiment," *IEEE Photonics Technology Letters*, vol. 9, pp. 247-249, 1997.

[26] A. Shooshtari, P. Meshkinfam, T. Touam, M. P. Andrews, and S. I. Najafi, "Ion-exchanged Er/Yb phosphate glass waveguide amplifiers and lasers," *Optical Engineering*, vol. 37, pp. 1188-1192, 1998.

[27] D. L. Veasey, D. S. Funk, N. A. Sanford, and J. S. Hayden, "Arrays of distributed-Bragg-reflector waveguide lasers at 1536 nm in Yb/Er codoped phosphate glass," *Applied Physics Letters*, vol. 74, pp. 789-791, 1999.

[28] E. R. Thoen, E. M. Koontz, D. J. Jones, D. Barbier, F. X. Kärtner, E. P. Ippen, and L. A. Kolodziejski, "Erbium-ytterbium waveguide laser mode-locked with a semiconductor saturable absorber mirror," *IEEE Photonics Technology Letters*, vol. 12, pp. 149-151, 2000.

[29] G. Sorbello, S. Taccheo, P. Laporta, O. Svelto, E. Cianci, V. Foglietti, S. Jiang, and N. Peyghambarian, "Singlemode Er:Yb waveguide laser array at 1.5 µm," *Electronics Letters*, vol. 37, pp. 1014-1015, 2001.

[30] F. Gardillou, L. Bastard, and J. E. Broquin, "4.25 dB gain in a hybrid silicate/phosphate glasses optical amplifier made by wafer bonding and ion-exchange techniques," *Applied Physics Letters*, vol. 85, pp. 5176-5178, 2004.

[31] F. D. Patel, S. DiCarolis, P. Lum, S. Venkatesh, and J. N. Miller, "A compact high-performance optical waveguide amplifier," *IEEE Photonics Technology Letters*, vol. 16, pp. 2607-2609, 2004.

[32] K. Liu and E. Y. B. Pun, "Modeling and experiments of packaged Er^{3+}-Yb^{3+} co-doped glass waveguide amplifiers," *Optics Communications*, vol. 273, pp. 413-420, 2007.

[33] I. Vasilief, S. Guy, B. Jacquier, B. Boulard, Y. P. Gao, C. Duverger, H. Haquin, V. Nazabal, J. L. Adam, M. Couchaud, L. Fulbert, C. Cassagnettes, F. Rooms, and D. Barbier, "Propagation losses and gain measurements in erbium-doped fluoride glass channel waveguides by use of a double-pass technique," *Applied Optics*, vol. 44, pp. 4678-4683, 2005.

[34] G. N. van den Hoven, R. Koper, A. Polman, C. van Dam, J. W. M. van Uffelen, and M. K. Smit, "Net optical gain at 1.53 µm in Er-doped Al_2O_3 waveguides on silicon," *Applied Physics Letters*, vol. 68, pp. 1886-1888, 1996.

[35] R. Serna and C. N. Afonso, "In situ growth of optically active erbium doped Al_2O_3 thin films by pulsed laser deposition," *Applied Physics Letters*, vol. 69, pp. 1541-1543, 1996.

[36] C. E. Chryssou and C. W. Pitt, "Er^{3+}-doped Al_2O_3 thin films by plasma-enhanced chemical vapor deposition (PECVD) exhibiting a 55-nm optical bandwidth," *IEEE Journal of Quantum Electronics*, vol. 34, pp. 282-285, 1998.

[37] S. Musa, H. J. van Weerden, T. H. Yau, and P. V. Lambeck, "Characteristics of Er-doped Al_2O_3 thin films deposited by reactive co-sputtering," *IEEE Journal of Quantum Electronics*, vol. 36, pp. 1089-1097, 2000.

[38] K. Solehmainen, M. U. Kapulainen, P. Heimala, and K. Polamo, "Erbium-doped waveguides fabricated with atomic layer deposition method," *IEEE Photonics Technology Letters*, vol. 16, pp. 194-196, 2004.

[39] T. Feuchter, E. K. Mwarania, J. Wang, L. Reekie, and J. S. Wilkinson, "Erbium-doped ion-exchanged waveguide lasers in Bk-7 glass," *IEEE Photonics Technology Letters*, vol. 4, pp. 542-544, 1992.

[40] J. Shmulovich, A. Wong, Y. H. Wong, P. C. Becker, A. J. Bruce, and R. Adar, "Er^{3+} glass waveguide amplifier at 1.5 µm on silicon," *Electronics Letters*, vol. 28, pp. 1181-1182, 1992.

[41] G. Nykolak, M. Haner, P. C. Becker, J. Shmulovich, and Y. H. Wong, "Systems evaluation of an Er^{3+}-doped planar waveguide amplifier," *IEEE Photonics Technology Letters*, vol. 5, pp. 1185-1187, 1993.

[42] E. Snoeks, G. N. Vandenhoven, A. Polman, B. Hendriksen, M. B. J. Diemeer, and F. Priolo, "Cooperative upconversion in erbium-implanted soda-lime silicate glass optical waveguides," *Journal of the Optical Society of America B*, vol. 12, pp. 1468-1474, 1995.

[43] P. Camy, J. E. Roman, F. W. Willems, M. Hempstead, J. C. vanderPlaats, C. Prel, A. Beguin, A. M. J. Koonen, J. S. Wilkinson, and C. Lerminiaux, "Ion-exchanged planar lossless splitter at 1.5 µm," *Electronics Letters*, vol. 32, pp. 321-323, 1996.

[44] R. N. Ghosh, J. Shmulovich, C. F. Kane, M. R. X. de Barros, G. Nykolak, A. J. Bruce, and P. C. Becker, "8-mW threshold Er^{3+}-doped planar waveguide amplifier," *IEEE Photonics Technology Letters*, vol. 8, pp. 518-520, 1996.

[45] M. P. Hehlen, N. J. Cockroft, T. R. Gosnell, A. J. Bruce, G. Nykolak, and J. Shmulovich, "Uniform upconversion in high-concentration Er^{3+}-doped soda lime silicate and aluminosilicate glasses," *Optics Letters*, vol. 22, pp. 772-774, 1997.

[46] C. Strohhöfer, S. Capecchi, J. Fick, A. Martucci, G. Brusatin, and M. Guglielmi, "Active optical properties of erbium-doped GeO_2-based sol-gel planar waveguides," *Thin Solid Films*, vol. 326, pp. 99-105, 1998.

[47] X. Orignac, D. Barbier, X. M. Du, R. M. Almeida, O. McCarthy, and E. Yeatman, "Sol-gel silica/titania-on-silicon Er/Yb-doped waveguides for optical amplification at 1.5 μm," *Optical Materials*, vol. 12, pp. 1-18, 1999.

[48] J. Fick, A. Martucci, and M. Guglielmi, "Fabrication of erbium-doped channel waveguides by a combination of ion exchange and sol-gel techniques," *Journal of Sol-Gel Science and Technology*, vol. 19, pp. 573-576, 2000.

[49] Y. B. Choi, S. H. Cho, and D. C. Moon, "Er-Al-codoped silicate planar light waveguide-type amplifier fabricated by radio-frequency sputtering," *Optics Letters*, vol. 25, pp. 263-265, 2000.

[50] J. Hübner, S. Guldberg-Kjær, M. Dyngaard, Y. Shen, C. L. Thomsen, S. Balslev, C. Jensen, D. Zauner, and T. Feuchter, "Planar Er- and Yb-doped amplifiers and lasers," *Applied Physics B-Lasers and Optics*, vol. 73, pp. 435-438, 2001.

[51] W. Huang, R. R. A. Syms, E. M. Yeatman, M. M. Ahmad, T. V. Clapp, and S. M. Ojha, "Fiber-device-fiber gain from a sol-gel erbium-doped waveguide amplifier," *IEEE Photonics Technology Letters*, vol. 14, pp. 959-961, 2002.

[52] L. Zampedri, G. C. Righini, H. Portales, S. Pelli, G. N. Conti, M. Montagna, M. Mattarelli, R. R. Gonçalves, M. Ferrari, A. Chiasera, M. Bouazaoui, and C. Armellini, "Sol-gel-derived Er-activated SiO_2-HfO_2 planar waveguides for 1.5 μm application," *Journal of Non-Crystalline Solids*, vol. 345-46, pp. 580-584, 2004.

[53] S. Banerjee, C. C. Baker, A. J. Steckl, and D. Klotzkin, "Optical properties of Er in Er-doped $Zn_2Si_{0.5}Ge_{0.5}$O4 waveguide amplifiers," *Journal of Lightwave Technology*, vol. 23, pp. 1342-1349, 2005.

[54] R. R. Thomson, H. T. Bookey, H. Ur-Rehman, S. Liu, N. Suyal, and A. K. Kar, "Optically active erbium-doped waveguides fabricated using a single-sol-gel-deposition technique," *Journal of Lightwave Technology*, vol. 23, pp. 4249-4256, 2005.

[55] P. T. Nga, C. Barthou, P. Benalloul, P. N. Thang, L. N. Chung, P. V. Hoi, L. V. Luat, and P. T. Cuong, "Effects of yttrium codoping on fluorescence lifetimes of Er^{3+} ions in SiO_2-Al_2O_3 sol-gel glasses," *Journal of Non-Crystalline Solids*, vol. 352, pp. 2385-2389, 2006.

[56] S. Berneschi, M. Bettinelli, M. BrenCi, R. Dall'Igna, G. N. Conti, S. Pelli, B. Profilo, S. Sebastiani, A. Speghini, and G. C. Righini, "Optical and spectroscopic properties of soda-lime alumino silicate glasses doped with Er^{3+} and/or Yb^{3+}," *Optical Materials*, vol. 28, pp. 1271-1275, 2006.

[57] A. P. Caricato, A. Fazzi, A. Jha, A. Kar, G. Leggieri, A. Luches, M. Martino, F. Romano, S. Shen, M. Taghizadeh, R. Thomson, and T. Tunno, "Er-doped oxyfluoride silicate thin films prepared by pulsed laser deposition," *Optical Materials*, vol. 29, pp. 1166-1170, 2007.

[58] Z. He, Y. G. Li, Y. W. Zhang, D. X. Li, L. Y. Liu, and L. Xu, "Er^{3+}/Yb^{3+} co-doped waveguide amplifier and lossless power splitter fabricated by a two-step

ion exchange on a commercial phosphate glass," *Journal of the Korean Physical Society*, vol. 49, pp. 2159-2163, 2006.

[59] M. W. Sckerl, S. Guldberg-Kjær, C. Laurent-Lund, and M. Rysholt Poulsen, "Loss-less planar waveguide 1:4 power splitter at 1550 nm," presented at Proceedings of ECOC'99, Nice, France, 1999.

[60] Y. Jaouën, L. du Mouza, D. Barbier, J.-M. Delavaux, and P. Bruno, "Eight-wavelength Er-Yb doped amplifier: combiner/splitter planar integrated module," *IEEE Photonics Technology Letters*, vol. 11, pp. 1105-1107, 1999.

[61] G. Jose, G. Sorbello, S. Taccheo, E. Cianci, V. Foglietti, and P. Laporta, "Active waveguide devices by Ag-Na ion exchange on erbium-ytterbium doped phosphate glasses," *Journal of Non-Crystalline Solids*, vol. 322, pp. 256-261, 2003.

[62] S. Taccheo, G. Della Valle, R. Osellame, G. Cerullo, N. Chiodo, P. Laporta, O. Svelto, A. Killi, U. Morgner, M. Lederer, and D. Kopf, "Er:Yb-doped waveguide laser fabricated by femtosecond laser pulses," *Optics Letters*, vol. 29, pp. 2626-2628, 2004.

[63] T. Kitagawa, K. Hattori, M. Shimizu, Y. Ohmori, and M. Kobayashi, "Guided-wave laser based on erbium-doped silica planar lightwave circuit," *Electronics Letters*, vol. 27, pp. 334-335, 1991.

[64] A. Yeniay, J.-M. P. Delavaux, J. Toulouse, D. Barbier, T. A. Strasser, and J. R. Pedrazanni, "High-performance integrated Erbium^{3+}-Ytterbium^{3+} codoped glass waveguide laser," *IEEE Photonics Technology Letters*, vol. 9, pp. 1099-1101, 1997.

[65] K. Hattori, T. Kitagawa, M. Oguma, Y. Hibino, Y. Ohmori, and M. Horiguchi, "Er-doped silica-based planar ring-resonator," *Electronics and Communications in Japan*, vol. 77, pp. 62-72, 1994.

[66] W. Sohler, B. K. Das, D. Dey, S. Reza, H. Suche, and R. Ricken, "Erbium-doped lithium niobate waveguide lasers," *IEICE Transactions on Electronics*, vol. E88c, pp. 990-997, 2005.

[67] T. Kitagawa, F. Bilodeau, B. Malo, S. Thériault, J. Albert, D. C. Jihnson, K. O. Hill, K. Hattori, and Y. Hibino, "Single-frequency Er^{3+}-doped silica-based planar waveguide laser with integrated photo-imprinted Bragg reflectors," *Electronics Letters*, vol. 30, pp. 1311-1313, 1994.

[68] S. Guldberg-Kjær, J. Hubner, M. Kristensen, C. Laurent-Lund, M. Rysholt Poulsen, and M. W. Sckerl, "Planar waveguide laser in Er/Al-doped germanosilicate," *Electronics Letters*, vol. 35, pp. 302-303, 1999.

[69] S. Blaize, L. Bastard, C. Cassagnètes, and J. E. Broquin, "Multiwavelengths DFB waveguide laser arrays in Yb-Er codoped phosphate glass substrate," *IEEE Photonics Technology Letters*, vol. 15, pp. 516-518, 2003.

[70] G. D. Marshall, P. Dekker, M. Ams, J. A. Piper, and M. J. Withford, "Directly written monolithic waveguide laser incorporating a distributed feedback waveguide-Bragg grating," *Optics Letters*, vol. 33, pp. 956-958, 2008.

[71] P. Madasamy, G. N. Conti, P. Poyhonen, Y. Hu, M. M. Morrell, D. F. Geraghty, S. Honkanen, and N. Peyghambarian, "Waveguide distributed Bragg reflector laser arrays in erbium doped glass made by dry Ag film ion exchange," *Optical Engineering*, vol. 41, pp. 1084-1086, 2002.

[72] D. Pudo, H. Byun, J. Chen, J. Sickler, F. X. Kärtner, and E. P. Ippen, "Scaling of passively mode-locked soliton erbium waveguide lasers based on slow saturable absorbers," *Optics Express*, vol. 16, pp. 19221-19231, 2008.

[73] Teem Photonics, http://www.teemphotonics.com/.
[74] CIP Technologies, http://www.ciphotonics.com/.
[75] M. K. Smit, G. A. Acket, and C. J. van der Laan, "Al_2O_3 films for integrated-optics," *Thin Solid Films*, vol. 138, pp. 171-181, 1986.
[76] G. N. van den Hoven, E. Snoeks, A. Polman, J. W. M. van Uffelen, Y. S. Oei, and M. K. Smit, "Photoluminescence characterization of Er-implanted Al_2O_3 films," *Applied Physics Letters*, vol. 62, pp. 3065-3067, 1993.
[77] K. Wörhoff, J. D. B. Bradley, F. Ay, D. Geskus, T. P. Blauwendraat, and M. Pollnau, "Reliable low-cost fabrication of low-loss $Al_2O_3:Er^{3+}$ waveguides with 5.4-dB optical gain," *IEEE Journal of Quantum Electronics*, vol. 45, pp. 454-461, 2009.
[78] J. D. B. Bradley, F. Ay, K. Wörhoff, and M. Pollnau, "Fabrication of low-loss channel waveguides in Al_2O_3 and Y_2O_3 layers by inductively coupled plasma reactive ion etching," *Applied Physics B-Lasers and Optics*, vol. 89, pp. 311-318, 2007.
[79] A. Suarez-Garcia, J. Gonzalo, and C. N. Afonso, "Low-loss Al_2O_3 waveguides produced by pulsed laser deposition at room temperature," *Applied Physics a-Materials Science & Processing*, vol. 77, pp. 779-783, 2003.
[80] A. Pillonnet, C. Garapon, C. Champeaux, C. Bovier, H. Jaffrezic, and J. Mugnier, "Fluorescence of Cr^{3+} doped alumina optical waveguides prepared by pulsed laser deposition and sol-gel method," *Journal of Luminescence*, vol. 87-9, pp. 1087-1089, 2000.
[81] Y. Kim, S. M. Lee, C. S. Park, S. I. Lee, and M. Y. Lee, "Substrate dependence on the optical properties of Al_2O_3 films grown by atomic layer deposition," *Applied Physics Letters*, vol. 71, pp. 3604-3606, 1997.
[82] S. Jakschik, U. Schroeder, T. Hecht, D. Krueger, G. Dollinger, A. Bergmaier, C. Luhmann, and J. W. Bartha, "Physical characterization of thin ALD-Al_2O_3 films," *Applied Surface Science*, vol. 211, pp. 352-359, 2003.
[83] C. J. Kang, J. S. Chun, and W. J. Lee, "Properties of aluminum oxide films prepared by plasma-enhanced metal-organic chemical vapor deposition," *Thin Solid Films*, vol. 189, pp. 161-173, 1990.
[84] M. Mahnke, S. Wiechmann, H. J. Heider, O. Blume, and J. Muller, "Aluminum oxide doped with erbium, titanium and chromium for active integrated optical applications," *AEU-International Journal of Electronics and Communications*, vol. 55, pp. 342-348, 2001.
[85] X. Multone, C. N. Borca, and P. Hoffmann, "Large area deposition of Al_2O_3 thin films with molecular beams in high vacuum," *Thin Solid Films*, vol. 515, pp. 7542-7545, 2007.
[86] M. Benatsou, B. Capoen, M. Bouazaoui, W. Tchana, and J. P. Vilcot, "Preparation and characterization of sol-gel derived $Er^{3+}:Al_2O_3-SiO_2$ planar waveguides," *Applied Physics Letters*, vol. 71, pp. 428-430, 1997.
[87] X. J. Wang and M. K. Lei, "Preparation and photoluminescence of Er^{3+}-doped Al_2O_3 films by sol-gel method," *Thin Solid Films*, vol. 476, pp. 41-45, 2005.
[88] S. M. Arnold and B. E. Cole, "Ion-beam sputter deposition of low-loss Al_2O_3 films for integrated-optics," *Thin Solid Films*, vol. 165, pp. 1-9, 1988.
[89] B. J. H. Stadler, M. Oliveria, and L. O. Bouthillette, "Alumina thin films as optical waveguides," *Journal of the American Ceramic Society*, vol. 78, pp. 3336-3344, 1995.

[90] Q. Song, C. R. Li, J. Y. Li, W. Y. Ding, S. F. Li, J. Xu, X. L. Den, and C. L. Song, "Photoluminescence properties of the Yb:Er co-doped Al_2O_3 thin film fabricated by microwave ECR plasma source enhanced RF magnetron sputtering," *Optical Materials*, vol. 28, pp. 1344-1349, 2006.

[91] G. N. van den Hoven, J. A. van der Elsken, A. Polman, C. van Dam, K. W. M. van Uffelen, and M. K. Smit, "Absorption and emission cross sections of Er^{3+} in Al_2O_3 waveguides," *Applied Optics*, vol. 36, pp. 3338-3341, 1997.

[92] P. K. Tien and R. Ulrich, "Theory of prism-film coupler and thin-film light guides," *Journal of the Optical Society of America*, vol. 60, pp. 1325-1337, 1970.

[93] H. P. Weber, F. A. Dunn, and W. N. Leibolt, "Loss measurements in thin-film optical waveguides," *Applied Optics*, vol. 12, pp. 755-757, 1973.

[94] RUMP website, http://www.genplot.com/doc/rump.htm.

[95] K. Wörhoff, J. D. B. Bradley, F. Ay, and M. Pollnau, "Low-loss Al_2O_3 waveguides for active integrated optics," presented at Conference on Lasers and Electro-Optics, Technical Digest 2007, Washington, DC, 2007.

[96] K. Wörhoff, L. T. H. Hilderink, A. Driessen, and P. V. Lambeck, "Silicon oxynitride: a versatile material for integrated optics applications," *Journal of the Electrochemical Society*, vol. 149, pp. F85-F91, 2002.

[97] G. N. vandenHoven, R. Koper, A. Polman, C. vanDam, J. W. M. vanUffelen, and M. K. Smit, "Net optical gain at 1.53 μm in Er-doped Al_2O_3 waveguides on silicon," *Applied Physics Letters*, vol. 68, pp. 1886-1888, 1996.

[98] T. H. Yau, "Design and Realisation of Erbium-doped Integrated Optical Amplifiers," vol. M.Sc. Enschede, The Netherlands: University of Twente, 2000.

[99] R. Dekker, "All-Optical Processes in Integrated Optical Devices Using Materials with Large Third-Order Nonlinearities and Gain," vol. Ph.D. Enschede, The Netherlands: University of Twente, 2006.

[100] W. G. M. Van den Hoek, "The etch mechanism for Al_2O_3 in fluorine and chlorine based RF dry etch plasmas," presented at Materials Research Society Plasma Processing Symposium, Palo Alto, CA, USA, 1986.

[101] Y. H. Lee, Z. H. Zhou, D. A. Danner, P. M. Fryer, and J. M. Harper, "Chemical sputtering of Al_2O_3 by fluorine-containing plasmas excited by electron-cyclotron resonance," *Journal of Applied Physics*, vol. 68, pp. 5329-5336, 1990.

[102] J. W. Kim, Y. C. Kim, and W. J. Lee, "Reactive ion etching mechanism of plasma-enhanced chemically vapor-deposited aluminum-oxide film in CF_4/O_2 plasma," *Journal of Applied Physics*, vol. 78, pp. 2045-2049, 1995.

[103] J. W. Lee, B. Pathangey, M. R. Davidson, P. H. Holloway, E. S. Lambers, B. Davydov, T. J. Anderson, and S. J. Pearton, "Comparison of plasma chemistries for dry etching thin film electroluminescent display materials," *Journal of Vacuum Science & Technology A*, vol. 16, pp. 2177-2186, 1998.

[104] D. P. Kim, J. W. Yeo, and C. I. Kim, "Etching properties of Al_2O_3 films in inductively coupled plasma," *Thin Solid Films*, vol. 459, pp. 122-126, 2004.

[105] S. Tegen and P. Moll, "Etch characteristics of Al_2O_3 in ICP and MERIE plasma etchers," *Journal of the Electrochemical Society*, vol. 152, pp. G271-G276, 2005.

[106] E. van der Drift, B. A. C. Rousseeuw, J. Romijn, E. C. M. Pennings, and F. H. Groen, "High resolution patterning of aluminumoxide for integrated optical devices," *Microelectronic Engineering*, vol. 9, pp. 499-502, 1989.

[107] D. R. Lide, Ed., *CRC Handbook of Chemistry and Physics*, 82nd ed. Boca Raton: CRC Press, 2001.

[108] C. H. Jeong, D. W. Kim, H. Y. Lee, H. S. Kim, Y. J. Sung, and G. Y. Yeom, "Sapphire etching with BCl_3/HBr/Ar plasma," *Surface & Coatings Technology*, vol. 171, pp. 280-284, 2003.

[109] D. W. Kim, C. H. Jeong, K. N. Kim, H. Y. Lee, H. S. Kim, Y. J. Sung, and G. Y. Yeom, "High rate sapphire (Al_2O_3) etching in inductively coupled plasmas using axial external magnetic field," *Thin Solid Films*, vol. 435, pp. 242-246, 2003.

[110] A. Crunteanu, M. Pollnau, G. Janchen, C. Hibert, P. Hoffmann, R. P. Salathe, R. W. Eason, C. Grivas, and D. P. Shepherd, "Ti:sapphire rib channel waveguide fabricated by reactive ion etching of a planar waveguide," *Applied Physics B*, vol. 75, pp. 15-17, 2002.

[111] Oxford Instruments, http://www.oxford-instruments.com.

[112] T. H. Hoekstra, "Erbium-doped Y_2O_3 Integrated Optical Amplifiers," vol. Ph.D. Enschede, The Netherlands: University of Twente, 1994.

[113] Y. C. Kim and C. I. Kim, "Etching mechanism of Y_2O_3 thin films in high density Cl_2/Ar plasma," *Journal of Vacuum Science & Technology A*, vol. 19, pp. 2676-2679, 2001.

[114] A. Kahn, H. Kühn, S. Heinrich, K. Petermann, J. D. B. Bradley, K. Wörhoff, M. Pollnau, Y. Kuzminykh, and G. Huber, "Amplification in epitaxially grown Er:(Gd, Lu)$_2O_3$ waveguides for active integrated optical devices," *Journal of the Optical Society of America B*, vol. 25, pp. 1850-1853, 2008.

[115] A. Kahn, S. Heinrich, H. Kühn, K. Petermann, J. D. B. Bradley, K. Wörhoff, M. Pollnau, and G. Huber, "Low threshold monocrystalline Nd:(Gd, Lu)$_2O_3$ channel waveguide laser," *Optics Express*, vol. 17, pp. 4412-4418, 2009.

[116] K. T. Koai and P. L. Liu, "Modeling of Ti:$LiNbO_3$ waveguide devices: part II - s-shaped channel waveguide bends," *Journal of Lightwave Technology*, vol. 7, pp. 1016-1022, 1989.

[117] B. E. A. Saleh and M. C. Teich, *Fundamentals of Photonics*. New York: John Wiley & Sons, Inc., 1991.

[118] S. F. Wong, E. Y. B. Pun, and P. S. Chung, "Er^{3+}-Yb^{3+} codoped phosphate glass waveguide amplifier using Ag^+-Li^+ ion exchange," *IEEE Photonics Technology Letters*, vol. 14, pp. 80-82, 2002.

[119] J. Shmulovich, "Er-doped glass waveguide amplifiers on silicon," presented at Proceedings of SPIE - The International Society for Optical Engineering, San Jose, CA, United states, 1997.

[120] Q. Song, J. S. Gao, X. Y. Wang, H. Chen, X. M. Zheng, T. T. Wang, C. R. Li, and C. L. Song, "Fabrication of Yb^{3+}:Er^{3+} co-doped Al_2O_3 ridge waveguides by the dry etching," *Optical Engineering*, vol. 46, pp. 040509/1-3, 2007.

[121] J. Shmulovich, A. J. Bruce, G. Lenz, P. B. Hansen, T. N. Nielsen, D. J. Muehlner, G. A. Bogert, I. Brener, E. J. Laskowski, A. Paunescu, I. Ryazansky, D. C. Jacobson, and A. E. White, "Integrated planar waveguide amplifier with 15 dB net gain at 1550 nm," presented at Conference on Optical Fiber Communication, Technical Digest Series, Piscataway, NJ, United States, 1999.

[122] H. J. van Weerden, T. H. Hoekstra, P. V. Lambeck, and T. J. A. Popma, "Low threshold amplification at 1.5µm in Er:Y_2O_3 IO-amplifiers," presented at Proceedings of the 8th European Conference on Integrated Optics, Stockholm, Sweden, 1997.

[123] K. Shuto, K. Hattori, T. Kitagawa, Y. Ohmori, and M. Horiguchi, "Erbium-doped phosphosilicate glass waveguide amplifier fabricated by PECVD," *Electronics Letters*, vol. 29, pp. 139-141, 1993.

[124] X. L. Zou and T. Izumitani, "Spectroscopic properties and mechanisms of excited state absorption and energy transfer upconversion for Er^{3+}-doped glasses," *Journal of Non-Crystalline Solids*, vol. 162, pp. 68-80, 1993.

[125] P. W. Milonni and J. H. Eberly, *Lasers*. New York: Wiley, 1988.

[126] D. E. McCumber, "Theory of phonon-terminated optical masers," *Physical Review A*, vol. 134, pp. A299-A306, 1964.

[127] W. J. Miniscalco and R. S. Quimby, "General procedure for the analysis of Er^{3+} cross sections," *Optics Letters*, vol. 16, pp. 258-260, 1991.

[128] W. J. Miniscalco, "Erbium-doped glasses for fiber amplifiers at 1500 nm," *Journal of Lightwave Technology*, vol. 9, pp. 234-250, 1991.

[129] W. L. Barnes, R. I. Laming, E. J. Tarbox, and P. R. Morkel, "Absorption and emission cross section of Er^{3+} doped silica fibers," *IEEE Journal of Quantum Electronics*, vol. 27, pp. 1004-1010, 1991.

[130] C. Strohhofer and A. Polman, "Absorption and emission spectroscopy in Er^{3+}-Yb^{3+} doped aluminum oxide waveguides," *Optical Materials*, vol. 21, pp. 705-712, 2003.

[131] M. Pollnau and S. D. Jackson, *Solid-State Mid-Infrared Laser Sources*. Berlin, Heidelberg: Springer-Verlag, 2003.

[132] G. N. van den Hoven, E. Snoeks, A. Polman, C. van Dam, J. W. M. van Uffelen, and M. K. Smit, "Upconversion in Er-implanted Al_2O_3 waveguides," *Journal of Applied Physics*, vol. 79, pp. 1258-1266, 1996.

[133] P. S. Golding, S. D. Jackson, T. A. King, and M. Pollnau, "Energy transfer processes in Er^{3+}-doped and Er^{3+},Pr^{3+}-codoped ZBLAN glasses," *Physical Review B*, vol. 62, pp. 856-864, 2000.

[134] T. Ohtsuki, S. Honkanen, S. I. Najafi, and N. Peyghambarian, "Cooperative upconversion effects on the performance of Er^{3+}-doped phosphate glass waveguide amplifiers," *Journal of the Optical Society of America B*, vol. 14, pp. 1838-1845, 1997.

[135] S. Taccheo, G. Sorbello, S. Longhi, and P. Laporta, "Measurement of the energy transfer and upconversion constants in Er-Yb-doped phosphate glass," *Optical and Quantum Electronics*, vol. 31, pp. 249-262, 1999.

[136] B. C. Hwang, S. B. Jiang, T. Luo, J. Watson, G. Sorbello, and N. Peyghambarian, "Cooperative upconversion and energy transfer of new high Er^{3+}- and Yb^{3+}-Er^{3+}-doped phosphate glasses," *Journal of the Optical Society of America B*, vol. 17, pp. 833-839, 2000.

[137] P. Blixt, J. Nilsson, T. Carlnäs, and B. Jaskorzynska, "Concentration-dependent upconversion in Er^{3+}-doped fiber amplifiers: experiments and modeling," *IEEE Photonics Technology Letters*, vol. 3, pp. 996-998, 1991.

[138] E. Desurvire and J. R. Simpson, "Evaluation of $^4I_{15/2}$ and $^4I_{13/2}$ Stark-level energies in erbium-doped aluminosilicate glass fibers," *Optics Letters*, vol. 15, pp. 547-549, 1990.

[139] L. Agazzi, J. D. B. Bradley, F. Ay, A. Kayn, H. Sheife, K. Petermann, G. Guber, R. M. de Riddder, K. Wörhoff, and M. Pollnau, "Static and migration-accelerated energy-transfer upconversion in amorphous Al_2O_3:Er^{3+}," to be submitted.

[140] S. F. Li, C. L. Song, Q. J. Xiong, and B. Ran, "A numerical analysis of gain characteristics of Er-doped Al_2O_3 waveguide amplifiers," *Optical and Quantum Electronics*, vol. 34, pp. 859-866, 2002.
[141] M. Pollnau, T. Graf, J. E. Balmer, W. Luthy, and H. P. Weber, "Explanation of the cw operation of the Er^{3+} 3-µm crystal laser," *Physical Review A*, vol. 49, pp. 3990-3996, 1994.
[142] PhoeniX, http://www.phoenixbv.com.
[143] R. S. Quimby, W. J. Miniscalco, and B. Thompson, "Excited state absorption at 980 nm in erbium doped glass," presented at proc. of SPIE Fiber Laser Sources and Amplifiers III, 1991.
[144] C. E. Chryssou, F. Di Pasquale, and C. W. Pitt, "Improved gain performance in Yb^{3+}-sensitized Er^{3+}-doped alumina (Al_2O_3) channel optical waveguide amplifiers," *Journal of Lightwave Technology*, vol. 19, pp. 345-349, 2001.
[145] M. Hoekman, "A characterization technique for loss in arbitrarily shaped IO waveguiding structures using camera imgaing," *internal communication, to be submitted*, 2009.
[146] K. Wörhoff, B. J. Offrein, P. V. Lambeck, G. L. Bona, and A. Driessen, "Birefringence compensation applying double-core waveguiding structures," *IEEE Photonics Technology Letters*, vol. 11, pp. 206-208, 1999.
[147] Y. M. Kang, H. D. Liu, M. Morse, M. J. Paniccia, M. Zadka, S. Litski, G. Sarid, A. Pauchard, Y. H. Kuo, H. W. Chen, W. S. Zaoui, J. E. Bowers, A. Beling, D. C. McIntosh, X. G. Zheng, and J. C. Campbell, "Monolithic germanium/silicon avalanche photodiodes with 340 GHz gain-bandwidth product," *Nature Photonics*, vol. 3, pp. 59-63, 2009.
[148] S. Ferber, R. Ludwig, C. Boerner, C. Schubert, C. Schmidt-Larighorst, M. Kroh, V. Marembert, and H. G. Weber, "160 Gbit/s DPSK transmission over 320 km fibre link with high long-term stability," *Electronics Letters*, vol. 41, pp. 200-202, 2005.
[149] L. H. Spiekman, *Semiconductor optical amplifiers*: Academic Press, 2002.
[150] D. R. Zimmerman and L. H. Spiekman, "Amplifiers for the masses: EDFA, EDWA, and SOA amplets for metro and access applications," *Journal of Lightwave Technology*, vol. 22, pp. 63-70, 2004.
[151] S. Demiguel, N. Sahri, M. Hartlaub, F. Blache, H. Gariah, S. Vuiye, D. Carpentier, D. Barbier, and J. C. Campbell, "Low-cost photoreceiver integrating an EDWA and waveguide PIN photodiode for 40 Gbit/s applications," *Electronics Letters*, vol. 43, pp. 51-52, 2007.
[152] M. Thual, D. Malarde, B. Abhervé-Guégen, P. Rochard, and P. Chanclou, "Truncated Gaussian beams through microlenses based on a graded-index section," *Optical Engineering*, vol. 46, pp. 015402/1-12, 2007.
[153] G. Girault, M. Gay, S. Lobo, L. Bramerie, M. Joindot, J. C. Simon, A. Shen, F. Blache, H. Gariah, F. Mallécot, O. Le Gouezigou, F. Poingt, L. Le Gouezigou, F. Pommereau, B. Rousseau, F. Lelarge, and G.-H. Duan, "Quantum dash actively modelocked Fabry-Perot laser module demonstrated as part of wavelength tunable RZ transmitter," *Electronics Letters*, vol. 44, pp. 873-874, 2008.
[154] F. Lelarge, B. Dagens, J. Renaudier, R. Brenot, A. Accard, F. van Dijk, D. Make, O. Le Gouezigou, J.-G. Provost, F. Poingt, J. Landreau, O. Drisse, E. Derouin, B. Rousseau, F. Pommereau, and G.-H. Duan, "Recent advances on InAs/InP quantum dash based, semiconductor lasers and optical amplifiers

operating at 1.55 mu m," *IEEE Journal of Selected Topics in Quantum Electronics*, vol. 13, pp. 111-124, 2007.

[155] A. Polman, B. Min, J. Kalkman, T. J. Kippenberg, and K. J. Vahala, "Ultralow-threshold erbium-implanted toroidal microlaser on silicon," *Applied Physics Letters*, vol. 84, pp. 1037-1039, 2004.

[156] H.-K. Hsiao and K. A. Winick, "Planar galss waveguide ring resonators with gain," *Optics Express*, vol. 15, pp. 17783-17797, 2007.

[157] J. D. B. Bradley, L. Agazzi, D. Geskus, F. Ay, K. Wörhoff, and M. Pollnau, "Gain bandwidth of 80 nm and 2 dB/cm peak gain in $Al_2O_3:Er^{3+}$ optical amplifiers on silicon," *Journal of the Optical Society of America B*, submitted, March 2009.

[158] I. Mozjerin, S. Ruschin, and A. Hardy, "Design of unidirectional erbium-doped waveguide ring laser with asymmetric distributed Bragg grating," *Electronics Letters*, vol. 41, pp. 1119-1121, 2005.

Acknowledgements

First and foremost I thank my supervisor Markus Pollnau for providing the opportunity to study and complete my Ph.D. in the Netherlands. I am extremely grateful for our many discussions which helped guide me in the right direction, his motivating attitude, his availability as a supervisor and his many insightful suggestions. I would also like to express my gratitude to my co-supervisor Kerstin Wörhoff for her patience, attention to detail and her work on the thin film growth technology, without which this project would not have achieved such positive results. I also thank her for her guidance, availability, many helpful discussions and motivation in both the good and the difficult times.

I would also like to acknowledge the rest of my graduation committee: Roel Baets, Klaus Boller, Jennifer Herek and Klaus Petermann for their valuable input, time and efforts in reviewing this thesis.

I would like to acknowledge all of my IOMS co-workers for being part of an outstanding work atmosphere and for all of their assistance. A special thanks goes to my officemate Feridun Ay, who was always there to assist and answer questions, even when he was busy with several other things. His work on building the loss measurement setup and thin film characterization was an important contribution to this thesis, and he provided valuable advice on measurements and simulations. Most of all I appreciate the many coffee breaks, the discussions about living abroad and his friendship. I would also like to express a specific thanks to my other co-workers in the active devices sub-group: Dimitri Geskus, Laura Agazzi, Jing Yang, Abu Aravazhi, Marko van Dalfsen and Christos Grivas for their help and friendship. My particular appreciation goes to Dimitri for his handiness in the lab, help with the optical setups (somehow knowing where everything was at all times) and making sure we didn't get too serious about work. And also particularly Laura, who helped with many enjoyable loss measurements and lifetime measurements and remained a positive person to work with, even during CLEO deadlines. An additional thanks to Jing for many nice conversations and not battling too hard for the equipment when we had to share. Also much appreciation to the old members of the sub-group Amaia Uranga and particularly Tom Blauwendraat for laying the important groundwork for the results achieved in this thesis.

I would like to express my appreciation to the rest of the IOMS scientific staff, including Alfred Driessen, Hugo Hoekstra and René de Ridder for their assistance and ideas and particularly Paul Lambeck for sharing his big corner office with a Canadian and sharing his experience in Er-doped amplifiers and lasers in many useful discussions. A special thanks goes to Rita ter Weele-Stokkers for her patience, her assistance and making sure everything was always looked after. I also specifically thank Meindert Dijkstra who took over the processing towards the end of my project and did an excellent job, helping to fabricate the final devices and freeing up a lot of time during the busy final months. I am also grateful to Gabriël Sengo for his good spirits and his timely processing advice. Certainly not least, I would like to thank Anton Hollink for always being friendly and helpful and making sure technical issues were solved quickly. The group would not run nearly as effectively without you. I thank Henk van Wolferen for his technical support, sense of humour and great help with the cover photos on this

thesis. I would also like express my gratitude to the other members of the IOMS group, Marcel Hoekman, Fei Sun, Chaitanya Dongre, Lasse Kauppinen, Nur Ismail, Edward Bernhardi, So Van Pham, Fehmi Civitci, Imran Akca, Francois Parsy and Leo Chauvin for a great atmosphere, many useful discussions, fun outings and a chance to learn a lot about different cultures. Thanks to Edward for many interesting discussions over the last year and help with the amplifier simulations. And much appreciation goes to Marcel for his assistance with software and design. A special thanks to past IOMS members Edwin Klein, Ronald Dekker, Gamar Hussein, Wico Hopman, Douwe Geuzebroek, Arne Leinse, and Murali Balakrishnan for invaluable help when I was learning my way. Ronald and Edwin in particular offered a lot of help and a few good jokes along the way. In addition, I would like to thank the floor 8 guys: Chris Roeloffzen, Leimeng Zhuang and David Marpaung for useful discussions and sharing equipment.

I would like to thank the various project partners from the Institut für Laser-Physik at the Universität Hamburg, the École Polytechnique Fédérale de Lausanne, the Instituto de Optica at CSIC in Madrid, Vacotec and PhoeniX with whom we collaborated on the European PI-OXIDE project. I would particularly like to express my appreciation to Günter Huber, Hanno Scheife, Klaus Petermann, Andreas Kahn, Sebastian Heinrich and Henning Kühn from the University of Hamburg for their collaboration on sesquioxide amplifiers and lasers. In addition a very big thank you goes to PhoeniX, our neighbours in Enschede. I especially thank Arjen Bakker and Remco Stoffer for their help and direction on the project. A major thanks goes to Remco for his work on the device design. Your patience, hard work and ideas for the laser and splitter designs were a big reason why the project was successful in the end. I would also like to express my appreciation to the companies LioniX and Xio Photonics for their technical support and assistance.

My thanks goes out to Mathilde Gay, Marcia Costa e Silva, Laurent Bramerie, Jean-Claude Simon, and all others who helped out at ENSSAT in Lannion, where the 170 Gbit/s transmission experiments were carried out. You were a very welcoming group of people to work with and I enjoyed my two visits in France, which even included attending the Christmas party. A special thanks to Mathilde for your time with the experiments, organization and input. I would also like to thank Günther Roelkens and Roel Baets from Ghent University for their recent collaboration on combining active and passive devices. We learned a great deal in these first experiments and it should lead to some very interesting work.

Many thanks to all of the MESA+ cleanroom staff, including Gerard Roelofs, Ite-Jan Hoolsema, Ton Jenneboer, Peter Linders, Hans Mertens, Marion Nijhuis-Groen, Samantha Ooijman-Geerdink, Eddy Ruiter, Huib van Vossen, Robert Wijn, Rene Wolf and Dominique Altpeter for their assistance and good humour throughout my time here. I would especially like to thank Peter Linders for his assistance with the etching equipment.

I would like to thank the IEEE LEOS Benelux student board members past and present, including Philippe, Milan, Dimitri, Laura, Bram, Patryk, Kivilcim, Toh, Wouter, Christophe, Cathy, Ronald, Bas, Els and Katrien who were all fun and positive to work with.

I appreciate the support of all my friends in the Netherlands, specifically Barbara, Katja, Chrissi, Marcel, Malte, Paul, Suzanne, Denis, Katya, Domi, Zhófi, Uros, Mila, Yana, Markus, Pavel, Alice, Natalie, Vas, Hichem, Didem, Semih, Peter, Connie,

Aimee, Federica, Amber, Adam, Des and Clare. There are way too many tales to mention all of them here. Thanks to Denis and Katya for an amazing year and a half together as a “family” at Rembrandtlaan and trips together, including London, Düsseldorf with Lenochka Belochka and Russia. A special acknowledgement goes to my Lions teammates, including my 3rd division championship linemates Hans and Marco, my fellow Canadian Paul “the Terrier” and especially Hans, Eric, Jeroen and Yvo for showing me a true sense of humour. I would like to acknowledge my many housemates at the Deurningerstraat, including Natcha, Romén, Neiler, Dave and Markus (seems like a long time ago!), for keeping things interesting. And I would like to thank those in Utrecht for making the first year one of the best, including Marloes, Gerry, Jim and of course Alex.

I would like to acknowledge my M.A.Sc. supervisor Andy Knights at McMaster University in Canada for encouraging me to do a Ph.D., giving helpful advice and providing many important Maple Leafs, Blue Jays and Raptors updates. I would also like to mention my great friends in Canada, especially Rory, Erin, Amy, Mikk, Alex, Keren, Lenny, Kenny and Banksy. And most importantly I thank my family, including mom, dad, Sarah, Jenn, Andrea, Steve, Todd, James, Marion, Miles, Tabitha and Natalie for their encouragement and support and for keeping me honest.

List of Publications

Peer-Reviewed Journal Articles

Published

1. K. Wörhoff, J. D. B. Bradley, F. Ay, D. Geskus, T. P. Blauwendraat, and M. Pollnau, "Reliable low-cost fabrication of low-loss $Al_2O_3:Er^{3+}$ waveguides with 5.4-dB optical gain," *IEEE Journal of Quantum Electronics*, vol. 45, no. 5, pp. 454-461, 2009.
2. A. Kahn, S. Heinrich, H. Kühn, K. Petermann, J. D. B. Bradley, K. Wörhoff, M. Pollnau, and G. Huber, "Low threshold monocrystalline Nd:$(Gd,Lu)_2O_3$ channel waveguide laser," *Optics Express*, vol. 17, no. 6, pp. 4412-4418, 2009.
3. A. Kahn, H. Kühn, S. Heinrich, K. Petermann, J. D. B. Bradley, K. Wörhoff, M. Pollnau, Y. Kuzminykh, and G. Huber, "Amplification in epitaxially grown Er:$(Gd, Lu)_2O_3$ waveguides for active integrated optical devices," *Journal of the Optical Society of America B*, vol. 25, no. 11, pp. 1850-1853, 2008.
4. J. D. B. Bradley, F. Ay, K. Wörhoff, and M. Pollnau, "Fabrication of low-loss channel waveguides in Al_2O_3 and Y_2O_3 layers by inductively coupled plasma reactive ion etching," *Applied Physics B*, vol. 89, no. 2-3, pp. 311-318, 2007.

Submitted

5. J. D. B. Bradley, R. Stoffer, L. Agazzi, F. Ay, K. Wörhoff, and M. Pollnau, "Integrated $Al_2O_3:Er^{3+}$ zero-loss optical power splitter," submitted to *IEEE Photonics Technology Letters*, September 2009.
6. J. D. B. Bradley, M. Costa e Silva, M. Gay, L. Bramerie, A. Driessen, K. Wörhoff, J. C. Simon, and M. Pollnau, "170 Gbit/s transmission in an erbium-doped waveguide amplifier on silicon," submitted to *Optics Express*, September 2009.
7. J. D. B. Bradley, R. Stoffer, L. Agazzi, F. Ay, K. Wörhoff, and M. Pollnau, "Integrated $Al_2O_3:Er^{3+}$ ring lasers on silicon with wide wavelength selectivity," submitted to *Optics Letters*, September 2009.
8. H. Kühn, S. Heinrich, A. Kahn, K. Petermann, J. D. B. Bradley, K. Wörhoff, M. Pollnau and G. Huber, "Monocrystalline Yb^{3+}:$(Gd,Lu)_2O_3$ channel waveguide laser at 976.8 nm," submitted to *Optics Letters*, July 2009.
9. J. D. B. Bradley, L. Agazzi, D. Geskus, F. Ay, K. Wörhoff, and M. Pollnau, "Gain bandwidth of 80 nm and 2 dB/cm peak gain in $Al_2O_3:Er^{3+}$ optical amplifiers on silicon," submitted to *Journal of the Optical Society of America B*, March 2009.

International Conferences

Proceedings

10. F. Ay, A. Uranga, J. D. B. Bradley, K. Wörhoff, R. M. de Ridder, and M. Pollnau, "Focused ion beam nano-structuring of Bragg gratings in Al_2O_3 channel waveguides," *Proceedings of the First International Workshop on FIB for Photonics*, R.M. de Ridder, F. Ay, and L.J. Kauppinen, eds. (University of Twente, Enschede, 2008), pp. 48-50.
11. K. Wörhoff, J. D. B. Bradley, F. Ay, D. Geskus, T. Blauwendraat, and M. Pollnau, "Optimization of Al_2O_3:Er^{3+} waveguide technology for active integrated optical devices," *Silicon Photonics and Photonic Integrated Circuits*, G.C. Righini, S.K. Honkanen, L. Pavesi, and L. Vivien, eds., Proceedings of the SPIE, vol. 6996, pp. 699618/1-8, 2008.
12. J. D. B. Bradley, F. Ay, T. Blauwendraat, K. Wörhoff, and M. Pollnau, "Rare-earth-ion-doped Al_2O_3 waveguides for active integrated optical devices," *Proceedings of the International Conference on Lasers, Applications, and Technologies*, Minsk, Belarus, 2007, V.A. Orlovich, V. Panchenko, and I.A. Scherbakov, eds., Proceedings of the SPIE, vol. 6731, 67310A, 2007.
13. J. D. B. Bradley, F. Ay, K. Wörhoff, and M. Pollnau, "Reactive ion etching of Y_2O_3 films applying F-, Cl-, and Cl/Br-based inductively coupled plasmas," *ECS Transactions*, vol. 3, no. 11, pp. 117-124, 2006.

Invited and Contributed Papers

14. F. Ay, L. J. Kauppinen, J. D. B. Bradley, K. Wörhoff, R. M. de Ridder, and M. Pollnau, "Focused ion beam milled on-chip resonator nanostructures for applications in rare-earth-ion-doped Al_2O_3 active waveguides," *The 22nd Annual Meeting of the IEEE Photonics Society*, Antalya, Turkey, 2009, paper TuDD 5.
15. M. Pollnau, J. D. B. Bradley, L. Agazzi, E. Bernhardi, F. Ay, K. Wörhoff, and R. M. de Ridder, "Al_2O_3:Er^{3+} as a new platform for active integrated optics", *International Conference on Transparent Optical Networks*, São Miguel, Azores, Portugal, 2009, paper We.D2.1, Invited Paper.
16. J. D. B. Bradley, L. Agazzi, F. Ay, K. Wörhoff, and M. Pollnau, "High-performance Al_2O_3:Er^{3+} integrated optical amplifiers", *International Laser Physics Workshop*, Barcelona, Spain, 2009, Invited Paper.
17. J. D. B. Bradley, L. Agazzi, D. Geskus, F. Ay, K. Wörhoff, and M. Pollnau, "2.0 dB/cm gain in an Al_2O_3:Er^{3+} waveguide on silicon," *Conference on Lasers and Electro-Optics*, Baltimore, Maryland, 2009, Technical Digest (Optical Society of America, Washington, DC 2009), paper CMW5.
18. J. D. B. Bradley, M. Gay, J. C. Simon, K. Wörhoff, and M. Pollnau, "40 Gbit/s transmission in a silicon-compatible Al_2O_3:Er^{3+} integrated optical amplifier,"

Conference on Lasers and Electro-Optics Europe, Munich, Germany, 2009, Conference Digest, paper CI4.3.

19. F. Ay, J. D. B. Bradley, K. Wörhoff, R. M. de Ridder, and M. Pollnau, "Optical performance investigation of focused ion beam nanostructured integrated Fabry-Perot microcavities in Al_2O_3," *Conference on Lasers and Electro-Optics Europe*, Munich, Germany, 2009, Conference Digest, paper CK.P.1.
20. J. D. B. Bradley, L. Agazzi, D. Geskus, F. Ay, K. Wörhoff, and M. Pollnau, "Higher gain in 977-nm-pumped $Al_2O_3:Er^{3+}$ integrated optical amplifiers," *Conference on Lasers and Electro-Optics Europe*, Munich, Germany, 2009, Conference Digest, paper CE.4.
21. L. Agazzi, J. D. B. Bradley, F. Ay, A. Kahn, H. Scheife, G. Huber, R. M. de Ridder, K. Wörhoff, and M. Pollnau, "Energy migration governs upconversion losses in Er^{3+}-doped integrated amplifiers," *Conference on Lasers and Electro-Optics Europe*, Munich, Germany, 2009, Conference Digest, paper CE.3.
22. F. Ay, J. D. B. Bradley, D. Geskus, K. Wörhoff, and M. Pollnau, "Towards rare-earth-ion-doped Al_2O_3 active integrated optical devices," *International Symposium on Modern Optics and its Applications*, Bandung, Indonesia, 2007, Program and Abstracts, pp. 63-66, Invited Paper.
23. A. Kahn, H. Kühn, S. Heinrich, T. Gün, F. Tellkamp, K. Petermann, J. D. B. Bradley, F. Ay, K. Wörhoff, M. Pollnau, Y. Kuzminykh, Y. Luo, P. Hoffmann, and G. Huber, "In-band pumping of epitaxially grown Er:(Gd, $Lu)_2O_3$ waveguides for active integrated optical devices," *EPS-QEOD Europhoton Conference on Solid-State and Fiber Coherent Light Sources*, Paris, France, 2008, Conference Digest, paper THoD.2.
24. K. Wörhoff, J. D. B. Bradley, L. Agazzi, D. Geskus, F. Ay, A. Kahn, H. Scheife, K. Petermann, G. Huber, and M. Pollnau, "Energy-transfer upconversion in $Al_2O_3:Er^{3+}$ thin layers," *International Workshop on Advanced Spectroscopy and Optical Materials*, Gdansk, Poland, 2008, Abstracts, paper 6-O-3.
25. L. Agazzi, J. D. B. Bradley, F. Ay, K. Wörhoff, and M. Pollnau, "Spectroscopy and gain in Al_2O_3:Er waveguides," *International Conference on Luminescence*, Lyon, France, 2008, Book of Abstracts, paper TuA2-O2.
26. F. Ay, A. Uranga, J. D. B. Bradley, K. Wörhoff, R. M. de Ridder, and M. Pollnau, "Focused ion beam nano-structuring of Bragg gratings in Al_2O_3 channel waveguides," *The FIB for Photonics Workshop*, Eindhoven, The Netherlands, 2008, Session 4, Paper 2.
27. L. Agazzi, J. D. B. Bradley, F. Ay, K. Wörhoff, and M. Pollnau, "Al_2O_3:Er waveguide amplifiers for Si-technology compatible integrated optical applications," *ePIXnet Spring School on Technology for Photonics Integration*, Portoferraio/Elba, Italy, 2008, Book of Abstracts, p. 66.
28. J. D. B. Bradley, L. Agazzi, D. Geskus, T. Blauwendraat, F. Ay, K. Wörhoff, and M. Pollnau, "Investigation of optical gain in Al_2O_3:Er channel waveguide amplifiers," *Conference on Lasers and Electro-Optics*, San Jose, California, 2008, Technical Digest (Optical Society of America, Washington, DC 2008), paper JTuA30.

29. D. Geskus, J. D. B. Bradley, S. Aravazhi, K. Wörhoff, and M. Pollnau, "Poor man's channel waveguide laser: $KY(WO_4)_2$:Yb," *Conference on Lasers and Electro-Optics*, San Jose, California, 2008, Technical Digest (Optical Society of America, Washington, DC 2008), paper CTuS4.

30. A. Kahn, T. Gün, B. Ileri, H. Kühn, K. Petermann, G. Huber, J. D. B. Bradley, F. Ay, K. Wörhoff, M. Pollnau, Y. Luo, and P. Hoffmann, "Mono-crystalline rare earth doped $(Gd, Lu)_2O_3$ waveguiding films produced by pulsed laser deposition and structured by reactive ion etching," *Conference on Lasers and Electro-Optics*, San Jose, California, 2008, Technical Digest (Optical Society of America, Washington, DC 2008), paper CTuS1.

31. K. Wörhoff, J. D. B. Bradley, F. Ay, D. Geskus, T. Blauwendraat, and M. Pollnau, "Optimization of Al_2O_3:Er waveguide technology for active integrated optical devices," *Photonics Europe,* Strasbourg, France, 2008, Technical Programme, Conference "Silicon Photonics and Photonic Integrated Circuits", Session 10 "Active Waveguides and Devices II", p. 43, paper 6996-43.

32. J. D. B. Bradley, D. Geskus, T. Blauwendraat, F. Ay, K. Wörhoff, M. Pollnau, A. Kahn, H. Scheife, K. Petermann, and G. Huber, "Growth, micro-structuring, spectroscopy, and optical gain in as-deposited Al_2O_3:Er waveguides," *Advanced Solid-State Photonics Conference*, Nara, Japan, 2008, paper WB10.

33. F. Ay, J. D. B. Bradley, W. C. L. Hopman, V. J. Gadgil, R. M. de Ridder, K. Wörhoff, and M. Pollnau, "Focused-ion-beam nano-structuring of Al_2O_3 dielectric layers for photonic applications," *International Conference on Micro- and Nano-Engineering*, Copenhagen, Denmark, 2007, Book of Abstracts, pp. 627-628.

34. J. D. B. Bradley, F. Ay, K. Wörhoff, and M. Pollnau, "Reactive ion etching of low-loss channel waveguides in Al_2O_3 and Y_2O_3 layers," *International Conference on Micro- and Nano-Engineering*, Copenhagen, Denmark, 2007, Book of Abstracts, pp. 375-376.

35. J. D. B. Bradley, F. Ay, K. Wörhoff, and M. Pollnau, "Low-loss rib waveguides in Al_2O_3 layers for active integrated optical devices," *Conference on Lasers and Electro-Optics Europe*, Munich, Germany, 2007, Conference Digest, paper CE7-6-THU.

36. F. Ay, J. D. B. Bradley, T. Blauwendraat, K. Wörhoff, and M. Pollnau, "Rare-earth-ion-doped Al_2O_3 waveguides for active integrated optical devices," *International Conference on Lasers, Applications, and Technologies*, Minsk, Belarus, 2007, Conference Program, paper L01/II-3.

37. K. Wörhoff, J. D. B. Bradley, F. Ay, and M. Pollnau, "Low-loss Al_2O_3 waveguides for active integrated optics," *Conference on Lasers and Electro-Optics*, Baltimore, Maryland, 2007, Technical Digest (Optical Society of America, Washington, DC 2007), paper CMW5.

38. J. D. B. Bradley, F. Ay, K. Wörhoff, and M. Pollnau, "Al_2O_3 and Y_2O_3 waveguides as building blocks for active integrated photonic devices," *ePIXnet Winter School on Applications of Photonic Integration*, Pontresina, Switzerland, 2007.

39. J. D. B. Bradley, F. Ay, K. Wörhoff, and M. Pollnau, "Reactive ion etching of Y_2O_3 films applying F-, Cl-, and Cl/Br-based inductively coupled plasmas," International

Conference of the Electro-Chemical Society, Cancun, Mexico, 2006, Meeting Abstracts (MA2006-02, ISSN 1091-8213), Abstract 1350.

40. F. Ay, K. Wörhoff, J. Bradley, and M. Pollnau, "Reliable fabrication of low-loss Al_2O_3 waveguides for active integrated optics," *EPS-QEOD Europhoton Conference on Solid-State and Fiber Coherent Light Sources*, Pisa, Italy, 2006, Europhysics Conference Abstracts, vol. 30J, paper TuC2.

National Conferences

Proceedings

41. F. Ay, J. D. B. Bradley, R. M. de Ridder, K. Wörhoff, and M. Pollnau, "Bragg gratings in Al_2O_3 channel waveguides by focused ion beam milling," *Proceedings of the Thirteenth Annual Symposium of the IEEE/LEOS Benelux Chapter*, Enschede, The Netherlands, 2008, pp. 215-217.
42. J. D. B. Bradley, L. Agazzi, D. Geskus, F. Ay, K. Wörhoff, M. Pollnau, and W. M. Arnoldbik, "Enhanced gain in Er-doped Al_2O_3 channel waveguide amplifiers," *Proceedings of the Thirteenth Annual Symposium of the IEEE/LEOS Benelux Chapter*, Enschede, The Netherlands, 2008, pp. 131-134.
43. L. Agazzi, J. D. B. Bradley, F. Ay, A. Kahn, H. Scheife, K. Petermann, G. Huber, R. M. de Ridder, K. Wörhoff, and M. Pollnau, "Upconversion spectroscopy of $Al_2O_3:Er^{3+}$," *Proceedings of the Thirteenth Annual Symposium of the IEEE/LEOS Benelux Chapter*, Enschede, The Netherlands, 2008, pp. 51-53.
44. D. Geskus, J. D. B. Bradley, S. Aravazhi, K. Wörhoff, and M. Pollnau, "Fibre top-loaded channel waveguide laser in $KY(WO_4)_2:Yb^{3+}$," *Proceedings of the Annual Workshop of the IEEE/LEOS Benelux Chapter*, Brussels, Belgium, 2008 (Vrije Universiteit Brussel, Brussels, 2008), pp. 13-14.
45. J. D. B. Bradley, L. Agazzi, D. Geskus, F. Ay, K. Wörhoff, and M. Pollnau, "Reactively co-sputtered $Al_2O_3:Er^{3+}$ for active photonic devices," *Proceedings of the Annual Workshop of the IEEE/LEOS Benelux Chapter*, Brussels, Belgium, 2008 (Vrije Universiteit Brussel, Brussels, 2008), pp. 9-10.
46. J. D. B. Bradley, D. Geskus, T. Blauwendraat, F. Ay, K. Wörhoff, and M. Pollnau, "Optimized deposition and structuring of reactively co-sputtered $Al_2O_3:Er^{3+}$ waveguide layers with net optical gain," *Proceedings of the Twelfth Annual Symposium of the IEEE/LEOS Benelux Chapter*, Brussels, Belgium, 2007, pp. 107-110.
47. A. Uranga, F. Ay, J. D. B. Bradley, R. M. de Ridder, K. Wörhoff, and M. Pollnau, "Focused ion beam nano-structuring of photonic Bragg gratings in Al_2O_3 waveguides," *Proceedings of the Twelfth Annual Symposium of the IEEE/LEOS Benelux Chapter*, Brussels, Belgium, 2007, pp. 247-250.
48. D. Geskus, J. D. B. Bradley, S. Aravazhi, K. Wörhoff, and M. Pollnau, "Progress on micro-structured $KY(WO_4)_2$ waveguides for optically active devices," *Proceedings of the Twelfth Annual Symposium of the IEEE/LEOS Benelux Chapter*, Brussels, Belgium, 2007, pp. 103-106.

49. J. D. B. Bradley, F. Ay, K. Wörhoff, and M. Pollnau, "Al_2O_3 and Y_2O_3 thin films for active integrated optical waveguide devices," *Proceedings of the Eleventh Annual Symposium of the IEEE/LEOS Benelux Chapter*, Eindhoven, The Netherlands, 2006, pp. 113-116.

Contributed Papers

50. K. Wörhoff, J. D. B. Bradley, F. Ay, D. Geskus, S. Aravazhi, and M. Pollnau, "Actively doped dielectric materials for on-chip integrated light sources," *Fotonica Evenement*, Den Haag, The Netherlands, 2007.